

RECEIVED

NOV 17 1995

OSTI

Low Frequency, Electrodynamics Simulation of Kinetic Plasmas with the Darwin Direct Implicit Particle-in-Cell (DADIPIC) Method

Matthew Richard Gibbons
(Ph.D. Thesis)

June 1995



DISCLAIMER

This document was prepared as an account of work sponsored by an agency of the United States Government. Neither the United States Government nor the University of California nor any of their employees, makes any warranty, express or implied, or assumes any legal liability or responsibility for the accuracy, completeness, or usefulness of any information, apparatus, product, or process disclosed, or represents that its use would not infringe privately owned rights. Reference herein to any specific commercial product, process, or service by trade name, trademark, manufacturer, or otherwise, does not necessarily constitute or imply its endorsement, recommendation, or favoring by the United States Government or the University of California. The views and opinions of authors expressed herein do not necessarily state or reflect those of the United States Government or the University of California, and shall not be used for advertising or product endorsement purposes.

This report has been reproduced
directly from the best available copy.

Available to DOE and DOE contractors from the
Office of Scientific and Technical Information
P.O. Box 62, Oak Ridge, TN 37831
Prices available from (615) 576-8401, FTS 626-8401

Available to the public from the
National Technical Information Service
U.S. Department of Commerce
5285 Port Royal Rd.,
Springfield, VA 22161

**Low Frequency, Electrodynamics Simulation of
Kinetic Plasmas with the DARwin Direct
Implicit Particle-in-Cell (DADIPIC) Method**

**Matthew Richard Gibbons
(Ph.D.Thesis)**

Manuscript date: June 1995

LAWRENCE LIVERMORE NATIONAL LABORATORY
University of California • Livermore, California • 94551



MASTER
DISTRIBUTION OF THIS DOCUMENT IS UNLIMITED
D&C

DISCLAIMER

Portions of this document may be illegible in electronic image products. Images are produced from the best available original document.

Low Frequency, Electrodynamic Simulation of Kinetic Plasmas with the
Darwin Direct Implicit Particle-in-Cell (DADIPIC) Method

By

Matthew Richard Gibbons

B.S. (Purdue University) 1982

M.S. (Air Force Institute of Technology) 1984

DISSERTATION

Submitted in partial satisfaction of the requirements for the degree of

DOCTOR OF PHILOSOPHY

in

ENGINEERING—APPLIED SCIENCE

in the

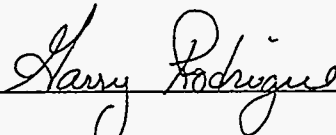
OFFICE OF GRADUATE STUDIES

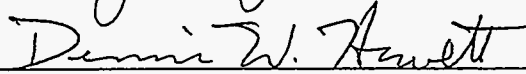
of the

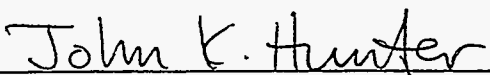
UNIVERSITY OF CALIFORNIA

DAVIS

Approved:







Committee in Charge

1995

Matthew Richard Gibbons
June 1995
Engineering Applied Science

Low Frequency, Electrodynamic Simulation of Kinetic Plasmas with the Darwin Direct
Implicit Particle-in-Cell (DADIPIC) Method

Abstract

This dissertation describes a new algorithm for simulating low frequency, kinetic phenomena in plasmas. Darwin Direct Implicit Particle-in-Cell (DADIPIC), as its name implies, is a combination of the Darwin and direct implicit methods. One of the difficulties in simulating plasmas lies in the enormous disparity between the fundamental scale lengths of a plasma and the scale lengths of the phenomena of interest. The objective is to create models which can ignore the fundamental constraints without eliminating relevant plasma properties. Over the past twenty years several PIC methods have been investigated for overcoming the constraints on explicit electrodynamic PIC. These models eliminate selected high frequency plasma phenomena while retaining kinetic phenomena at low frequency. This dissertation shows that the combination of Darwin and Direct Implicit allows them to operate better than they have been shown to operate in the past.

Through the Darwin method the hyperbolic Maxwell's equations are reformulated into a set of elliptic equations. Propagating light waves do not exist in the formulation so the Courant constraint on the time step is eliminated. The Direct Implicit method is applied only to the electrostatic field with the result that electrostatic plasma oscillations do not have to be resolved for stability. With the elimination of these constraints spatial and temporal discretization can be much larger than that possible with explicit, electrodynamic PIC. The code functions in a two dimensional Cartesian region and has been implemented with all components of the particle velocities, the E-field, and the B-field. Internal structures, conductors or dielectrics, may be placed in the simulation region, can be set at desired potentials, and driven with specified currents.

The linear dispersion and other properties of the DADIPIC method are investigated in order to deduce guidelines for its use. Linear theory and simulations verifying the theory are used to generate the desired guidelines as well as show the utility of DADIPIC for a wide range of low frequency, electromagnetic phenomena. The separation of the fields

has made the task of predicting algorithm behavior easier and produced a robust method without restrictive constraints.

Finally, the code is used to simulate Inductively Coupled Plasmas similar to those used for plasma processing in the microelectronics industry. Collisionless heating in these low frequency systems is one of the important kinetic effects for which DADIPIC is well suited. Agreement with 1-D linear, analytic theory is shown. The utility of DADIPIC is shown in simulation results for 2-D and nonlinear effects which are not amenable to analytic solution.

Contents

Abstract	iii
List of Figures	vii
List of Tables	xi
Acknowledgements	xii
1 Introduction	1
1.1 Explicit Electrodynamic PIC	5
1.1.1 Algorithm	5
1.1.2 Constraints	7
1.2 Low Frequency, Kinetic Phenomena	8
1.3 Long Time Scale Simulation Methods	9
1.3.1 Physics Reduction Methods	10
1.3.2 Implicit Methods	12
1.3.3 The DARwin Direct Implicit (DADIPIC) Method	14
1.4 Overview of Chapters	14
2 Implementation of DARwin Direct Implicit Particle-in-Cell	15
2.1 Direct Implicit Electrostatic Method	15
2.1.1 Particle Integration	15
2.1.2 Differencing of the Field Equation and Boundary Conditions	17
2.1.3 Numerical Solution of the Field Equation	21
2.2 Darwin Method	24
2.2.1 Field Equations	24
2.2.2 Streamlined Darwin Field (SDF) Formulation	26
2.2.3 Boundary Conditions on A_y , B_y , and \mathbf{E}_{sol}	26
2.2.4 Numerical Solution of the SDF Equations	28
2.3 Dielectrics	31
2.4 DADIPIC Algorithm and GYMNOS	32

3	Theory of DADIPIIC Operation	41
3.1	Effect of the Direct Implicit Method	41
3.1.1	Accuracy of the Field Equation	41
3.1.2	Linear Kinetic Theory	44
3.1.3	Conditions for a Nonsingular Implicit Electrostatic Field Equation Matrix	49
3.2	Effect of the Darwin Method	51
4	Characterization of DADIPIIC with Doubly Periodic Test Cases	56
4.1	Uniform Plasma: Fluctuations	56
4.2	Uniform Plasma: Change in Energy due to Fluctuations	58
4.3	Uniform Plasma: Drift Through the Grid	61
4.4	Uniform Plasma: Imposed Magnetic Field	62
4.5	Large Density Gradients: Expanding Slab	66
4.6	Large Density Gradients: Electron Beam Filamentation	68
4.7	DADIPIIC mode of operation	70
5	Heating in Inductive Plasma Processing Reactors	87
5.1	Plasma Processing	87
5.2	Collisional and Collisionless Heating	90
5.2.1	Collisional Heating	91
5.2.2	Collisionless Heating: Half-Infinite Plasma	93
5.2.3	Collisionless Heating: Finite Plasma	96
5.3	1-D Simulation of Collisionless Heating	99
5.4	2-D Simulation of Collisionless Heating	102
5.5	Collisionless Heating in a 2-D Idealized ICP Reactor	105
5.5.1	Simulation with Stationary Ion Background	105
5.5.2	Simulation with Sheath and Plasma Absorption at the Walls	106
5.6	ICP Reactor Simulation	110
5.6.1	Simulation Methodology	111
5.6.2	Example of Methodology using Analytic Theory	114
5.7	Summary	117
6	Conclusion	141
A	Calculation of Dispersion Relations and the Spectral Density	144
	Bibliography	150

List of Figures

2.1	Position of the surfaces for a Gaussian box around a node at the surface of a conducting boundary.	36
2.2	Region for testing the numerical solution of the implicit electrostatic field equation a) the boundary conditions b) the spatial variation of X^{xx} ($a=.255$ and $j=3.74$).	37
2.3	Test results of the numerical solution to the implicit electrostatic field equation a) the potential calculated by the bi-conjugate gradient routine ($a=-.90$ and $j=.90$) and b) the difference between the bi-conjugate gradient and DADI solutions ($a=-6.6e-10$ and $j=5.3e-10$).	38
2.4	Results of the CEDADI test: a) the original \mathbf{E}_{sol} (longest vector=.809) and b) the spatial variation of μ ($a=.200$ and $j=3.80$)	39
2.5	Results of the CEDADI test: a) vector plot of Ξ (longest vector=1.19) b) contour plot of ψ ($a=-1.53$ and $j=1.53$), and c) vector plot of $\mathbf{E}_{sol}^o - \mathbf{E}_{sol}$ (longest vector=.0907)	40
3.1	Comparison of strict differencing to simplified differencing. The difference in the implicit susceptibility terms of the implicit field equation is plotted for a harmonically varying potential. The terms agree well for wavelengths greater than $5\Delta x$	53
3.2	Maximum $\omega_{ce}\Delta t$ to guarantee nonsingular matrix for the implicit electrostatic field equation. This is a sufficient but not necessary condition.	54
3.3	Magnitude of the least damped mode vs $\omega_{ce}\Delta t$ from the linear analysis of the Darwin field equation and finite difference equations of motion in a constant B-field.	55
4.1	Comparison of DADIPIC spectral density results to predictions from continuous and PIC linear theory for uniform plasma. a) $\Delta x/\lambda_{De} = .5$ and $\omega_{pe}\Delta t = .2$, b) $\Delta x/\lambda_{De} = 5$. and $\omega_{pe}\Delta t = .2$, c) $\Delta x/\lambda_{De} = 5$. and $\omega_{pe}\Delta t = 5$. The DADIPIC results are in reasonable agreement with PIC linear theory.	72

4.2	Time histories of particle and field energies for a doubly periodic, uniform plasma DADIPIC simulation with $\Delta x/\lambda_{De} = 10$. and $\omega_{pe}\Delta t = 5$: a) total system energy, b) E_{irr} field energy, c) E_{sol} field energy, and d) B-field energy. All are normalized to the initial total system energy E_o . Notice the much smaller magnitude of the electromagnetic field energies compared to the electrostatic field energy.	73
4.3	Contour plot of $\Delta E/E_o N$ in $\Delta x/\lambda_{De}$ and $\omega_{pe}\Delta t$ space. The dots are the locations of the simulations run to generate the contours. The upper left hand region and the region near $v_{th}\Delta t/\Delta x = 1$ show heating. The region between with the dashed contours lines has cooling. Simulations were not run in the region where $v_{th}\Delta t/\Delta x > 1$	74
4.4	Particle velocity distributions vs v/v_{th} resulting for different values of $\omega_{pe}\Delta t$: a) in the first heating region where $3v_{th}\Delta t/\Delta x < 1$, b) along the energy conserving contour where $3v_{th}\Delta t/\Delta x \simeq 1$, c) in the cooling region, d) in the second heating region where $v_{th}\Delta t/\Delta x = 1$, and e) in the direction out of the simulation plane.	75
4.5	The grid velocity, v_y , and the generated fields, B_x and $E_{sol,y}$, for an electron cyclotron wave initialized in the particle distribution of a DADIPIC simulation.	76
4.6	Electron cyclotron wave dispersion relation for the real part of the frequency. The solid line is the analytic result for the cold magnetoplasma. The points are the DADIPIC results. The error bars are the fwhm of the peaks in the FFT's.	77
4.7	The time evolution of an electron cyclotron wave simulation b) the oscillating B-field, b) the B-field energy with an exponential curve fit, and c) the change in the total system energy normalized to the initial total system energy. . .	78
4.8	Electron cyclotron wave damping rate as the hot species mass is changed. The solid line is the analytic damping, and the dots are damping rates measured from DADIPIC simulations. The simulations were all initialized with the same wavelength, $ck/\omega_{pe} = .6$	79
4.9	Expanding slab simulation: a) density contours showing the expansion of the slab, b) the electrostatic field concentrated near the edge of the slab (longest vector=5.25 V/cm), c) solenoidal E-field (longest vector=.0194 V/cm) and d) B-field (longest vector=4.77e-3 gauss) concentrated in the plasma where currents exist, e) total system energy, f) ion particle phase space with the $c_s + (x - x_i)/t$ dependence for the velocity.	80
4.10	Beam filamentation B-field and particle energies showing the exponential increase of the B-field during growth of the instability: a) the uniform plasma and b) the finite beam.	81
4.11	Beam filamentation growth rates. The solid curve is the theoretical dispersion curve. The large dashed line (uniform plasma) and small dashed line (finite beam) show the grow rates observed in DADIPIC simulations. The lines extend to the minimum wavenumbers available in the simulations.	82

4.12	Beam filamentation electron particle plots for the finite beam: a) beam electrons and b) target electrons. These are snapshots at $\omega_{pe}\Delta t = 1600$ after saturation of the instability where the beam electrons have coalesced into one filament.	83
4.13	Beam filamentation B-field plots for the uniform plasma showing a change in the unstable mode. a) At early time, $\omega_{pe}\Delta t = 320$, a shorter wavelength has the fastest growth rate (longest vector=.0531 gauss). b) At late time, $\omega_{pe}\Delta t = 1600$, the initial mode stabilizes and the slower growing longest wavelength mode dominates (longest vector=.356 gauss).	84
4.14	Beam filamentation total system energy. Even with the large changes in T_e changes in the total system energy are 2% or less.	85
4.15	Recommended operating region (shaded) for DADIPIC in the $\Delta x/\lambda_{De}$ vs $\omega_{pe}\Delta t$ plane. The width of the region depends on the tolerable numerical effect on electron kinetic energy. The region can extend to $\Delta x/\lambda_{De}$ and $\omega_{pe}\Delta t \gg 1$	86
5.1	Idealized capacitively and inductively driven plasma reactors. The rf source drives electrostatic fields between the parallel plates of the capacitive reactor and inductive fields along the coiled antenna of the inductive reactor. The reactors are typically cylindrically symmetric.	118
5.2	Ionization rate constants ($\# \text{ cm}^3/\text{s}$) in Ar versus electron temperature of a Maxwellian distribution from Vahedi[vah93].	119
5.3	Comparison of the fluid and kinetic theories for the power deposition into a plasma versus ν/ω	120
5.4	Contour plot of the power into a finite plasma slab versus the slab width, a , and the skin depth transit parameter, β : a) $\nu/\omega = 0$ and b) $\nu/\omega = 1$. The line across a) is for an electron with $\langle v_x \rangle = 2a\omega/\pi$	121
5.5	Current density versus position from theory and driven E-field versus position from DADIPIC calculation for finite plasmas.	122
5.6	The real and imaginary parts of $I/ I ^2$. The dots and circles are from simulations with the B-field while the Δ s are for simulations where the B-field was turned off.	123
5.7	Picture of the simulation region for the 1-D DADIPIC simulations of inductively couple plasma heating. E_y is specified on the conducting wall while conducting surface boundary conditions are used for all other field quantities. Electrons are specularly reflected off the walls.	124
5.8	Change in the electron thermal energy in the x and y directions for 1-D simulations: a) B-field included in the simulation and b) B-field not included. Essentially no heating occurs in the direction normal to the driven field without the B-field.	125
5.9	$I/ I ^2$ normalized to the vanishingly small driven field value versus v_{osc}/v_{th} : a) the real part and b) the imaginary part. The circles are simulation results. The line in a) is the reduction in electron flux to the wall due to the B-field. The line in b) is where $v_{osc}/c \sim E_y / B_z $	126

5.10	Picture of 2-D periodic simulations where the driven inductive E-field has a sinusoidal variation in z.	127
5.11	Results of the 2-D simulations with the spatial variation of the driving field parallel to the wall. The powers are normalized to the simulation with $k_z = 0$ and the B-field turned off. Simulations without the B-field are Δ s, simulations with the B-field are dots, and the simulation with the B-field and $k_z = 0$ is the horizontal line. Theory not including the B-field is the dashed line.	128
5.12	Picture of the 2-D inductively coupled reactor simulation.	129
5.13	Contours of E_y at the peak of J_y in the antenna in the 2-D ICP simulation with uniform plasma density.	130
5.14	Vector plot of $B_{x,z}$ (largest vector = .177 gauss) at the peak of the driven E-field in the 2-D ICP simulation.	131
5.15	Change in particle total kinetic energy (normalized to the initial energy) for the 2-D ICP simulation with uniform plasma density.	132
5.16	Assumed plasma potential profile for calculating the unresolved sheath potential, V_s . ϕ_{max} is the potential on the most positive conducting wall node.	133
5.17	Density ($\#/cm^3$) profile at the end of the 2-D reactor simulations with the unresolved sheath boundary condition and electron/ion pair volume injection. The reactor dimensions are in cm.	134
5.18	Potential (Volts) profile at the end of the 2-D reactor simulations with the unresolved sheath boundary condition and electron/ion pair volume injection. The reactor dimensions are in cm.	135
5.19	Driven E-field (V/cm) profile at the end of the 2-D reactor simulations with the unresolved sheath boundary condition and electron/ion pair volume injection. The reactor dimensions are in cm.	136
5.20	Time histories of the particle kinetic energies. The electrons loose energy as their particle number decreases and the electrostatic sheath builds. The ions gain energy falling through the sheath. At late time the energy levels off indicating the approach toward equilibrium.	137
5.21	Comparison of the unresolved sheath voltage time histories for simulations with average differences between ion and electron particle numbers of: a) 12 particles, b) 120 particles, and c) 680 particles. The a) simulation has the most noisy V_s even though it was a 1-D simulation with the more particles per cell than the 2-D simulation of c).	138
5.22	Electron velocity distribution (dots) of the 2-D unresolved sheath reactor simulation compared to a Maxwellian distribution (line) at the same temperature.	139
5.23	Picture of the idealized circuit to model a cylindrical ICP as the one turn secondary of a transformer.	140

List of Tables

2.1	Coefficients for the Implicit Field Equation Operator	18
4.1	Change in Energy $\Delta E/E_o N$ in $\Delta x/\lambda_{De}$, $\omega_{pe}\Delta t$ Parameter Space	59
4.2	Change in energy $\Delta E/E_o N$ for a plasma drifting through the grid	62
4.3	Plasma parameters for electron cyclotron wave damping	65
4.4	Real, ω , and imaginary, γ , parts of the frequency from the Darwin dispersion relation in a constant B-field	66
4.5	Species parameters for filamentation simulations	69
5.1	Impedance of the example ICP	116

Acknowledgements

This work is the result of my introduction to particle simulation of plasmas which occurred several years before my return to graduate studies. I must thank my supervisor at the time, John Justice, for assisting me in my request for acceptance to the Air Force's military research associate program. It was this program which sent me for a two year sojourn at the Lawrence Livermore National Laboratory. It was here that I learned about particle simulation while working for Dr. Bert Weinstein. I also was helped in physics and running by Drs. Scott Brandon and Debbie Wojtowicz. During this time I also became aware of the student/employee program at LLNL.

After my tour at the lab was over the Air Force actually decided to use my newly gained skills and sent me to Air Force Weapons Laboratory to work on modeling high power microwaves. So I continued to push particles and advance Maxwell's equations. I consider myself fortunate to have worked with an exceptional group of computationalists Dr. Doug Beason, Dr. Kirk Hackett, Dr. Ray Lemke, Tom Dipp, Carl Sovinec, Dr. Chris Clouse, Chuck Beason, and Les Bowers. I am also grateful to the experimentalists, Drs. Kyle Hendricks, Collins Clarke, and Dale Coleman, who put up with my poking around the lab to find out what was really happening.

Two years at AFWL was enough to complete my obligation to the Air Force. My request for discharge was approved, and I was accepted at LLNL as a student/employee. At this point my friends at the lab steered me toward my choice for a research advisor, Dr. Dennis Hewett. It is through his guidance that I have progressed from a user of codes to a builder of codes and, hopefully, a competent computational physicist. I consider myself very fortunate to have had the chance to learn from and work with Dennis. I must also thank Prof. Garry Rodrigue my thesis advisor for keeping me on the right track. Prof. John Hunter kindly set aside time to serve on both my oral and dissertation committee's. Prof. John DeGroot, Prof. William Hoover, Dr. John Ambrosiano, and Prof. Jean-Jacques Chattot also contributed to make my orals the unique experience that it was.

This work would not have been possible without those who have developed the Darwin and Direct Implicit methods to their present advanced state. In addition I wish to thank Dr. David Anderson for help with the CPDES2 routine and Dr. David Larson who provided help with the CEDADI routine. I must also include the many colleagues,

Dr. Greg DiPeso, Eric Sonnendrucker, Dr. Lou Ann Tung, Dr. Vahid Vahedi, and Michael Lambert, who kept the ideas flowing and made sure our end of the hall was a lively place. I am also grateful to the administrative staff, Christy Shannon and Karen Pangelina, who made sure I did not mess up the really important stuff.

My intellectual journey into science would never have begun without the support of my parents, Richard (Dick) and Antoinette (Dolly) Gibbons. They instilled in me and my siblings Terrace, Rachel, and Tim an interest and excitement about discovering the secrets of the world around us. Thanks for your love and support.

This work was performed under the auspices of the United States Department of Energy by the Lawrence Livermore National Laboratory under contract number W-7405-ENG-48.

Chapter 1

Introduction

In physics we have a wide range of uses for computers including the experimentalist who needs to store and tabulate data, the theorist who wants numerical solutions to complex analytic expressions, and the computationalist who performs numerical experiments. This thesis falls into the last category where the computer is used to simulate physical phenomena based on the discretized form of a mathematical model for the phenomena. Given these discrete equations, we apply numerical methods to solve them as part of a simulation scheme which mimics the physical system. Here the simulation scheme is in the form of an initial value-boundary value problem. The simulation “universe” is initialized in the computer with certain boundary conditions, and the discretized mathematical model is allowed to evolve the system for a specified time. As with analytic theory the relevance of computational results is constrained by the limitations in the mathematical model of the phenomena. Numerical simulation has the advantage of being able to model systems where nonlinear effects, geometric complexities, etc. prevent analytic solutions. The ability to measure any quantity in the system and to simplify systems can lead to physical insight unattainable through experiment.

Because of finite computer resources, we are limited in either the scale (spatial and temporal) of our simulation or the completeness of our mathematical model. We try to include the relevant physical effects with the least computational cost. This dissertation describes a method developed to simulate plasma phenomena which have been hard or impossible to investigate in the past due to computer resource constraints. The thrust is on developing the mathematical model, implementing the model in a code, and characterizing the operation of the code. While care has been taken to find and adapt numerical algorithms

well suited for efficient and fast operation of the method, the objective of the dissertation has not been to remove every extraneous clock cycle from each operation. The developed code has proven to be more than efficient enough to study the phenomena of interest. Further investigation of the method could be used for fine tuning of the numerical algorithms. The objective has also not been to simulate a single phenomena with all of its particular characteristics. The method is designed to simulate a wide range of phenomena. Routines to include the unique features of certain phenomena could be added for future studies of particular cases.

Specifically, a new algorithm, the DARwin Direct Implicit Particle-in-Cell (DADIPIC) method, has been developed to simulate kinetic, low frequency phenomena in plasmas. This algorithm, which combines the features of Direct Implicit PIC[lan83] with the Streamline Darwin Field method[hew87a], provides a flexible, robust alternative to implicit, fully electromagnetic field models. DADIPIC is implemented in a code which functions in a two dimensional x, z region with all three components of the particle velocities, the electric field, and the magnetic field. Internal structures in the simulation region may be conductors or dielectrics, can be set at desired potentials, and driven with specified currents.

Before delving into the specifics of DADIPIC, a review of particle simulation of plasmas will provide a basis for discussion of the differences, advantages, and limitations of the new algorithm compared to other plasma simulation methods. A plasma is a collection of charged particles dense enough to exhibit group behavior; thus, we have the many body problem with electromagnetic force fields. The particles obey the equations of motion

$$\begin{aligned}\dot{\mathbf{x}} &= \mathbf{v} \\ \dot{\mathbf{v}} &= \frac{q}{m} \left[\mathbf{E} + \frac{\mathbf{v} \times \mathbf{B}}{c} \right]\end{aligned}\tag{1.1}$$

To attack the many body problem we turn to statistical mechanics and kinetic theory. In kinetic theory we consider distribution functions which give the number density or probability density, f_α , for particles of species α in phase space (the combination of configuration and velocity space). The mathematical model needed for the plasma distribution depends on the nature of the plasma. While the plasmas of interest to us are dense enough to exhibit collective effects, they are not so dense as to cause correlations between particles. The long range forces due to groups of particles are larger than any effects from nearby particles. The exception to this is binary collisions where two particles approach each other very closely. However, in these plasmas the time spent in a collision is extremely short

compared to the time between collisions. This allows us to use the Boltzmann equation for the change in the distribution with time[kra86].

$$\frac{\partial f_\alpha}{\partial t} + \mathbf{v} \cdot \frac{\partial f_\alpha}{\partial \mathbf{x}} + \frac{\mathbf{F}}{m} \cdot \frac{\partial f_\alpha}{\partial \mathbf{v}} = \frac{\partial f_\alpha}{\partial t}|_{coll} \quad (1.2)$$

where the distribution function is the single particle distribution function. If the collision term on the right hand side of Eq. (1.2) is dropped, we have the Vlasov equation[kra86]. The force, \mathbf{F} , in Eq. (1.2) is an averaged force which does not take into account correlations between particles. For plasmas the force is provided by the electric and magnetic fields which themselves obey a set of partial differential equations, Maxwell's equations,

$$\begin{aligned} \nabla \times \mathbf{E} &= -\frac{1}{c} \frac{\partial \mathbf{B}}{\partial t} & \nabla \cdot \mathbf{D} &= 4\pi\rho \\ \nabla \times \mathbf{B} &= \frac{4\pi}{c} \mathbf{J} + \frac{1}{c} \frac{\partial \mathbf{E}}{\partial t} & \nabla \cdot \mathbf{B} &= 0. \end{aligned} \quad (1.3)$$

The source terms, ρ and \mathbf{J} , are the charge density and current density.

We can work with Eq. (1.2) as it is, or we can get a further reduced description by taking velocity moments of this equation to get the fluid equations. The fluid equations describe the change in time of macroscopic fluid quantities (usually density, velocity, and internal energy).

In many cases the plasma phenomena described by these equations involves non-linear effects and requires boundaries which are not amenable to analytic solutions. For this reason computers have been used to simulate plasmas according to the various descriptions mentioned above. Codes based on the fluid description are faster, but kinetic descriptions are usually needed for correct results given non-Maxwellian distributions and interpenetrating flows. Of course, fluid codes cannot be used to simulate strictly kinetic phenomena. Particle-in-Cell (PIC) simulation has proven to be a successful way of kinetically modeling the particle distribution function by using a number of simulation particles. Each particle has its own position, \mathbf{x} , and velocity, \mathbf{v} , which change according to the forces on the particles due to electromagnetic fields. Particles are loaded into a simulation by sampling a distribution function for the desired initial state of the plasma. The plasma and field quantities are then followed in time. It has been shown that plasma behavior can be reproduced even though the number of simulation particles is orders of magnitude fewer than the number of particles in the actual plasma[bir85]. The objective of these models is to mimic the collective particle behavior without the need to correctly follow the trajectories of the individual particles composing the plasma.

The forces on the particles could be found by summing up the interparticle forces on each particle, but this would involve N^2 operations per time step. A quicker method is to store field quantities on a grid and then interpolate them to the particle positions[hoc65], [yu65]. The grid also designates cells in which the particles reside. Particle quantities (charge density, ρ , and current density, \mathbf{J}) are interpolated to the grid points and are used as sources in the field equations. The interpolation effectively gives the particles a finite size. So particles and fields are smoothed out reducing the statistical noise due to using a relatively small number of simulation particles[bir85]. Note that we now have particles in cells thus justifying the name PIC codes.

The averaged fields on a grid are also in keeping with the Vlasov equation and its averaged force. Since the Vlasov equation has the form of the dynamics of a single particle subject to a force field, we can treat the simulation particles as a system of noninteracting particles under the action of the averaged force field[lib90]. Particles simply obey the single particle equations of motion (1.1). These equations of motion are finite differenced and used to update particle positions and velocities. The field quantities, \mathbf{E} and \mathbf{B} , are stored on the grid and are advanced according to finite difference versions of Maxwell's equations.

The typical time cycle has the following four steps: 1) find the particle forces by interpolating the fields from the grid to the particles, 2) integrate the particle equations of motion, 3) find the field sources by interpolating the particle quantities to the grid, and 4) integrate the field equations. The main differences between PIC codes come down to methods of integrating the particle equations of motion, methods of solving for the fields, interpolation of particle and field quantities, and boundary conditions. The differences are driven by the plasma properties resulting from the particular applications of interest to the investigator. In the remainder of this section the explicit, fully electrodynamic PIC algorithm will be outlined as a basis for concepts used in the development of the Darwin Direct Implicit PIC algorithm. Constraints on the explicit method which are overcome by DADIPIC will be presented. Finally, the motivation for constructing a new method, the need for low frequency, kinetic plasma simulation along with the limitations of previous methods, will be presented.

1.1 Explicit Electrodynamic PIC

The most straight forward and the computationally quickest individual time step involves the explicit finite difference formulation of the equations (1.1) and (1.3). We now have a way to carry out the time advance of the particles and fields in steps 2) and 4) of the time cycle. With this explicit formulation we retain all of the electromagnetic and kinetic behavior of the plasma. However, as with any finite difference advance of a hyperbolic set of equations, constraints on the spatial and temporal discretization are needed in order to avoid numerical instability.

1.1.1 Algorithm

Many sources outline the following widely used second order accurate scheme for fully electrodynamic PIC[bir85]. The particle quantities and fields are time advanced with a leap-frog scheme. The particle positions and the electric field are stored at integer times, the particle velocities are stored at half-integer times, and the magnetic field is stored at both.

Start with \mathbf{E}_j^n , \mathbf{B}_j^n , \mathbf{x}_i^n , $\mathbf{v}_i^{n-1/2}$, and $\mathbf{B}_j^{n-1/2}$

Loop over particles

- 1) Interpolate \mathbf{E}_j^n , \mathbf{B}_j^n to particle i
- 2) Push particle i

$$\begin{aligned}\mathbf{v}_i^{n+1/2} &= \mathbf{v}_i^{n-1/2} + \frac{q\Delta t}{m} \left[\mathbf{E}_i^n + \frac{\mathbf{v}_i^{n+1/2} + \mathbf{v}_i^{n-1/2}}{2c} \times \mathbf{B}_i^n \right] \\ \mathbf{x}_i^{n+1} &= \mathbf{x}_i^n + \Delta t \mathbf{v}_i^{n+1/2}\end{aligned}\tag{1.4}$$

- 3) Interpolate \mathbf{x}_i^{n+1} , $\mathbf{v}_i^{n+1/2}$ to the grid to get ρ_j^{n+1} , $\mathbf{J}_j^{n+1/2}$
- 4) Integrate the field equations

$$\begin{aligned}\mathbf{B}_j^{n+1/2} &= \mathbf{B}_j^{n-1/2} - c\Delta t \nabla \times \mathbf{E}_j^n \\ \mathbf{E}_j^{n+1} &= \mathbf{E}_j^n + c\nabla \times \mathbf{B}_j^{n+1/2} - 4\pi\mathbf{J}_j^{n+1/2} \\ \mathbf{B}_j^{n+1} &= \mathbf{B}_j^{n+1/2} - \frac{c\Delta t}{2} \nabla \times \mathbf{E}_j^{n+1}\end{aligned}\tag{1.5}$$

In these equations the i subscripts refer to quantities at the particle locations, and the j subscripts refer to quantities at the grid node locations. The interpolation from particles to the grid and vice versa is accomplished through shape functions. The effects of

these functions on the simulation have been extensively studied[lan70],[oku72], [bir85]. The form of the function is $S(\mathbf{x}_j - \mathbf{x}_i)$ where \mathbf{x}_j is a grid node coordinate and \mathbf{x}_i is a particle position. For this dissertation linear shape functions will be used with the form

$$S(\mathbf{x}_j - \mathbf{x}_i) = (x_j + \Delta x - x_i)(z_j + \Delta z - z_i)/\Delta x \Delta z \quad (1.6)$$

for $-\Delta x < x_j - x_i < 0$ and $-\Delta z < z_j - z_i < 0$. Otherwise

$$S(\mathbf{x}_j - \mathbf{x}_i) = 0. \quad (1.7)$$

Equation (1.6) is for a particle in the cell located in the positive x and z direction with respect to the grid node. The other nodes of a cell have similar functions. The sources, for the field equations on the grid, are obtained by sums over the particles in a particular cell of the appropriate particle quantity multiplied by the shape function. As an example the charge density is defined to be

$$\rho_j = \frac{1}{\Delta x \Delta z} \sum_i q_i S(\mathbf{x}_j - \mathbf{x}_i). \quad (1.8)$$

Since ρ and \mathbf{J} on the grid are interpolated from particle quantities, they need not satisfy the continuity equation

$$\dot{\rho} + \nabla \cdot \mathbf{J} = 0. \quad (1.9)$$

Thus even if Gauss's Law is initially satisfied, deviation from the continuity equation can lead to errors in the electrostatic part of the E-field. A widely used correction to the field has the form[bir85]

$$\mathbf{E}_{corrected}^{n+1} = \mathbf{E}^{n+1} - \nabla \psi \quad (1.10)$$

where

$$\nabla^2 \psi = \nabla \cdot \mathbf{E}^{n+1} - 4\pi \rho^{n+1} \quad (1.11)$$

Notice that equation (1.4) is implicit with respect to the velocity. This equation can be reformulated with the Boris algorithm so that the advanced velocity is exclusively on the left hand side[bor70]. Using tensor notation the equation becomes

$$\mathbf{v}_i^{n+1/2} = \mathbf{R}_i^n \cdot \mathbf{v}_i^{n-1/2} + \frac{q\Delta t}{2m} (\mathbf{I} + \mathbf{R}_i^n) \cdot \mathbf{E}_i^n \quad (1.12)$$

where \mathbf{I} is the identity tensor and \mathbf{R} , the rotation due to $\mathbf{v} \times \mathbf{B}$, is given by

$$\begin{aligned} \mathbf{R}_i^n &= \left[\left(1 - (\Theta_i^n)^2\right) \mathbf{I} - 2\Theta_i^n \times \mathbf{I} + 2\Theta_i^n \Theta_i^n \right] / \left(1 + (\Theta_i^n)^2\right) \\ \Theta_i^n &= q\mathbf{B}_i^n \Delta t / 2mc. \end{aligned} \quad (1.13)$$

1.1.2 Constraints

We can do a von Neumann stability analysis of the hyperbolic system of equations (1.4) and (1.5)[roa76]. Considering fields of the form $\mathbf{E}_o \exp[i(\mathbf{k} \cdot \mathbf{x} - \omega t)]$, exponential (numerical) growth of the fields will not occur as long as ω has an imaginary part which is less than or equal to zero. Substituting into the finite difference equations, we find as in[bir85]

$$\begin{aligned}\Omega \mathbf{B} &= c\boldsymbol{\kappa} \times \mathbf{E} \\ \Omega \mathbf{E} &= -c\boldsymbol{\kappa} \times \mathbf{B}\end{aligned}\tag{1.14}$$

where

$$\begin{aligned}\kappa_x &= k_x \sin(k_x \Delta x / 2) / (k_x \Delta x / 2) \\ \kappa_z &= k_z \sin(k_z \Delta z / 2) / (k_z \Delta z / 2) \\ \Omega &= \omega \sin(\omega \Delta t / 2) / (\omega \Delta t / 2).\end{aligned}\tag{1.15}$$

Eliminating \mathbf{E} and \mathbf{B} from equation (1.14), we find

$$\left[\frac{\sin(\omega \Delta t / 2)}{c \Delta t} \right]^2 = \left[\frac{\sin(k_x \Delta x / 2)}{\Delta x} \right]^2 + \left[\frac{\sin(k_z \Delta z / 2)}{\Delta z} \right]^2.\tag{1.16}$$

ω is real for all \mathbf{k} if

$$c \Delta t \leq \frac{1}{\sqrt{1/\Delta x^2 + 1/\Delta z^2}}.\tag{1.17}$$

This Courant condition imposes a limit on Δt for a given spatial discretization. Physically it corresponds to limiting the propagation of light to less than one cell in a time step. For low frequency phenomena where the time for light propagation across the system is insignificant compared to the time for changes in the system, this constraint would require an unnecessarily small time step. The Darwin formulation of Maxwell's equations will be used to overcome this constraint.

The particle equations of motion also impose a time constraint. This analysis will be taken up more rigorously in chapter 3; however, a simplified calculation is presented here to show the magnitude of this constraint. Consider a plasma with a uniform background density of ions and a one dimensional perturbation in the electron density. The electrons will oscillate electrostatically in a longitudinal standing wave at the plasma frequency, $\omega_{pe}^2 = 4\pi n e^2 / m_e$ [che74]. For a zero temperature plasma the density (thus the

particles) will oscillate harmonically at ω_{pe} . Analyzing equation (1.4) for a simple harmonic oscillator, where $qE/m = -\omega_{pe}x$, we find

$$x_o e^{-i\omega(t+\Delta t)} - 2x_o e^{-i\omega t} + x_o e^{-i\omega(t-\Delta t)} = -(\Delta t)^2 \omega_{pe}^2 x_o e^{-i\omega t}. \quad (1.18)$$

The resulting dispersion relation is

$$\sin^2(\omega\Delta t/2) = (\omega_{pe}\Delta t/2)^2 \quad (1.19)$$

leading to the stability requirement $\omega_{pe}\Delta t < 2$. If high frequency plasma oscillations are not important for the phenomena of interest, this constraint is very restrictive. The Direct Implicit method is used to overcome this constraint. Note that this constraint is applicable to any explicit code (full Maxwell or Darwin). In fact in high density plasmas the ω_{pe} constraint would force the Darwin time step to be almost as small as the Courant limited time step. Under these circumstances the full Maxwell algorithm would be more efficient since it requires less computer time per simulation time step.

1.2 Low Frequency, Kinetic Phenomena

One of the difficulties in simulating plasmas lies in the enormous disparity between the fundamental scale lengths of a plasma and the scale lengths of the phenomena of interest. The fundamental parameters involve the Debye length, $\lambda_{De}^2 = \kappa_B T_e / 4\pi n e^2$, the plasma frequency, ω_{pe} , and the propagation time of electromagnetic waves. The Debye length is the distance over which a test charge placed in a plasma will be shielded. It is near the lower limit of scale lengths for collective effects, and systems are usually many Debye lengths in size. Reduced physics models such as fluid algorithms would allow the computationalist to ignore the constraints imposed by these fundamental parameters, but in many cases the kinetic properties of the plasma are intimately involved in the transport of energy and particles. The explicit, electrodynamic PIC of the previous section would correctly model all of the physics in the plasma, but the discretization in space and time required due to the constraints on the algorithm would be prohibitive. The problems would demand more storage and speed than present computers can provide.

The objective is to create models which can ignore the fundamental constraints without eliminating relevant plasma properties. Properties to retain include: kinetic effects

such as collisionless damping of low frequency waves and nonanalytic particle velocity distributions, electrostatic as well as magnetoinductive fields, finite electron mass effects, and nonlinear processes.

Two examples of low frequency, kinetic phenomena are magnetic reconnection and plasma processing. Magnetic reconnection is, as its name implies, the connection of magnetic field lines in resistive media. This process itself exists over a wide range of spatial and temporal scale lengths in astrophysical, geophysical, and magnetic fusion plasmas[hew88]. It is considered important in the transport processes of these plasmas and can depend on the ion and electron velocity distributions. Fluid descriptions of the phenomena require empirical additions to the equations which are not consistent with the known properties of the plasmas. Kinetic simulations remain the best vehicle for studying magnetic reconnection, even though it may occur over widths of 10s of Debye lengths and times equal to $1000\omega_{pe}^{-1}$.

Plasma processing is an important application of plasmas where boundaries need to be considered. Plasma processing involves the use of plasmas in the treatment of material surfaces for microelectronic and other industries[hop92]. The plasmas are used to clean surfaces, deposit materials on surfaces, and etch surfaces. There are various ways of generating the plasma. Among these are inductive reactors which excite the plasma with inductive fields operating a frequency, ω_{rf} , near 10 MHz with sufficient power to generate plasma densities of $n_p = 10^{11} \text{ cm}^{-3}$. Typical sizes of these reactors are $L = 10 \text{ cm}$. This results in parameters of $L > \Delta x = .1 \text{ cm} \gg \lambda_{De} = .005 \text{ cm}$ and $c/\Delta x = 3 \times 10^{11} \text{ s}^{-1} > \omega_{pe} = 2 \times 10^{10} \text{ s}^{-1} \gg \omega_{rf}$. Since electron collisions are a main source of ionization and other chemical reactions in the chamber, the electron velocity distribution has a major impact on the reactor operation. Because the inductive fields cause heating through both resistive and collisionless processes, the distribution need not be Maxwellian.

1.3 Long Time Scale Simulation Methods

Over the past twenty years several PIC methods have been developed to overcome the constraints on explicit electrodynamic PIC. These methods eliminate selected high frequency plasma phenomena while retaining long time-scale, kinetic phenomena. The approaches can be split into two broad categories according to the way they remove the high frequency, short wavelength phenomena. The first category starts with the original set of equations and reduces the physics. The set of equations is no longer hyperbolic for

certain types of waves (usually light waves and plasma oscillations). The second category works with the finite difference equations in an implicit form. All of the waves still exist in the implicit simulation, but those which are not resolved are numerically damped out.

1.3.1 Physics Reduction Methods

The Darwin method is the minimum reduction in Maxwell's equations necessary to eliminate the propagation of light waves[[dar20](#)], [[nie76](#)]. The essence of this radiation free limit is obtained by ignoring the solenoidal part of the displacement current in Ampere's law. This results in a particle Lagrangian which is correct to order v^2/c^2 . The set of Darwin equations can be rewritten in elliptic form. Chapter 3 will elaborate on the form of the equations and their numerical solution.

Significant progress has been made in the numerical implementation of Darwin for PIC codes. The initial Darwin algorithms decomposed the plasma source terms into an irrotational, or curl free, part and a solenoidal, or divergence free, part in order to solve the partial differential equation for the B-field and solenoidal E-field[[nie76](#)]. This process was both numerically time consuming and conceptually daunting. In many cases the boundary conditions needed to solve for the irrotational and solenoidal parts of the plasma source terms are beyond the physical insight of the investigator. The derivation of the Streamlined Darwin Field (SDF) equations by Hewett and Boyd removed the need for a decomposition and reformulated the equation with variables which require relatively simple boundary conditions[[hew87a](#)]. However, SDF consists of two strongly coupled partial differential equations. The linear system due to the finite differencing of these equations was found to be difficult to solve. This problem was overcome with the extension of the iterative matrix solution technique Dynamic Alternating Direction Implicit (DADI) to coupled equations[[hew92a](#)].

With these improvements the Darwin equations can be solved quickly and efficiently in a plasma simulation code. The method eliminates the CFL constraint on light propagation while retaining all kinetic effects for the particles in the radiation free fields. The Darwin field equations reduce the size of electromagnetic fluctuations compared to fully electromagnetic codes[[nie76](#)]. This allows the use of fewer particles resulting in a further increase in computational speed beyond the use of a larger time step. Unfortunately, for higher density plasmas the constraint due to ω_{pe} can be almost as restrictive as the Courant

condition.

In quasi-neutral or hybrid codes the Debye length is assumed to be negligible everywhere so the electron density is approximately equal to the ion density. This assumption leads to a modification of the electrostatic field calculation and the electron dynamics. The exact form of the modified charge density continuity equation leads to either a zero electron mass, actually inertia, (ZEM) formulation or a finite electron mass (FEM) formulation. Since in either case the total charge density and its time derivative are approximately zero everywhere, the continuity equation sets the divergence of the current density equal to zero or

$$\nabla \cdot (\mathbf{J}_i + \mathbf{J}_e) = 0. \quad (1.20)$$

There can be no high frequency plasma oscillations since the electrons, which must be specified as a fluid, are moving with the ions. The slow moving ions are treated explicitly as particles or fluid.

In ZEM codes the lack of electron inertia means that the electrons instantly follow the motion of the ions, and they are useful in cases where electron dynamics can be ignored [sgr76], [bye78], [hew80]. The continuity equation result is taken to mean $\mathbf{J}_{irr}^e = -\mathbf{J}_{irr}^{ion}$. So after the explicit advance of the ions both \mathbf{J}_{irr}^e and \mathbf{J}^{ion} are known. An equation for the E-field is found by neglecting the inertia terms in the electron momentum equation.

$$\mathbf{E} = -\frac{\nabla \rho T_e}{e\rho} - \frac{\mathbf{u}_e \times \mathbf{B}}{c} + \eta \cdot \mathbf{J} \quad (1.21)$$

where T_e is the electron temperature, \mathbf{u}_e is the electron drift, η is the resistivity, and \mathbf{J} is the total current density. This equation is substituted into Faraday's law to give a time advance for the B-field

$$\mathbf{B}^{n+1} = \mathbf{B}^n - c \nabla \times \mathbf{E} \quad (1.22)$$

The new solenoidal part of the current density is found from Ampere's law in which the solenoidal displacement current has been neglected

$$\mathbf{J}_{sol}^{n+1} = (c/4\pi) \nabla \times \mathbf{B}^{n+1} \quad (1.23)$$

Finally, the E-field equation is used with all of the advanced quantities to find the new E-field.

FEM codes solve for a scalar function such that[hew78]

$$\nabla^2\psi = \nabla \cdot \mathbf{J}_i \quad (1.24)$$

which coupled with the quasi-neutral continuity equation (1.20) results in

$$\mathbf{J}_{irr}^e = -\nabla\psi \quad (1.25)$$

\mathbf{J}^e is then advanced with an explicit electron momentum equation in which the actual \mathbf{J}_{irr}^e is removed and replaced with $-\nabla\psi$. Again the electrons have been tied to the ion time scale. An ambipolar electrostatic field still exists through a quasi-neutral ‘‘Poisson’’ equation obtained from the continuity equation and the sum of the electron and ion momentum equations[hew78], [dip94b]. With all of the above source terms advanced to the new time step, the new \mathbf{E}_{sol} and \mathbf{B} can be found from the Darwin field equations[dip94b], [hew94].

With these hybrid codes both the Courant and ω_{pe} constraints have been eliminated. Since the electrons are now a fluid, the number of particles has been reduced improving storage and cpu time. Ion kinetic effects have been retained, but electron kinetic effects are completely absent as are short range electrostatic fields.

1.3.2 Implicit Methods

Implicit methods achieve stability by including information from the next time step in the equations for the time advance of present quantities. Contributions from previous time steps may also be retained depending on the amount of numerical dispersion which is desired or tolerable. If all quantities are stored on the grid and the dynamic equations depend on the local values of grid quantities, the implicit system can be formulated into a set of simultaneous equations. The solution of the simultaneous equations gives the grid quantities at the next time step.

For PIC simulation the situation is more complicated. The particles have positions and velocities independent of the grid, and the field equations can be elliptic requiring global solutions much more involved than a simple relationship to local grid quantities. For this reason the methods used are actually predictor-corrector. The source terms (usually ρ and \mathbf{J}) are found at an intermediate level using the present field values. Equations for the time advanced fields are derived by expanding the field equations around the arguments at the intermediate level[lan85]. Truncating the expansion gives approximate equations for the

time advanced fields in terms of the present fields and the intermediate level sources. The particles are then pushed to the next time step by using the time advanced fields. The estimated fields are not necessarily consistent with final particle positions and velocities. In principle iterations over the above steps could be done to improve convergence, but this has not been found to be necessary[lan85]. If one did iterate to convergence, the methods would be truly implicit. The two approaches to implicit PIC, the moment method and the direct method, differ primarily in how the source terms are advanced to the intermediate level.

In the moment method the source terms to be advanced are the fluid quantities which have been interpolated to the grid from the particles. The moment or fluid equations are used to give the time variation of these quantities, and the terms in the fluid equations are found from additional accumulations of particle quantities. The fluid quantities are then advanced to the intermediate time level through a finite difference of the time derivatives where the numerical accuracy of advection schemes can play a role. Initial work with electrostatic codes can be found in Mason[mas81] and Denavit[den81]. Overviews of moment method electromagnetic algorithms are in Brackbill and Forslund[bra85] and Mason[mas85].

The direct method avoids the inconsistencies of taking moments by continuing to work directly with the particles. Both the particle positions and velocities are moved to the intermediate level. The particle quantities are then interpolated to the grid to provide the source terms for the implicit field equations. This leads to a double push and interpolation of the particle quantities. Since dealing with the particles can take most of the cpu time, a computational cost is paid for the greater accuracy of the direct method. Dispersion characteristics and grid effects have been thoroughly investigated in several sources[lan83], [coh84]. An overview of the method including electromagnetics and energy conservation characteristics can be found in Langdon and Barnes[lan85]. Hewett and Langdon[hew87b] and Tanaka [tan93] provide results from fully electromagnetic implicit codes.

These implicit methods provide plasma simulation with large temporal and spatial discretization while retaining electron kinetics. The strength of the implicit scheme is that those phenomena which are not resolved are numerically damped. This becomes a constraint when the numerical dispersion cooling effects and grid heating effects cause significant numerical changes in total system energy. Energy conservation is achieved only if Δx and Δt are chosen correctly[hew87b], [coh89]. The other limitation to these methods has been finding reasonable boundary conditions for the implicit electromagnetic fields.

1.3.3 The DARwin Direct Implicit (DADIPIC) Method

As its name suggests DADIPIC is a combination of the Darwin and direct implicit methods. The direct implicit algorithm is only applied to the electrostatic part of the E-field. The SDF equations are used to solve for the solenoidal E-field and the B-field. The particles are advanced explicitly in time with respect to the solenoidal E-field and the B-field. As will be shown in the remainder of this dissertation, DADIPIC combines the previously mentioned useful features of these two methods while eliminating or at least mitigating previous shortcomings. Darwin is no longer limited by $\omega_{pe}\Delta t$ because of the electrostatic direct implicit particle advance. Boundary conditions are much simpler since they are applied separately to the implicit electrostatic field and the SDF equations. The issue of energy nonconservation also appears to be manageable since fluctuations due to the electrostatic field appear to be the only culprits.

1.4 Overview of Chapters

In the remainder of this dissertation the DADIPIC algorithm is presented along with tests of its performance and applications to idealized plasma processing reactors. Chapter 2 contains the details of the algorithm. The equations for advancing particle quantities and for solving the fields are presented. The necessary boundary conditions for the field equations are derived, the finite difference forms of the field equations are shown, and the numerical methods for solving the resulting linear systems of equations are presented. The next two chapters characterize DADIPIC and give guidelines for accurate and stable simulation using the method. Chapter 3 covers analytic theory which predicts the behavior of DADIPIC as Δt and Δx are varied while Chapter 4 shows the actual performance of the method in 2-D both as verification of theory and proof of robustness under stressful circumstances. The final section of Chapter 4 condenses the guidelines into a region of operation for DADIPIC simulation. Chapter 5 has the results of the application of DADIPIC simulation to the phenomenon of collisionless heating in inductively coupled plasma processing reactors. After the applicability of the method is verified by agreement between simulation and 1-D analytic theory, DADIPIC is then used to simulate reactor geometries in 2-D.

Chapter 2

Implementation of DARwin Direct Implicit Particle-in-Cell

The implementation of DADIPIC results in an algorithm in which the implicit electrostatic step and the Darwin step each stand alone. So each step will be described separately before presenting the combined algorithm.

2.1 Direct Implicit Electrostatic Method

In this section the particle advance and field solve necessary to carry out the implicit electrostatic part of the DADIPIC algorithm are described.

2.1.1 Particle Integration

The particles are time integrated according to the D_1 implicit scheme[lan83]. This scheme damps high frequency oscillations while retaining low frequency oscillations by keeping significant contributions from all previous time steps in the electrostatic part of the particle acceleration. The D_1 scheme also extends the region of energy conservation in $\Delta x/\lambda_{De}$, $\omega_{pe}\Delta t$ space as compared to the more time centered C_1 scheme[coh89]. In fact good energy conservation was found when $3v_{th}\Delta t/\Delta x \sim 1$. The finite differenced equations take the form

$$\begin{aligned} \mathbf{v}^{n+1/2} &= \mathbf{v}^{n-1/2} + \Delta t \bar{\mathbf{a}}^n + \frac{q\Delta t}{m} \left[\mathbf{E}_{sol}^n + \frac{\mathbf{v}^{n+1/2} + \mathbf{v}^{n-1/2}}{2c} \times \mathbf{B}^n \right] \\ \mathbf{x}^{n+1} &= \mathbf{x}^n + \Delta t \mathbf{v}^{n+1/2} \end{aligned} \quad (2.1)$$

$$\bar{\mathbf{a}}^n = \frac{1}{2} \left[\bar{\mathbf{a}}^{n-1} + \frac{q}{m} \mathbf{E}_{irr}^{n+1} \right]$$

where \mathbf{E}_{sol} is the solenoidal part of the field, and \mathbf{E}_{irr} is the irrotational part of the field. Notice that $\bar{\mathbf{a}}$ includes the time advanced electrostatic field. Unlike other electromagnetic implicit algorithms, the particle push is still explicit with respect to \mathbf{E}_{sol} and \mathbf{B} . So a time advanced field solution is required only for \mathbf{E}_{irr} . This particle push is broken up into two steps[hew87b]. The first push uses only known quantities to advance \mathbf{v} and \mathbf{x} to a \sim level, and the \sim quantities are used to estimate the advanced \mathbf{E}_{irr} . The predicted \mathbf{E}_{irr} is then used to complete the advance to the $n+1$ time step. As mentioned above the method is a predictor-corrector as opposed to truly implicit.

Using the notation of Eq. (1.13), we obtain

$$\begin{aligned} \tilde{\mathbf{v}} &= \mathbf{R}^n \cdot \mathbf{v}^{n-1/2} + \frac{\Delta t}{2} (\mathbf{I} + \mathbf{R}^n) \cdot \left(\frac{1}{2} \bar{\mathbf{a}}^{n-1} + \frac{q}{m} \mathbf{E}_{sol}^n \right) \\ \tilde{\mathbf{x}} &= \mathbf{x}^n + \Delta t \tilde{\mathbf{v}} \end{aligned} \quad (2.2)$$

The final positions and velocities are obtained from

$$\begin{aligned} \mathbf{v}^{n+1/2} &= \tilde{\mathbf{v}} + \delta \mathbf{v} \\ \mathbf{x}^{n+1} &= \tilde{\mathbf{x}} + \Delta t \delta \mathbf{v} \\ \delta \mathbf{v}(\mathbf{x}^n, \mathbf{x}^{n+1}) &= \frac{q \Delta t}{4m} (\mathbf{I} + \mathbf{R}^n) \mathbf{E}_{irr}^{n+1}(\mathbf{x}^{n+1}) \end{aligned} \quad (2.3)$$

Note that \mathbf{R} should be evaluated at \mathbf{x}^n , and \mathbf{E}_{irr} should be evaluated at \mathbf{x}^{n+1} for $\delta \mathbf{v}$. With this scheme $\delta \mathbf{v}$ cannot be found until the advanced \mathbf{E}_{irr} is computed. An approximate field equation is obtained by taking the first two terms of a Taylor expansion of the accumulated charge density at time $n+1$ about $\tilde{\mathbf{x}}$.

$$\rho^{n+1} = \sum_i \frac{q_i}{\Delta x} \left[S(\mathbf{x}_j - \tilde{\mathbf{x}}_i) + \Delta t \delta \mathbf{v}_i(\mathbf{x}_i^n, \mathbf{x}_i^{n+1}) \cdot \nabla_i S(\mathbf{x}_j - \tilde{\mathbf{x}}_i) + \dots \right] \quad (2.4)$$

Noting the first term is $\tilde{\rho}$, Eq. (2.4) can be rewritten

$$\rho^{n+1} \simeq \tilde{\rho} + \sum_i \frac{q_i}{\Delta x} \left[\Delta t \delta \mathbf{v}_i(\mathbf{x}_i^n, \mathbf{x}_i^{n+1}) \cdot \nabla_i S(\mathbf{x}_j - \tilde{\mathbf{x}}_i) \right] \quad (2.5)$$

In the second term the gradient can be changed to a derivative on the grid position and removed from the sum. Several methods of calculating the remaining sum have been investigated[coh84], [lan85]. Calculation of the sum in Eq. (2.5) with the actual field interpolation to the particles in $\delta \mathbf{v}$ and the weighting of the particles to the grid is called

strict differencing[lan85]. One of the least computationally intensive and most stable calculations of the sum has been termed simplified differencing[lan83]. In simplified differencing \mathbf{R} and the E-field are evaluated on the grid leaving

$$\begin{aligned}\rho^{n+1} &= \bar{\rho} - \nabla \cdot (\mathbf{X} \cdot \mathbf{E}_{irr}^{n+1}) \\ \mathbf{X} &= \frac{\Delta t^2}{4} \sum_s (\mathbf{I} + \mathbf{R}^n) \left[\frac{q_s \bar{\rho}_s}{m_s} \right]\end{aligned}\quad (2.6)$$

where the sum is now over species. The \mathbf{X} tensor is easily formed from the B-field and charge density already stored on the grid. This differencing provides a significant reduction in computation since it avoids extra interpolation of particle quantities to the grid and leads to a simpler finite difference field solution. For instance in 1-D the field solution goes from a pentadiagonal solution matrix with strict differencing to a tridiagonal solution matrix with simplified differencing. With the simplified differencing expression for ρ^{n+1} the field equation becomes

$$\nabla \cdot \left[(\mathbf{I} + 4\pi\mathbf{X}) \cdot \nabla \phi^{n+1} \right] = -4\pi\bar{\rho} \quad (2.7)$$

Because of the similarity of this equation to the electrostatic field equation in dielectric media, the \mathbf{X} term is usually referred to as an implicit susceptibility [lan83].

2.1.2 Differencing of the Field Equation and Boundary Conditions

Simplified differencing is implemented in the code as follows. In the x-z plane the implicit field equation has the form

$$\left[\nabla^2 + 4\pi \left(\nabla_x (X^{xx} \nabla_x + X^{xz} \nabla_z) + \nabla_z (X^{zx} \nabla_x + X^{zz} \nabla_z) \right) \right] \phi^{n+1} = -4\pi\bar{\rho} \quad (2.8)$$

These terms are finite differenced with second order accuracy as

$$\begin{aligned}\nabla_x (X^{xx} \nabla_x \phi^{n+1}) &= \frac{1}{(\Delta x)^2} \left[X_{i+1/2,j}^{xx} \phi_{i+1,j}^{n+1} + X_{i-1/2,j}^{xx} \phi_{i-1,j}^{n+1} \right. \\ &\quad \left. - \left(X_{i+1/2,j}^{xx} + X_{i-1/2,j}^{xx} \right) \phi_{i,j}^{n+1} \right]\end{aligned}\quad (2.9)$$

$$\begin{aligned}\nabla_x (X^{xz} \nabla_z \phi^{n+1}) &= \frac{1}{4\Delta x \Delta z} \left[X_{i+1/2,j}^{xz} \left(\phi_{i+1,j+1}^{n+1} + \phi_{i,j+1}^{n+1} - \phi_{i+1,j-1}^{n+1} - \phi_{i,j-1}^{n+1} \right) \right. \\ &\quad \left. - X_{i-1/2,j}^{xz} \left(\phi_{i,j+1}^{n+1} + \phi_{i-1,j+1}^{n+1} - \phi_{i,j-1}^{n+1} - \phi_{i-1,j-1}^{n+1} \right) \right]\end{aligned}\quad (2.10)$$

Table 2.1: Coefficients for the Implicit Field Equation Operator

$\phi_{i+1,j+1}$	dpp	$(1/4\Delta x\Delta z)\left(X_{i+1/2,j}^{zz} + X_{i,j+1/2}^{zz}\right)$
$\phi_{i+1,j}$	cxp	$(1/\Delta x^2)\left(1 + X_{i+1/2,j}^{xx}\right)(1/4\Delta x\Delta z)\left(X_{i,j+1/2}^{zz} - X_{i,j-1/2}^{zz}\right)$
$\phi_{i+1,j-1}$	dpm	$-(1/4\Delta x\Delta z)\left(X_{i+1/2,j}^{zz} + X_{i,j-1/2}^{zz}\right)$
$\phi_{i,j+1}$	czp	$(1/\Delta z^2)\left(1 + X_{i,j+1/2}^{zz}\right)(1/4\Delta x\Delta z)\left(X_{i+1/2,j}^{zz} - X_{i-1/2,j}^{zz}\right)$
$\phi_{i,j}$	ccc	$-2(1/\Delta x^2 + 1/\Delta z^2) - (1/\Delta x^2)\left(X_{i+1/2,j}^{xx} + X_{i-1/2,j}^{xx}\right) - (1/\Delta z^2)\left(X_{i,j+1/2}^{zz} + X_{i,j-1/2}^{zz}\right)$
$\phi_{i,j-1}$	czm	$(1/\Delta z^2)\left(1 + X_{i,j-1/2}^{zz}\right) - (1/4\Delta x\Delta z)\left(X_{i+1/2,j}^{zz} - X_{i-1/2,j}^{zz}\right)$
$\phi_{i-1,j+1}$	dmp	$-(1/4\Delta x\Delta z)\left(X_{i-1/2,j}^{zz} + X_{i,j+1/2}^{zz}\right)$
$\phi_{i-1,j}$	cxm	$(1/\Delta x^2)\left(1 + X_{i-1/2,j}^{xx}\right) - (1/4\Delta x\Delta z)\left(X_{i,j+1/2}^{zz} - X_{i,j-1/2}^{zz}\right)$
$\phi_{i-1,j-1}$	dmm	$(1/4\Delta x\Delta z)\left(X_{i-1/2,j}^{zz} + X_{i,j-1/2}^{zz}\right)$

with the other terms having similar expressions. This leads to a nine point scheme of coefficients in the solution matrix, \mathbf{A} , for each potential node to be solved. The resulting coefficients are in table 2.1. \mathbf{A} is formed with $\phi(i, j)$ ordered in a 1-D vector as $[\phi_{1,1}, \dots, \phi_{imax,1}, \phi_{1,2}, \dots, \phi_{imax,2}, \dots]$. \mathbf{A} is a banded matrix, and to save on storage only the diagonals with nonzero components are stored by the code. Note that the components of the \mathbf{X} tensor are needed at the half grid point positions. The offset is in x for X^{xx} and X^{xz} , and in z for X^{zx} and X^{zz} . These are calculated by averaging the densities and B-fields which are stored at the grid points. As an example $X(i - 1/2, j)$ generates its rotation tensor from the B-field: $B(i - 1/2, j) = .5(B(i - 1, j) + B(i, j))$.

Periodic, Dirichlet and Neumann boundary conditions on ϕ are allowed by the code. Periodic boundaries represent an infinite repetition of the simulation region along the periodic direction. Essentially there is no boundary only a limitation on maximum wavelength. For periodic boundaries, nodes outside one of the four periodic walls of the simulation region are the same as nodes just inside the opposite wall. This moves the coefficient for that node to a different diagonal in the solution matrix. As a result the number of diagonals changes for periodic boundary conditions (15 for periodic, 21 for doubly

periodic). The resulting matrix is also nonsymmetric. Consider a doubly periodic simulation with an $m \times n$ grid; therefore, a $m \times n$ solution matrix, A . The $A_{1,mn}$ term in the matrix is given by the dmm coefficient (see Table 2.1) for the 1,1 node in the simulation grid or

$$dmm(1,1) = \frac{1}{8\Delta x\Delta z} \left(X_{m,1}^{xz} + X_{1,1}^{xz} + X_{1,n}^{zx} + X_{1,1}^{zx} \right). \quad (2.11)$$

The $A_{mn,1}$ term in the matrix is given by the dpp coefficient for the m,n node in the simulation grid or

$$dpp(m,n) = \frac{1}{8\Delta x\Delta z} \left(X_{m,n}^{xz} + X_{1,n}^{xz} + X_{m,1}^{zx} + X_{m,n}^{zx} \right). \quad (2.12)$$

Given that X's at different nodes are not necessarily equal, it follows that $A_{1,mn} \neq A_{mn,1}$, or the matrix is nonsymmetric.

For Dirichlet nodes such as a conductor with a specific potential, the coefficient on the diagonal is set to one, the other coefficients are set to zero, and the right hand side is set to the value of ϕ desired for that node. For Neumann nodes exterior nodes required by the finite difference template are found from interior nodes according to

$$\phi_{imax+1,j} = \phi_{imax-1,j} + \Delta x \frac{\partial \phi}{\partial x} \quad (2.13)$$

The exterior node coefficient is simply added to the interior node coefficient, and the derivative term is added to the right hand side of the matrix equation. This condition is most commonly used along axes of symmetry where $\partial\phi/\partial x$ is set to zero.

Once ϕ is calculated, the electric field must be found. For interior points the gradient of ϕ is used

$$E_{i,j}^x = -(\phi_{i+1,j} - \phi_{i-1,j})/(2\Delta x) \quad (2.14)$$

Conducting boundaries present a unique situation. Under long time scale conditions a confined plasma will generally rise to a positive potential with respect to the confining walls. This potential drop retards the more mobile electrons and accelerates the heavier ions causing an equalization of the electron and ion currents being absorbed by the walls. The resulting potential sheath is typically large compared to a Debye length, but may be small compared to the region to be simulated. This leads us to use different boundary conditions at conducting boundaries depending on whether a sheath is spatially resolved or not.

When the sheath is resolved an implicit Gauss' law is used to overcome the lack of ϕ values exterior to the conducting boundary[vah93]. The integral form of the implicit field equation is

$$\int \left(\mathbf{I} + 4\pi \mathbf{X} \right) \mathbf{E} \cdot \hat{n} dS = 4\pi \int \tilde{\rho} dV + 4\pi \int \sigma dS \quad (2.15)$$

where σ is the surface charge density on the conductor. Consider a conducting wall with surface normal in the positive x direction and a boundary node at i,j with a Gaussian box around it located at half grid points as in Fig. 2.1. The integral on the left hand side of Eq. (2.15) can be split over the four surfaces. Assuming the variables are constant over a surface and are equal to the value of the variables at the center of the surface, the integrals are easily evaluated.

$$\begin{aligned} \int_1 (\mathbf{I} + 4\pi \mathbf{X}) \mathbf{E} \cdot (-\hat{x}) dy dz &= 0 \\ \int_2 (\mathbf{I} + 4\pi \mathbf{X}) \mathbf{E} \cdot (\hat{z}) dx dy &= [4\pi X^{zz} E^x + (1 + 4\pi X^{zz}) E^z]_{i,j+1/2} \Delta x \Delta y \\ \int_3 (\mathbf{I} + 4\pi \mathbf{X}) \mathbf{E} \cdot (\hat{x}) dy dz &= [(1 + 4\pi X^{xx}) E^x + 4\pi X^{xz} E^z]_{i+1/2,j} \Delta y \Delta z \\ \int_4 (\mathbf{I} + 4\pi \mathbf{X}) \mathbf{E} \cdot (-\hat{z}) dx dy &= -[4\pi X^{zz} E^x + (1 + 4\pi X^{zz}) E^z]_{i,j-1/2} \Delta x \Delta y \end{aligned} \quad (2.16)$$

Inside the conducting wall the field is zero so the integral over surface one is zero. Fields tangent to the equipotential surface are also zero. Finally at the surface $E_{i,j}^x = 4\pi\sigma$ so

$$4\pi \int \sigma dS = E_{i,j}^x \Delta y \Delta z \quad (2.17)$$

Putting all this into Eq. (2.15), the result for the surface field is

$$E_{i,j}^x = \frac{2\pi\rho_{i,j} \Delta x \Delta z + [(1 + 4\pi X_{i+1/2,j}^{xx}) E_{i+1/2,j}^x + 4\pi X_{i+1/2,j}^{xz} E_{i+1/2,j}^z] \Delta z}{[\Delta z + 4\pi \Delta x (X_{i,j-1/2}^{zz} - X_{i,j+1/2}^{zz})]} \quad (2.18)$$

Similar expressions are found for walls with surface normals $-\hat{x}$, \hat{z} , and $-\hat{z}$.

When a sheath is not resolved and $\omega_{pe} \Delta t$ is large, Eq. (2.18) is dominated by X^{xx} . This results in a large, nonphysical electric field at the conducting surface. Since a sheath is not resolved, the field at the boundary fluctuates due to the simulation particle noise. This is the same as the fluctuating electrostatic fields in the bulk of the plasma, but the anomalously large magnitude of the boundary field causes excessive numerical heating of the plasma. To get realistic fields a sheath boundary condition must be applied which imposes the normal E-field. The field must be set according to the potential drop calculated from

an analytic or numerical sheath model. Such sheath boundary conditions are the subject of ongoing investigations[dip94c]. Most of the results presented in this dissertation use a relatively simple sheath model. The ions are represented as a uniform, stationary positive background. The potential drop of the sheath is represented by a boundary condition on the particles as well as the field. An infinite potential drop in the sheath is implemented by specularly reflecting all of the particles at conducting walls. Since the potential drop is already represented by particle reflection the E-field is set to zero at the walls. The result is that the particles remain in the simulation region instead of being absorbed, and they are not heated due to anomalously large fluctuating fields at the walls. In chapter 5 a more complex sheath model is explained and used for the simulation of a typical plasma processing reactor.

2.1.3 Numerical Solution of the Field Equation

Given the nine-point stencil for the difference equation and the large, sparse, non-diagonally dominant matrix, the bi-conjugate gradient (BCG) method was chosen to solve the implicit electrostatic equation. As will be shown in section 2.2, the remaining field equations rely on five-point stencils and can be solved more efficiently with Dynamic ADI. The BCG method is a variation of the conjugate gradient method applicable to nonsymmetric matrices. The conjugate gradient method is an iterative minimization of the functional $\phi(x) = .5x^T Ax - x^T b$ [gol89]. At the minimum $\nabla\phi = Ax - b = 0$, so we have solved the matrix equation $Ax = b$. Given an approximate solution, x_{k-1} , at the $k-1$ iteration, the new solution is $x_k = x_{k-1} + \alpha_k p_k$ where p_k depends on $k-1$ quantities. The α_k are chosen so that $\phi(x_{k-1} + \alpha_k p_k)$ is minimized with respect to α , and the p_k are chosen to be linearly independent. The residual is $r_k = b - Ax_k = r_{k-1} - \alpha_k A p_k$. Since the x_k are the sum of the p_k , $x_k \in span\{p_1, \dots, p_n\}$. The result is each x_k solves

$$\min_{x \in span\{p_1, \dots, p_k\}} \phi(x) \quad (2.19)$$

A solution is found after n iterations for a n dimensional space since $span\{p_1, \dots, p_n\}$ includes the whole space. In the BCG method two residual and two conjugate vectors are defined[fle75]. It is equivalent to solving the system $A^T Ax = A^T b$ so the scheme is working with a symmetric matrix. The method is not guaranteed to converge. For those cases where it does converge, the method is guaranteed to converge in n iterations for an n dimensional space. In practice a useful solution can usually be obtained in far fewer than n iterations.

The conjugate gradient method converges rapidly for well conditioned matrices. Preconditioning transforms $Ax = b$ into a well conditioned system through an incomplete LU decomposition of the matrix A . The sparsity pattern of A is used in determining which terms in L and U are calculated thus minimizing the computations required to perform the decomposition. From Anderson, et. al.[and88] the preconditioned system is $Mu = C$ where $M = L^{-1}AU^{-1}$, $u = Ux$, and $C = L^{-1}b$. The BCG algorithm is

```

choose  $x_o$ 
 $r_o = b - Ax_o$ 
 $\bar{r}_o = U^T L^{-1}r_o$ 
 $k = 0$ 
while  $r_k \neq 0, \bar{r}_k \neq 0$ 
   $k = k + 1$ 
  if  $k = 1$ 
     $p_1 = (LU)^{-1}r_o$ 
     $\bar{p}_1 = (LL^T)^{-1}r_o$ 
  else
     $\beta_k = \bar{r}_{k-1}^T (LU)^{-1}r_{k-1} / (\bar{r}_{k-2}^T (LU)^{-1}r_{k-2})$ 
     $p_k = (LU)^{-1}r_{k-1} + \beta_k p_{k-1}$ 
     $\bar{p}_k = (LU)^{-1}\bar{r}_{k-1} + \beta_k \bar{p}_{k-1}$ 
  end
   $\alpha_k = \bar{r}_{k-1}^T (LU)^{-1}r_{k-1} / (\bar{p}_k^T A p_k)$ 
   $x_k = x_{k-1} + \alpha_k p_k$ 
   $r_k = r_{k-1} - \alpha_k A p_k$ 
   $\bar{r}_k = \bar{r}_{k-1} - \alpha_k A^T \bar{p}_k$ 
end

```

The optimized preconditioned bi-conjugate gradient routine CPDES2[and88] was used for nonperiodic and periodic simulations, and a separate BCG routine was written for doubly periodic problems. Convergence is reached when $|x_k - x_{k+1}|/|x_k|$ and $|r_{k+1}|/|b|$ are both less than a given error criterion. None of the simulations run thus far have had problems with convergence. Before using the routines in simulations; however, tests were run to ensure they correctly derived the matrix coefficients for all boundary conditions and converged to the correct solution for ϕ . The tests were accomplished by comparing the solution from the bi-conjugate gradient routine to the solution of Poisson's equation from

an already tested iterative linear system solution routine based on dynamic ADI. Dynamic ADI will be further discussed in the Darwin method sections to follow. The test algorithm proceeds as follows:

1) Set arrays for the potential, $\psi(i,j)$, and the implicit susceptibility tensor, $\mathbf{X}(i,j)$, from the analytic functions

$$\psi(x,z) = \exp(-x^2/L^2)\sin(k_z z) \quad (2.20)$$

$$\mathbf{X}(x,z) = 2 + \cos(2k_x x) - \sin(2k_z z). \quad (2.21)$$

The functional form for the susceptibility tensor is based on its density dependence (a nonnegative spatially varying quantity). The value at a grid node for each component of the tensor is offset by the proper half-grid amount. The solution region is set as in Fig. 2.2a with Neumann boundary points along the left boundary, periodic points along the upper and lower boundaries, and Dirichlet points along the right boundary and a rectangular structure inside the region. The potential is set to zero on all Dirichlet points.

2) Calculate the right hand side, $\text{rhs}(i,j)$, of the equation using the given $\psi(i,j)$ and $\mathbf{X}(i,j)$ with the finite difference form of the implicit field equation

$$\text{rhs}(i,j) = \nabla[(\mathbf{I} + \mathbf{X}(i,j))\nabla\psi(i,j)]. \quad (2.22)$$

3) Call the routines to set up and solve the linear system with the given boundary conditions. The bi-conjugate gradient routine places the solution into the array $\text{phin}(i,j)$.

4) Calculate a second right hand side from the finite difference form of Poisson's equation and use the DADI routine to find $\text{phi}(i,j)$. Given that the same boundary conditions and finite difference schemes are used, $\text{phin}(i,j)$ and $\text{phi}(i,j)$ should be the same.

Figure 2.3a is a contour plot of the calculated $\text{phin}(i,j)$ while Fig. 2.3b is a measure of the difference from $\text{phi}(i,j)$. The points in Fig. 2.3b were calculated by taking $\text{phin}(i,j) - \text{phi}(i,j)$ and dividing by the average value of $\text{phin}(i,j)$ over the whole grid. As shown by the figure the differences are quite small, $\sim 10^{-9}$, which indicates agreement between the two methods. CPDES2 took 32 iterations to meet the error criteria of 10^{-5} for a 41x41 grid. Tests were also carried out with variations between the \mathbf{X} tensor component magnitudes, different numbers of grid points in the two directions, and no periodic boundaries with similar positive results.

2.2 Darwin Method

2.2.1 Field Equations

The Darwin limit of Maxwell's equations is obtained by dropping the solenoidal part of the displacement current [nie76] to obtain

$$\begin{aligned} \nabla \cdot \mathbf{E}_{irr} &= 4\pi\rho & \nabla \times \mathbf{E} &= -\frac{1}{c} \frac{\partial \mathbf{B}}{\partial t} \\ \nabla \cdot \mathbf{B} &= 0 & \nabla \times \mathbf{B} &= \frac{4\pi}{c} \mathbf{J} + \frac{1}{c} \frac{\partial \mathbf{E}_{irr}}{\partial t} \end{aligned} \quad (2.23)$$

Using the charge continuity equation, $\dot{\mathbf{E}}_{irr}$ is replaced with $-4\pi\mathbf{J}_{irr}$ and rewrite Ampere's law as

$$\nabla \times \mathbf{B} = \frac{4\pi}{c} \mathbf{J}_{sol}. \quad (2.24)$$

Consider \mathbf{E} and \mathbf{B} in terms of the potentials ϕ and \mathbf{A} in the Coulomb gauge ($\nabla \cdot \mathbf{A} = 0$).

$$\begin{aligned} \mathbf{B} &= \nabla \times \mathbf{A} \\ \mathbf{E} &= -\nabla\phi - \frac{1}{c} \frac{\partial \mathbf{A}}{\partial t} \end{aligned} \quad (2.25)$$

Using these potentials in the Darwin field equations gives the following equations for the fields. For the electrostatic potential the result is the usual Poisson's equation

$$\nabla^2 \phi = -4\pi\rho. \quad (2.26)$$

This equation was modified in section 2.1 to allow an implicit particle advance with respect to the electrostatic field. As shown below, the time advanced \mathbf{E}_{irr} can then be used along with the time advanced particle quantities to construct a source term for the \mathbf{E}_{sol} equation. In a 2-D code two forms are used to solve for the B-field in order to ensure that $\nabla \cdot \mathbf{B} = 0$ and $\nabla \cdot \mathbf{A} = 0$. For the component of \mathbf{B} which is out of the simulation plane, the y component, the curl of Ampere's law gives

$$\nabla^2 B_y = -\frac{4\pi}{c} (\nabla \times \mathbf{J})_y. \quad (2.27)$$

Since there is no variation of quantities in the y direction, this component of \mathbf{B} cannot contribute to the divergence of \mathbf{B} . The second equation is obtained by replacing \mathbf{B} in Ampere's law with its vector potential form. This gives

$$\nabla^2 A_y = -\frac{4\pi}{c} J_{sol,y}. \quad (2.28)$$

Again with no variation in y , A_y and J_y are automatically solenoidal. Finally Ampere's law and Faraday's law are combined to give

$$\nabla^2 \mathbf{E}_{sol} = \frac{4\pi}{c^2} \dot{\mathbf{J}}_{sol}. \quad (2.29)$$

Now the first velocity moment of the Boltzmann equation, summed over species, gives $\dot{\mathbf{J}}$ in terms of present particle quantities

$$\begin{aligned} \frac{4\pi}{c^2} \dot{\mathbf{J}} &= \mu \mathbf{E}_{sol} + \mu \mathbf{E}_{irr} + \zeta \times \mathbf{B} + \mathbf{K} \\ &= \mu \mathbf{E}_{sol} + \mathbf{Q} \end{aligned} \quad (2.30)$$

where

$$\begin{aligned} \mu &= \sum_s \frac{\omega_{ps}^2}{c^2} \\ \zeta &= \frac{4\pi}{c^3} \sum_s \frac{q_s}{m_s} \mathbf{J}_s \\ \mathbf{K} &= -\frac{4\pi}{c^2} \sum_s q_s \nabla \cdot \langle \mathbf{v}\mathbf{v} \rangle_s. \end{aligned} \quad (2.31)$$

Putting Eq. (2.30) in terms of a direct accumulation of the particle quantities [lar92] produces

$$\dot{\mathbf{J}}_s(\mathbf{x}_j) = -q_s \sum_i \mathbf{v}_i \mathbf{v}_i \cdot \nabla_j S(\mathbf{x}_j - \mathbf{x}_i) + \left(\frac{q_s^2}{m_s} \right) \sum_i S(\mathbf{x}_j - \mathbf{x}_i) \left[\mathbf{E}(\mathbf{x}_i) + \frac{\mathbf{v}_i \times \mathbf{B}(\mathbf{x}_i)}{c} \right]. \quad (2.32)$$

This solution is implemented since the use of a finite difference of $\dot{\mathbf{B}}$ or $\dot{\mathbf{J}}$ leads to a problem size limit of less than $2\pi c/\omega_p$ in order to prevent instability[nie76]. We now have a set of elliptic equations (2.24), (2.26), and (2.29) that generates instantaneous fields given the time advanced particle source terms.

The effect of the Darwin approximation is evident in the change of the solution to the vector potential form of Ampere's law. The fully electrodynamic form is

$$\nabla^2 \mathbf{A} - \frac{1}{c^2} \frac{\partial^2 \mathbf{A}}{\partial t^2} = -\frac{4\pi}{c} \mathbf{J}_{sol} \quad (2.33)$$

with solution

$$\mathbf{A}(\mathbf{x}, t) = \int \frac{\mathbf{J}_{sol}(\mathbf{x}', t - |\mathbf{x} - \mathbf{x}'|/c)}{|\mathbf{x} - \mathbf{x}'|} d^3 x'. \quad (2.34)$$

If the partial derivative with respect to time is dropped in Eq. (2.33), the solution becomes

$$\mathbf{A}(\mathbf{x}, t) = \int \frac{\mathbf{J}_{sol}(\mathbf{x}', t)}{|\mathbf{x} - \mathbf{x}'|} d^3 x'. \quad (2.35)$$

It is obvious that retardation effects due to the finite propagation time of light have been eliminated. In vacuum light waves no longer exist.

2.2.2 Streamlined Darwin Field (SDF) Formulation

Eq. (2.29) presents some difficulties in finding its solution. A computationally intensive vector decomposition of $\dot{\mathbf{J}}$ is required to find its solenoidal part, and this can only be done if boundary conditions can be specified for the decomposition. In many applications boundary conditions on the irrotational part of $\dot{\mathbf{J}}$ cannot be determined. Early applications generally considered problems where boundaries were distant from the plasma. A uniform plasma with doubly periodic boundaries is an example of this kind of simulation. Even in this case a slow iterative process must be used to solve Eq. (2.29) since \mathbf{E}_{sol} appears in $\dot{\mathbf{J}}_{sol}$ which is on the right hand side of the equation. First an expression for $\dot{\mathbf{J}}$ must be generated, decomposed, and used as the right hand side for Eq. (2.29). After solving Eq. (2.29) for \mathbf{E}_{sol} , the process is repeated until convergence.

Hewett and Boyd derived the Streamlined Darwin Field (SDF) formulation to avoid both boundary condition and vector decomposition problems[hew87a]. They defined new field quantities as follows

$$-\nabla^2(\nabla\psi) \equiv \frac{4\pi}{c^2}\dot{\mathbf{J}}_{irr} \quad (2.36)$$

$$\Xi \equiv \mathbf{E}_{sol} - \nabla\psi. \quad (2.37)$$

Recalling the form of the \mathbf{E}_{sol} field equation

$$\nabla^2\mathbf{E}_{sol} = \mathbf{Q} + \mu\mathbf{E}_{sol} - \frac{4\pi}{c^2}\dot{\mathbf{J}}_{irr}, \quad (2.38)$$

two coupled partial differential equations are found in terms of Ξ and ψ

$$\nabla^2\Xi - \mu\Xi = \mathbf{Q} + \mu\nabla\psi \quad (2.39)$$

$$\nabla^2\psi = -\nabla \cdot \Xi. \quad (2.40)$$

Many of the previous problems in solving \mathbf{E}_{sol} have now been eliminated. A vector decomposition of \mathbf{Q} is no longer required so nonintuitive boundary conditions do not have to be determined. Eq. (2.40) ensures that the solution for \mathbf{E}_{sol} is in fact solenoidal. As we shall see in the next section, boundary conditions on Ξ and ψ are straight forward and depend on the boundary conditions for \mathbf{E}_{sol} .

2.2.3 Boundary Conditions on A_y , B_y , and \mathbf{E}_{sol}

As with the electrostatic potential, the SDF field solution routines in the code allow periodic, Dirichlet, and Neumann boundary conditions for A_y , B_y , and \mathbf{E}_{sol} . While

periodic and symmetric boundaries require the same conditions for all fields as described in section 2.1, conducting surfaces impose conditions which must be applied separately for the different field components. Since the B-field has no divergence and is zero inside a perfect conductor, the normal component of the field is zero on the surface of the conductor. To meet this condition A_y must be a constant along the surface of a conductor. Thus we have a Dirichlet zero boundary condition on A_y .

Considering \mathbf{E} on a perfectly conducting surface, Ampere's law and Gauss' law result in $E_t = 0$ and $E_n = 4\pi\sigma$ on the surface where t is for tangential and n is for normal. $E_t^{sol} = 0$ along the boundary implies $\partial_t E_t^{sol} = 0$. Since $\nabla \cdot \mathbf{E}_{sol} = 0$, this implies $\partial_n E_n^{sol} = 0$. Given that $\mathbf{E}_{sol} = 0$ inside the conductor, we have $E_n^{sol} = 0$ on the surface. The surface charge must be accounted for by E_{irr} so $E_n^{irr} = 4\pi\sigma$. Thus Gauss' law is still satisfied by $-\nabla\phi$. This leaves us with $\mathbf{E}_{sol} = 0$ on conductors.

Boundary conditions on Ξ and ψ are needed which will enforce the above condition while still maintaining $\nabla \cdot \mathbf{E}_{sol} = 0$. This is done with the following set of equations:

- 1) For nonboundary and Neumann points, solve the SDF equations (2.39) and (2.40). For Neumann zero points, require $\partial_n \psi = 0$ and $\partial_n \Xi = 0$.
- 2) For conductor interiors set

$$\Xi = -\nabla\psi \quad \psi = 0. \quad (2.41)$$

This gives a simple Dirichlet boundary condition on ψ while maintaining $\mathbf{E}_{sol} = 0$. The divergence of \mathbf{E}_{sol} remains zero since \mathbf{E}_{sol} is constant everywhere inside the conductor.

- 3) For conductor surfaces set

$$\Xi = -\nabla\psi \quad \nabla^2\psi = -\nabla \cdot \Xi. \quad (2.42)$$

This ensures that $\Xi + \nabla\psi$ is zero and solenoidal at the surface of the conductor. Since $\Xi = -\nabla\psi$ applies only inside and on the surface of the conductor, the derivative of the equation may be discontinuous as the interface is crossed. So the divergence cleaning relation must be explicitly enforced on the surface.

- 4) Driven conductors can be treated in two ways. The first option is as Dirichlet points where \mathbf{E}_{sol} is specified. The second is as nonboundary points where the driven current density \mathbf{j}_d^{sol} is added to the appropriate component of \mathbf{Q} in each of the nodes inclusive to the conductor. Since this is an imposed current density not dependent upon what occurs in the simulation, we simply define this current density to be whatever we want. Given that

we may choose not to resolve the skin depth of the conductor with our grid, the current density is set to get the correct total current given the size of the conductor. This still leads to reasonably correct fields outside the conductor.

2.2.4 Numerical Solution of the SDF Equations

Dynamic Alternating Direction Implicit (DADI) is the method used to find solutions to the system of finite difference equations resulting from SDF. As shown below, the technique is optimized for use with a five-point finite difference stencil of the Laplacian operator. DADI is an iterative, operator-splitting technique where a fictitious time step is added to the equation to be solved.

$$-\frac{\partial\psi}{\partial t} = L\psi \quad (2.43)$$

where L is the operator resulting from the finite difference form of the original equations. For a discussion of the basic technique see Press, et. al.[pre89]. A solution to $L\psi = 0$ is found by iterating Eq. (2.43) to the time-asymptotic state. The idea is to split the operator into pieces which can be easily solved implicitly and to take several steps to advance ψ from fictitious time step n to $n+1$. For L split into L_1, L_2, \dots, L_m we have

$$\begin{aligned} (-\omega - L_1)\psi^{n+1/m} &= (-\omega + L_2 + \dots + L_m)\psi^n \\ (-\omega - L_2)\psi^{n+2/m} &= (-\omega + L_1 + L_3 + \dots + L_m)\psi^{n+1/m} \\ &\vdots \\ (-\omega - L_m)\psi^{n+(m-1)/m} &= (-\omega + L_1 + \dots + L_{m-1})\psi^{n+(m-1)/m} \end{aligned} \quad (2.44)$$

where $\omega = 2/\delta t$. The splitting can be chosen to ensure convergence of the method[hew92a]. The subtlety comes in choosing ω each time step to maximize the rate at which the time asymptotic state is approached or, equivalently, the rate of convergence. The method used here is due to Doss and Miller as applied to the Laplacian operator[dos79]. For this case consider a single splitting into the horizontal, H , and vertical, V , parts of the Laplacian operator

$$\begin{aligned} (-\omega + H)\psi^{n+1/2} &= (-\omega - V)\psi^n + \sigma \\ (-\omega + V)\psi^{n+1} &= (-\omega - H)\psi^{n+1/2} + \sigma \end{aligned} \quad (2.45)$$

where

$$\begin{aligned} H\psi &= (\psi_{i+1,j} - 2\psi_{i,j} + \psi_{i-1,j})/\Delta x^2 \\ V\psi &= (\psi_{i,j+1} - 2\psi_{i,j} + \psi_{i,j-1})/\Delta z^2. \end{aligned} \quad (2.46)$$

Each time step a HV pass is made using ω to get ψ_1^{n+1} . After this ψ^n is operated on twice (HV, HV) using 2ω or half the time step to get ψ_2^{n+1} . The L2 norm of the difference between ψ_1^{n+1} and ψ_2^{n+1} is divided by the L2 norm of the difference between ψ_2^{n+1} and ψ^n . This ratio determines a multiplicative factor used to change ω for the next time step. For a large ratio the time step is reduced, and for a small ratio the time step is increased. The idea is that a large numerator indicates unresolved behavior which could lead to instability. If the denominator is too large, the time step is too small for fast convergence. Given the form of the operator a simple tridiagonal solution is all that is necessary for each H or V pass. This method is used for the B-field and vector potential, Eqs. (2.27) and (2.28), respectively.

For the SDF equations Coupled Equation DADI (CEDADI) as discussed by Hewett, Larson and Doss[hew92a] is used. The horizontal and vertical passes in this case become

$$\begin{aligned} &H - PASS \\ (-\omega + H - f\mu)\Xi_x^{n+1/2} &= (-\omega - V + (1-f)\mu)\Xi_x^n + \mu D_x \psi^n + Q_x \\ (-\omega + H - f\mu)\Xi_y^{n+1/2} &= (-\omega - V + (1-f)\mu)\Xi_y^n + Q_y \\ (-\omega + H - f\mu)\Xi_z^{n+1/2} &= (-\omega - V + (1-f)\mu)\Xi_z^n + \mu D_z \psi^n + Q_z \\ (-\omega + H)\psi^{n+1/2} &= (-\omega - V)\psi^n - D_x \Xi_x^n - D_z \Xi_z^n \\ &V - PASS \\ (-\omega + V - f\mu)\Xi_x^{n+1} &= (-\omega - H + (1-f)\mu)\Xi_x^{n+1/2} + \mu D_x \psi^n + Q_x \\ (-\omega + V - f\mu)\Xi_y^{n+1} &= (-\omega - H + (1-f)\mu)\Xi_y^{n+1/2} + Q_y \\ (-\omega + V - f\mu)\Xi_z^{n+1} &= (-\omega - H + (1-f)\mu)\Xi_z^{n+1/2} + \mu D_z \psi^n + Q_z \\ (-\omega + V)\psi^{n+1} &= (-\omega - H)\psi^{n+1/2} - D_x \Xi_x^n - D_z \Xi_z^n \end{aligned} \quad (2.47)$$

where

$$\begin{aligned} D_x \psi_{i,j} &= (\psi_{i+1,j} - \psi_{i-1,j})/(2\Delta x) \\ D_z \psi_{i,j} &= (\psi_{i,j+1} - \psi_{i,j-1})/(2\Delta z) \\ 0 &\leq f \leq 1. \end{aligned} \quad (2.48)$$

The factor f can be set for different degrees of implicitness for the $\mu\Xi$ term in the Dynamic ADI iteration. Notice that all of the first-order derivative terms are lagged (evaluated with n th iteration values). This allows the continued use of a tridiagonal solution for the implicit terms. The CEDADI method has been shown to be considerably faster than bi-conjugate gradient for this set of equations. The convergence criteria is for the largest value of $|L\Phi|$ on the grid divided by the average value of Φ is less than a given error test. Here Φ represents ψ and all components of Ξ .

As with the implicit electrostatic field equation, the CEDADI routine was tested to ensure that the conductor and other boundary conditions were implemented properly. The test region is the same as that shown in Fig. 2.3. The following steps are taken to define an initial \mathbf{E}_{sol}^o and self consistent \mathbf{Q} . CEDADI is then used to solve for \mathbf{E}_{sol} which is compared to the original.

- 1) Define an array $\phi(i,j)$ from the function

$$\phi(x, z) = \exp(-x^2/L^2)\sin(k_z z). \quad (2.49)$$

Set ϕ to zero on conductors and one node outside conductors.

- 2) Calculate

$$\mathbf{E}_{sol}^o(i, j) = \nabla \times (\phi(i, j)\hat{y}). \quad (2.50)$$

So \mathbf{E}_{sol}^o has no divergence, and it is zero on conductors. The calculated $\mathbf{E}_{sol}^o(i,j)$ is shown in Fig. 2.4a.

- 3) Calculate

$$\dot{\mathbf{J}}_{sol}(i, j) = \nabla^2 \mathbf{E}_{sol}^o(i, j) \quad (2.51)$$

- 4) Calculate

$$\dot{\mathbf{J}}_{irr}(i, j) = \nabla \phi(i, j) \quad (2.52)$$

- 5) Calculate

$$\mathbf{Q}(i, j) = \dot{\mathbf{J}}_{sol}(i, j) + \dot{\mathbf{J}}_{irr}(i, j) - \mu \mathbf{E}_{sol}^o(i, j) \quad (2.53)$$

where

$$\mu(x, z) = \mu_o(\sin(2k_x x) + 2 - \cos(2k_z z)) \quad (2.54)$$

$\mu(i,j)$ is shown in Fig. 2.4b.

6) Use CEDADI to solve for Ξ and ψ , and then find \mathbf{E}_{sol} .

7) Calculate the error from $\mathbf{E}_{sol} - \mathbf{E}_{sol}^o$.

With a μ_o of one CEDADI takes 81 iterations to converge to an error criteria of 10^{-4} on the 41x41 grid. Figure 2.5a is a vector plot of the calculated Ξ , and Fig. 2.5b is a contour plot of ψ . The difference between the original and calculated \mathbf{E}_{sol} is shown in Fig. 2.5c. The error here is more a function of the finite difference operators especially the $\nabla\psi$ operation, then any error due to the convergence criterion of the CEDADI scheme. In fact while $\nabla^2\psi(i,j) - \nabla \cdot \Xi(i,j)$ is small ($\sim 10^{-5}$), $\nabla \cdot \mathbf{E}_{sol}(i,j)$ is significantly larger ($\sim .05$ for this example).

2.3 Dielectrics

For many problems of interest dielectric as well as conducting structures are needed. Since fields penetrate through dielectrics, one cannot simply treat them as surfaces with boundary conditions which ignore the interior. For dielectrics Ampere's law in the Darwin limit becomes

$$\nabla \times \mathbf{B} = \frac{4\pi}{c} \mathbf{J} + \frac{1}{c} \frac{\partial \mathbf{D}_{irr}}{\partial t}. \quad (2.55)$$

Here \mathbf{D} is the electric displacement which is defined as

$$\mathbf{D} = (1 + 4\pi X_d) \mathbf{E} \quad (2.56)$$

where X_d is the dielectric susceptibility. Notice that in the plasma where X_d is zero, the equations are the same as in the previous section. So the accuracy for the particle Lagrangian remains the same.

In the dielectric region Gauss' law

$$\nabla \cdot \mathbf{D} = 4\pi\rho \quad (2.57)$$

and the charge continuity equation are used to replace \mathbf{D}_{irr} with $-4\pi\mathbf{J}_{irr}$. Again Ampere's law can be written as Eq. (2.24). The result is that the equations for \mathbf{E}_{sol} and \mathbf{B} are unchanged. All the solutions of the previous section still apply. This is not the case for the electrostatic field equation where Gauss' law in terms of the components of the E-field

becomes

$$\nabla \cdot \left[(1 + 4\pi X_d) \nabla \phi \right] - \nabla \cdot (4\pi X_d \mathbf{E}_{sol}) = -4\pi \rho. \quad (2.58)$$

Solving for the electrostatic potential including the direct implicit susceptibility, \mathbf{X}_I , the new electrostatic field equation becomes

$$\nabla \cdot \left[(\mathbf{I} \cdot + 4\pi \mathbf{X}_I \cdot + 4\pi X_d) \nabla \phi^{n+1} \right] = -4\pi \tilde{\rho} + 4\pi \nabla \cdot (X_d \mathbf{E}_{sol}) \quad (2.59)$$

This equation introduces a possible stability problem since the electrostatic and electromagnetic field equations allow an explicit connection between \mathbf{E}_{sol}^n and \mathbf{E}_{sol}^{n+1} during a time step. This should only be a problem in regions where dense plasma and dielectric meet. In the plasma X_d is zero so the connection through the electrostatic equation is removed. In regions of dielectric and vacuum the $\mu \mathbf{E}_{irr}$ term is absent from \mathbf{Q} as defined by Eq. (2.30). It does not contribute to the SDF Eq. (2.39); therefore, there is no contribution to \mathbf{E}_{sol} . Since in the future plasma/wall interfaces will be treated with analytic sheath boundary conditions, the potential region of instability will be eliminated from the simulation. As a second option for those cases where \mathbf{E}_{sol} makes little contribution to Eq. (2.59), the $\mathbf{E}_{sol}^n \cdot \nabla X_d$ term could be removed while retaining most of the contribution of X_d . This is true for situations in which \mathbf{E}_{sol} is driven in the direction perpendicular to the simulation plane, and the only contributions to \mathbf{E}_{sol} in the plane are plasma fluctuations.

2.4 DADIPIC Algorithm and GYMNOS

The field solutions of sections 2.1 and 2.2 can now be integrated into a combined algorithm for the time advance of particle and field quantities. The result is a time cycle of two sets of the four steps mentioned in chapter 1. Given initial values of \mathbf{E}^n , \mathbf{B}^n , \mathbf{x}_i^n , $\mathbf{v}_i^{n-1/2}$, and $\bar{\mathbf{a}}_i^{n-1}$, the cycle proceeds as follows.

I. Advance to \sim level

- 1) Interpolate $\mathbf{E}_{sol,j}^n$ and \mathbf{B}_j^n to particles.
- 2) Push particles to $\tilde{\mathbf{v}}_i$ and $\tilde{\mathbf{x}}_i$ using Eq. (2.2).
- 3) Interpolate the $\tilde{\mathbf{v}}_i$ and $\tilde{\mathbf{x}}_i$ to the grid finding $\tilde{\rho}_j$ and \mathbf{X}_j .
- 4) Solve the implicit electrostatic field Eq. (2.59) to find $\mathbf{E}_{irr,j}^{n+1}$.

II. Advance to n+1 level

- 1a) Interpolate $\mathbf{E}_{irr,j}^{n+1}$ and \mathbf{B}_j^n to particles

- 2a) Push particles to $\mathbf{v}_i^{n+1/2}$ and \mathbf{x}_i^{n+1} using Eq. (2.3) and evaluating $\delta\mathbf{v}$ at $\bar{\mathbf{x}}$. Save $\bar{\mathbf{a}}_i^n$.
- 1b) Interpolate $\mathbf{E}_{irr,j}^{n+1}$, $\mathbf{E}_{sol,j}^n$, and \mathbf{B}_j^n to the particles.
- 2b) Find \mathbf{v}_i^{n+1} from

$$\mathbf{v}^{n+1} = \mathbf{R}^n \cdot \mathbf{v}^{n+1/2} + \frac{q\Delta t}{4m} (\mathbf{I} + \mathbf{R}^n) \cdot \left(\mathbf{E}_{irr}^{n+1} + \mathbf{E}_{sol}^n \right). \quad (2.60)$$

- 3) Interpolate the \mathbf{v}_i^{n+1} and \mathbf{x}_i^{n+1} to the grid finding \mathbf{J}_j^{n+1} , ρ_j^{n+1} , and \mathbf{K}_j^{n+1} .
- 4) Solve the B-field and SDF Eqs. (2.27), (2.28), (2.39), and (2.40) to find \mathbf{B}_j^{n+1} and $\mathbf{E}_{sol,j}^{n+1}$.

Since the solution of the electrostatic and SDF fields are separated in this algorithm, there is a certain flexibility with respect to the method used for the implicit electrostatic particle advance. For this work the D_1 direct implicit scheme has been chosen, but other direct implicit schemes or the moment implicit method could be substituted with little change to the overall algorithm.

Note that steps 1), 2), and 3) are inside a loop over all the particles. The steps are completed for one particle before the next particle is considered. Each particle adds its contribution individually to the grid source terms in step 3). Also \mathbf{v}^{n+1} is not stored for each particle. The advance of one-half a time step is needed to find \mathbf{J}^{n+1} and \mathbf{K}^{n+1} . Only the second order accurate, leap-frogged $\mathbf{v}^{n+1/2}$ passes through to the next time cycle.

This algorithm has been incorporated into an already existing 2.5-D PIC code developed by Hewett called GYMNOS[hew92b]. This magnetostatic code based on elliptic solution algorithms using DADI is an excellent framework for the DADIPIC algorithm. The code is written in R-Z geometry and has the ability to generate its own internal structures. Both structure and field quantities are stored on cell corners. Particles may be perfectly reflected, fully absorbed, absorbed with a fraction thermally reemitted, field-emitted, or injected with a prescribed distribution. The particle pusher is a fully vectorized Boris pusher. Below is an overview of GYMNOS followed by the major changes made to implement DADIPIC.

1) To begin the code sets physical constants, creates files, initializes graphics, and opens the input file with a call to the subroutine FIRS.

2) The code reads the namelist NDATA which defines the simulation region, the time step, the simulation stop time, and diagnostic dump times.

3) The code calls subroutine INIT to initialize the run. In the nonperiodic case four bounding structures are set around the simulation region. Namelist GSET1 is read to get position and imposed potential or current information for internal structures. The status of nodes in relation to structures is stored in the arrays SKEY, KEY, and KORNT. Elements in the arrays which correspond to cell centers or corners which are not in structures are designated by 0. SKEY indicates whether a cell center is inside a structure with -1., KEY designates nodes which are part of structures with -1, and KORNT indicates nodes which are on the surface of structures with several integer designators (depending on the surface orientation and whether it is flat or a corner). These arrays are needed in the field solve and particle trapping routines since the handling of nodes in the routines is controlled with integer switches. The arrays are set in the routine GEOMSET based on the information from GSET1.

INIT next reads a namelist NECHSP for each particle species. This gives information on the initial plasma state along with the physical properties of structure surfaces with respect to particles. With this information INIT initializes the particles for each species and prepares for any required particle injection.

4) Control returns to the MAIN routine and the time integration loop. Each time step the routine TRANS is called to move, inject, and absorb particles. At the same time particle quantities are accumulated on the grid. A call is then made to FIELD to solve the field equations on the grid. Diagnostics are also saved during the time step.

5) After the last time step MAIN closes all files with a call to ENDPLT and then terminates the run.

For the implementation of DADIPIC, GYMNOS was converted to XZ geometry. This allowed the investigation of DADIPIC in a uniform doubly periodic plasma where comparisons could be made to analytic kinetic theory for basic test cases. The main changes in going from cylindrical to Cartesian geometry occurred in the volume calculations for source accumulation, in the r,x components of the particle equations of motion, and in the r,x direction finite difference terms in the field equation solutions. The two parts of the time cycle in DADIPIC manifest themselves in the duplication of the routines called during a time step. TRANS1 and FIELD1 are called to do the particle advance to the \sim level and solve for the implicit electrostatic field. In TRANS1 the X tensor is found from the B-field, $\bar{\rho}$, and the dielectric susceptibility on the grid. TRANS2 and FIELD2 are called to do the particle advance to the $n+1$ level and solve for the B-field and solenoidal E-field.

The number of geometry arrays has been increased to allow different structure types. KEYIM and KORNTIM are set based on all the structures in the simulation and are used to determine when particles cross structure boundaries. KEYIMF and KORNTF are set according to grid points enclosed by conducting structures. Dielectric structures have KEYIMF=0 and are not considered boundary nodes. The grid nodes do have an associated dielectric susceptibility stored in DIECHI which is set based on the locations of the dielectric structures. Before each field solve KEY and KORNT are set based on KEYIMF and KORNTF with any driven structures removed. The field routines use KEY and KORNTF to set the finite difference coefficients for each node. As an example consider a conducting structure which has a driven current density in the y direction. For the electrostatic field solution KEY=-1, and the structure would have Dirichlet nodes at some designated potential. For the A_y solution KEY=0, the structure is not a boundary region, and the structure nodes have some imposed current density added to any particle density at each point.

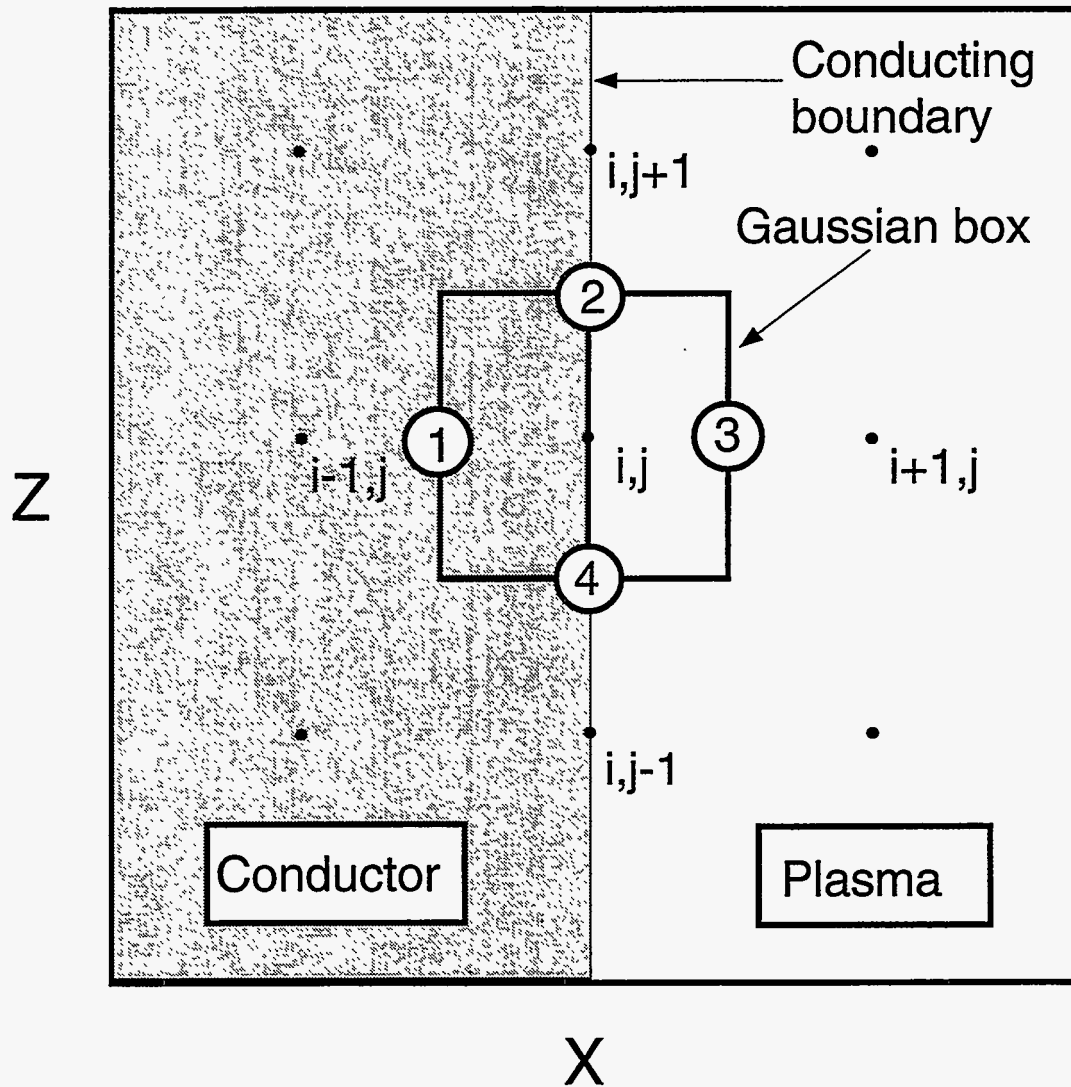


Figure 2.1: Position of the surfaces for a Gaussian box around a node at the surface of a conducting boundary.

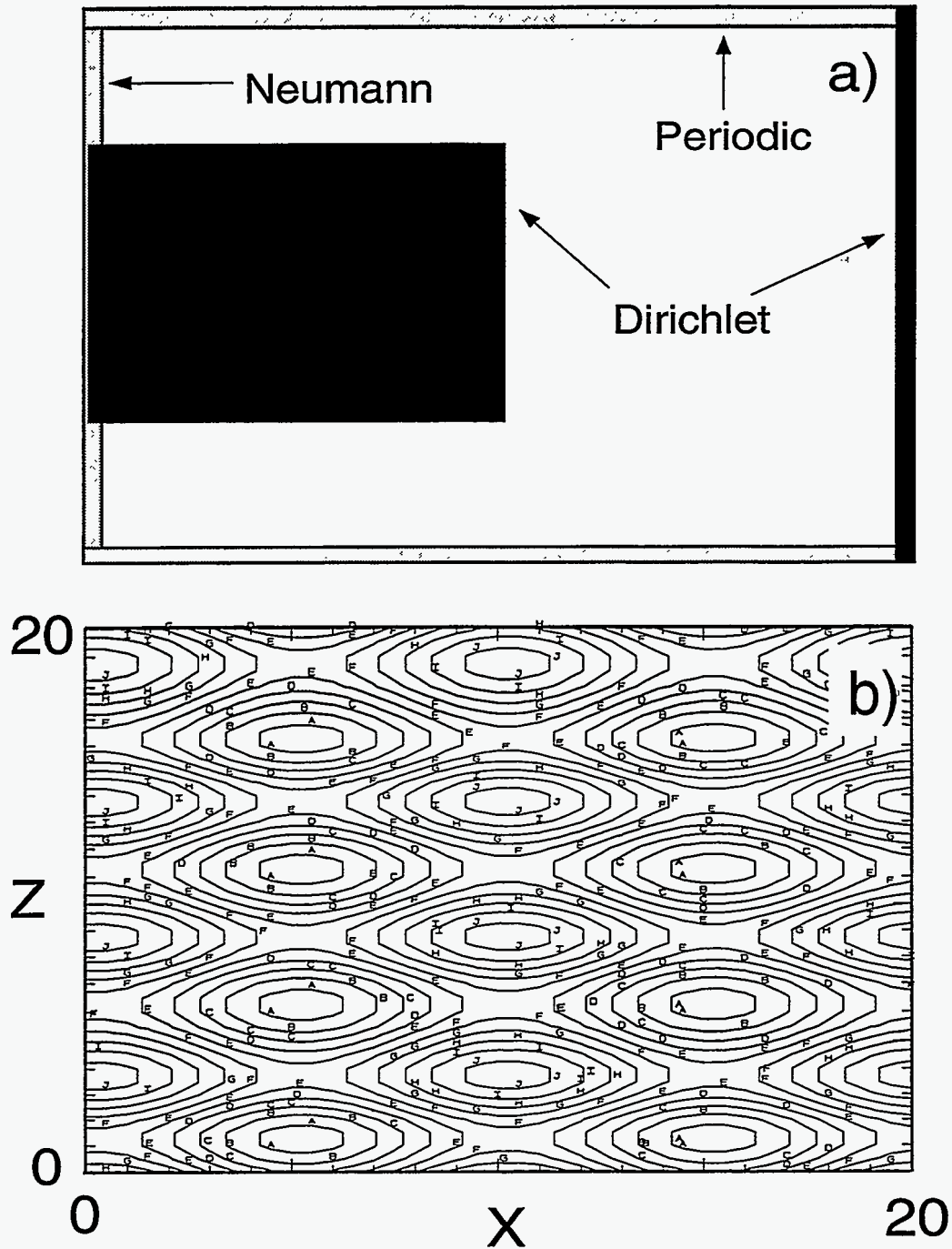


Figure 2.2: Region for testing the numerical solution of the implicit electrostatic field equation a) the boundary conditions b) the spatial variation of X^{xx} ($a=.255$ and $j=3.74$).

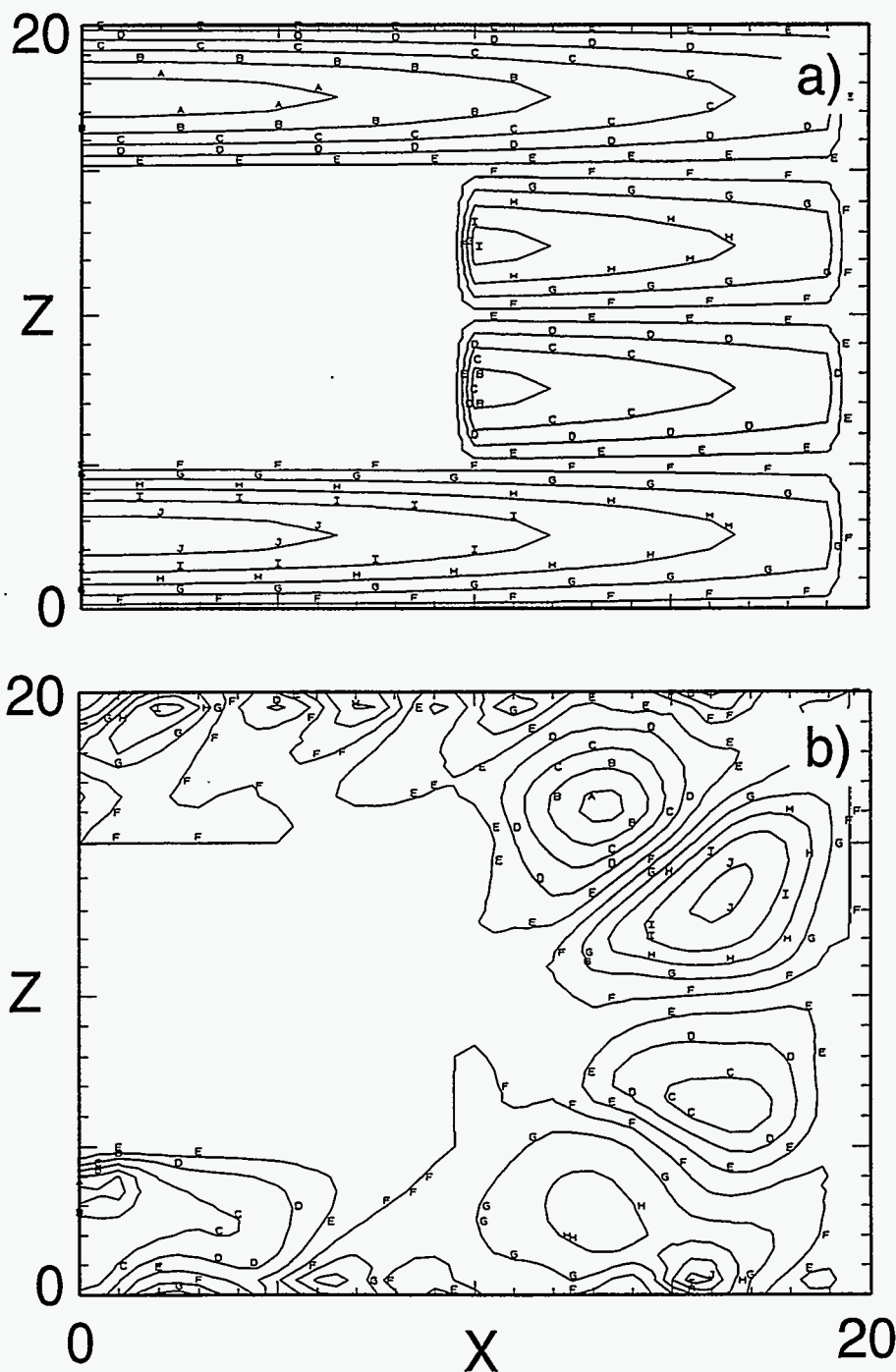


Figure 2.3: Test results of the numerical solution to the implicit electrostatic field equation
 a) the potential calculated by the bi-conjugate gradient routine ($a=-.90$ and $j=.90$) and
 b) the difference between the bi-conjugate gradient and DADI solutions ($a=-6.6e-10$ and
 $j=5.3e-10$).

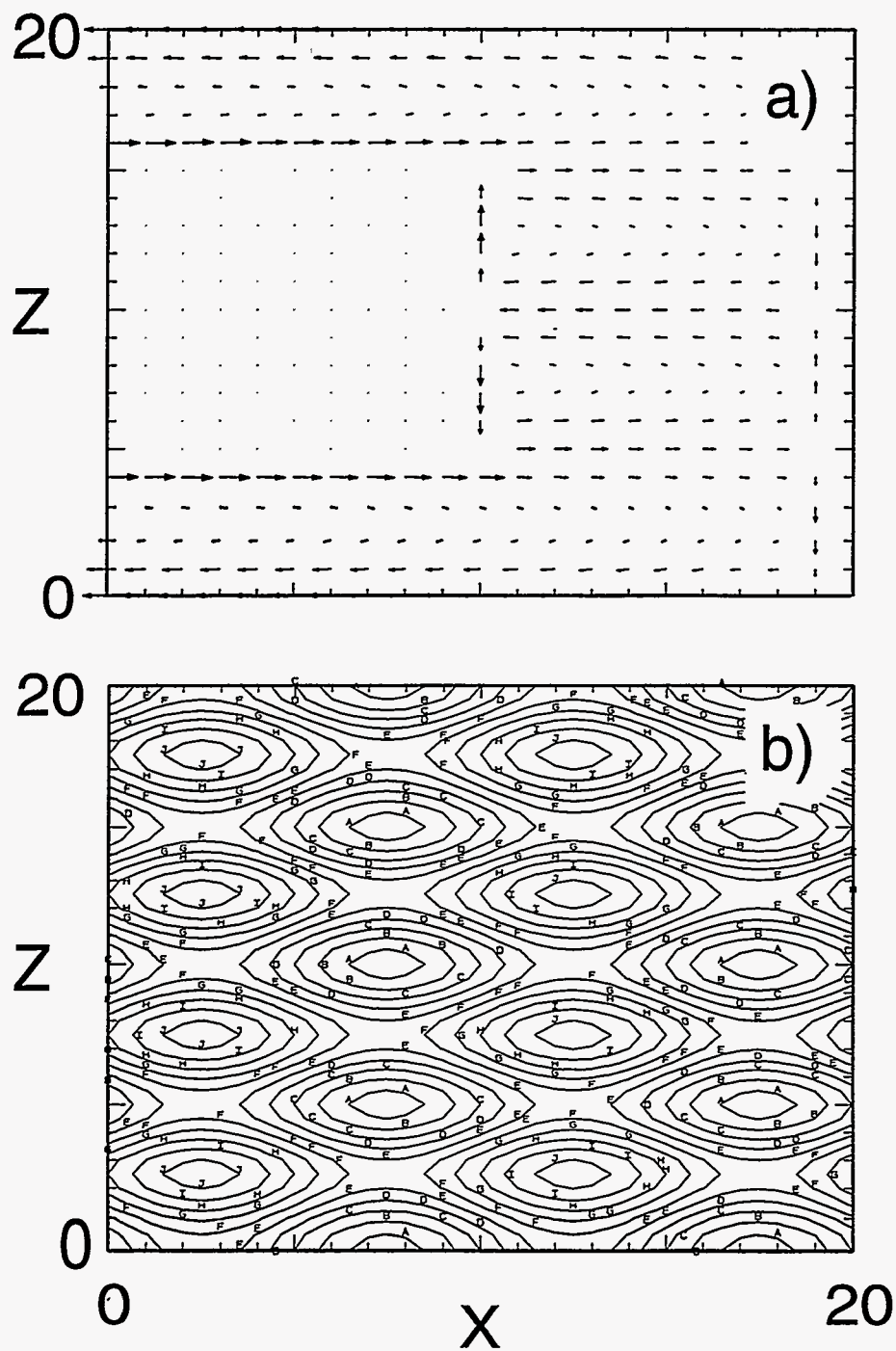


Figure 2.4: Results of the CEDADI test: a) the original E_{sol} (longest vector=.809) and b) the spatial variation of μ ($a=.200$ and $j=3.80$)

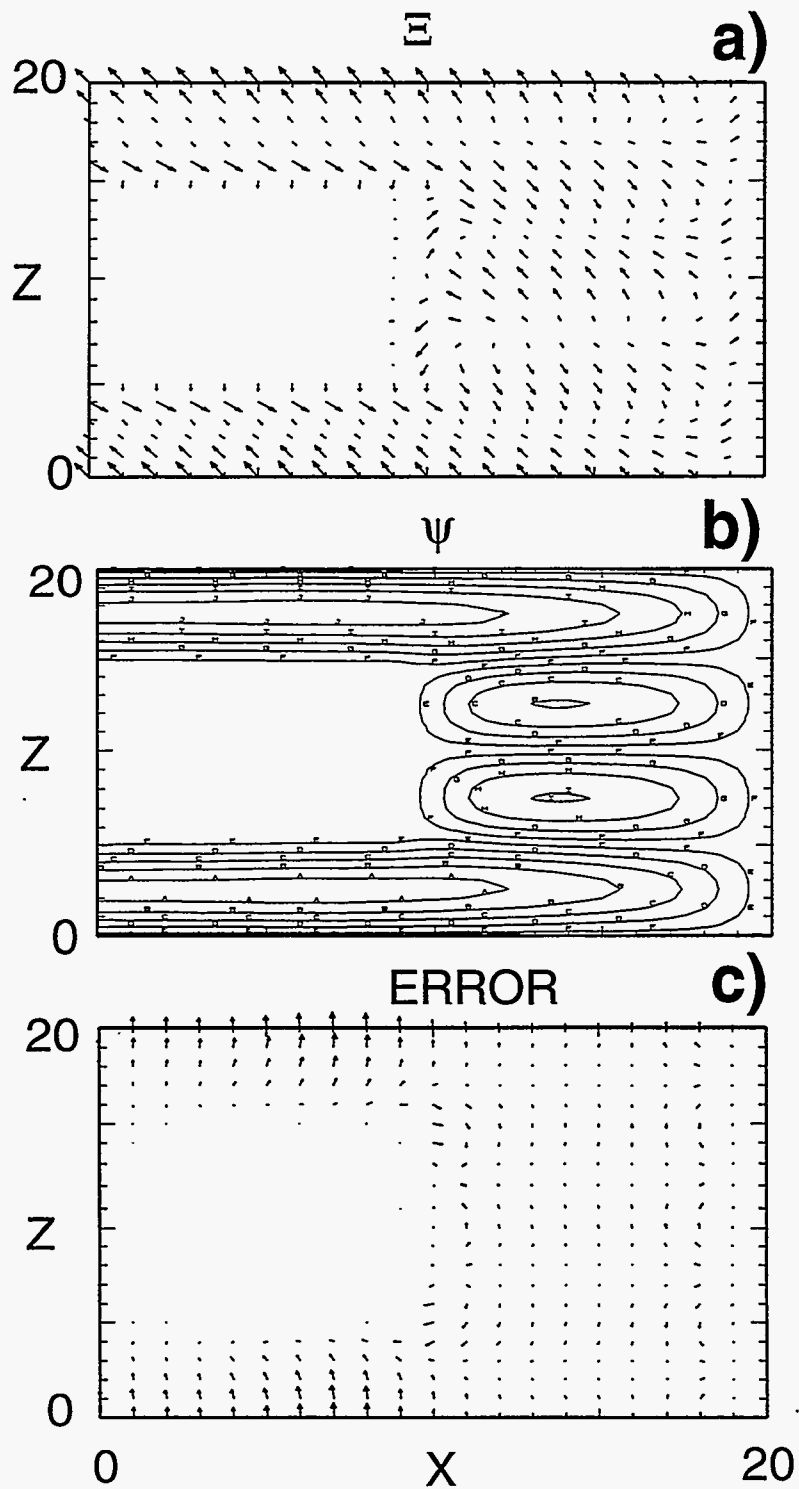


Figure 2.5: Results of the CEDADI test: a) vector plot of Ξ (longest vector=1.19) b) contour plot of ψ ($a=-1.53$ and $j=1.53$), and c) vector plot of $E_{sol}^0 - E_{sol}$ (longest vector=.0907)

Chapter 3

Theory of DADIPIC Operation

Given a method for low frequency, kinetic plasma simulation, its performance must be evaluated. In this chapter analytic theory is used to predict the behavior of DADIPIC giving guidance about conditions to be met for stable and accurate simulation. This gives a framework of understanding for choosing the test cases of Chapter 4. Those test cases are used to verify the theory in an actual 2-D code as well as provide information not obtainable from theory.

3.1 Effect of the Direct Implicit Method

Several sources discuss the effect of finite spatial and temporal discretization on the direct method [lan85], [lan83], [coh84]. In this section we investigate the constraints to be met for accurate solution of the field equation, and then cover linear kinetic theory to predict the effect of electrostatic fluctuations which are not properly resolved.

3.1.1 Accuracy of the Field Equation

First we must consider whether Eq. (2.4) is a reasonable approximation of ρ^{n+1} . For a linear shape function it is exact as long as the particle remains within the cell in which it started or

$$\frac{\delta \mathbf{v} \Delta t}{\Delta x} = \frac{q \Delta t^2}{4m \Delta x} (\mathbf{I} + \mathbf{R}) \mathbf{E} \ll 1 \quad (3.1)$$

The evaluation of Eq. (2.4) at $\bar{\mathbf{x}}$ further restricts the predictor term to only be accurate for \mathbf{R} and \mathbf{E} which have scale lengths long compared to $\Delta t \delta \mathbf{v}$. Since the gridding limits the variation of these quantities, the constraint of Eq. (3.1) should be sufficient. For higher

order shape functions the other terms in the expansion have been neglected, but again constraint (3.1) would cause these terms to be small. Under conditions where Eq. (3.1) is a valid expansion, an accurate solution can be expected from the electrostatic field equation with strict differencing. It remains necessary to determine the minimum density fluctuation scale lengths for which the simplified differencing of Eq. (2.6) agrees with strict differencing.

Here large density fluctuations which change on long time scales shall be investigated; thus, they are temporally resolved in simulations of low frequency phenomena. Low frequency behavior may be due to long scale lengths or externally imposed fields. Acceptable scale lengths are estimated by comparing the difference between the second terms in the ρ^{n+1} expansion. Consider a one dimensional unmagnetized system. For simplified differencing we have

$$\begin{aligned} \nabla_j \cdot \left[\frac{(q\Delta t)^2}{2m} n \nabla_j \phi \right] = \\ \frac{1}{4m} \left(\frac{q\Delta t}{\Delta x} \right)^2 \{ (n_{j+1} + n_j) \phi_{j+1} - (n_{j+1} + 2n_j + n_{j-1}) \phi_j + (n_j + n_{j-1}) \phi_{j-1} \} \end{aligned} \quad (3.2)$$

where

$$\begin{aligned} n_j &= \sum_i \frac{1}{\Delta x} \left[S^+(x_j - \tilde{x}_i) + S^-(x_j - \tilde{x}_i) \right] \\ S^+(x_j - x) &= (x - x_j)/\Delta x \text{ for } x_j < x < x_j + \Delta x \\ S^-(x_j - x) &= (x_j - x)/\Delta x \text{ for } x_j - \Delta x < x < x_j \end{aligned} \quad (3.3)$$

For strict differencing[coh84]

$$\begin{aligned} \sum_i \frac{(q_i \Delta t)^2}{2m \Delta x} \left[\sum_{k=j}^{j+1} E_k S(x_k - \tilde{x}) \cdot \nabla_i S(x_j - \tilde{x}) \right] = \\ \frac{1}{4m} \left(\frac{q\Delta t}{\Delta x} \right)^2 \sum_i \frac{1}{\Delta x} \left[-S^+(x_{j-1} - \tilde{x}_i) (\phi_j - \phi_{j-2}) - S^-(x_j - \tilde{x}_i) (\phi_{j+1} - \phi_{j-1}) \right. \\ \left. + S^+(x_j - \tilde{x}_i) (\phi_{j+1} - \phi_{j-1}) + S^-(x_{j+1} - \tilde{x}_i) (\phi_{j+2} - \phi_j) \right] \end{aligned} \quad (3.4)$$

In these terms only the electrons need to be included since the large mass of the ions makes their contribution small. Approximating the particles with a continuous density function, we can replace the sum over i with an integral over \tilde{x} . Each shape function is multiplied by the density function, $\tilde{n}(x)$, and then integrated over the limits specified by Eq. (3.3). Given functions for \tilde{n} and ϕ we can solve (3.2) and (3.4). The electron density, n_e , ion density, n_i , and potential, ϕ , are assumed to vary sinusoidally as

$$n_e(x) = n_o [Re(e^{ikx}) + \gamma] \quad \gamma \geq 1$$

$$\begin{aligned}
n_i(x) &= (1 + \delta)n_e(x) \\
\phi(x) &= \phi_o Re(e^{ikx})
\end{aligned} \tag{3.5}$$

With small δ the electron and ion densities are almost the same, and fields large enough to violate Eq. (3.1) are avoided. This linear form is a solution to Poisson's equation, and it is used to gauge the difference between simplified and strict differencing. Plugging the quantities of Eq. (3.5) into Eqs. (3.2) and (3.4), the simplified differencing term is

$$\begin{aligned}
SiD &= \frac{1}{4m} \left(\frac{q\Delta t}{\Delta x} \right)^2 n_o \phi_o \left[4\gamma \cos(kx_i) (\cos(k\Delta x) - 1) \right. \\
&+ \cos(2kx_i) \left[\frac{1}{(k\Delta x)^2} [\cos(3k\Delta x) - 2\cos(2k\Delta x) - \cos(k\Delta x) + 2] \right. \\
&\left. \left. + \frac{1}{k\Delta x} [\sin(3k\Delta x) - 3\sin(k\Delta x)] \right] \right] \tag{3.6}
\end{aligned}$$

and the strict differencing term is

$$\begin{aligned}
StD &= \frac{1}{4m} \left(\frac{q\Delta t}{\Delta x} \right)^2 n_o \phi_o \left[\gamma \cos(kx_i) (\cos(2k\Delta x) - 1) \right. \\
&\left. - \frac{1}{(k\Delta x)^2} \cos(2kx_i) [\cos(3k\Delta x) - 2\cos(2k\Delta x) - \cos(k\Delta x) + 2] \right] \tag{3.7}
\end{aligned}$$

Figure 3.1 shows $|StD - SiD|/|StD|$ vs. $2\pi/k\Delta x$ for $\gamma = 1$. As one can see for wavelengths of $5\Delta x$ or more simplified differencing agrees well with strict differencing. This is because the exact position of particles in a cell is relatively less important for modes with wavelengths of many cells. For smaller wavelengths the simplified differencing term becomes much larger than the strict differencing term. Larger terms on the left hand side of the field equation would force the potential to be smaller for a given charge density distribution. Such a reduction of the field would be stabilizing in cases where the field is large enough to violate Eq. (3.1) for small scale length variations.

Finally, an estimate of the time step needed to resolve a phenomena with frequency ω_o can be found from a von Neumann stability analysis of the time-advance difference equations, assuming a time harmonic oscillation of only the electrostatic field [roa76]. A dispersion relation results for the normal modes at ω dependent on the driven frequency ω_o . For the D₁ implicit scheme the dispersion relation is [lan83]

$$(\omega_o \Delta t)^2 z^3 + (2z - 1)(z - 1)^2 = 0 \tag{3.8}$$

where $z = \exp(-i\omega t)$. $\|z\|$ for the least damped simple-harmonic oscillator mode shows large damping for large $\omega_o \Delta t$; however, the damping is quite small for $(\omega_o \Delta t)^2$ less than

.05. Thus the constraints for resolving electrostatic phenomena are Eq. (3.1) and

$$k\Delta x \leq 1 \quad \omega_o\Delta t \leq .2 \quad (3.9)$$

3.1.2 Linear Kinetic Theory

While we meet the above constraints for resolving the low frequency phenomena that we are trying to simulate, we probably will not resolve the high frequency, electrostatic plasma oscillations which cause the unavoidable fluctuation background in the plasma. This section reviews the results of linear kinetic theory which have been applied to the discretized plasma of the PIC simulation. The expected results will be compared to test runs of the DADIPIC code in Chapter 4 to ensure its correct implementation. Most studies of the numerical dispersion effects of the implicit method have concentrated on the electrostatic field. Since the electromagnetic fluctuation fields are much smaller than the electrostatic fluctuations fields, the numerical effects of the EM fluctuation fields should also be relatively small. As will be shown in Chapter 4, this has proven to be the case. Despite the presence of B-fields which contribute to the \mathbf{X} tensor, the electrostatic fluctuation fields appear to agree with electrostatic kinetic theory. The numerical heating/cooling is also similar to that reported in Cohen, et. al. [coh89] for a 1-D electrostatic algorithm.

In linear theory the plasma is assumed to have a small perturbation, f_{s1} , of the plasma distribution around some plasma equilibrium, f_{s0} . We must solve the first order Vlasov equation[kra86]

$$\left(\frac{d}{dt} + \mathbf{v} \cdot \nabla\right) f_{s1} = \frac{q_s}{m_s} \nabla\phi_1 \nabla_{\mathbf{v}} f_{s0} \quad (3.10)$$

and the field equations (for electrostatics just Poisson's equation)

$$\nabla^2\phi_1 = -4\pi \sum_s \bar{n}_s q_s \int f_{s1} d\mathbf{v}. \quad (3.11)$$

A solution is found by taking the Fourier transform with respect to the spatial variables and solving the resulting algebraic equations. The result is an equation $D(k, \omega)\phi(k, \omega) = 0$ where D is the dispersion function. The normal modes which can exist in the plasma are found for k and ω which satisfy $D(k, \omega) = 0$. For the electrostatic case we find [kra86]

$$D_c(k, \omega) = 1 + \sum_s \frac{\omega_{ps}^2}{k^2} \int_L \frac{\mathbf{k} \cdot \nabla_{\mathbf{v}} f_{s0}}{\omega - \mathbf{k} \cdot \mathbf{v}} d\mathbf{v} = 0 \quad (3.12)$$

where L indicates integration over the Landau contour. In the equilibrium plasma the various normal modes (Langmuir waves, ion-acoustic waves, etc.) exist as fluctuations and are damped modes. A uniform plasma with a Maxwellian velocity distribution is in equilibrium and no net change in the particle total kinetic energy will occur. As we shall see, this is not the case for the PIC plasma.

Dispersion Relations

In deriving dispersion relations for the PIC plasma discrete Fourier transforms must be used for those quantities which are discrete in space and time. For a continuous quantity such as particle position, $P(x)$, the Fourier transform is

$$P(k) = \int_{-\infty}^{\infty} dx P(x) e^{-ikx} \quad (3.13)$$

For grid quantities

$$G(k) = \delta x \sum_{j=-\infty}^{\infty} G_j e^{ikX_j} \quad (3.14)$$

With these transforms the forms of source and field quantities can be found in Fourier space which are appropriate for Eq. (3.11). These quantities have been derived by Langdon in several sources [lan70], [lan79a], [lan79b] and only an abbreviated overview will be presented here. Investigations of the direct implicit method in particular are in [lan85], [lan83], [coh84]. First consider the spatial transforms [lan70]. Assuming the simulation particle density is sufficient to approximate as a continuous quantity, the density interpolated to the grid is

$$n_j(t) = \int dx S(x_j - x) n(x, t) \quad (3.15)$$

The Fourier transform of the grid quantity is

$$n(k, t) = \sum_{p=-\infty}^{\infty} S(k_p) n(k_p, t) \quad (3.16)$$

where $k_p = k - pk_g$ and $k_g = 2\pi/\Delta x$. The force on a particle is given by

$$\mathbf{F}(k, t) = -iqS(-k)\kappa(k)\phi(k, t) \quad (3.17)$$

where κ is a function resulting from the finite difference form of the gradient operator. Again this is similar to the continuous case modified by the Fourier transform of the shape

function. The result for Poisson's equation is

$$K^2(k)\phi(\mathbf{k}, t) = 4\pi q \sum_p S(\mathbf{k}_p) n(\mathbf{k}_p, t) \quad (3.18)$$

where K is a function resulting from the finite difference form of the Laplacian operator.

The time behavior was investigated by considering deflections of the electrons, $x^{(1)}$, from zero-order orbits, $x^{(0)}$, caused by the fields [lan79a]. The deflection of a particle from a straight path is computed for an E-field of the form $\mathbf{E}^{(1)}(\mathbf{x}, t) = \mathbf{E} \exp[i(\mathbf{k} \cdot \mathbf{x} - \omega n \Delta t)] = \mathbf{E} \exp[i\mathbf{k} \cdot \mathbf{x}] z^n$. Note that if ω has a negative imaginary part then the field magnitude will exponentially increase with time. Using the finite difference equations for the advance of the particle positions and velocities, $x_n^{(1)}$ at time step n can be found as a summation over past accelerations. This gives us a function

$$\left[\frac{X}{A} \right]_{\omega - \mathbf{k} \cdot \mathbf{v}} = \frac{x_n^{(1)}}{a_n^{(1)}} \quad (3.19)$$

which involves summations over $z = \exp(-i\omega \Delta t)$. The exact form of the function depends on the particle integration scheme implemented (explicit, D₁ implicit, etc.). As n goes to infinity the $[X/A]$ take on limiting forms.

$$\begin{aligned} \left[\frac{X}{A} \right]_{\text{explicit}} &= (\Delta t)^2 \frac{z}{(z-1)^2} \\ \left[\frac{X}{A} \right]_{D_1} &= (\Delta t)^2 \left[\frac{z}{(z-1)^2} + \frac{1}{2-1/z} \right] \end{aligned} \quad (3.20)$$

Now regard the result of the perturbed move to $x^{(0)} + x^{(1)}$ as a superposition of monopoles q at $x^{(0)}$ and dipoles with q at $x^{(0)} + x^{(1)}$ and $-q$ at $x^{(0)}$. The monopole density is cancelled by the neutralizing background, and the dipole polarization density is

$$P(\mathbf{x}, t) = q n_o \int d\mathbf{v} f_o(\mathbf{v}) \mathbf{x}^{(1)}(\mathbf{x}, \mathbf{v}, t) \quad (3.21)$$

Since $\rho^{(1)} = -\nabla \cdot \mathbf{P}$, we can find the form of $n(\mathbf{k}, \omega)$. The result is

$$q n(\mathbf{k}, \omega) = -\mathbf{k} \cdot \vec{\kappa}(\mathbf{k}) S(-\mathbf{k}) X(\mathbf{k}, \omega) \phi(\mathbf{k}, \omega) \quad (3.22)$$

where the finite grid effects on the force of equation (3.17) have been included and

$$X(\mathbf{k}, \omega) = \frac{q^2 n_o}{m} \int d\mathbf{v} f_o(\mathbf{v}) \left[\frac{X}{A} \right]_{\omega - \mathbf{k} \cdot \mathbf{v}} \quad (3.23)$$

Substituting this into equation (3.18) gives the dispersion relation

$$D_{pic}(\mathbf{k}, \omega) = 1 + \frac{4\pi}{K^2(k)} \sum_p \mathbf{k}_p \cdot \vec{\kappa}(\mathbf{k}_p) S^2(\mathbf{k}_p) \mathbf{X}(\mathbf{k}, \omega) = 0 \quad (3.24)$$

where $k_{xp} = k_x - 2\pi p/\Delta x$. Notice the similarity to equation (3.12). It can be found that as Δx and Δt go to zero equation (3.24) converges to the continuum result. It is this dispersion relation which indicates instability ($Im(\omega) < 0$) when $\omega_{pe}\Delta t > 1.62$ for an explicit time integration and a Maxwellian velocity distribution. The implicit particle advance eliminates this constraint. The implicit case, however, requires $(kv_{th}\Delta t)^2 < 1$ for correct Debye shielding[lan83]. This is a particle transit time effect similar to the restriction (3.1) since the maximum k equals $\pi/\Delta x$.

Electrostatic Fluctuations

Vlasov theory treats the plasma as a fluid in \mathbf{x} - \mathbf{v} phase space with a continuous distribution function. This was the assumption used above to calculate the dispersion function for the PIC plasma. However this theory cannot describe the field fluctuations in a plasma. For fluctuations the test-particle picture is used. In this picture each plasma particle leads a double life. It is a test particle moving in a Vlasov fluid, and it is also part of the Vlasov fluid participating in the shielding of charges. First the potential in a plasma due to a test charge is found, then fluctuations in densities, fields, and other properties which depend on particle discreteness are calculated by ensemble averaging over all particles.

As shown by various sources, the potential due to a test charge is [kra86]

$$\phi(\mathbf{k}, \omega) = \frac{\rho_t(\mathbf{k}, \omega)}{k^2 D_c(\mathbf{k}, \omega)} \quad (3.25)$$

The form for the PIC case is[lan79b]

$$\phi(\mathbf{k}, \omega) = \frac{\rho_t(\mathbf{k}, \omega)}{K^2(k) D_p(\mathbf{k}, \omega)} \quad (3.26)$$

where $\rho_t(\mathbf{k}, \omega)$ is the Fourier transform of the charge density for the test particle in either the continuous or PIC case. Given ϕ we can find the value of other quantities. We can then find the average fluctuation level of some quantity $g(\mathbf{k}, \omega)$ by taking the inverse Fourier transform and ensemble averaging

$$\langle g(\mathbf{x}, t) \rangle = \sum_s n_{os} \int d\mathbf{v}' d\mathbf{x}' f_{os}(\mathbf{v}') g(\mathbf{x}, \mathbf{x}', \mathbf{v}', t) \quad (3.27)$$

A useful quantity to measure in the PIC plasma is the E-field energy density. In terms of the spectral density, $W(\mathbf{k}, \omega)$, it is

$$\frac{\mathbf{E} \cdot \mathbf{E}^*}{8\pi} = \int \frac{d\mathbf{k}}{(2\pi)^3} \int \frac{d\omega}{2\pi} W(\mathbf{k}, \omega) \quad (3.28)$$

For the uniform, Maxwellian plasma with electrostatic fluctuations the spectral density is [kra86]

$$W(\mathbf{k}, \omega) = \sqrt{\frac{\pi}{2}} \frac{v_{the} \lambda_{De} m_e}{(k \lambda_{De})^3} \frac{1}{|D_c(\mathbf{k}, \omega)|^2} \exp\left[-\frac{1}{2} \left(\frac{\omega}{\omega_{pe}}\right)^2 \frac{1}{(k \lambda_{De})^2}\right] \quad (3.29)$$

For the PIC case [lan79b]

$$W(\mathbf{k}, \omega) = \frac{n_o}{n_p} \sqrt{\frac{\pi}{2}} \frac{v_{the} \lambda_{De} m_e}{(K(k) \lambda_{De})^4} \frac{(\kappa(k) \lambda_{De})^2}{|D_p(\mathbf{k}, \omega)|^2} \sum_{\mathbf{p}, r} \frac{S^2(\mathbf{k}_p)}{|k_p \lambda_{De}|} \exp\left[-\frac{1}{2} \left(\frac{\omega_r}{\omega_{pe}}\right)^2 \frac{1}{(k_p \lambda_{De})^2}\right] \quad (3.30)$$

where $\omega_r = \omega - 2\pi r / \Delta t$. Note that the fluctuations for the PIC plasma are larger by the ratio of the actual particle number density, n_o , to the simulation particle number density, n_p . As expected the fewer the number of simulation particles the larger the background noise in the simulation. In Chapter 4 these functions will be compared to the Fourier transform in space and time of the E-field measured in PIC simulations. The measured spectral density is found from

$$W(\mathbf{k}, \omega) = \frac{\langle (2\pi)^4 \mathbf{E}_{sim}(\mathbf{k}, \omega) \cdot (2\pi)^4 \mathbf{E}_{sim}^*(\mathbf{k}, \omega) \rangle}{8\pi T} \quad (3.31)$$

where T is the time interval of the simulation.

Particle Kinetic Energy Change Due to Fluctuations

The change in the total kinetic energy density of the plasma particle distribution is

$$\frac{d\langle KE \rangle}{dt} = n_o \int d\mathbf{v} \frac{\partial f}{\partial t} \frac{1}{2} m v^2 \quad (3.32)$$

The Fokker-Planck equation can be used to describe the change in the particle distribution function, $\partial f / \partial t$, for a plasma as long as individual collisions produce only small changes in the velocity of a particle. This is the case when fluctuation fields in the plasma are the cause of the velocity changes.

For the continuum plasma a Maxwellian distribution is an equilibrium (ie. Eq. (3.32) gives zero). It has been known for some time and quantified with computations that

the uniform, Maxwellian PIC plasma does suffer a continuous change in energy [hoc71]. For this reason explicit PIC codes are usually operated with $\omega_{pe}\Delta t$ and $\Delta x/\lambda_{De}$ less than .2. Langdon used the kinetic theory outlined above to find the terms in the Fokker-Planck equation to give an analytic form for the PIC plasma $d \langle KE \rangle / dt$ [lan79b]. The function is directly proportional to the number of actual particles per simulation particle, N_o/N_p , and has arguments of $\Delta x/\lambda_D$ and $\omega_p\Delta t$ or

$$\frac{d\langle KE \rangle}{dt} = n_o \frac{N_o}{N_p} G(\Delta x/\lambda_D, \omega_p\Delta t). \quad (3.33)$$

It was shown that explicit methods would cause only heating of the plasma while implicit methods could also cause cooling for some Δx and Δt [bir85]. From Eq. (3.33) one can see that a set of simulations of uniform plasma at different $\Delta x/\lambda_D$ and $\omega_p\Delta t$ with N_o/N_p constant would give a contour plot of G . The energy change in any simulation could then be found from n_o and N_o/N_p of that particular simulation. Again as will be shown in Chapter 4, electromagnetic fluctuations do not have an appreciable effect since they are much smaller than the electrostatic fluctuations. The plot should also hold for nonuniform plasmas with electromagnetic phenomena other than fluctuations as long as the other phenomena are well resolved spatially and temporally. For these cases the main cause for numerical changes in energy should still be the electrostatic fluctuations in the densest plasma regions.

3.1.3 Conditions for a Nonsingular Implicit Electrostatic Field Equation Matrix

Because of the explicit advance with respect to the B-field, certain constraints on time step occur in relation to the electron gyrofrequency, ω_{ce} . The implicit electrostatic field equation must be considered since the rotation tensor depends on the B-field. A condition to ensure a nonsingular implicit field solution matrix is found from the theorem [nob77]:

Let M and C be $n \times m$ matrices with M being nonsingular and let $\| \cdot \|$ denote any of the operator norms. If $\alpha = \|M^{-1}C\| < 1$ (or $a = \|CM^{-1}\| < 1$) then $M + C$ is nonsingular.

The field matrix can be analyzed to find the constraint on Δt necessary for this condition to be met. In order to simplify the analysis without significant effects on the constraint, consider a uniform plasma with doubly periodic boundaries and with B_x and B_z comparable. Assuming only small perturbations in the density, the X tensor and matrix

coefficients simplify to

$$\begin{aligned}
4\pi X^{ii} &= \frac{(\omega_p \Delta t)^2}{4} \left[1 + (1 - \theta^2 + 2\theta_i^2) / (1 + \theta^2) \right] \\
4\pi X^{ij} &= \frac{(\omega_p \Delta t)^2}{4} \left[2(\theta_i \theta_j + \theta_j) / (1 + \theta^2) \right] \\
cc &\approx -\frac{4}{\Delta^2} (1 + X^{xx}) \\
tp &\approx tm \approx cp \approx cm \approx \frac{1}{\Delta^2} (1 + X^{xx}) \\
cpp &\approx cpm \approx cmp \approx cmm \approx \frac{1}{4\Delta^2} (X^{xz} + X^{zx}).
\end{aligned} \tag{3.34}$$

The variable θ is the normalized B-field multiplied by Δt as defined in Eq. (1.13), and the coefficients are labeled as in Table 2.1. Now split the matrix into two parts so $A = M + C$. Let M contain the five-point template, and C contain the corner coefficients of the nine-point template. Factoring the variables from M and C, the matrices take the form

$$M = \frac{1 + X^{xx}}{\Delta^2} \begin{pmatrix} -4 & 1 & 0 & 0 & \dots \\ 1 & -4 & 1 & 0 & \dots \\ 0 & 1 & -4 & 1 & \dots \\ 0 & 0 & 1 & -4 & \dots \\ \vdots & \vdots & \vdots & \vdots & \ddots \end{pmatrix} = \frac{1 + X^{xx}}{\Delta^2} \tilde{M} \tag{3.35}$$

$$C = \frac{X^{xz} + X^{zx}}{4\Delta^2} \begin{bmatrix} \text{sparse matrix} \\ \text{of ones} \end{bmatrix} = \frac{X^{xz} + X^{zx}}{4\Delta^2} \tilde{C} \tag{3.36}$$

thus

$$\|M^{-1}C\| = \frac{X^{xz} + X^{zx}}{4(1 + X^{xx})} \|\tilde{M}^{-1}\tilde{C}\| \tag{3.37}$$

The assumption $\omega_{pe}\Delta t \gg 1$ leads to the most restrictive constraint. In addition for all components of θ approximately the same and $\alpha = \|\tilde{M}^{-1}\tilde{C}\|$, the matrix is nonsingular if

$$\frac{\theta^2 + \theta}{2(1 + \theta^2)} \alpha < 1. \tag{3.38}$$

Solving for θ , the constraint on Δt is

$$\omega_{ce}\Delta t < \frac{-\alpha + \sqrt{\alpha^2 + 8(\alpha - 2)}}{\alpha - 2}. \tag{3.39}$$

The norm $\|\tilde{M}^{-1}\tilde{C}\|$ was solved numerically for different sized problems. Figure 3.2 shows the results for an $n \times n$ grid. Large enough grids might eventually impose a more restrictive constraint than that needed to resolve cyclotron oscillations. While violating the constraint will not necessarily result in a singular matrix, meeting the constraint does guarantee a nonsingular matrix.

3.2 Effect of the Darwin Method

Linear theory gives the dispersion characteristics of the Darwin limit in plasma. As expected longitudinal waves, such as plasma oscillations, are unaffected. However, the absence of the solenoidal part of the displacement current does have major consequences for transverse waves. Fast waves (those with phase velocities larger than c) are nonpropagating. For example in a Darwin plasma with no imposed fields the dispersion relation for transverse waves is $-c^2k^2 = \omega_{pe}^2(1 + Zm_e/m_i)$. This results in imaginary k or spatially damped fields. The magnitude of the effect on slow waves depends on the plasma characteristics. As discussed by Kaufman and Rostler[kau71], in a magnetized plasma $(ck/\omega)_{Darwin}^2 \sim (ck/\omega)_{Maxwell}^2 - 1$. So Darwin is best used for those phenomena where transverse wave velocities as well as particle velocities are significantly less than the speed of light.

A constraint on time step occurs for the numerical Darwin plasma with an imposed B-field. This can be seen in the dispersion relation for a neutral, magnetized plasma in which we neglect electrostatic fields and follow the fluid motion of the numerical plasma. A B-field is applied in the z direction, and spatial variation is allowed only in z . The linearized finite difference Eqs. (2.1), (2.60), and (2.38) become

$$\mathbf{V}^{n+1/2} = \mathbf{V}^{n-1/2} + \frac{\Delta tq}{m} \left(\mathbf{E}^n + \frac{\mathbf{V}^{n+1/2} + \mathbf{V}^{n-1/2}}{2c} \times B_o \hat{z} \right) \quad (3.40)$$

$$\mathbf{V}^{n+1} = \mathbf{V}^{n+1/2} + \frac{\Delta tq}{2m} \left(\mathbf{E}^n + \frac{\mathbf{V}^{n+1} + \mathbf{V}^{n+1/2}}{2c} \times B_o \hat{z} \right) \quad (3.41)$$

$$-(k^2 + \omega_{pe}^2/c^2)\mathbf{E}^{n+1} = \frac{\omega_{pe}^2}{c^3}\mathbf{V}^{n+1} \times B_o \hat{z} \quad (3.42)$$

Splitting these into components for V_x and V_y , we have six equations and eight unknowns. A system of two equations and two unknowns results given time harmonic variation, $z = \exp(-i\omega\Delta t)$, for all quantities. Setting the determinant of the 2x2 matrix to zero gives the dispersion relation

$$\begin{aligned} &\lambda^2(1 + \alpha^2)(1 + 4\alpha^2)z^4 - 2[\lambda^2(1 + \alpha^2)(1 - 4\alpha^2) + 18\lambda\alpha^2]z^3 \\ &+ [\lambda^2(1 + \alpha^2)(1 + 4\alpha^2) + 8\lambda\alpha^2(1 - 2\alpha^2) + 36\alpha^2]z^2 \\ &- 4\alpha^2[\lambda(1 + 4\alpha^2) + 6]z + 4\alpha^2(1 + 4\alpha^2) = 0 \end{aligned} \quad (3.43)$$

where $\alpha = \omega_{ce}\Delta t/4$ and $\lambda = 1 + (ck/\omega_{pe})^2$. The magnitude of z versus $\omega_{ce}\Delta t$ is plotted in Fig. 3.3 for various ck/ω_{pe} . $\|z\|$ is larger than one which indicates instability. However, even in the worst case when $ck/\omega_{pe} \simeq 1$, $\|z\| = 1.0002$ for $\omega_{ce}\Delta t = .4$. For applications without large, imposed B-fields $\omega_{ce}\Delta t$ is usually much less than .4 and the number of time steps before this instability grows significantly is more than required by the simulation. This analysis is also overly conservative for those cases where the imposed field varies in space and time. See Chapter 4 for further discussion of our experience with simulations having imposed B-fields.

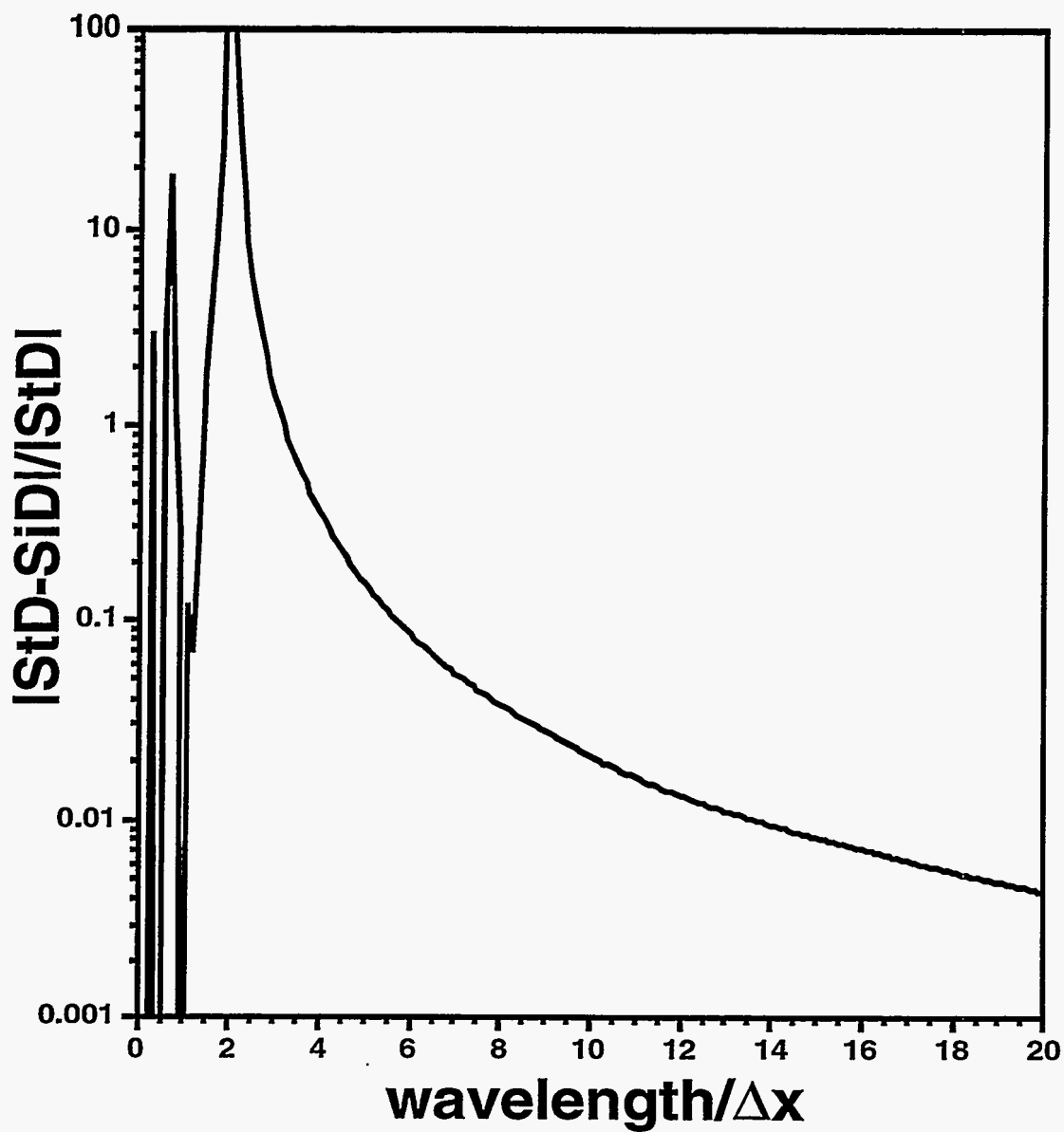


Figure 3.1: Comparison of strict differencing to simplified differencing. The difference in the implicit susceptibility terms of the implicit field equation is plotted for a harmonically varying potential. The terms agree well for wavelengths greater than $5\Delta x$.

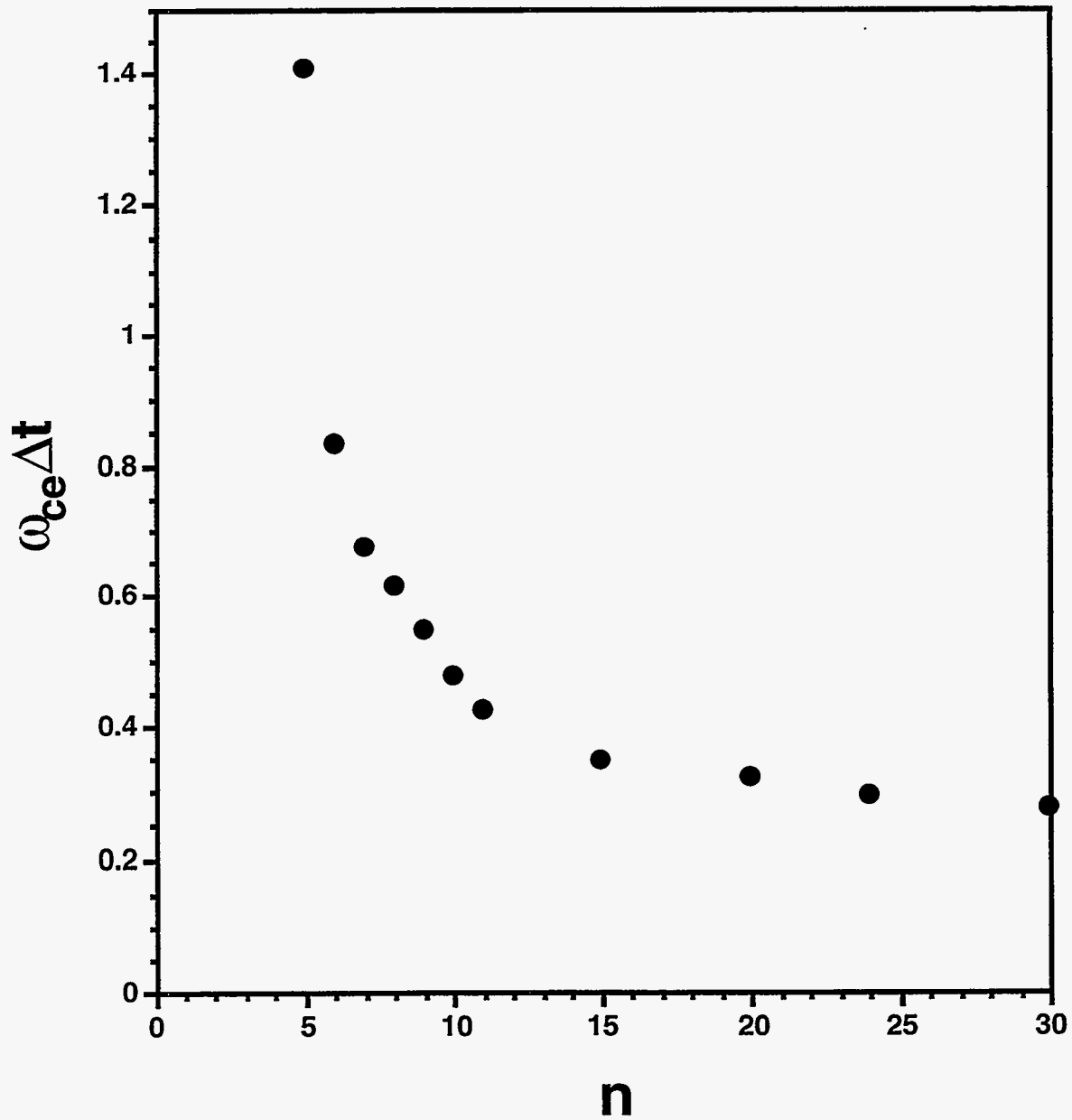


Figure 3.2: Maximum $\omega_{ce} \Delta t$ to guarantee nonsingular matrix for the implicit electrostatic field equation. This is a sufficient but not necessary condition.

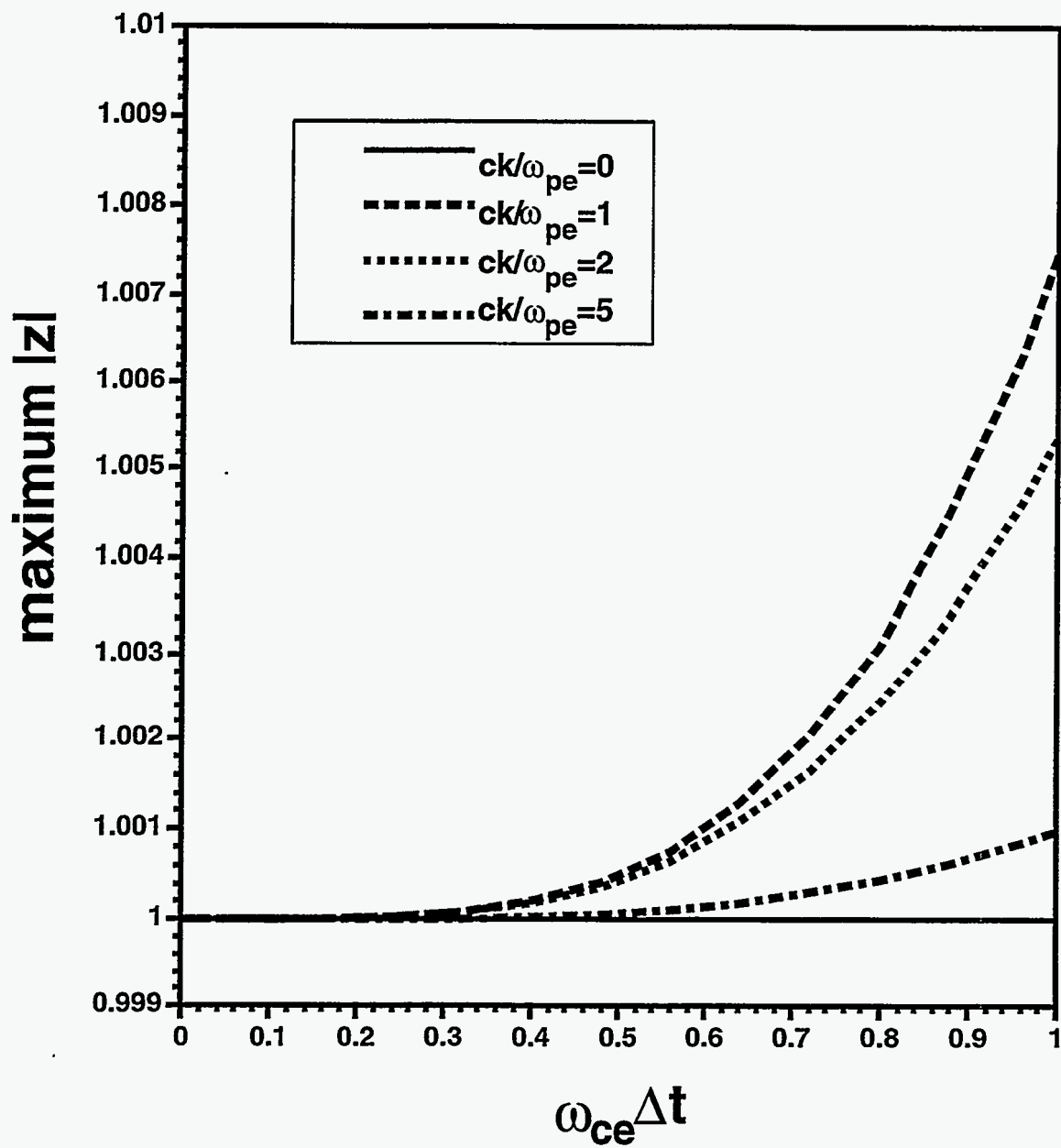


Figure 3.3: Magnitude of the least damped mode vs $\omega_{ce}\Delta t$ from the linear analysis of the Darwin field equation and finite difference equations of motion in a constant B-field.

Chapter 4

Characterization of DADIPIC with Doubly Periodic Test Cases

Several test cases follow which characterize the accuracy and robustness of DADIPIC under circumstances that are increasingly stressful to the algorithm. The simulations are doubly periodic to investigate the core algorithm without the effects of boundaries and to allow comparison to the kinetic theory of section 3.1.2. The first case is a uniform, Maxwellian plasma used to determine the numerical effects on what should be an equilibrium situation. The plasma is magnetized to check the applicability of the Darwin dispersion results. Finally the reaction of the algorithm to large density gradients is tested with expanding plasma columns.

4.1 Uniform Plasma: Fluctuations

The first test case is a comparison of fluctuations in a uniform, Maxwellian DADIPIC plasma to the fluctuation spectral density predicted by the kinetic theory of section 3.1.2. The analytic results in the figures are due to Eqs. (3.29) and (3.30) for continuum and PIC plasmas respectively. A simulation with 32×32 cells was initialized with 30000 particles each of electrons and protons at a density of 10^8cm^{-3} . The size of the problem was set at 1cm^2 . The plasma temperature ($T_e = T_i$) and time step were varied to get desired values for $\Delta x / \lambda_{DE}$ and $\omega_{pe} \Delta t$. Fast Fourier transforms of the electrostatic field were taken in space at each time step with the results stored for several k . Temporal FFT's of these results were taken at the end of the simulation giving $(2\pi)^4 \mathbf{E}(\mathbf{k}, \omega)$, and Eq. (3.31) was then used to get the measured spectral density.

Fig. 4.1a shows the spectral density for the electrostatic field when $\Delta x/\lambda_{DE} = .5$ and $\omega_{pe}\Delta t = .2$. For this plot k_z and k_x correspond to the longest wavelength in the system, $2\pi/L$. As expected in this case the DADIPIC calculation is close to the continuum result. Notice the peak in the spectral density near the frequency of plasma oscillations. For intermediate $k\lambda_{DE}$ this peak occurs since the root of the dispersion relation is almost real (small Landau damping), and the argument for the exponential decay of the spectral density is inversely proportional to $k\lambda_{DE}$. At high frequency the finite number of particles in the simulation causes a floor of noise above the analytic result.

For larger spatial and temporal discretization the PIC results become substantially different than the continuous plasma. The aliases due to the finite grid keep energy in modes which would have very little in the real plasma. Since the Debye length and plasma frequency are no longer resolved, this result is not unexpected. It is not a problem as long as the fluctuations do not cause unacceptable numerical heating or affect low frequency phenomena of interest. These concerns will be investigated in the following sections. Figures 4.1b and 4.1c have the case of large Δx and the case of large Δx and Δt respectively. Notice that the simulation still agrees well with the discrete analytic theory of section 3.1.2.

These results indicate that DADIPIC has the desired quality of reproducing continuum plasma phenomena as $\Delta x/\lambda_{DE}$ and $\omega_{pe}\Delta t$ are decreased. Of course, this is not the discretization that would be used in practice since explicit PIC would run such problems much faster. One can also see that no unexpected behavior is occurring as Δx and Δt are increased, allowing reliance on the results of the discrete theory to predict the trends in DADIPIC due to fluctuations. The implication is that DADIPIC can operate with large temporal and spatial discretization as long as the criterion of particles moving less than a cell in a time step is met.

These simulations also provide a standard for algorithm timings. The code was run on the C machine (Cray 2) at the National Energy Research Supercomputer Center (NERSC). For the given simulation parameters a time step takes ~ 3.2 s. The portion of the time taken to complete the various components of a time step is 42% for particle operations, 25% for solution of the SDF equations, and 32% for solution of the implicit electrostatic field equation. Of course, these results serve as typical examples. For other simulations the time for particle operations should simply scale with the number of particles, but different boundary conditions and grid sizes effect the convergence of the DADI and bi-conjugate gradient routines. The solution of the fields may take a larger or smaller proportion of the

run time as the simulation is changed.

These results can be used to compare DADIPIC to a fully electrodynamic, explicit PIC code. For an explicit code solving for the fields should take negligible time. Because of the direct implicit particle advance, DADIPIC effectively has two particle pushes. So an explicit code would take half the time for particle operations. Thus we can expect that an explicit code would complete a time step five times faster than DADIPIC for a similar sized simulation. Of course, DADIPIC can run with much larger time steps and grid size than an explicit code. As a typical example consider a DADIPIC simulation with $\Delta x/\lambda_{De} = 30$ and $\omega_{pe}\Delta t = 10$. With an explicit code we would typically run with $\Delta x/\lambda_{De} = \omega_{pe}\Delta t = .2$. So DADIPIC would be able to run $(30/.2) \times (30/.2) \times (10/.2)/5 = 225000$ times faster for a 2-D simulation with the same number of particles per cell as an explicit code. This neglects the huge expense in memory due to the factor of 22500 more particles in the explicit simulation.

4.2 Uniform Plasma: Change in Energy due to Fluctuations

This section presents the results of a set of simulations as suggested in chapter 3 to find the form of the function in Eq. (3.33) for the change in kinetic energy of the DADIPIC plasma due to fluctuations. A set of 28 simulations with characteristics described in the previous section were completed with $\Delta x/\lambda_{De}$ and $\omega_{pe}\Delta t$ ranging from .2 to 20.

Figure 4.2 is a set of typical time histories for the particle and field energies. Notice that the initial relaxation of the field energy occurs quickly in the first few time steps, followed by a general trend of heating or cooling. In the simulations the field energy represented only a small fraction of the total energy, and the ions showed almost no change from their initial kinetic energy. For all practical purposes the change in energy was due to the change in the thermal energy of the electrons in the x and z directions. In these 2-D simulations there is no electrostatic field in the y direction, and the fluctuation electromagnetic fields had no perceptible impact on the particle kinetic energy in the y direction.

Several trends in the field and particle energies occur. As $\Delta x/\lambda_{De}$ is increased the ratio of electrostatic field energy to particle energy increases from 2×10^{-4} to .044. This is due to the grid aliasing of wavelengths which causes the spectral density to be larger at short wavelengths than in a real plasma [bir85]. As $\omega_{pe}\Delta t$ increases the electrostatic field

Table 4.1: Change in Energy $\Delta E/E_o N$ in $\Delta x/\lambda_{De}$, $\omega_{pe}\Delta t$ Parameter Space

	$\omega_{pe}\Delta t$						
	0.2	0.5	1.0	2.0	5.0	10.0	20.0
20.0	2.2e-3	3.5e-3	3.3e-3	2.1e-3	2.7e-4	-2.0e-4	1.0e-3
10.0	4.8e-4	8.0e-4	8.0e-4	3.3e-4	-2.3e-4	6.5e-4	
5.0	1.0e-4	1.7e-4	8.5e-5	-1.4e-4	3.3e-4		
$\frac{\Delta x}{\lambda_{De}}$ 2.0	3.0e-6	-2.4e-5	-1.3e-4	-4.5e-5			
1.0	-2.6e-6	-3.2e-5	-5.9e-5				
0.5	-3.2e-6	-1.7e-5					
0.2	-1.7e-6						

energy decreases. For $\Delta x/\lambda_{De} = 20$ the electrostatic field energy decreases by a factor of 2500 as Δt is changed from its minimum to its maximum value. The reduction is due to the smoothing caused by simplified differencing which effectively reduces short wavelength fields by $1/(1 + (\omega_{pe}\Delta t)^2/2)$, and to the damping of high frequency oscillations caused by the implicit time advance.

As expected the energy in the electromagnetic fields is much smaller than the electrostatic field energy. Linear kinetic theory predicts the electromagnetic fluctuation field energy to be approximately v^2/c^2 less than the electrostatic field energy [kra86]. For the DADIPIC plasma it is even less. For small Δt as $\Delta x/\lambda_{De}$ is varied from .2 to 20, $E_{sol}^2/E_{irr}^2 \sim 10^{-10}$ to 10^{-14} , and $B^2/E_{irr}^2 \sim 10^{-5}$ to 10^{-8} . As the time step is increased E_{sol}^2 does not decrease as fast as E_{irr}^2 , and B^2 remains essentially constant. For large enough $\omega_{pe}\Delta t$ the B-field energy may even overtake the electrostatic field energy. However, the electromagnetic field energy was not a significant fraction of the electrostatic field energy in any of our simulations.

The contour plot of Fig. 4.3 shows the change in energy in the form $\Delta E/E_o N$ where ΔE is the change in the total energy over the simulation, E_o is the initial energy in fields and particles, and N is the number of time steps in the simulation. Table 4.1 has the results of the simulations which were interpolated to form the contour plot. The general trend is heating for large Δx due to the interpolation of the grid force [bir85] and cooling for large Δt due to the implicit electrostatic solve. Simulations with and without the electromagnetic fields gave indistinguishable results for heating. This is consistent with the relatively small magnitude of the electromagnetic fields.

These results are similar to Cohen, et. al. [coh89] where the 1-D electrostatic direct implicit D_1 scheme was investigated. A difference between these results and theirs occurs in the region where $\Delta x/\lambda_{De} = \omega_{pe}\Delta t$. The differences appear to be the result of the type of simulations performed. Cohen, et. al. simulated periodic expanding plasma slabs and always observed cooling in the $\Delta x/\lambda_{De} = \omega_{pe}\Delta t$ region while in our uniform plasma simulations heating occurs in this region. The difference is in the initial state of the expanding slab with a step function in density. As shown in several sources [fri90] even for cases where the implicit solution eventually results in a net gain in total system energy, the behavior at early time is a decrease in total system energy. This is due to the effect of the implicit particle push on the spatially and temporally unresolved initial expansion of the slab. If the slab had been started with a slight slope to its sides the expansion would have been resolved, and only the fluctuations in the densest part of the plasma would affect the change in total energy. The return of heating as $v_{th}\Delta t/\Delta x \simeq 1$ is due to the breakdown of the predictor-corrector solution for the electrostatic field. That solution depended on an expansion which is accurate only when particles move less than a cell in a time step.

As was stated in chapter 3 our intent is only to quantify the impact of fluctuations assuming the other phenomena of interest are well resolved. With this qualification in mind, the contour plot can be used for any simulation by adjusting for the particle density, $n_p = 30000 \text{ cm}^{-3}$, and plasma density, $n_o = 10^8 \text{ cm}^{-3}$, used here. The plot shows two contours where energy is conserved. Note the upper contour is a stable equilibrium. Plasmas with $\Delta x/\lambda_{De}$ above the contour will heat and move down to the contour. Plasmas with $\Delta x/\lambda_{De}$ below the contour will cool and move up to the contour. However, plasmas in the heating region to the right will continue to heat and reach the point where $v_{th}\Delta t/\Delta x > 1$. It is therefore advisable to run in the region where $3v_{th}\Delta t/\Delta x \simeq 1$ in the densest part of the plasma. Parts of the plasma with lower densities will be at a point of smaller $\Delta x/\lambda_{De}$ and $\omega_{pe}\Delta t$ where energy is even better conserved.

Figure 4.4 has the final particle velocity distribution (dots) compared to the initial Maxwellian (dashed line) and a Maxwellian at the calculated temperature of the plasma at the end of the simulation (solid line) from several of the simulations used to generate the energy conservation contour plot. In all of these cases $\Delta x/\lambda_{De}$ is 10. The sequence of the plots is for increasing time step showing the effect of the first heating region (Fig. 4.4a), the energy conserving contour (Fig. 4.4b), the cooling region (Fig. 4.4c), and the second heating region (Fig. 4.4d). Fig. 4.4e gives the distribution in the direction out of

the simulation plane. Fig. 4.4e provides computational evidence that there is no change in the distribution in the direction which has no \mathbf{E}_{irr} indicating no other significant numerical heating or cooling mechanisms at work.

In the first heating region the particle distribution is mostly Maxwellian except at the largest velocities where the faster electrons appear somewhat cooled by the implicit particle advance. Along the energy conserving contour the final distribution is not much different than the initial distribution. More pronounced changes have occurred for 1-D simulations with a larger grid that were run for more time steps. A decrease in the tails and center of the distribution balanced by a bulging near the thermal velocity is observed. This indicates that faster particles are being cooled by the implicit advance while the slower particles are still heating due to the grid force. In the cooling region again the distribution remains essentially Maxwellian as the whole distribution cools due to the implicit particle advance. The only distribution which deviates substantially from a Maxwellian is that from the second heating region. Here the slower particles appear to remain near the initial distribution, but the faster particles heat dramatically. The heating appears to occur for those particles with speeds of v_{th} and above. In this region these are particles which are moving more than one cell in a time step. These results indicate that it is possible to use DADIPIC with large temporal and spatial discretization while not causing large numerical effects to the particle velocity distribution. However, the constraint of a relationship between Δt and Δx must be met.

4.3 Uniform Plasma: Drift Through the Grid

The last test case of fluctuations involves the drift of a Maxwellian plasma through the grid. For the same simulation parameters as described above, the magnitude for the drift velocity, v_d , was chosen so that it was resolved ($v_d \Delta t / \Delta x = .2$). $\omega_{pe} \Delta t$ was set at one. $\Delta x / \lambda_{De}$ was then varied to give different ratios of the drift velocity to the thermal velocity. The results are listed in table 4.2. The numerical heating or cooling of the plasma is not greatly affected by motion through the grid. So the contours of the previous section still apply. The relative change in energy of the drift is significantly less than that of the plasma as long as the drift motion ($v_d + v_{th}$) is resolved. Unfortunately, we cannot resolve the drift motion and sit on the energy conservation contour at the same time when $v_d / v_{th} > 1$. Using small Δt allows smaller Δx for a given drift, but this removes the need to be implicit. So

Table 4.2: Change in energy $\Delta E/E_o N$ for a plasma drifting through the grid

$\Delta x/\lambda_{De}$	v_d/v_{th}	$(v_d + v_{th})\Delta t/\Delta x$	$\Delta E_d/E_{od}N$	$\Delta E_{th\perp}/E_{oth\perp}N$	$\Delta E_{th\parallel}/E_{oth\parallel}N$
1	0.2	1.2	6.0e-4	-1.9e-4	-1.5e-4
2	0.4	0.7	-3.0e-5	-3.2e-4	-3.8e-4
5	1.0	0.4	-1.1e-4	1.9e-4	2.9e-4
10	2.0	0.3	-4.4e-5	1.9e-3	1.9e-3

DADIPIIC appears to be well suited for plasmas with drifts less than v_{th} , but something further will have to be done to handle plasmas with large drifts. One possible solution may be to apply a δf formulation[dip91] for the plasma instead of particles. This would reduce fluctuations and the fluctuation induced heating.

4.4 Uniform Plasma: Imposed Magnetic Field

Electron cyclotron waves were investigated to test the algorithm's ability to simulate low frequency oscillations without the complications of boundary conditions. These right circularly polarized waves propagate along the B-field lines in a magnetized plasma. The dominant interaction is between the particles and the electromagnetic (Darwin) fields. The electrostatic field maintains charge neutrality in the fluctuating but essentially uniform plasma. Without large density gradients or nonneutral regions the direct implicit method only serves the function of allowing us to use large time steps while retaining electron kinetics. The B-field is chosen so $\omega_{ce} \ll \omega_{pe}$, where ω_{ce} is taken as a positive quantity. This gives a phase velocity much less than c , making the Darwin approximation reasonable. The cold plasma dispersion relation is[kra86]

$$\frac{c^2 k^2}{\omega^2} = 1 + \frac{\omega_{pe}^2}{(\omega_{ce} - \omega)\omega} \quad (4.1)$$

In the simulations $\omega_{ce}/\omega_{pe} = .01$, the density is 10^8 cm^{-3} , and the number of particles per cell is 30. The simulation region is periodic in both the x and z directions, and the imposed B-field, B_o , is applied in the z direction. The spatial and temporal discretization is set so that $\omega_{pe}\Delta t = 20$ and $\Delta x/\lambda_{De} = 70$ or $\omega_{pe}\Delta t = 40$ and $\Delta x/\lambda_{De} = 140$. These parameters are chosen to satisfy the constraints of resolving the wavelengths, resolving the frequency, and residing near the energy conserving contour, $3v_{th}\Delta t/\Delta x \sim 1$. The plasma

thermal velocities needed to achieve these constraints are not large enough to make any observable change in the oscillation frequency from the cold plasma dispersion relation.

Several simulations both with and without initial perturbations were run. In the first type a wave is initialized in the plasma with the size of the simulation region in the z direction set to one wavelength. The grid is 64 nodes in z and 8 in x . Two spatial dimensions are not necessary here, but this does verify the operation of the 2-D field solvers. The relationships between the perturbed fluid velocities and perturbed fields derived from linear theory are

$$\begin{aligned} \mathbf{B}_1 &= v_1 B_o \frac{k(\omega - \omega_{ce})}{\omega \omega_{ce}} [-\hat{x} \sin(kz) - \hat{y} \cos(kz)] \\ \mathbf{E}_1 &= v_1 B_o \frac{(\omega - \omega_{ce})}{c \omega_{ce}} [-\hat{x} \cos(kz) + \hat{y} \sin(kz)] \\ v_1 &= v_1 [\hat{x} \sin(kz) + \hat{y} \cos(kz)]. \end{aligned} \quad (4.2)$$

The particles are loaded according to a drifted maxwellian with the drift velocity having the functional form of equation (4.2). To ensure resolution of v_1 given the set ratio of Δt and Δx , v_1 is set to $.25v_{the}$. The resulting perturbed B-fields are less than 5% of B_o .

The resulting fields verified that the right hand sides of the \mathbf{B} and \mathbf{E}_{sol} equations were derived correctly and that the field solving routines were calculating the expected solutions. This also allowed us to determine if particle noise in terms such as the kinetic energy tensor, \mathbf{K} , might cause excessive noise in the resulting fields. Given the magnitude of v_1 , the fluctuations in \mathbf{v} are not much smaller than the imposed perturbation. As shown in Fig. 4.5, the initial fields agree with Eq. (4.2). The initialized parameters are $v_1 = 1.025 \times 10^7$ cm/s and $ck/\omega_{pe} = 1$ which should give field magnitudes of $|\mathbf{E}_1|/B_o = 1.7 \times 10^{-4}$ and $|\mathbf{B}_1|/B_o = .034$. Energy conservation for this whole group of simulations ranged from 1% to 3% due to electrostatic fluctuations. The frequency of oscillation was recorded for several different initial wavelengths to compare to the analytic dispersion curve for the real part of the frequency.

The second type of simulation is a uniform, unperturbed plasma where peaks in the electromagnetic spectral density indicate the dispersion relation for electron cyclotron waves. The Fourier transform in space and time is recorded for $B_x^2(k_z, \omega)$. A square 32×32 grid is used in this case. The results of both types of simulations agree with the analytic dispersion relation as indicated by Fig. 4.6.

In the warm plasma the particles see the Doppler shifted frequency of the wave,

$\omega' = \omega - v_{\parallel}k$, where v_{\parallel} is the particle velocity along the B-field. When the force on the particles due to the transverse E-field varies in time near the gyrofrequency of the particles, ω_{ce} , a resonant interaction between the wave and the particles occurs, providing a kinetic test for DADIPIC. However, to get the correct damping, the distribution function near $(\omega - \omega_{ce})/kv_{the}$ must be well resolved. Unfortunately, damping which is smaller than the oscillation frequency occurs when the resonance is with particles far out in the tail of the distribution. To overcome this we set up a plasma with two negative species. The first is a dense, cold species which determines the real part of the frequency. The second is a sparse, hot species which determines the damping. The dispersion relation for the warm plasma becomes [sch79]

$$\begin{aligned} \omega^2 - c^2k^2 - \frac{\omega_{pe,cold}^2\omega}{(\omega_{ce,cold} - \omega)\omega} \left(1 + \frac{k^2v_{the,cold}^2}{(\omega - \omega_{ce,cold})^2}\right) \\ - i\sqrt{\frac{\pi}{2}} \frac{\omega_{pe,cold}\omega}{k\lambda_{De,cold}} \exp\left[-\frac{(\omega - \omega_{ce,cold})^2}{2(kv_{the,c})^2}\right] - \frac{\omega_{pe,hot}^2\omega}{(\omega_{ce,hot} - \omega)\omega} \left(1 + \frac{k^2v_{the,hot}^2}{(\omega - \omega_{ce,hot})^2}\right) \\ - i\sqrt{\frac{\pi}{2}} \frac{\omega_{pe,hot}\omega}{k\lambda_{De,hot}} \exp\left[-\frac{(\omega - \omega_{ce,hot})^2}{2(kv_{the,hot})^2}\right] = 0 \end{aligned} \quad (4.3)$$

The plasma parameters are chosen so only the second, third, and sixth terms contribute. The second species with its low density can be set to cause small damping while its particles are near resonance. In this way there are sufficient PIC particles in the desired region of the distribution. The simulations are 1-D so electrostatic fluctuations exist only parallel to the B-field. The cold species has a temperature parallel to the B-field so $\Delta x/\lambda_{De,cold}$ and $\omega_{pe,cold}\Delta t$ can be set to prevent heating due to the electrostatic fluctuations. The temperature perpendicular to the B-field is set very low so v_1 can damp significantly before being swamped by thermal noise. The plasma parameters are shown in table 4.3. The damping was varied in several simulations by changing the mass and temperature of the hot species while maintaining $v_{the,hot}$ constant. This allows us to change the damping and continue to resolve $v_{the,hot}$.

Figure 4.7 shows the time histories from a simulation where the hot species mass was two m_e . The B-field recorded at a point (Fig. 4.7a) is a damped sinusoid as expected. An exponential curve fit to the B-field energy time history (Fig. 4.7b) provides the estimate to the damping. There is an initial jump in the total system energy (Fig. 4.7c) of about 1% as the initial load of particles relaxes. Over the rest of the simulation the damping of the electron cyclotron wave and electrostatic fluctuations have little effect on the total system

Table 4.3: Plasma parameters for electron cyclotron wave damping

$\omega_{pe,cold}\Delta t = 40$	$\Delta x/\lambda_{De,cold} = 140$	$n_{grid} = 64$
$ck/\omega_{pe,cold} = .6$	$v_1/v_{the,cold} = .014$	
$n_o = 1 \times 10^8 \text{cm}^{-3}$	$n_{cold} = .98n_o$	$n_{hot} = .02n_o$
	$T_{cold} = .683eV$	$T_{hot} = 4(m_{hot}/m_{cold})T_{cold}$
	$\omega_{ce,cold} = .01\omega_{pe,cold}$	$\omega_{ce,hot} = (m_{cold}/m_{hot})\omega_{ce,cold}$

energy. Note that the energy time histories do not include the energy of the applied B-field. The damping observed in several simulations is compared with the damping derived from Eq. (4.3) in Fig. 4.8. The damping becomes largest near $m_h/m_e = 4$ since the oscillation frequency matches the cyclotron frequency of the hot species. The agreement between DADIPIC and theory is very good over an order of magnitude change in damping rate.

As shown in Chapter 3, this implementation of the Darwin method results in a scheme which is slightly unstable even at small Δt . In the above simulations $\omega_{ce}\Delta t$ was kept at less than .4, and no adverse numerical instability effects were apparent. In addition, no problems with solution of the electrostatic field equation matrix were encountered on the 32×32 grids. Next the effects of the numerical instability in simulations are quantified to gauge the applicability of the linear theory result of Chapter 3 for the actual code.

A series of 1-D periodic simulations were run with $\Delta x/\lambda_{De} = 10$ and $\omega_{pe}\Delta t = 3.1$, parameters which minimized numerical effects from the direct implicit scheme. The length of the simulations was 167 cm with 64 grid nodes. The plasma density of $1 \times 10^8 \text{cm}^{-3}$ gave $ck_{max}/\omega_{pe} = 2$ where k_{max} corresponds to the longest wavelength in the system. Larger wavenumbers are available, but as shown by Fig. 3.3 oscillations at such wavenumbers are less unstable. If the theoretical dispersion relation applies, only the longest wavelength in the system should grow noticeably. The simulations were run long enough to show a significant increase in the magnitude of the unstable mode (at least a factor of 20), and the growth rate was calculated from an exponential curve fit to the B-field energy time history. The results are shown in Table 4.4. The DADIPIC results agree with the linear theory to within a few percent for both the oscillation frequency and growth of the instability. This means we can rely on the linear theory to predict the effects of this instability. The dispersion relation can be used to set the time step with the goal of keeping the effect of the numerical instability small given the size of the system, the magnitude of the B-field,

Table 4.4: Real, ω , and imaginary, γ , parts of the frequency from the Darwin dispersion relation in a constant B-field

$\omega_{ce}\Delta t$	analytic $\omega\Delta t$	PIC $\omega\Delta t$	analytic $\gamma\Delta t$	PIC $\gamma\Delta t$
0.8	0.617	0.61	0.00244	0.0021
1.2	0.889	0.88	0.00965	0.0097
1.6	1.13	1.1	0.0227	0.021

and the plasma frequency.

4.5 Large Density Gradients: Expanding Slab

Several authors have used the expansion of a plasma slab into vacuum as a test of implicit electrostatic algorithms [coh89], [fri90]. The expanding slab is well suited for this purpose since it involves large density gradients in the plasma and significant electrostatic fields which drive the expansion. The expansion of a 1-dimensional, collisionless plasma slab into vacuum has been considered in detail both analytically [all70] and numerically [den79]. The plasma expands due to the thermal velocity of the particles. The electrons move out ahead of the ions causing an electrostatic field which drags the ions along. A rarefaction wave propagates back into the plasma at the ion-acoustic speed, $c_s = (Z\kappa_B T_e/m_i)^{1/2}$, and the plasma density falls off exponentially behind the wave front. The ion velocity in the wave, v_i , is a function of position with respect to the initial edge of the plasma, x_i .

$$v_i = c_s + (x - x_i)/t \quad (4.4)$$

DADIPIC responded to the plasma slab in a manner similar to previous implicit electrostatic models. Fortunately, as with fluctuations in the uniform plasma the addition of the electromagnetics did not impact significantly on the results. Several simulations with different ion masses show the expected variation in the rate of expansion. The problem parameters were: number of grid points ($n_x = n_z = 32$), system width ($L = 395$ cm), plasma width ($L_{slab} = 157$ cm), plasma density (10^8 cm $^{-3}$), number of particles ($n_p = 30000$), number of time steps ($N = 256$), and plasma temperature ($T_e = 29$ eV). The parameters were chosen so that the plasma interior would reside near the energy conserving contour with $\omega_{pe}\Delta t = 10$ and $\Delta x/\lambda_{De} = 32$.

Figure 4.9 highlights the results of a typical simulation with $m_i/m_e = 1836$ and $c_s\Delta t/\Delta x = .007$. Figure 4.9a shows contours of electron density as a reference for the position of the plasma slab. Notice that the implicitly calculated E_{irr} (Fig. 4.9b) is excluded from the plasma because of the large $\omega_{pe}\Delta t$. The electrostatic field exists mainly near the edge of the plasma where the electrons have separated from the ions, and the plasma density has decreased. E_{sol} and B are too small to have much effect on the expansion. Both are concentrated in the plasma where the fluctuation current densities exist.

Figure 4.9e is a time history of the total system energy. Several different phenomena are interacting to cause the initial drop and then increase of the total system energy. The electrostatic field energy drops off rapidly after the first 10% of the simulation. During the time of the large electrostatic field (due to the electrons out running the ions), the total system energy drops by 5%. This is due to the implicit scheme artificially slowing the electrons while the macroscopic field is large and the slab edge is spatially unresolved. In other words the implicit scheme is damping short time-scale (high frequency) motion.

After the initial expansion the slab edge becomes well resolved, and any changes in total energy are due to fluctuations in the bulk of the plasma. At this time the total energy begins to increase. The final result is a total energy only 2% below the initial energy. Other cases showed a significant increase above the initial energy by the end of the simulation. The cause of the late time increase in system energy is the change in the electron temperature due to the expansion. Since the electrons are pulling the ions with them converting thermal into directed motion, the electron distribution cools in the expansion. For our example the electrons lost 50% of their thermal energy in the x and z directions a 30% decrease in λ_{De} . The decrease moves $\Delta x/\lambda_{De}$ above the energy conservation contour. The result is numerical heating of the electrons and thus a numerically caused increase in the total energy. Since the numerically caused change in the total energy was small, there was not an adverse affect on the results. This is shown by the correct profile for the ion expansion velocity in Fig. 4.9f.

DADIPIC appears to operate stably in situations with large electrostatic fields and density gradients along with vacuum regions. At the same time low frequency, electrostatic phenomena is simulated correctly in the lower density regions, and energy is conserved to within a few percent. The loss in system energy was avoided by initializing the sides of the slab with a finite slope. One would not expect DADIPIC to correctly mimic the short time-scale expansion from the step function slab.

4.6 Large Density Gradients: Electron Beam Filamentation

Electron beam filamentation serves as the final doubly periodic test case for DADIPIIC. In these tests density gradients, electrostatic fields, and electromagnetic fields are all significant. The results obtained here can be compared to those obtained with the fully electromagnetic implicit code AVANTI [hew87b]. Consider a neutral plasma column aligned along the y axis with electrons flowing in the column. The electrons have two components uniformly distributed across the column, a dense target, T, flowing in the negative y direction and a faster beam, B, flowing in the positive y direction. This results in a Weibel-type electromagnetic instability in which the electron components breakup into filaments [wei59]. For the case where the total momentum in the system is zero and the electron components are at the same temperature the dispersion relation is [mom66]

$$(\omega^2 - k^2 v_{the}^2)(\omega^2 - \omega_{pe}^2 - c^2 k^2) - k^2(\omega_{pT}^2 u_{oT}^2 + \omega_{pB}^2 u_{oB}^2) = 0 \quad (4.5)$$

A purely imaginary root to this equation, indicating growth of an instability, results when

$$\frac{k v_{th}}{\omega_{pe}} < \left[\sum_s \left(\frac{\omega_{ps}}{\omega_{pe}} \right)^2 \left(\frac{u_{os}^2}{c^2} - \frac{v_{th}^2}{c^2} \right) \right]^{1/2} \quad (4.6)$$

So for any particular initial conditions the instability will only grow for certain wavelengths. As the transverse temperature increases, progressively longer wavelengths will become stable.

Two simulations were initialized to investigate this instability. The first was a uniform, doubly periodic plasma where the size of the simulation region sets the longest wavelength. This allows the electromagnetic instability to grow with minimal electrostatic effects. The second was a finite size column which could expand during the simulation. Here nonuniformity, electromagnetic, and electrostatic effects were significant at the same time. The parameters for these runs are 32×32 grid, $\omega_{pe} \Delta t = 10$, $\Delta x / \lambda_{De} = 48$, length of problem 395 cm, 30000 particles of each species, ion density of 10^8 cm^{-3} , and 160 time steps. In these simulations the initial temperature was chosen to allow the heating due to the filamentation to increase λ_{De} and bring $\Delta x / \lambda_{De}$ to the energy conservation contour. The electron densities and velocities normalized to the ion density and the speed of light respectively are shown in Table 4.5. Since the streaming velocities are in the y direction

Table 4.5: Species parameters for filamentation simulations

	Beam electrons	Target electrons	ions
Density	1/11	10/11	1
v_{drift}/c	.05	.005	0
v_{th}/c	.005	.005	1.2×10^{-4}

where there is no electrostatic field, the electrostatic two-stream instability will not occur. This significantly simplifies the interactions to be observed.

Figure 4.10 shows the B-field energy and particle energy for the uniform plasma and finite beam problems. The beam energy (KE_{\parallel}) is converted into field energy and perpendicular thermal energy as the instability grows. Note that KE_{\perp} does not grow as much in the finite beam case since not as large a v_{th} is required to move the stable point to k less than k_{min} . The growth rate can be found quite easily from the slope of the initially linear increasing B-field energy on the log plots. The variation of linear theory growth rate with wavenumber is shown in Fig. 4.11. The horizontal lines in the figure are the results from simulation. The simulation results have been cut off at the maximum wavelengths attainable corresponding to the width of the simulation in the uniform plasma case and the width of the beam in the finite beam case. In both cases the size of Δx was set so that the shorter wavelengths available in the simulations would be stable. In the simulations the instability should grow at the largest rate within the band of available wavelengths. Considering the largest available linear theory growth rate, there is a variation of $\simeq 10\%$ from the simulation results ($\gamma_{PIC} = .01\omega_{pe}$ vs $\gamma_{theory} = .0095\omega_{pe}$ for the finite beam case).

The fastest growing mode for the finite beam is also the longest wavelength which can fit within the beam width and the last mode to stabilize. The longest wavelength mode is thus the only mode to grow to perceptible size as shown in the particle plots of the beam and target electrons in Fig. 4.12 where the beam electrons have coalesced into a single filament. The uniform plasma, on the other hand, is wide enough to allow longer wavelength modes to continue to grow after the fastest mode has stabilized. This is evidenced by the second spurt of growth in the B-field energy. Fig. 4.13 illustrates the change in mode with B-field plots at early and late time. At early time the fastest growing mode with $ck/\omega_{pe} = 1.5$ dominates while at late time the mode saturates at the longest wavelength available.

Finally, there is the question of whether any changes in energy due to numerical effects are important. Fig. 4.14 has the time histories of the total energy for the two simulations. In the uniform case the electrons are heated in the perpendicular direction by the instability. In the finite beam case the electrons are heated by the instability and cooled by the plasma column expansion. In both cases the change in temperature causes a change in $\Delta x/\lambda_{De}$ in the plane of the electrostatic field. In addition to the heating effects, the B-fields have grown to significant size by the end of the simulations. The fields reach magnitudes where $\omega_{ce}\Delta t = .1$ and the off diagonal terms in the implicit susceptibility tensor are 5% of the diagonal terms. However, in both cases the initial choice of $\Delta x/\lambda_{De}$ allowed the plasmas to remain near enough to the energy conservation contour to cause negligible change in the total energy ($\sim 2\%$) compared to the 60% change in the target electron thermal energy and 730% change in the beam electron thermal energy (uniform case). This results in $v_{th}\Delta t/\Delta x = 3.8$ and 1.8 at the end of the simulation for the beam and target electrons respectively. Remember the energy conservation contour is approximately $3v_{th}\Delta t/\Delta x = 1$. As shown by the excellent agreement with theory of the growth rates and mode wavelengths, any numerical effects did not adversely affect the final results.

4.7 DADIPIC mode of operation

The theory of chapter 3 and its verification in this chapter lead us to some general guidelines to ensure stable and accurate DADIPIC simulation. These guidelines combine to give a region of operation in $\Delta x/\lambda_{De}$ vs $\omega_{pe}\Delta t$ space as shown in Fig. 4.15. In order to resolve the phenomenon of interest we are constrained by $k\Delta x < 1$ and $\omega_o\Delta t < .2$. The cyclotron instability requires $\omega_{ce}\Delta t < .4$ which may be more or less stringent a constraint than the requirement to resolve the low frequency phenomenon. We must stay near the line $3v_{th}\Delta x/\Delta t = 1$ to prevent numerical heating as well as ensure accuracy of the implicit field equation and particle accelerations. The width of the allowed region around the energy conserving contour depends on the amount of numerical heating which can be tolerated. Essentially the condition

$$\Delta KE_{numerical}/\Delta KE_{phenomena} \ll 1. \quad (4.7)$$

must be met. In any particular simulation the change in the total kinetic energy due to the phenomena can probably be estimated. As the temperature of the plasma changes during

a simulation the ratio $\Delta x/\lambda_{De}$ changes as represented by the vertical bar in Fig. 4.15. One could find the numerical effect on the kinetic energy from

$$\Delta K E_{numerical} = \int \frac{\Delta E}{E_o N} \left(\frac{\Delta x}{\lambda_{De}}(t) \right) dt \quad (4.8)$$

The bounding lines around the energy conserving contour are set by the condition of Eq. (4.7). The simulation should be run where the bar for the change in $\Delta x/\lambda_{De}$ fits between the allowed limits due to numerical changes in energy.

With this method one can simulate two different types of situations. The first is equilibrium phenomena where T_e remains basically unchanged. Large but nearly balanced fluxes of energy into and out of the system are still possible. In this case we set the spatial and temporal discretization so the simulation resides on the energy conserving contour and the phenomenon of interest is resolved. Second, we can handle systems where the plasma temperature is changing by initializing the simulation so that the energy conserving contour is crossed minimizing numerical heating/cooling effects.

There are two schemes which may further minimize numerical heating/cooling and further increase the width of the simulation region. The time step could be varied dynamically during a simulation in order to stay near the energy conserving contour. An alternative is to implement a δf scheme [dip91] to minimize the electrostatic fluctuations which are the cause of the numerical change in kinetic energy.

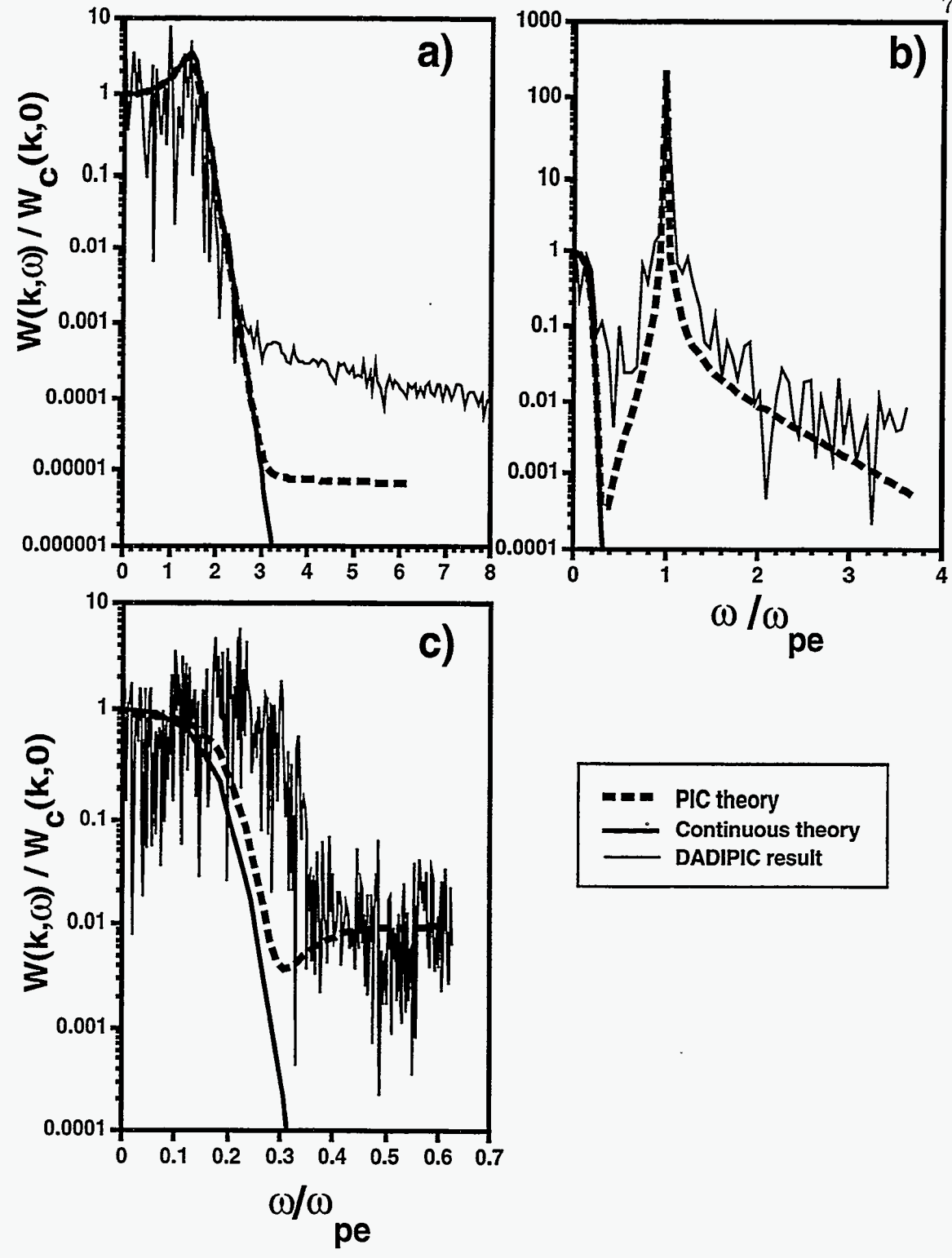


Figure 4.1: Comparison of DADIPIC spectral density results to predictions from continuous and PIC linear theory for uniform plasma. a) $\Delta x / \lambda_{De} = .5$ and $\omega_{pe} \Delta t = .2$, b) $\Delta x / \lambda_{De} = 5$ and $\omega_{pe} \Delta t = .2$, c) $\Delta x / \lambda_{De} = 5$ and $\omega_{pe} \Delta t = 5$. The DADIPIC results are in reasonable agreement with PIC linear theory.

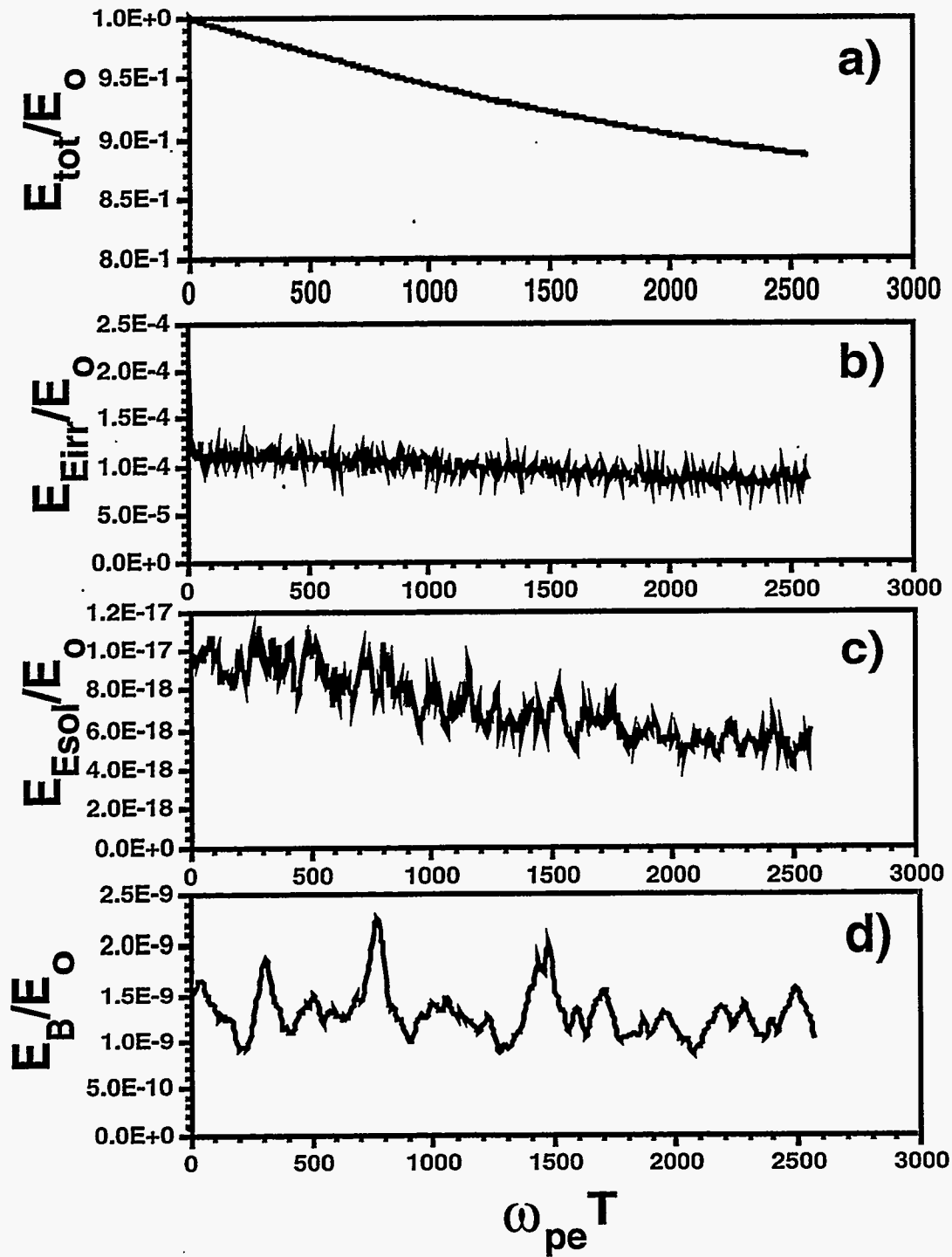


Figure 4.2: Time histories of particle and field energies for a doubly periodic, uniform plasma DADIPIC simulation with $\Delta x/\lambda_{De} = 10$. and $\omega_{pe}\Delta t = 5$.: a) total system energy, b) E_{irr} field energy, c) E_{sol} field energy, and d) B-field energy. All are normalized to the initial total system energy E_0 . Notice the much smaller magnitude of the electromagnetic field energies compared to the electrostatic field energy.

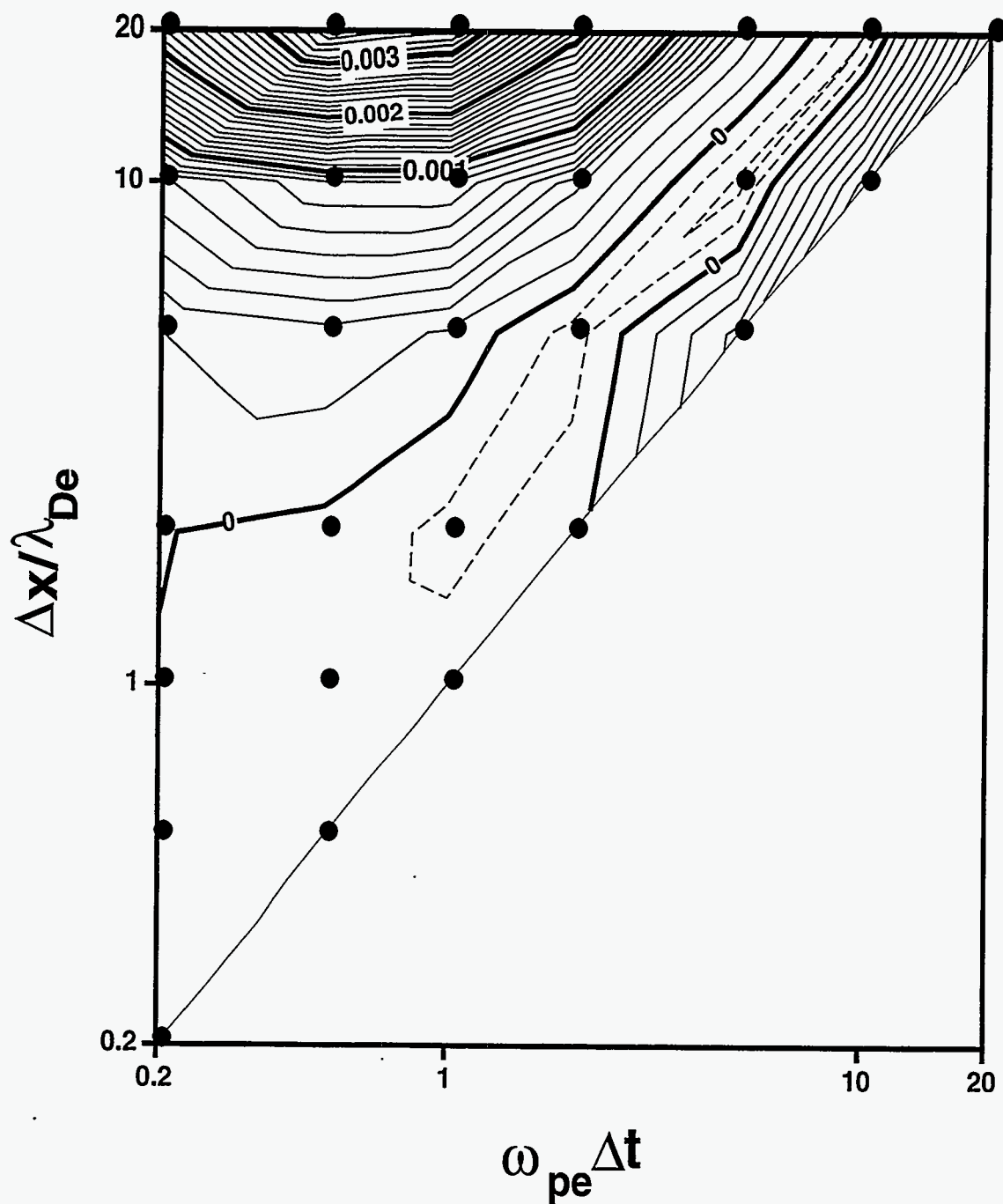


Figure 4.3: Contour plot of $\Delta E / E_0 N$ in $\Delta x / \lambda_{De}$ and $\omega_{pe} \Delta t$ space. The dots are the locations of the simulations run to generate the contours. The upper left hand region and the region near $v_{th} \Delta t / \Delta x = 1$ show heating. The region between with the dashed contours lines has cooling. Simulations were not run in the region where $v_{th} \Delta t / \Delta x > 1$.

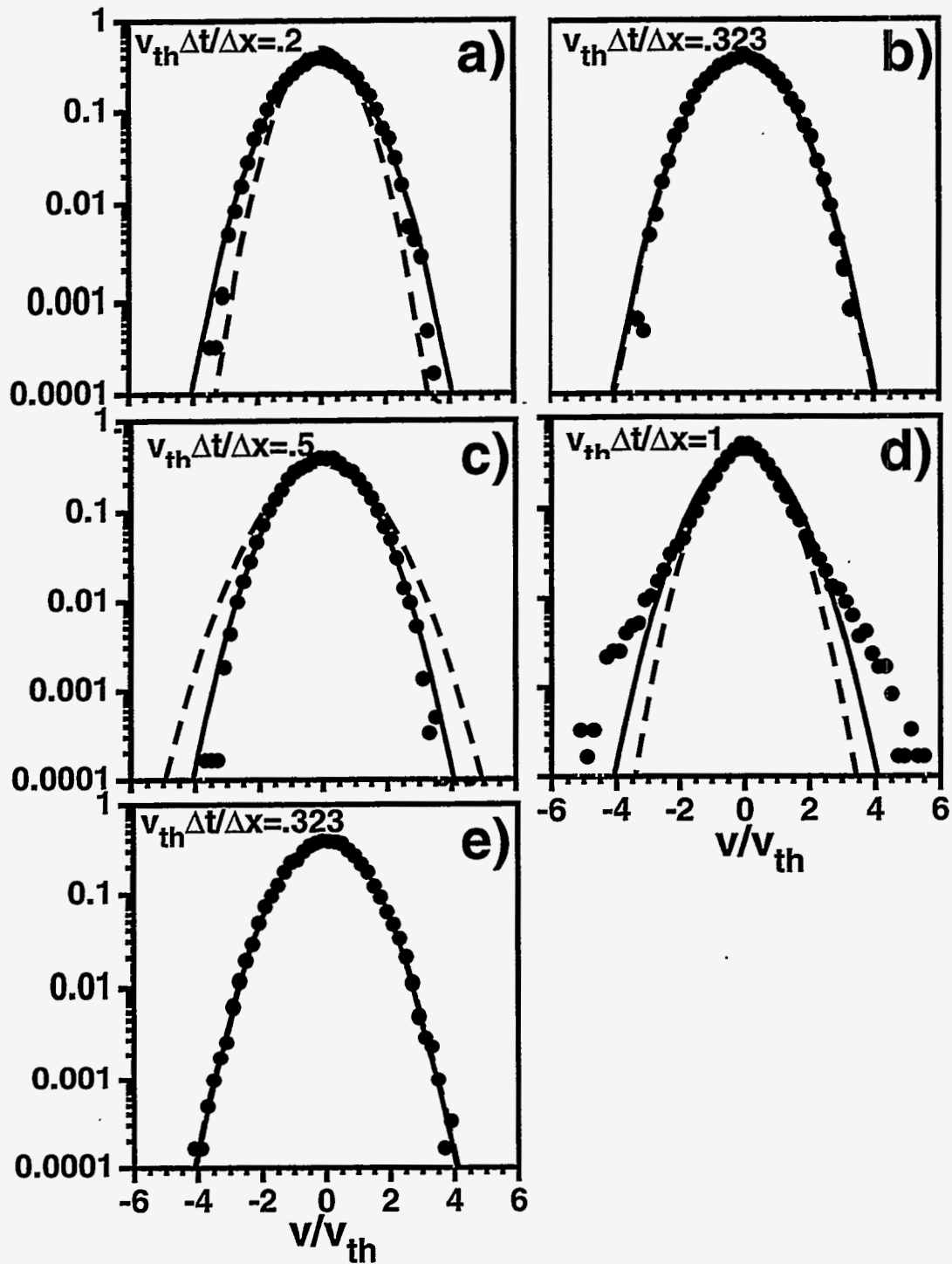


Figure 4.4: Particle velocity distributions vs v/v_{th} resulting for different values of $\omega_{pe} \Delta t$: a) in the first heating region where $3v_{th} \Delta t / \Delta x < 1$, b) along the energy conserving contour where $3v_{th} \Delta t / \Delta x \simeq 1$, c) in the cooling region, d) in the second heating region where $v_{th} \Delta t / \Delta x = 1$, and e) in the direction out of the simulation plane.

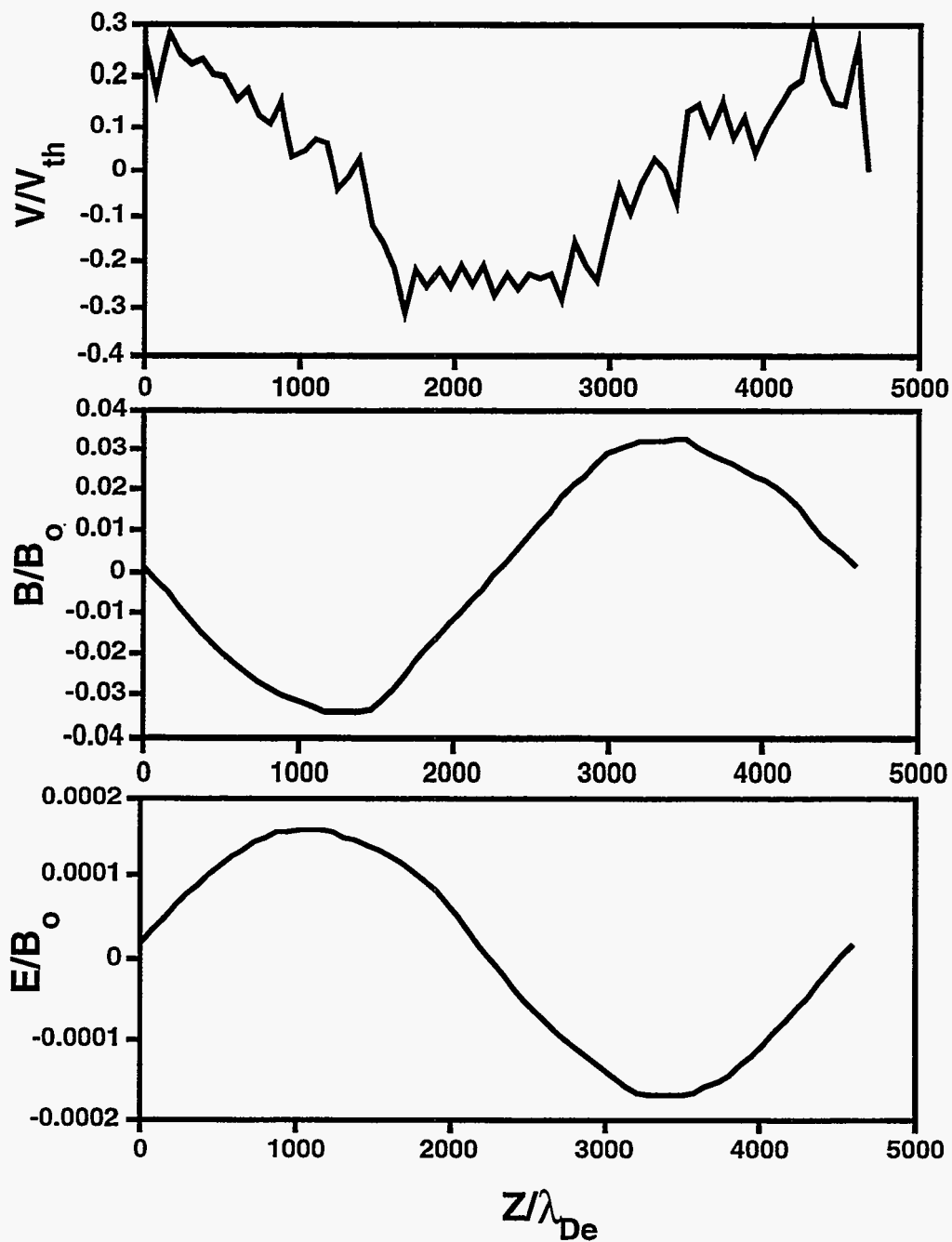


Figure 4.5: The grid velocity, v_y , and the generated fields, B_x and $E_{sol,y}$, for an electron cyclotron wave initialized in the particle distribution of a DADIPIIC simulation.

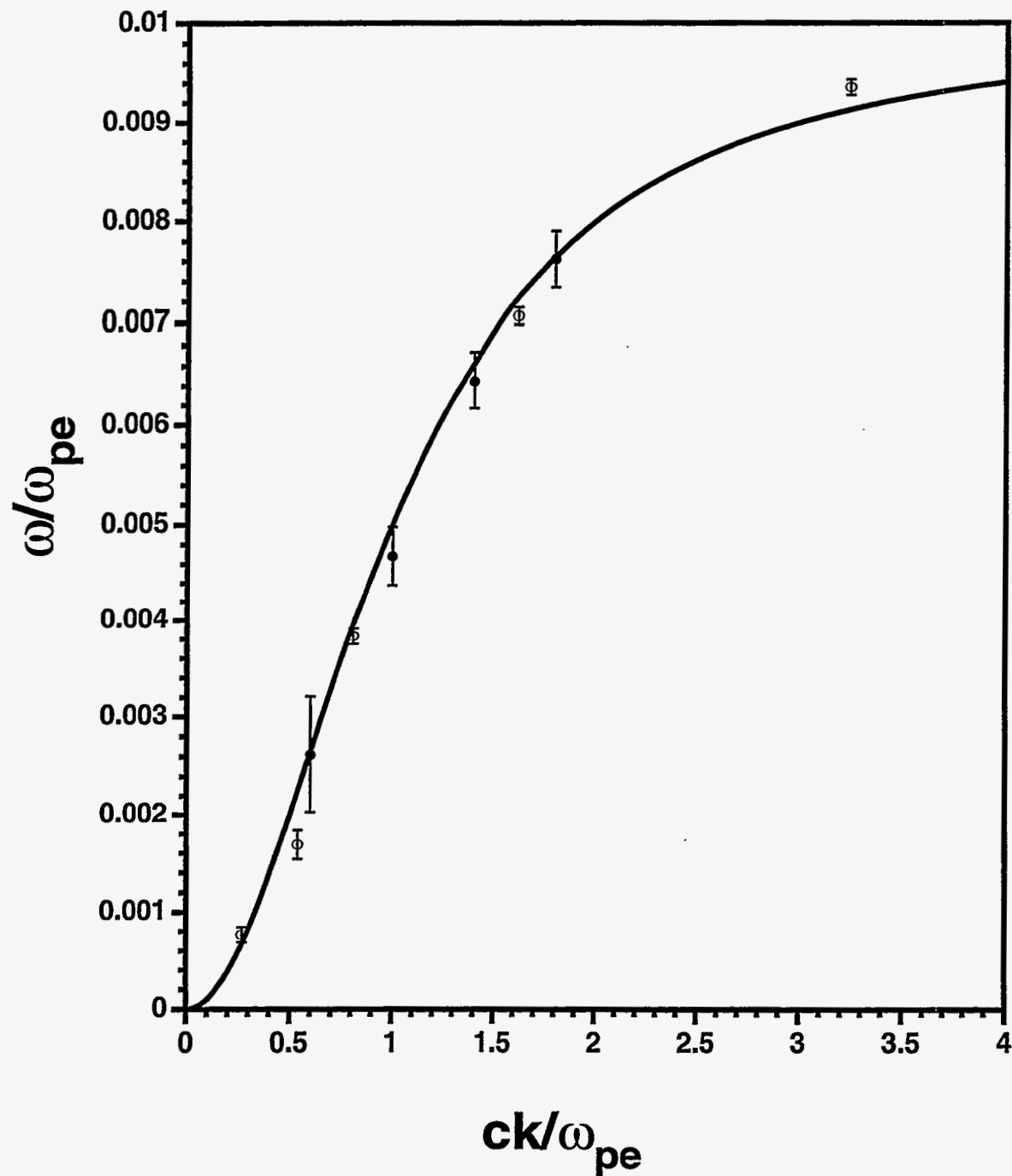


Figure 4.6: Electron cyclotron wave dispersion relation for the real part of the frequency. The solid line is the analytic result for the cold magnetoplasma. The points are the DADIPIC results. The error bars are the fwhm of the peaks in the FFT's.

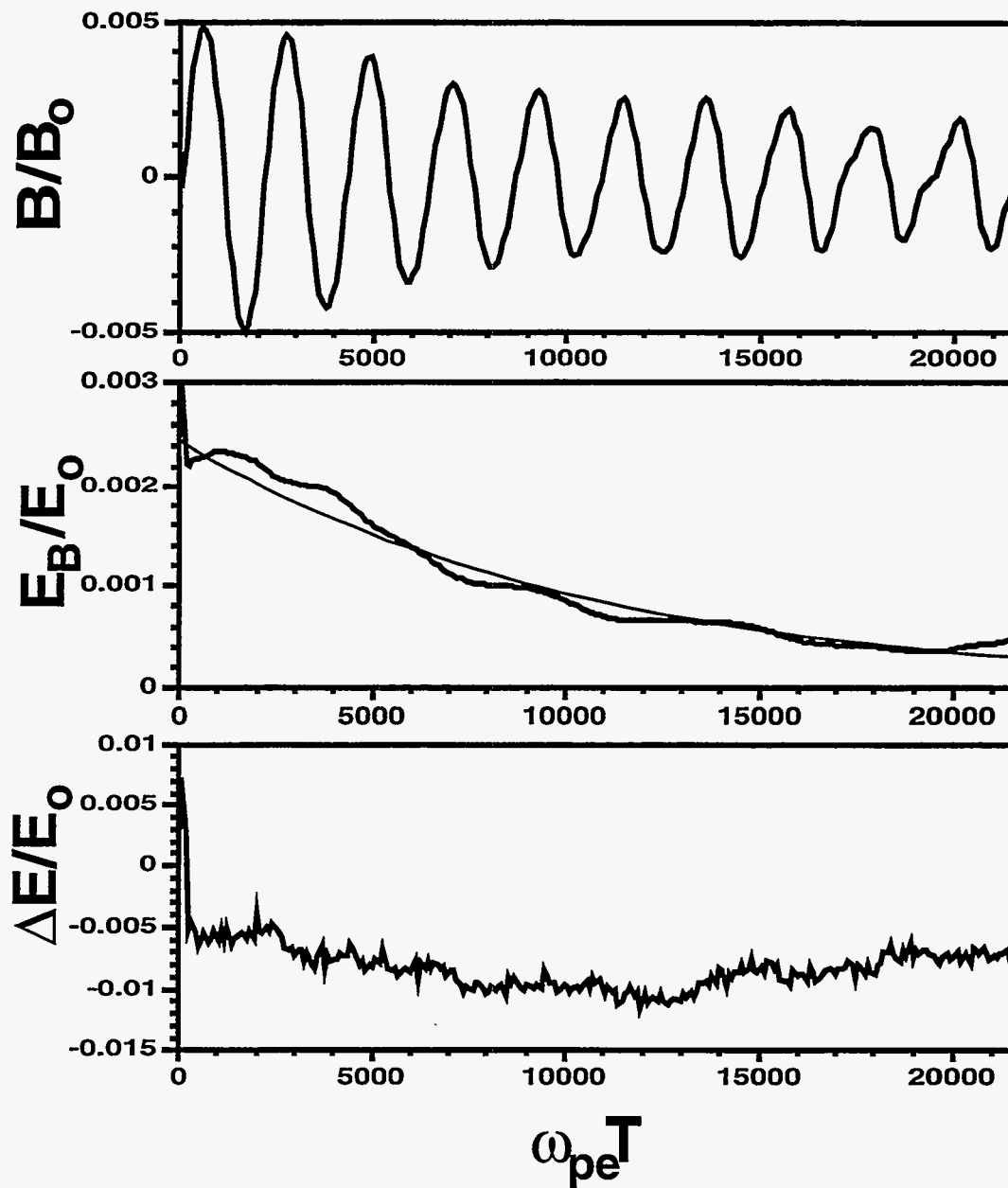


Figure 4.7: The time evolution of an electron cyclotron wave simulation b) the oscillating B-field, b) the B-field energy with an exponential curve fit, and c) the change in the total system energy normalized to the initial total system energy.

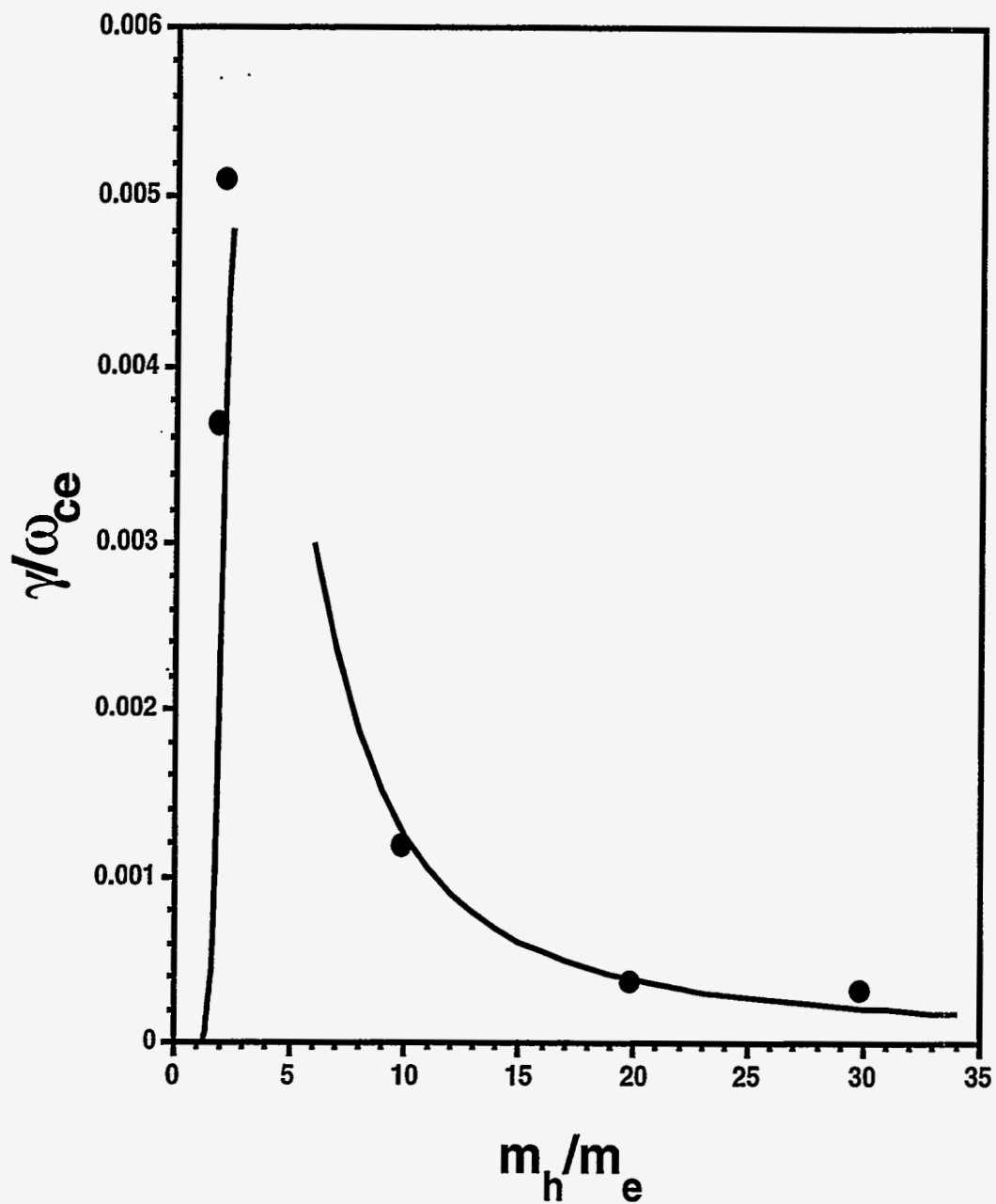


Figure 4.8: Electron cyclotron wave damping rate as the hot species mass is changed. The solid line is the analytic damping, and the dots are damping rates measured from DADIPIC simulations. The simulations were all initialized with the same wavelength, $ck/\omega_{pe} = .6$.

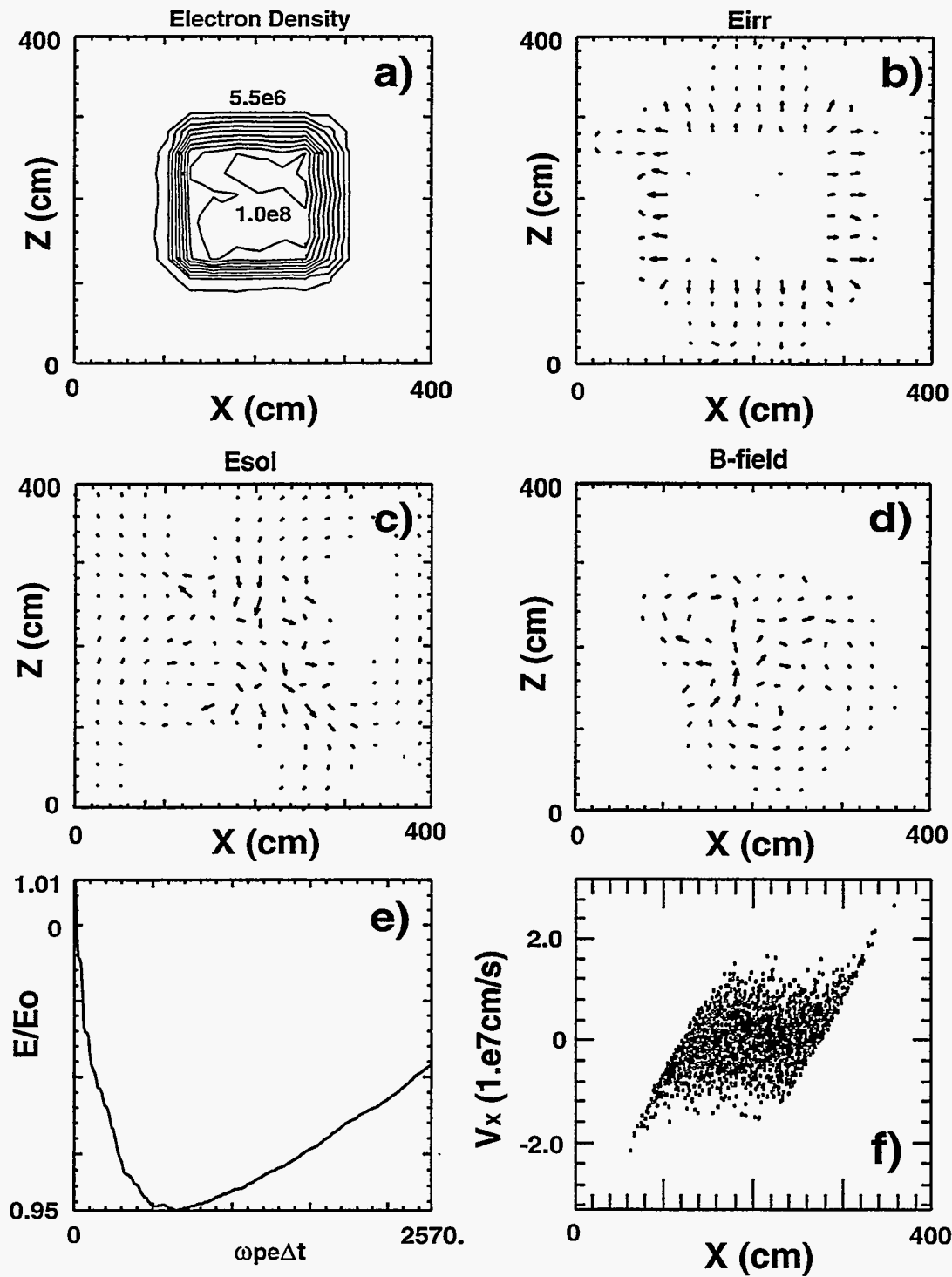


Figure 4.9: Expanding slab simulation: a) density contours showing the expansion of the slab, b) the electrostatic field concentrated near the edge of the slab (longest vector= 5.25 V/cm), c) solenoidal E-field (longest vector= 0.0194 V/cm) and d) B-field (longest vector= $4.77e-3$ gauss) concentrated in the plasma where currents exist, e) total system energy, f) ion particle phase space with the $c_s + (x - x_i)/t$ dependence for the velocity.

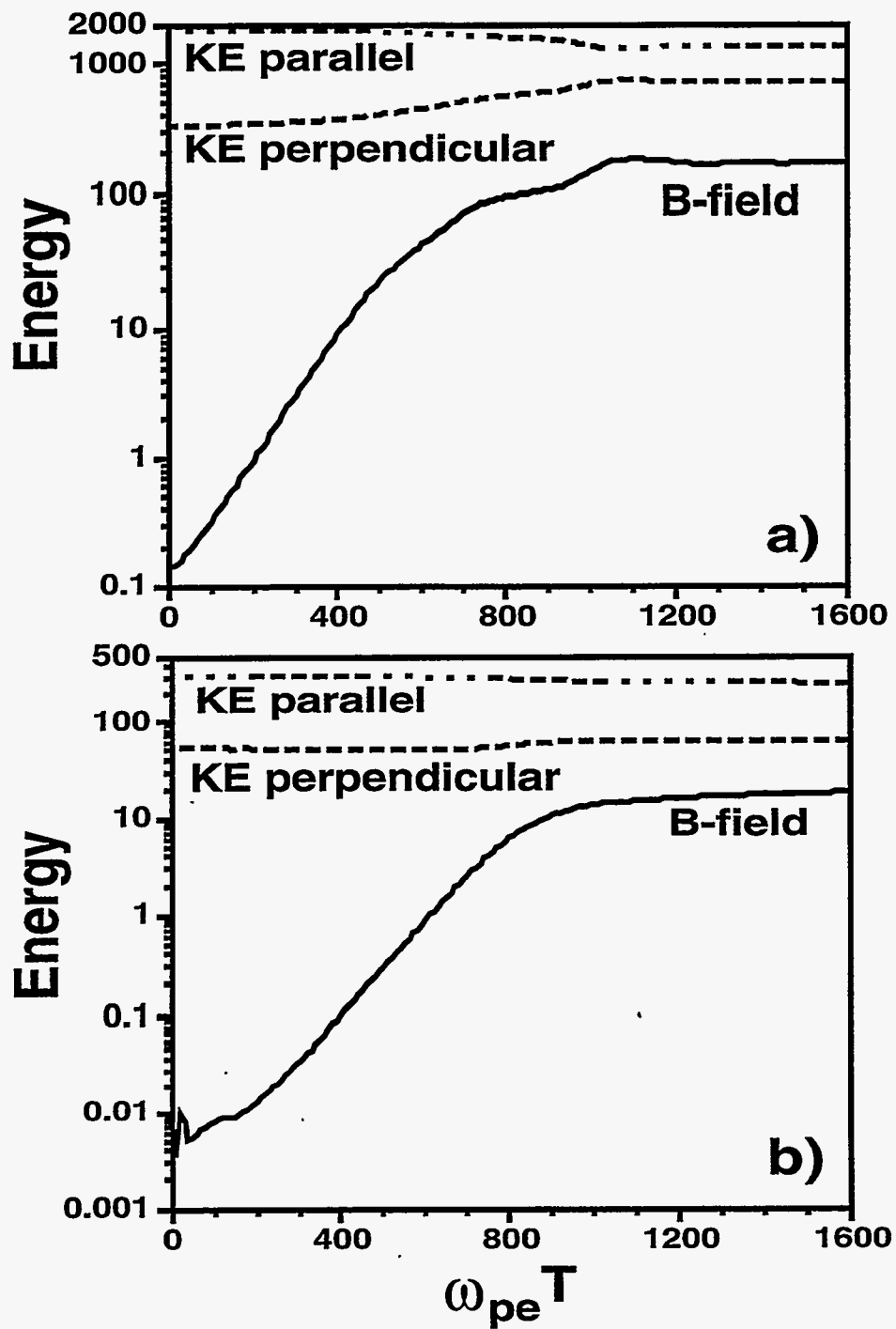


Figure 4.10: Beam filamentation B-field and particle energies showing the exponential increase of the B-field during growth of the instability: a) the uniform plasma and b) the finite beam.

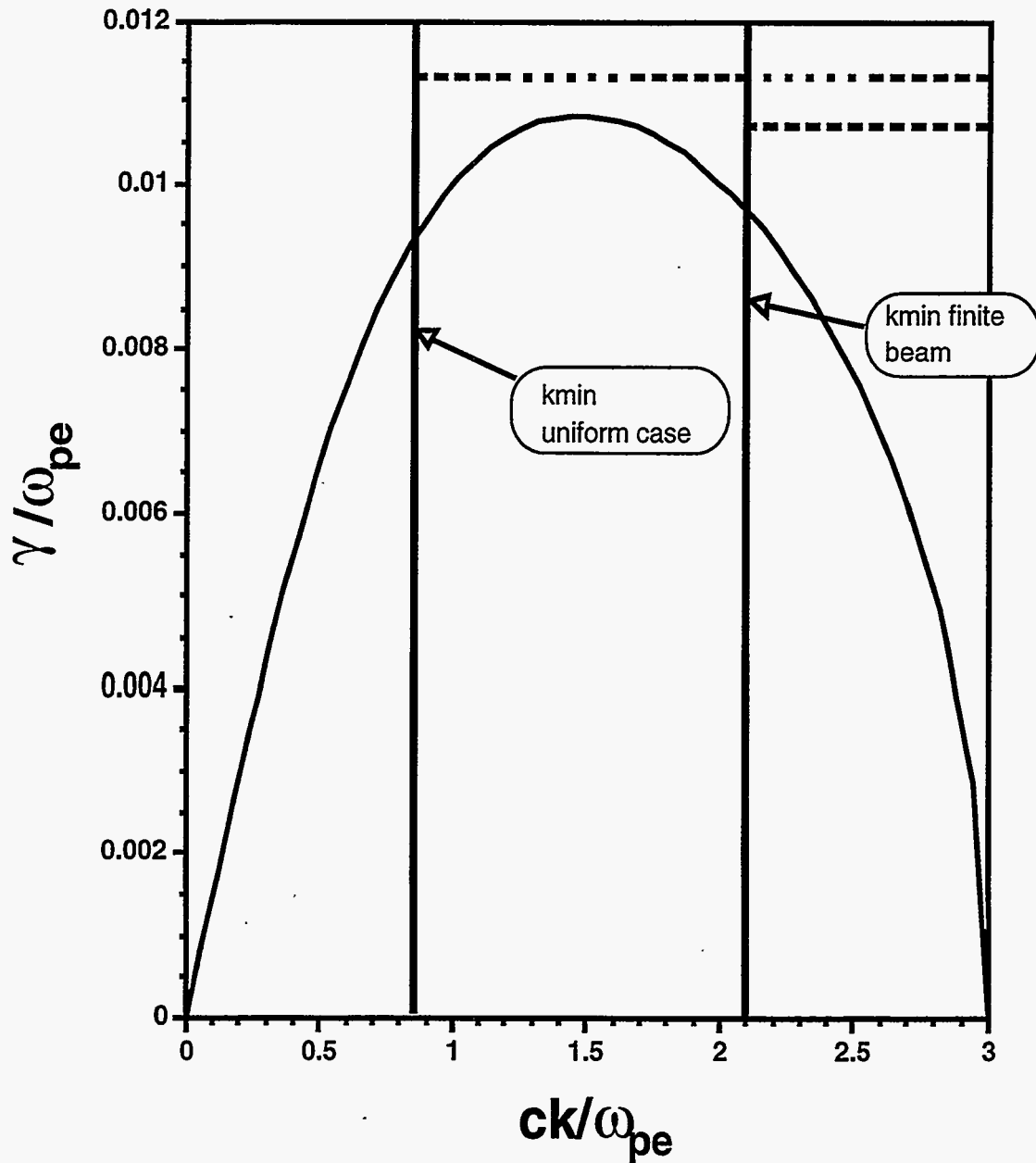


Figure 4.11: Beam filamentation growth rates. The solid curve is the theoretical dispersion curve. The large dashed line (uniform plasma) and small dashed line (finite beam) show the grow rates observed in DADIPIC simulations. The lines extend to the minimum wavenumbers available in the simulations.

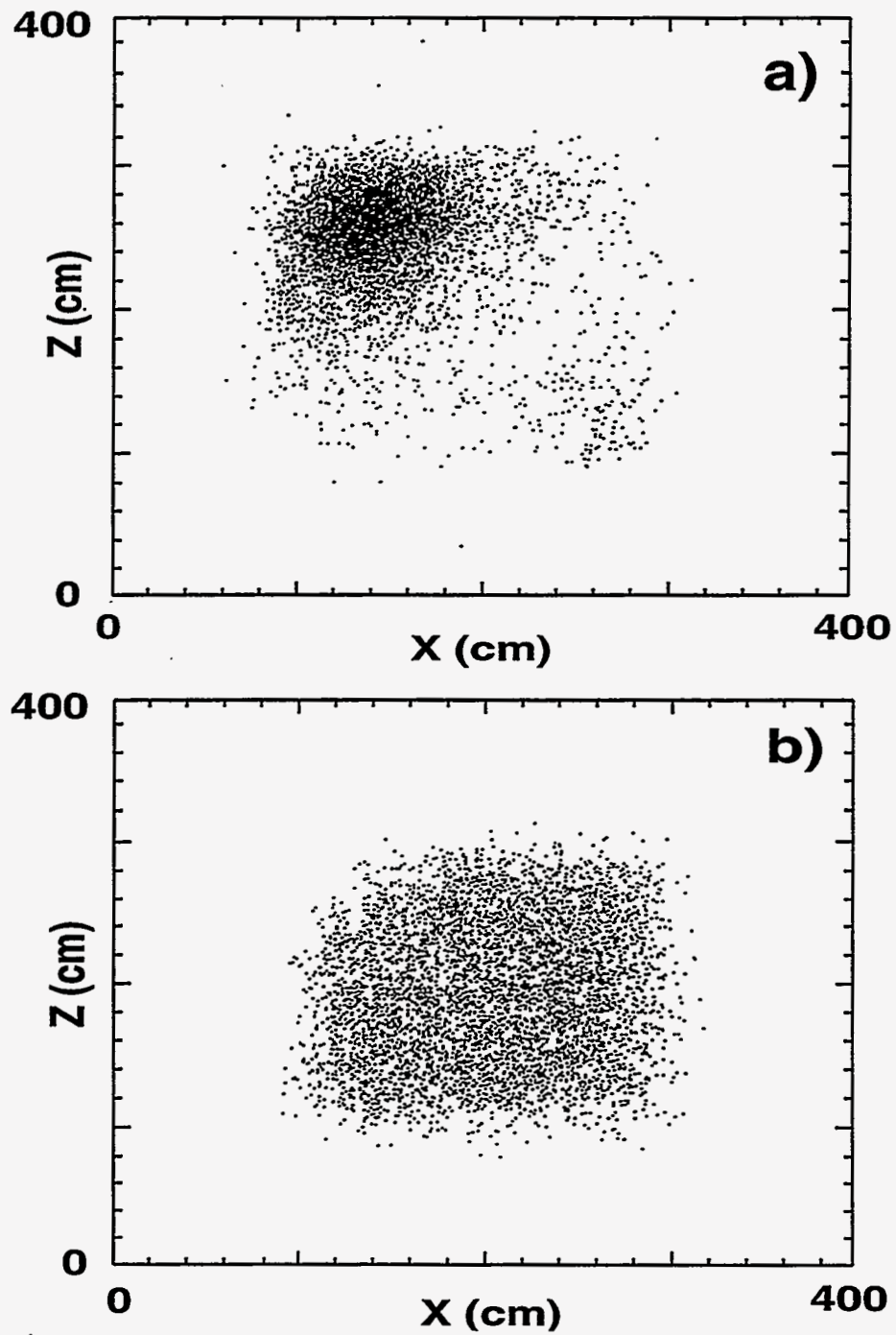


Figure 4.12: Beam filamentation electron particle plots for the finite beam: a) beam electrons and b) target electrons. These are snapshots at $\omega_{pe}\Delta t = 1600$ after saturation of the instability where the beam electrons have coalesced into one filament.

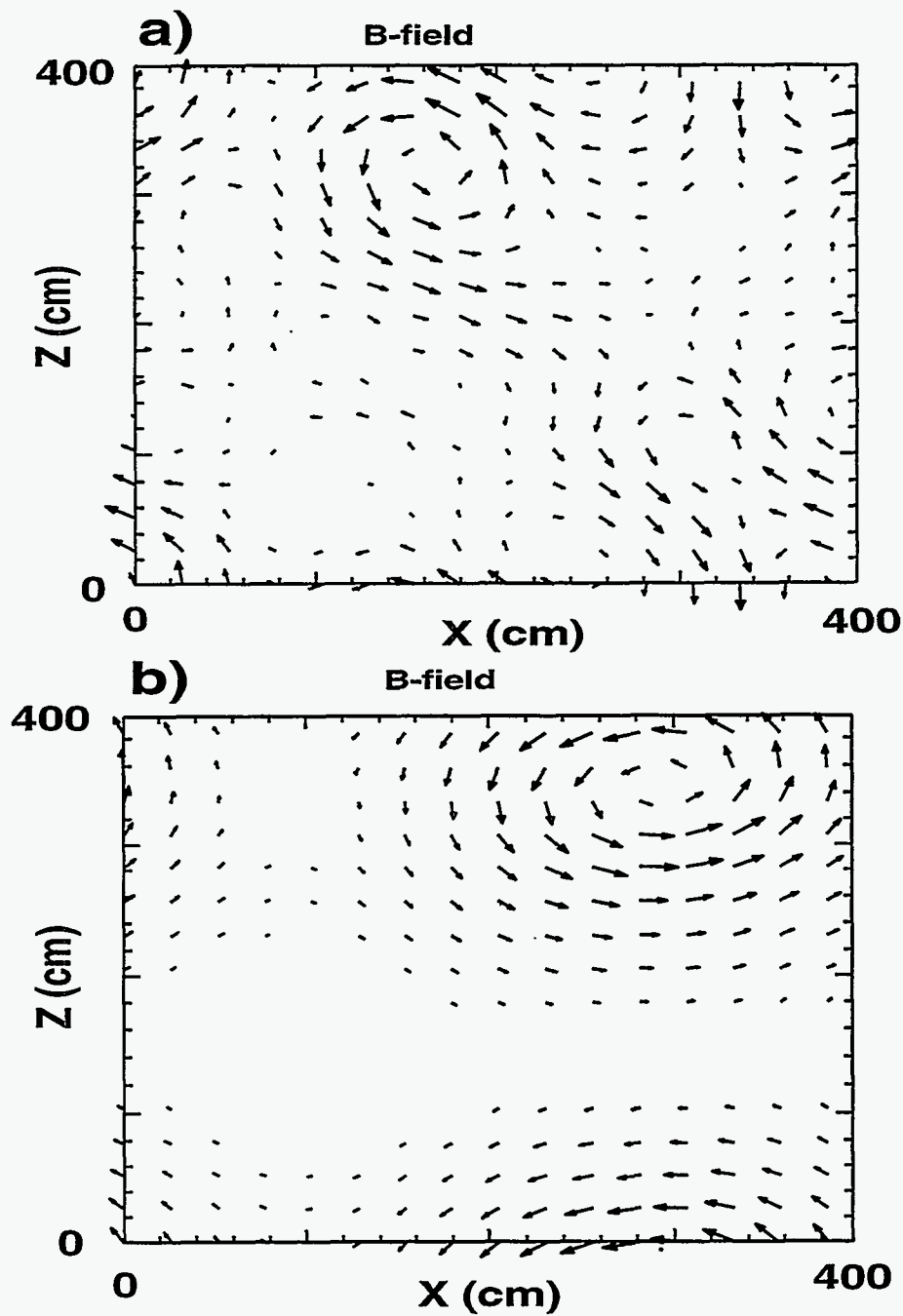


Figure 4.13: Beam filamentation B-field plots for the uniform plasma showing a change in the unstable mode. a) At early time, $\omega_{pe}\Delta t = 320$, a shorter wavelength has the fastest growth rate (longest vector = 0.0531 gauss). b) At late time, $\omega_{pe}\Delta t = 1600$, the initial mode stabilizes and the slower growing longest wavelength mode dominates (longest vector = 0.356 gauss).

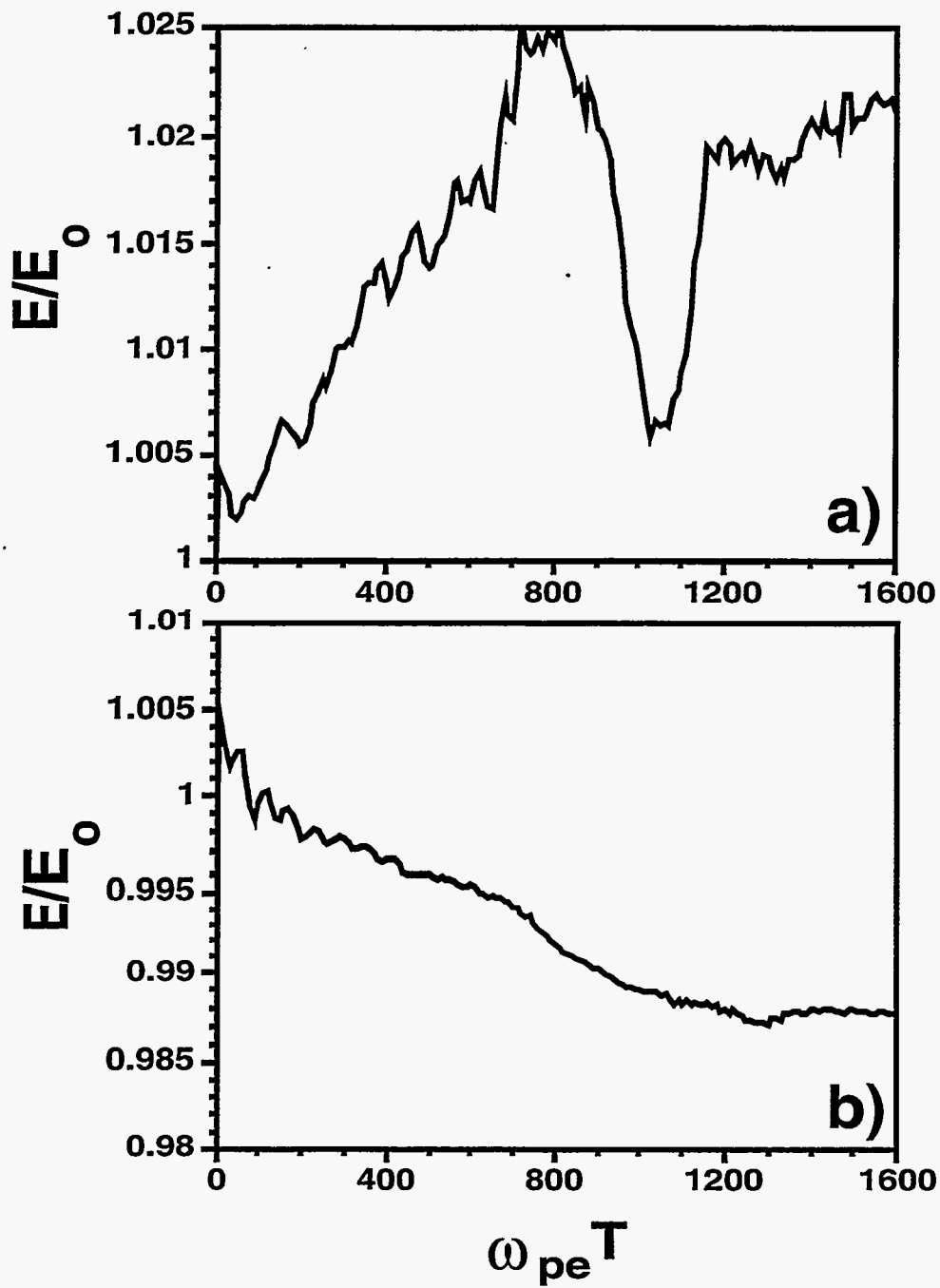


Figure 4.14: Beam filamentation total system energy. Even with the large changes in T_e changes in the total system energy are 2% or less.

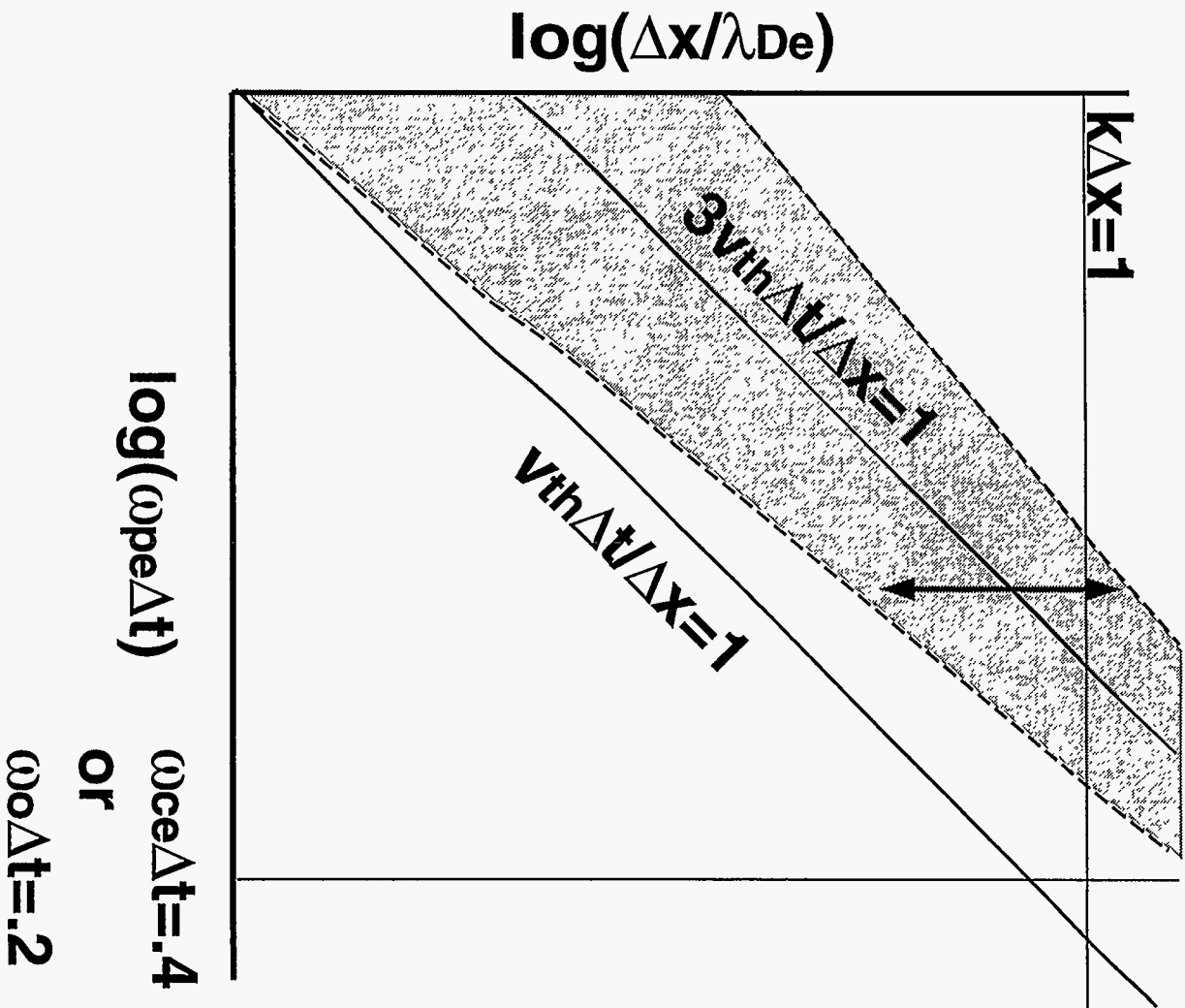


Figure 4.15: Recommended operating region (shaded) for DADIPIC in the $\Delta x / \lambda_{De}$ vs $\omega_{pe}\Delta t$ plane. The width of the region depends on the tolerable numerical effect on electron kinetic energy. The region can extend to $\Delta x / \lambda_{De}$ and $\omega_{pe}\Delta t \gg 1$.

Chapter 5

Heating in Inductive Plasma Processing Reactors

5.1 Plasma Processing

Plasma enhanced chemical processes are widely used to chemically alter the surface properties of materials used in electronics, automotive, steel, biomedical and toxic waste management industries[lie94]. This plasma processing usually falls into the categories of removing material from a surface for cleaning or etching, depositing films of material on top of a surface, or modifying the surface through doping. The basic design of a plasma processing reactor is an enclosed, evacuated conducting box into which a gas is pumped and partially ionized. The plasma electrons and ions move toward the walls and are neutralized. The plasma is replenished through ionizing collisions of the higher velocity electrons with the neutral gas. In these reactors radio-frequency, rf, electromagnetic fields pump power into the electrons in order to maintain the discharge.

As with any confined plasma, the plasma rises to a positive potential with respect to the walls. This retards the more mobile electrons, allowing the net current to the walls to be zero and maintaining charge neutrality in the plasma. Since the plasma tends to exclude DC E-fields, most of the potential drop occurs in a narrow region next to the walls called a sheath. The object to be processed is also placed in the reactor, and usually it is set at a negative potential with respect to the reactor walls. As a result a larger sheath forms around the object, and the ions are accelerated to its surface with an energy equal to the plasma potential plus the potential difference between the object and the walls. The reactor acts as a container in which the chemical processing of the material surface take place. Reactant

agents for the chemical processes may be pumped into the reactor or formed by the plasma itself.

Plasmas have advantages and disadvantages in processing material surfaces. One of the main advantages is that the chemical processes in the plasma greatly increase the rate at which reactions occur. In low pressure discharges the object or substrate is at a much lower temperature than the plasma, and processes such as Plasma Enhanced Chemical Vapor Deposition (PECVD) can proceed much faster than conventional Chemical Vapor Deposition (CVD). In CVD the substrate is at the same temperature as the gas so reaction and deposition rates must be kept low in order to prevent melting of the substrate. Features on a surface can be made smaller with plasma reactors because the etching can be more anisotropic. The ion bombardment of the substrate increases the reaction rate in the direction of ion motion and removes any passivating films which may build up on the surface. For coating the surface of an irregular object, Plasma-Immersion Ion Implantation (PIII) has proven to be superior to beams because the narrow sheath closely follows the contours of the object.

Of course, there are disadvantages in the use of plasmas which has led to the experimental and theoretical efforts to improve plasma processing reactors. Plasmas tend to have less selectivity, the ability to etch only specific materials and not others, than wet or purely chemical etches. In addition unlike a gas or liquid in a box, the loss of plasma at the walls causes a variation in the plasma density across the reactor. Since the flux of ions depends on the density, this variation results in less uniformity of the etch or deposition process.

The reactors for processing microelectronic chips are being designed to meet certain requirements. The desirability of high processing or etching rates increases the importance of high plasma density. At the same time neutral densities must be minimized to ease the removal and disposal of effluent and keep feedstock costs down. Uniformity to greater than 1% is desired over diameters of 20 cm or greater. Finally, the ion energies must be kept low to prevent damage to the chips and to minimize contamination from reactor wall sputtering. The typical steps in etching a wafer include: depositing a film on a substrate (PP), depositing photoresist on top of the film, exposing the resist to light through a pattern, developing the resist and removing the exposed resist regions (PP), etching the film regions exposed by the resist removal (PP), and removing the remaining photoresist (PP). Those steps designated with (PP) can be accomplished with plasma processing.

Two general types of reactors for wafer processing, capacitive and inductive, are shown in Fig. 5.1. Capacitive reactors are essentially two parallel conducting plates with an rf variation of the potential between the plates. This time varying potential, which manifests itself as E-fields in the plasma sheaths near the plates, both maintains the discharge through heating and accelerates the ions to the substrate. Inductively-coupled plasma, ICP, sources use a current-driven antenna, producing mainly inductive fields. The antenna is usually separated from the plasma by a dielectric and possibly a Faraday shield which minimizes capacitive effects. A potential different than the wall potential may be applied to the chip, allowing an additional adjustable parameter to achieve desired ion energies. Unlike capacitive reactors this potential can be unrelated to plasma generation. Typically both types of reactors operate with electron temperatures of a few eV and input power of a few hundred watts.

The differences between the reactors lead to certain disadvantages for each type in terms of the requirements listed above. A more extensive comparison of these reactors may be found in Lieberman and Lichtenberg[lie94]. In capacitive reactors the ion acceleration energies in the electrostatic sheaths are higher (200-1000 eV instead of 20-500 eV), and the ionization fraction is lower (10^{-6} to 10^{-3} instead of 10^{-4} to 10^{-1}). The lower ionization fraction results in capacitive reactors operating at higher pressures (10 to 1000 mTorr instead of .5 to 50 mTorr) and lower plasma densities (10^{10}cm^{-3} instead of 10^{11}cm^{-3}). In inductive reactors uniformity is more of an issue since the close parallel plates of a capacitive reactor minimize any geometric effects. Inductive reactors also suffer from degradation of the dielectric window due to ion bombardment and have greater pumping requirements because of the lower operating pressures. The higher plasma densities and adjustable wafer potential of the ICP sources have caused significant interest in these type of reactors over recent years. Eckert[eck74] describes some of the 100 year history of the sources and their uses. Hopwood[hop92] gives an overview of more recent designs with an emphasis on wafer processing.

The objective of experimental and theoretical projects has been to understand and then optimize the operation of ICP sources in configurations useful for semiconductor wafer processing. The operational equilibrium which an ICP reaches is a matter of particle balance and power balance. In order for the plasma density, n_p , to be in equilibrium the

particle flux to the walls, Γ , must balance with the electron-ion pair creation rate or

$$\Gamma A = n_p \nu_{iz} V \quad (5.1)$$

where ν_{iz} is the electron-neutral ionizing collision frequency, A is the ICP surface area, and V is the ICP volume. The flux to the walls is governed by diffusion of the plasma particles through the neutral gas and the electrostatic sheath potential built up to keep the time-average of the electron and ion fluxes equal. Models for the plasma density profile from the collisional to collisionless regimes can be found in [god86], [eck62], [ton29], [sel63], and [lie94].

The power lost can be characterized by two terms: the collisional energy loss per electron-ion pair created, \mathcal{E}_c , and energy lost per electron, \mathcal{E}_e , or ion, \mathcal{E}_i , lost at the walls. Ionization, excitation, and momentum transfer collisions contribute to \mathcal{E}_c , and the rate of these collisions is dependent on n_p and the particle velocity distribution. The power out of the reactor takes the form

$$\mathcal{P}_{out} = \mathcal{E}_c n_p \nu_{iz} V + \Gamma A (\mathcal{E}_e + \mathcal{E}_i) = \Gamma A (\mathcal{E}_c + \mathcal{E}_e + \mathcal{E}_i) \quad (5.2)$$

where the second equality is due to the particle balance equation. The power into the system has two main sources: Ohmic heating and stochastic/collisionless inductive heating [pip49]. Stochastic capacitive heating [lie88], [god90], which is due to the particle interaction with the time varying electrostatic sheath, is not as important in ICPs where the sheaths are smaller. The simulation of the collisionless heating and the velocity distribution dependence of the ionization rate require the use of a kinetic code. In the following sections DADIPIC simulation of collisionless heating and a method of integrating this into a methodology for investigating ICPs will be described.

5.2 Collisional and Collisionless Heating

Now that we have an appreciation for the importance of heating in the ICP, we shall determine its magnitude. In order to understand the underlying physics and to provide results for verification of correct DADIPIC operation, 1-D analytic theory for the heating is investigated. In this section collisional heating is derived and then compared to results which include the stochastic heating, giving a measure of where stochastic effects become important. For the theory consider a transverse E-field, E_y , and B-field, B_z , incident upon

a plasma slab of uniform density and temperature. The relevant linearized electromagnetic equations are[reu49]

$$\frac{\partial^2 E_y}{\partial x^2} = \frac{4\pi i\omega}{c^2} J_y \quad (5.3)$$

and

$$B_z = \frac{ic}{\omega} \frac{\partial E_y}{\partial x} \quad (5.4)$$

where a harmonic time-dependence is assumed. The difference between fluid and kinetic results lies in the treatment of the plasma for determining J_y .

5.2.1 Collisional Heating

If collisionless effects are ignored, the plasma can be treated as a collisional fluid, and the linearized fluid momentum transport equation can be used.

$$i\omega V_y + eE_y = -m_e \nu_{ne} V_y \quad (5.5)$$

where ν_{ne} is the electron-neutral collision frequency. Solving for V_y , we arrive at an expression for J_y

$$J_y = -en_e V_y = \frac{n_e e^2 E_y \nu_{ne} - i\omega}{m_e \nu_{ne}^2 + \omega^2} \quad (5.6)$$

Substituting into Eq. (5.3), we have

$$\frac{\partial^2 E_y}{\partial x^2} - \alpha^2 E_y = 0 \quad (5.7)$$

where

$$\alpha = \frac{\omega_{pe}}{c} \frac{\omega}{(\nu_{ne}^2 + \omega^2)^{1/2}} \left[\left(\frac{r+1}{2} \right)^{1/2} + i \left(\frac{r-1}{2} \right)^{1/2} \right] \equiv a + ib \quad (5.8)$$

and $r = (1 + (\nu_{ne}/\omega)^2)^{1/2}$.

Given the boundary conditions $E_y(0) = E_o$ and $E_y(L) = 0$, we find expressions for the fields and the energy flux, S_x , into the plasma

$$E_y(x) = \frac{E_o}{\exp(\alpha L) - \exp(-\alpha L)} [\exp[-\alpha(x-L)] - \exp[\alpha(x-L)]] \quad (5.9)$$

$$B_z(x) = -\frac{ic}{\omega} \frac{\alpha E_o}{\exp(\alpha L) - \exp(-\alpha L)} [\exp[\alpha(x-L)] + \exp[-\alpha(x-L)]] \quad (5.10)$$

$$\begin{aligned}
S_x &= \frac{c}{8\pi} \text{Re} \left\{ \frac{E_y}{B_z} |B_z|^2 \right\} \\
&= -\frac{c^2 E_o^2 \cosh(2aL) + \cosh(2bL) 2a \sin(2bL) - b(\exp(2aL) - \exp(-2aL))}{8\pi\omega \cosh(2aL) - \cosh(2bL) \exp(2aL) + \exp(-2aL) + 2\cos(2bL)} \quad (5.11)
\end{aligned}$$

If the slab is very large so $La, Lb \gg 1$, then

$$E_y(x) \simeq E_o e^{(a+ib)x}. \quad (5.12)$$

From this expression a skin depth, the distance for the field magnitude to decrease by an e-folding, can be defined

$$\delta = \frac{1}{a} = \frac{c}{\omega_{pe}} \frac{(\nu_{ne}^2 + \omega^2)^{1/2}}{\omega} \left(\frac{2}{r+1} \right)^{1/2}. \quad (5.13)$$

This leads to the expected result for the power deposition per unit area

$$\begin{aligned}
S_x &\simeq \frac{1}{2} \frac{E_o^2 \omega_{pe}^2 \delta \nu_{ne}}{8\pi (\nu_{ne}^2 + \omega^2)} \\
&= \frac{c E_o^2 \omega_{pe} [(1 + (\nu_{ne}/\omega)^2)^{1/2} - 1]^{1/2}}{8\sqrt{2}\pi \omega (1 + (\nu_{ne}/\omega)^2)^{1/2}}. \quad (5.14)
\end{aligned}$$

Here and in the rest of this chapter, expressions for S_x will be written in terms of E_o^2 . In this way we can normalize with respect to the driven E-field for comparisons between various results. Note that given constant ω , the power deposition has a peak for $\nu/\omega \sim 3$, and it goes to zero for very small or very large ν/ω . For small ν/ω the skin depth is approximately c/ω_{pe} . For large ν/ω the real and imaginary parts of α are approximately equal, and the field oscillates as well as damps in space.

The appropriate collision frequency for the electrons is found by averaging over the velocity distributions of the electrons and the particle type with which they are colliding. In these slightly ionized plasmas the main effect on the electrons is due to collisions with neutrals. The average is taken over the electron-neutral collision cross section, σ_{ne} , and the relative particle velocity, v_r

$$\begin{aligned}
\nu_{ne} = n_n K &= n_n \langle \sigma_{ne}(v_r) v_r \rangle \\
&= \int dv_e dv_n f_e(v_e) f_n(v_n) \sigma_{ne}(v_r) v_r \quad (5.15)
\end{aligned}$$

Neglecting the velocity of the low temperature neutral gas particles and assuming the electrons have a Maxwellian velocity distribution, the rate constants, K , can be found given the cross sections for various types of collisions. These assumptions are certainly consistent with the fluid description being used above. As an example, the rate constants for Ar versus electron temperature, as compiled by Vahedi[vah93], are shown in Fig. 5.2.

5.2.2 Collisionless Heating: Half-Infinite Plasma

As shown by Fig. 5.2, at a neutral pressure of 2 mTorr and an electron temperature of 2 eV the collision frequency in Ar becomes less than 10 MHz. As a result low pressure reactors operating near 10 MHz can have an electron-neutral collision frequency less than the driving frequency. Under such conditions collisionless or stochastic heating of the electrons can be greater than collisional heating.

The phenomena of collisionless heating in the ICP is basically the same as that of the anomalous skin effect in metals. Electrons in the conducting medium pass through the skin depth and are stochastically heated. Heating is significant for those electrons that reside in the field region for a time short compared to the field oscillation period or $\delta/v_{th} < \omega^{-1}$. These electrons receive a transverse kick since the inductive E-field remains in one direction over the time of the electron transit of the skin depth. Two analytic solutions for the collisionless heating shall be described. The first simpler theory, introduced by Wendt[wen93] and quantified in Liebermann[lie94] and Vahedi, et. al.[vah94], considers the effect on a single electron reflecting off the driven wall and then averages over electrons of all phases. This method is presented since it lends itself more easily to some 2-D collisionless results presented in section 5.4.

As before consider a transverse field incident on a plasma slab but assume a field profile of the form $E_y(x) = E_o \exp(-x/\delta)$. Electrons travel toward the driven wall beginning at time t_1 , reflect at $t = 0$, and move away from the wall over time t_2 . To determine heating consider only electrons which reflect off the wall, and assume negligible change in an electron's velocity normal to the wall, v_x , during this period. In other words collisions are neglected. For a time harmonic field the change in the electron transverse velocity is

$$\Delta u_{ey} = \frac{q}{m_e} \int_{t_1}^{t_2} E_o e^{v_x t / \delta} \sin(\omega t + \phi_o) dt \quad (5.16)$$

where ϕ_o is the phase of the electron. Because of the exponential decrease in $E_y(x)$, let $t_1 \rightarrow -\infty$ and $t_2 \rightarrow \infty$. Integration results in

$$\Delta u_{ey} = \frac{q E_o}{m_e} \frac{2(\delta/v_x) \sin \phi_o}{1 + (\omega \delta/v_x)^2}. \quad (5.17)$$

Given the energy gain of $\frac{1}{2} m \Delta u_{ey}^2$ and averaging over all phases, the average energy gain of electrons with velocity v_x is found as

$$\langle \Delta \mathcal{E} \rangle = \frac{q^2 E_o^2}{m_e} \frac{(\delta/v_x)^2}{(1 + (\delta/v_x)^2)^2}. \quad (5.18)$$

The power per unit area taken by the electrons back into the plasma is found by averaging over the distribution of the electron flux reflecting off the wall

$$S_{st} = \int_{-\infty}^{\infty} dv_y \int_{-\infty}^{\infty} dv_z \int_0^{\infty} dv_x < \Delta \mathcal{E} > v_x f_o(v_x, v_y, v_z). \quad (5.19)$$

For a Maxwellian distribution the result is

$$S_{st} = \frac{E_o^2 \omega_{pe}^2 \delta^2}{8\pi v_{th}} \sqrt{\frac{\pi}{2}} I_{sim}(\alpha) \quad (5.20)$$

where

$$I_{sim}(\alpha) = \frac{1}{\pi} \int_0^{\infty} dx \frac{x e^{-x}}{(x + \alpha)^2} \quad (5.21)$$

and

$$\alpha = \frac{1}{2} \left(\frac{\delta \omega}{v_{th}} \right)^2 = \left(\frac{\text{Transit time of an electron across the skin depth}}{\text{RF period}} \right)^2. \quad (5.22)$$

Note that as α becomes large (≥ 10), $I_{sim}(\alpha) \simeq 1/(\pi\alpha^2)$, and the heating monotonically decreases. The bulk of the electrons are moving too slowly to interact stochastically with the field. They simply oscillate back and forth with no net gain in energy, and the kinetic heating is small. In the other extreme of small α $I_{sim}(\alpha) \simeq \pi/2$, and stochastic effects are significant. The earlier fluid theory result can be added to this result to get an estimate for the magnitude of the total heating. The coupling of these two results works best for plasmas which are either in the collisionless or collisional regimes. Such an approach is more approximate in the intermediate regime where neither effect is dominant. Though this theory gives an estimate for the regime where collisionless heating is maximized, a value for δ must still be found to get the magnitude of the heating.

The following is an outline of the derivation of the complete kinetic result which is correct for all ν/ω and can provide an estimate for the δ of the simple theory. Reuter and Sondheimer derived the 1-D kinetic theory for the effect in metals[reu49] while more recently Weibel[wei67], Ichimaru[ich73], and Batchelor, et. al.[bat93] have made the changes necessary for the plasma case. Again begin with Eqs. (5.3) and (5.4), but instead of Eq. (5.5) the linearized Boltzmann equation is used

$$i\omega f_1 + v_x \frac{\partial f_1}{\partial x} + \frac{e v_y f_o}{m v_{th}^2} E_y = -\nu f_1 \quad (5.23)$$

where $f_1(\mathbf{x}, \mathbf{v}, t)$ and $f_o(\mathbf{x}, \mathbf{v}, t)$ are the perturbed and equilibrium particle distribution functions respectively. The collision term on the right results from the Krook model[kra86]. A

Maxwellian distribution of uniform density is assumed for f_0 . This equation is a first order ordinary differential equation which can be solved using an integrating factor. The solution for f_1 has two forms: $f_1^{(1)}$ when $v_x > 0$ and $f_1^{(2)}$ when $v_x < 0$. The functions are determined with the boundary conditions: 1) for $v_x > 0$, $f_1^{(1)}$ must be finite as $x \rightarrow -\infty$ and 2) the electrons specularly reflect at $x = 0$ so $f_1^{(2)}(v_x, v_y, v_z, x = 0) = f_1^{(1)}(-v_x, v_y, v_z, x = 0)$.

Given the resulting functions, the current density is found from

$$J_y(x) = -e \int dv v_y f_1(x, \mathbf{v}). \quad (5.24)$$

Using this J_y with Eqs. (5.3) and (5.4) yields, after some manipulation, the ratio of the fields at the plasma surface

$$\frac{E_y}{B_z} = \frac{\sqrt{8} i v_{th}}{\pi c (i + \nu/\omega)} \int_0^\infty \frac{dt}{t^2 - \frac{\beta}{(1-i\nu/\omega)^3} K(t)} = \frac{\sqrt{8} v_{th}}{\pi c} I(\nu/\omega, \beta). \quad (5.25)$$

The variable β is the square of the distance a thermal electron travels in an rf cycle divided by the collisionless skin depth, or

$$\beta = \frac{4}{\sqrt{\pi}} \left(\frac{v_{th} \omega_{pe}}{\omega c} \right)^2. \quad (5.26)$$

It is closely related to the inverse of α derived in the simple collisionless theory. $K(t)$ is a function dependent on the unperturbed electron velocity distribution function. For a Maxwellian plasma we have

$$K(t) = \int_0^\infty dx \frac{2xe^{-x^2}}{t^3} [(1 + (xt)^2) \tan^{-1}(xt) - xt]. \quad (5.27)$$

The power into the plasma is

$$S_x = \frac{cE_0^2}{8\pi} \text{Re} \left\{ \frac{B_z^*}{E_y^*} \right\} = \frac{cE_0^2}{8\pi} \frac{\sqrt{8} v_{th}}{\pi c} \frac{I}{|I|^2}. \quad (5.28)$$

The integral I of Eq. (5.25) can be solved numerically giving the values of E_y/B_z and S_x for a particular plasma. For large β when the particle transit time is short compared to an rf period, the analytic expressions

$$\frac{E_y}{B_z} = \sqrt{\frac{8}{\pi}} \frac{\pi v_{th}}{3c} \left(\frac{2}{\pi\beta} \right)^{1/3} \left(\frac{1}{\sqrt{3}} + i \right) \quad (5.29)$$

and

$$S_x = \frac{cE_0^2}{8\pi} \sqrt{\frac{3}{8\pi}} \frac{3c}{4v_{th}} \left(\frac{\pi\beta}{2} \right)^{1/3}. \quad (5.30)$$

are found. The power deposition has become independent of the collision frequency.

The S_x of Eq. (5.28) can be set equal to Eq. (5.20) to find the necessary δ_{sim} for the simplified theory. The result for large β is $\delta_{sim} = .37(v_{th}c^2/\omega_{pe}^2\omega)^{1/3}$. Assuming an exponential form for $E_y(x) = E_o \exp[(a + ib)x]$, a skin depth can be derived from Faraday's law

$$\frac{\partial E_y}{\partial x} = -\frac{i\omega}{c} \left(\frac{B_z}{E_y} \right) E_y. \quad (5.31)$$

This results in

$$\frac{1}{a} = \delta_{exp} = \left(\frac{\pi v_{th} c^2}{\omega_{pe}^2 \omega} \right)^{1/3}. \quad (5.32)$$

There is also an oscillatory variation in $E_y(x)$ since $b = \alpha/\sqrt{3}$. Since $\delta_{exp} \neq \delta_{sim}$, the assumption in the simple theory of an exponential drop in $E_y(x)$ is not quite right. The simple theory, however, does maintain the essential physics, a finite skin depth region which the faster electrons traverse in less than an oscillation period. The important result is that δ_{sim} adjusts itself to give the correct heating rate when Eqs. (5.20) and (5.28) are set equal. Significant deviations should only occur when the skin depth is not much less than the plasma width or the spatial oscillations in $E_y(x)$ have much smaller wavelengths than the skin depth. The simple theory will be used in section 5.4 to determine trends in a 2-D configuration. In addition section 5.2.3 gives information on the actual spatial variation of E_y so we can determine when the simple theory is applicable.

Figure 5.3 is a comparison of the fluid and total kinetic theories for the power deposition into a plasma versus ν/ω for $f = 10$ MHz, $T_e = 3.75$ eV, $n_e = 2 \times 10^{11}$ cm⁻³. At low ν/ω the total theory indicates a leveling off of the power which is missed by the collisional theory and is due to collisionless heating. Since ICPs can operate where $\nu/\omega \leq 1$, the collisionless heating must be included or the power balance will be incorrect. The magnitude of ν/ω required for collisionless heating to be important depends on the value of β . Larger β pushes the anomalous region to larger ν/ω .

5.2.3 Collisionless Heating: Finite Plasma

Several authors have investigated the attenuation of a transverse electromagnetic wave in a kinetic plasma of finite extent[wei67], [rey69], and [ble70]. The theory was even extended to plasmas with an assumed parabolic density profile[ble73], [jol76]. In these

papers the theory was tested with experiments on cylindrical plasmas driven by currents in coaxial solenoids[jol76]. In such plasmas the electrons entering the skin depth and reflecting off the wall can return after reflection off the opposite wall. If the electron mean free path is significant compared to the plasma dimensions, the electrons' velocities will not be randomized between passes through skin depth regions leading to interference effects with previous kicks to the transverse velocity. The plasmas studied are either a slab with E_y antisymmetric about $x = 0$ or a cylinder with no azimuthal variation in E_θ . For the slab the electrons are specularly reflected at $x = \pm a$; however, with the E-field boundary condition this is the same as plasma entering the problem from $|x| > a$. This makes the problem infinite and periodic so the defining functions can be expanded in Fourier series.

The results for E_y , B_z , and J_y are

$$E_y(x) = -2aiB_a \exp(i\omega t) \frac{4}{\pi^2} \sum_{n=\text{odd}} \frac{1}{1+\epsilon} \frac{\sin(n\pi/2)}{n^2} \sin\left(\frac{n\pi x}{2a}\right), \quad (5.33)$$

$$B_z(x) = B_a \exp(i\omega t) \left[1 - \frac{4}{\pi} \sum_{n=\text{odd}} \left(\frac{\epsilon}{1+\epsilon} \right) \frac{\sin(n\pi/2)}{n} \cos\left(\frac{n\pi x}{2a}\right) \right], \quad (5.34)$$

and

$$J_y(x) = -\frac{cB_a}{2a\pi} \exp(i\omega t) \sum_{n=\text{odd}} \left(\frac{\epsilon}{1+\epsilon} \right) \sin\left(\frac{n\pi}{2}\right) \sin\left(\frac{n\pi x}{2a}\right) \quad (5.35)$$

where

$$\epsilon = \frac{(a\omega_{pe}/c)^2}{(n\pi/2)^2} \frac{2a\omega}{\sqrt{2\pi}v_{th}} \frac{\mathcal{Z}(\xi)}{n}, \quad (5.36)$$

$$\xi = \frac{2a}{n\sqrt{2\pi}v_{th}} (-\omega + i\nu), \quad (5.37)$$

and \mathcal{Z} is the plasma dispersion function

$$\mathcal{Z}(\xi) = \frac{1}{\sqrt{\pi}} \int_{-\infty}^{\infty} \frac{\exp(-\gamma^2)}{\gamma - \xi} d\gamma. \quad (5.38)$$

The algorithm used for calculating these sums is similar to that shown in Appendix A for the dispersion relations. From Eqs. (5.33) and (5.34) we can find the power into the plasma, S_x , and determine when the size of the plasma begins to effect the heating. Figure 5.4 shows the change in $8\pi S_x(a\omega_{pe}/c, \sqrt{\beta})/cE_0^2$ versus the width of the plasma and $\sqrt{\beta}$ for two different collision frequencies, $\nu/\omega = 0$ and $\nu/\omega = 1$.

Several features are apparent on these contour plots. In both cases the heating converges to the half-infinite plasma result for $a \sim 10\omega_{pe}/c$. For the collisionless case a peak in the heating occurs as $a\omega_{pe}/c$ varies for constant β . The peak is due to electrons which bounce back and forth across the slab in phase with the driven E-fields. If they always see the same sign for fields on either side of the slab, they will continually be accelerated in the y direction. The maximum heating falls close to the line across the plot satisfying

$$\sqrt{\frac{2}{\pi}}v_{th} = 8\pi a\omega \quad (5.39)$$

which is the requirement for $\langle |v_x| \rangle$ of a Maxwellian distribution to be in phase. As ac/ω_{pe} becomes very small the plasma becomes smaller than the skin depth, and the electrons are no longer in phase with the oscillation so S_x falls to zero.

For $\nu/\omega = 1$ the collisional heating dominates for smaller β . In the small β region the contour lines are nearly straight vertical lines down to $a\omega_{pe}/c < 3$ indicating that the collisional heating reaches the half-infinite result for plasmas only a few skin depths thick. This is expected given the local nature of the collisional heating. For larger β the collisionless effects once again become important as evidenced by the small change in the heating between Fig. 5.4a and b near $\sqrt{\beta} = 5$.

Another useful result of this theory is the prediction of the spatial variation for the fields and current density. The theoretical spatial dependence of the current density for the defined plasma with half-width $a\omega_{pe}/c = 25$ is shown in Fig. 5.5a. As surmized in the previous section, the current density does not have an exactly exponential fall, and does oscillate before reaching zero. In fact given that \mathbf{J} has a real and imaginary part, the shape of the current density also changes with time. With these caveats in mind we see that the basic picture of the current density and fields falling off monotonically within a skin depth is a reasonable approximation, and the simple collisionless theory is applicable as long as an appropriate effective skin depth is used. The result from a 1-D DADIPIC simulation with a slab driven on only one side is shown in Fig. 5.5b. Results from simulations are expanded in the next section. This plot is given to show the same type of oscillatory behavior in a nonsymmetric drive and the agreement between simulation and theory.

5.3 1-D Simulation of Collisionless Heating

A number of 1-D simulations compare DADIPIC's ability to reproduce the above analytic results. Equation (5.25) can be solved numerically for small ν to find E_y/B_z in the collisionless limit. It is more convenient to consider the integral I which depends on the dimensionless parameter β without the proportionality to a particular v_{th} . Figure 5.6 shows the real and imaginary parts of $I/|I|^2$ vs β . Notice that at small β , $Re\{I\} \ll Im\{I\}$. The effective resistivity, dependent on $Re\{I\}$, is small compared to the inductance, dependent on $Im\{I\}$, and the electrons simply oscillate in the field without gaining net energy. As β increases the resistive component accounts for a progressively larger proportion of the total surface impedance. These simulations are similar to those of Turner[tur93] except without collisions only collisionless heating was investigated. On the other hand, Turner was limited to smaller plasma sizes, much finer discretization, and 1-D simulations because of reliance on an explicit PIC code. Extension to 2-D simulations would be even more difficult without DADIPIC.

In the simulations conducting walls are placed at the minimum and maximum boundaries in x as shown in Fig. 5.7. Electrons are specularly reflected off of the walls while ions are defined as a stationary neutralizing background. The electron particle number is 16384, and temperature is 3.75 eV. The total problem length is 14 cm with Δx of .14 cm. Δx is chosen to give reasonable resolution of the skin depth which is around 1.5 cm for these simulations. A time-harmonic, solenoidal E-field is imposed on the wall at x maximum. While Turner investigated the relative importance of collisionless heating with respect to collisional heating, our interest is the change of the surface impedance for a collisionless plasma vs β . To vary β between simulations both the plasma density, 10^{11}cm^{-3} to $3 \times 10^{11}\text{cm}^{-3}$, and the frequency of the imposed E-field, 3.33 MHz to 20 MHz were varied. These densities and frequencies are typical of those in actual plasma processing reactors. The spatial and temporal discretization for the 10^{11}cm^{-3} density is $\Delta x/\lambda_{De} = 31$ and $\omega_{pe}\Delta t = 9$. These values are chosen, as usual, to minimize any numerical heating or cooling.

Among the quantities measured were E_y^{sol} and B_z at the driven wall as well as the change in the total thermal energy of the electrons, ΔE_{th} . With this information the components of I resulting from the simulations with their various β 's can be found. The

real part is

$$Re\left\{\frac{I}{|I|^2}\right\} = \frac{\pi c}{\sqrt{8}v_{th}} \frac{8\pi(\Delta E_{th}/TA)}{c|E_y^{sol}|^2}. \quad (5.40)$$

T is the time over which ΔE_{th} is measured, and A is the effective surface area of the driven wall, .14 cm². The magnitudes of E_y^{sol} and B_z along with $Re\{I\}$ give $Im\{I\}$.

$$Im\left\{\frac{I}{|I|^2}\right\} = \sqrt{\left(\frac{\sqrt{8}v_{th}}{\pi c} \frac{|B_z|}{|E_y^{sol}|}\right)^2 - Re\left\{\frac{I}{|I|^2}\right\}^2}. \quad (5.41)$$

The results for the simulations appear as Δ s, dots, and circles in Fig. 5.6. The results for both the imaginary and real parts of I are within 5% to 20% of the analytic solution over an order of magnitude change in β . These results are not in perfect agreement, but the discrepancy appears correctable with finer resolution in the simulations. More particles would also decrease the numerical heating/cooling and the noise floor in the simulations due to fluctuations.

Because of the noise level, the driven E-field had to be set at a minimum level in order to reliably discern the change in total particle energy. For this reason the driven fields are not arbitrarily small and second order effects on the heating due to the B-field are apparent. In fact two sets of heating simulations were run one set with the B-field turned off (the Δ s in the plot), and one set with the B-field (the circles and dots in the plot). Of course, $Im\{I\}$ could not be calculated in the simulations without a B-field. The heating in the simulations without the B-field was consistently within 10% or better of theory while the other simulations could be off by over 20%. Before delving further into these B-field effects it is instructive to consider the numerical soundness of the DADIPIIC simulations.

Though the numerical heating is small, < 1%, the inductive heating is only about 10% of the total initial particle energy. Numerical heating was measured in simulations without driven inductive fields but with all other parameters the same as simulations with driven fields in order to account for the numerical heating. The amount of numerical heating or cooling was then subtracted or added to the inductive heating results. This is only an approximate correction since the rate of numerical heating changes as the total thermal energy changes. In fact some simulations were repeated without the electrostatic field. Since these simulations involve a warm, uniform plasma, any unphysical clumping should be prevented by the thermal motion of the particles. Those simulations without the electrostatic field confirmed the previously calculated heating rates, and showed that the

implicit electrostatic field was not affecting the v_x distribution. Bulges in the distribution, described below, grew with or without E_{irr} indicating that E_{sol} was the cause as opposed to some numerical effect. This confirmation of the calculations with the electrostatic field is important because 2-D, nonuniform plasmas must be simulated with the electrostatic field included.

Other improvements to the simulations would be finer resolution of the skin depth and a longer simulation region to better approximate a half infinite plasma. Even though better agreement may be possible, the accuracy of these simulations using only modest resolution is encouraging. The resolution presented above is typical in 2-D simulations given finite computer resources. This gives us confidence that DADIPIC can correctly predict the anomalous skin effect in more convoluted 2-D geometries where analytic theory cannot be applied.

An interesting feature of the electron heating in both the 1-D simulations of this section and the 2-D simulations of section 5.6 is the significant amount of heating occurring in v_x as well as v_y . In fact, almost all of the heating in the 2-D case occurred in the v_x and v_z distributions. Time histories of the change in electron thermal energy in the x and y directions for a $\beta = 10.64$ simulation are shown in Fig. 5.8. Given the small magnitude of E_{sol} in comparison to B_z , the force on a thermal electron due to the B-field is the same order of magnitude as the force due to the E-field ($|E|/|B| \sim v_{th}/c \sim 3 \times 10^{-3}$). The B-field itself cannot cause heating of the electrons, but it can convert the heating in v_y into changes in v_x and v_z . Heating in only the y direction for simulations with the B-field turned off, as shown in Fig. 5.8b, confirms these hypotheses.

The electron distributions are flattened near $v_x = 0$ and bulge near $v_x = v_{th}$ indicating that the slow particles in the x direction are picking up energy. This is a clue to the cause of heating in the nondriven direction. Those particles with small v_x spend more time in the skin depth region. These particles are accelerated most in the y direction by the driving E-field, and B_z changes their trajectory decreasing v_y and increasing v_x . The v_y distribution is replenished because of the stochastic heating. For lower field magnitudes the results appear to remain close to the 1-D linear kinetic theory even though much of the heating shows up in a direction normal to E_y .

For large enough B-fields some of the electrons are turned around before striking the wall. They do not receive the full kick from the E-field, and the heating becomes less than expected for the given field magnitude. In other words the pondermotive force excludes

those electrons with the greatest velocities in the direction normal to the wall. These are the very electrons which are participating in the stochastic heating. Such a process is studied by Cohen[coh94] where he finds the instantaneous flux reaching the wall to be

$$\Gamma_e = \left(\frac{n_p v_{th}}{2\sqrt{\pi}} \right) \operatorname{erfc} \left[\frac{\delta\omega_{ce}}{\sqrt{2}v_{th}} \right] = \Gamma_{eo} \operatorname{erfc} \left[\frac{\delta\omega_{ce}}{\sqrt{2}v_{th}} \right]. \quad (5.42)$$

This result is found by assuming the ratio of the magnetic force to the electric force is $v/\omega\delta$. ω_{ce} is the instantaneous cyclotron frequency at the wall. To find the average flux to the wall we can average Eq. (5.42) over an rf cycle, $\langle \Gamma_e \rangle$, assuming a sinusoidal time dependence for the B-field magnitude.

To measure this effect several simulations with $n_p = 2 \times 10^{11} \text{ cm}^{-3}$ and $f = 10 \text{ MHz}$ ($\beta = 10.64$) were run. The E-field was varied from .001 StatV/cm to .012 StatV/cm. The results in terms of $S = I / |I|^2$ versus the oscillation velocity, $v_{osc} = qE/m\omega$, are shown as circles in Fig. 5.9. The real part of S , representing the heating, closely follows the decrease in $\langle \Gamma_e \rangle / \Gamma_{eo}$ which is the line in the Fig. 5.9a. The decrease becomes greater than 50% as v_{osc}/v_{th} becomes greater than .5. At about $v_{osc}/v_{th} = 1.$, $\operatorname{Im}\{S\}$ begins to decrease from the small field value. Here the average plasma velocity in the direction of the driven field, contributed to most by particles with small velocities in the wall normal direction, is large enough for $|E| / |B| \sim V/c$. The current is then deflected from the transverse direction. Since the source for B_z is the transverse current, the B-field no longer increases along with the E-field, and the $|E| / |B|$ ratio begins to decrease. Note that these B-field effects are occurring for E-fields less than .012 StatV/cm or 3.6 V/cm which are average fields for ICP sources.

5.4 2-D Simulation of Collisionless Heating

The importance of 2-D effects will be shown in this section. Change the uniform plasma slab simulations of section 5.3 by allowing a spatial variation of the driven field in the z direction so

$$E_y(z, t) = E_o \cos(k_z z) \sin(\omega t). \quad (5.43)$$

If the wavelength is long enough, no 2-D effects should be present. The average power deposited per unit area should be half that for a spatially uniform field since $\langle \mathcal{P} \rangle \propto \langle E_y^2 \rangle$. DADIPIC simulations were run with a sinusoidal spatial variation of the driven E-field as

shown in Fig. 5.10. A 32×32 grid was initialized with 50000 electrons and a neutralizing background charge. The region has reflecting, conducting walls at x_{min} and x_{max} , and it is periodic in z . The plasma properties are $n_p = 2 \times 10^{11} \text{ cm}^{-3}$, $T_e = 3.9 \text{ eV}$, $\Delta x / \lambda_{De} = 152.$, and $\omega_{pe} \Delta t = 45.4$. The region is 15 cm wide with $\Delta x = .5 \text{ cm}$ and a skin depth of $\sim 1.5 \text{ cm}$. The driven frequency of 5 MHz and Eq. (5.26) give a β of 11.1. As done before in 1-D, simulations were run with and without the B-field. To confirm that no numerical problems surfaced with the switch to 2-D, simulations with an E-field driven uniformly along the wall at x_{max} with the B-field turned off resulted in $8\pi S_{x0}^B / cE_0^2 = 209$ compared to 191 from Eq. (5.25). This indicates accuracy approximately the same as the earlier 1-D simulations. A simulation with $E_0 = .004 \text{ statV/cm}$ and the B-field gave $8\pi S_{x0}^B / cE_0^2 = 87.3$ showing the previously seen B-field effect.

The rest of the simulations were run with $k_z = 2\pi / (z_{max} - z_{min})$ and the same E_0 . The wavelength was varied by changing $z_{max} - z_{min}$. In order to avoid numerical heating, the electrostatic field was not used. As with the 1-D calculations, any unphysical clumping should be minimal given the warm, uniform plasma. The simulation results are shown in Fig. 5.11. The Δ s are simulations with no B-field, the dots are simulations including the B-field, and the dotted horizontal line was the $k_z = 0$ case with the B-field. All results are normalized to the $k_z = 0$ case without the B-field.

One might expect the simulations with $k_z \neq 0$ to have absorbed powers of $S_{xk} = S_{x0}/2$. Since the variation of the field in z would prevent particles with a drift in z from receiving a uniform kick, S_{xk} would be expected to drop off even further for wavelengths on the order of the skin depth. As shown in Fig. 5.11, for short wavelengths this is the case, but for a significant region S_{xk} is greater than $S_{x0}/2$. S_{xk} does approach $S_{x0}/2$ as the wavelength becomes very long. A clue to the unexpectedly large values of S_{xk} lies in the position of the peak in S_{xk} . The wavelength is $\sim 15 \text{ cm}$, and in these simulations $2\pi v_{th} / \omega = 10 \text{ cm}$. A particle in the skin depth region with $v_x \sim 0$ and $v_z \sim v_{th}$ would be in phase with the driven E-field, and it would receive a continuous acceleration from E_y . Besides the mechanism of sampling the field for a short time and receiving a transverse kick, electrons may also be gaining energy by being in phase with the surface wave. This is a new spatial effect. An effect of comparable importance to the effect described in section 5.2.3 due to resonance of the particle as it crossed the plasma slab.

This new effect is even more pronounced in the simulations with the B-field included. These runs have driven fields large enough to cause the exclusion of electrons from

the skin depth as discussed previously. With the addition of nonlinear, kinetic magnetic effects the non-uniform heating even surpasses the uniform heating for certain wavelengths. The z variation in the B-field must be sufficient to allow enough electrons back into the skin depth, causing the combined heating mechanisms to be greater than the single heating mechanism of the uniform drive.

The wavelength dependence of this effect can be analyzed with a slight change to the simple collisionless heating theory of section 5.2.2. If the resonance with the surface wave exists, including v_z in the theory should give a wavelength dependence similar to that of the simulations. Assume the field has the form

$$E_y(x, z, t) = E_o \sin(2\pi/L) \sin(\omega t) e^{-x/\delta}. \quad (5.44)$$

Over one rf period the change in velocity for an electron is

$$\Delta u_{ey} = \int_{\pi/\omega}^{\pi/\omega} \frac{qE_o}{m} \sin\left[\frac{2\pi}{L}(z + v_z t)\right] \sin(\omega t) e^{-x/\delta} dt \quad (5.45)$$

where the electron starts at (x, z) with some v_z and with $v_x \sim 0$. After integrating we find

$$\Delta u_{ey} = \frac{qE_o b}{m\omega} e^{-x/\delta} \cos\left(\frac{2\pi z}{L}\right) A \quad (5.46)$$

where

$$A = \frac{(b + 2\pi s) \sin(\pi(b - 2\pi s)) - (b - 2\pi s) \sin(\pi(b + 2\pi s))}{(b + 2\pi s)(b - 2\pi s)}, \quad (5.47)$$

$b = L\omega/v_{th}$, and $s = v_z/v_{th}$. The change in energy is $\Delta\mathcal{E} = \frac{1}{2}m\Delta u_{ey}^2$. To get the average change in energy per unit surface area, we average over space and the velocity distribution. To get an average over v_x , we assume the theory applies to those electrons which move less than a skin depth in x over an rf period or $v_x/v_{th} < \omega\delta/2\pi v_{th}$. The resulting integral is

$$\langle \Delta\mathcal{E} \rangle = \frac{q^2 E_o^2 b^2}{2m\omega^2 L} \left(\frac{m}{2\pi\kappa T_e}\right) \int_0^L dz \cos^2\left(\frac{2\pi z}{L}\right) \int_0^\infty dx e^{-2x/\delta} \int_{-\omega\delta/2\pi}^{\omega\delta/2\pi} dv_x e^{-mv_x^2/2\kappa T_e} \int_{-\infty}^\infty dv_z e^{-mv_z^2/2\kappa T_e} A^2. \quad (5.48)$$

The power deposited per unit surface area is Eq. (5.48) divided by the rf period. The result is

$$S_x = \frac{cE_o^2}{8\pi} \left(\frac{\omega_{pe}^2 \delta b^2}{8\pi c\omega}\right) \frac{1}{\sqrt{2\pi}} \int_{-\omega\delta/2\pi v_{th}}^{\omega\delta/2\pi v_{th}} du e^{-u^2/2} \int_{-\infty}^\infty ds e^{-s^2/2} A^2. \quad (5.49)$$

A reasonable estimate for δ , ~ 1.5 cm, is found from the 1-D theory. The particular plasma properties give b , and the integral can be evaluated numerically. The result is included in Fig. 5.11 as the dashed line. The match with the simulation data gives credibility to the surface wave heating hypothesis. This result leads to greater heating for the same current and, therefore, a larger plasma resistance.

5.5 Collisionless Heating in a 2-D Idealized ICP Reactor

5.5.1 Simulation with Stationary Ion Background

The configuration of an idealized 2-D ICP reactor, simulated to observe collisionless heating effects, is shown in Fig. 5.12. The region to the left is the plasma. The electrons are particles while the ions are again represented as a uniform, stationary background of positive charge. The same sheath boundary condition as used in previous simulations (ie. all electrons specularly reflected at the walls) confines the electrons.

The four bounding walls of the reactor are conductors. The two internal structures on the right are current driven antennas which have peak currents in each of 13 A oscillating at a frequency of 10 MHz. The structure between the antennas and the plasma is a dielectric. The plasma density is 10^{11} cm $^{-3}$, and the temperature is 4.65 eV. The time step, $\Delta t = .5$ ns ($\omega_{pe}\Delta t = 8.9$), and spatial discretization, $\Delta x = .14$ cm ($\Delta x/\lambda_{De} = 27.6$), were chosen after simulations without driven fields bracketed the numerical energy conserving contour.

Figure 5.13 shows the structures of the reactor with superimposed contours of $E_{y,sol}$ at its maximum. $E_{y,sol}$ peaks between the driven antennas and falls off due to the conducting walls and the plasma. $E_{y,sol}$ drives a J_y in the plasma as evidenced by the circular pattern of the B-field vectors in Fig. 5.14. The B-field is not quite zero at the E-field peak because the driving antenna currents were gradually ramped up. This leaves an initial offset of the current out of phase with the oscillation.

As with the 1-D runs the kinetic energy of the electrons increased due to collisionless heating (see Fig. 5.15). For these plasma parameters β is 1.65 which gives $|E_y| / |B_z| = 3.6 \times 10^{-3}$ from the analytic theory of Eq. (5.25). At the center of the dielectric window on the plasma side, $|E_y| = 8 \times 10^{-3}$ statV/cm and $|B_z| = 3.3$ gauss which gives $|E_y| / |B_z| = 2.4 \times 10^{-3}$ showing some effect of the 2-D geometry. It is the power density into the plasma that is greatly affected in 2-D. From analytic theory the

power is 5.8×10^6 erg/cm²s while the measured power divided by the area of the dielectric window gives 4.2×10^5 erg/cm²s. The differences occur because of the decrease in E_{sol} near the bounding conducting walls in z and the finite extent of the plasma in x . This is a combination of the effects discussed in sections 5.4 and 5.2.3.

5.5.2 Simulation with Sheath and Plasma Absorption at the Walls

As a culmination of this investigation, this section presents a reactor simulation with mobile ions and absorbing walls in order to get a qualitative feel for DADIPIC's handling of the total reactor simulation. Collisions and an external circuit will not be included, but the reaction of DADIPIC to nonuniform plasma with internal structures and driven currents will be seen. The ion to electron mass ratio was set to 100 which allows a quick relaxation to equilibrium.

As mentioned in chapter 3, a sheath boundary condition is used to minimize any anomalous capacitive heating. Since the plasma is collisionless and not driven capacitively, the static collisionless sheath result[ton29], [sel63] is used as an estimate for the sheath voltage. At the edge of the sheath the ions have approximately reached the Bohm velocity[for88], $u_B = \sqrt{\kappa T_e/m_i}$. For a plasma where the sheath is narrow compared to the plasma width, the sheath potential is approximately[for88]

$$V_s = \frac{\kappa T_e}{2e} \ln \left[\frac{m_i}{2\pi m_e} \right]. \quad (5.50)$$

The width of the sheath is around 5 to $10\lambda_{De}$ which is significantly less than the cell width in the simulation.

Our simple unresolved sheath model has a form based on the requirement for equal ion and electron currents to the walls at equilibrium. Each conducting wall node has a given potential, $\phi(i, j)$. A sheath voltage, V_x , is defined as the difference between the voltage at the beginning of the sheath and the most positive wall node voltage, ϕ_{max} . As shown in Fig. 5.16, the various wall nodes may have different voltages resulting in larger potential drops near nodes with more negative potentials. A charge neutral plasma is initialized in the simulation. Since the electrons escape faster, the plasma rises to a positive potential with respect to the walls. When the average ion velocity reaches the Bohm velocity, u_B , at the edge of the plasma, a sheath is assumed to have formed which causes equal ion and electron currents out of the plasma. At each wall node the ion current density at the wall, J_i , is given by $n_{ion}(i, j)u_{\perp, ion}(i, j)$. The electron current density, J_e , reaching the wall through

the sheath is estimated as the outward flux from a Maxwellian distribution at the electron density of the presheath,

$$\begin{aligned} J_e &= n_e(i, j) \sqrt{\frac{\kappa T_e(i, j)}{2\pi m_e}} \exp\left[\frac{-e(V_s + \phi_{max} - \phi(i, j))}{\kappa T_e(i, j)}\right] \\ &= cden_e(i, j) \exp(-eV_s/\kappa T_e). \end{aligned} \quad (5.51)$$

Thus escaping current density has been reduced by the potential drop in the sheath. The total escaping ion and electron currents are found by summing over all the wall nodes. Equating these escaping currents, results in

$$\sum_{i,j} J_{ion}(i, j) = \exp\left(\frac{-eV_s}{\kappa T_e}\right) \sum_{i,j} cden_e(i, j). \quad (5.52)$$

The potential drop in the sheath is

$$V_s = \frac{\kappa T_e}{e} \left[\ln \left[\frac{\sum_{i,j} cden_e(i, j)}{\sum_{i,j} J_{ion}(i, j)} \right] - .5 \right]. \quad (5.53)$$

If the ion velocity falls below u_B at time step $n + 1$, V_s is slowly ramped down using $V_s^{n+1} = \alpha V_s^n$ where $\alpha \sim .9$ works well. Notice that V_s has been reduced by the Bohm potential to allow formation of the presheath in the simulation. This helps prevent the estimated V_s from being too large and retarding too many electrons. The resulting collapse of the charge imbalance would eliminate the presheath potential drop, and the ions would no longer accelerate to u_B . At this point the algorithm would drive V_s to zero, resulting in a numerically noisy, large change in V_s that is undesirable.

Once V_s is known, boundary conditions for the fields and particles must be determined. The potential given by $\Phi(i, j) = V_s + \phi_{max} - \phi(i, j)$ is the potential at the plasma side of the sheath at node i, j . $\Phi(i, j)$ is the Dirichlet value set for node i, j in the implicit electrostatic field equation, Eq. (2.7). After solving Eq. (2.7), the E-field normal to the surface is found with the first order differencing

$$E_{\perp}(i, j) = -\frac{\phi(idel, jdel) - \Phi(i, j)}{\Delta}. \quad (5.54)$$

The node inside the plasma next to the surface node is at $idel$ and $jdel$, and Δ is either Δx or Δz depending on the normal direction to the surface.

The particle boundary condition depends on the particle type and energy. Since the sheath accelerates ions, any ions which pass through a structure boundary are absorbed.

Those electrons which have a velocity toward the wall greater than $\sqrt{2e\Phi(i,j)/m_e}$ are also absorbed. All other electrons are specularly reflected by the sheath.

The generation of plasma through ionizing collisions is modeled by a uniform injection of electron/ion pairs across the plasma region. The velocity distribution is obtained by the standard Monte-Carlo technique for generating a Maxwellian distribution

$$\begin{aligned}
 v_{\perp} &= v_{th} \sqrt{-2 \ln(1 - R_1)} & \theta_1 &= 2\pi R_2 \\
 v_{\parallel} &= v_{th} \sqrt{-2 \ln(1 - R_3)} & \theta_2 &= 2\pi R_4 \\
 v_x &= (u_{\parallel} v_{th} + v_{\perp}) \cos \theta_1 \\
 v_z &= (u_{\parallel} v_{th} + v_{\perp}) \sin \theta_1 \\
 v_y &= v_{\parallel} \cos \theta_2
 \end{aligned} \tag{5.55}$$

where the R_i are random numbers between 0 and 1. In this way a Maxwellian distribution is injected in y, but a minimum speed, u_{\parallel} , greater than zero is ensured in the x,z plane. Since only the tail electrons are lost through the sheath, the injected electrons must have enough energy to get over the sheath. This maintains particle balance keeping the plasma density constant.

The system will reach equilibrium when particle balance and power balance is reached as explained in section 5.1. The flux lost to the walls can be estimated from collisionless analytic theory [for88] and get a particle creation rate from the particle balance equation

$$g = .688 n_e \sqrt{\frac{2\kappa T_e}{m_i} \frac{SurfaceArea}{Volume}}. \tag{5.56}$$

Since the particles injected do not exactly replace the tail in the Maxwellian, this creation rate will not initially maintain a constant plasma density. The plasma temperature will also change as the energy lost by particles absorbed at the walls balances with the energy injected with the created particles and gained by the electrons through stochastic heating.

The same simulation as specified at the beginning of this section was run with the addition of the sheath boundary condition and volume injection of particles. The simulation was run for 500 ns, five rf periods, to observe the evolution of the system. The electron density and potential profiles in the plasma are shown in Figs. 5.17 and 5.18. As expected, the plasma has risen to a positive potential, and the electron density follows the shape of that potential. The density has changed only $\pm 20\%$ from the initial 10^{11} cm^{-3} . Both the electron

and ion particle number in the simulation decreased $\sim 20\%$ from their initial number of 30000. The noise due to particle fluctuations is evident in both plots. Notice, a Dirichlet zero boundary condition has been imposed on ϕ for all nodes outside of the plasma region. The solenoidal E-field, resulting from current driven in the antenna structures, is shown in Fig. 5.19. It maintains a significant magnitude right up to the conducting surfaces in the vacuum but is falls off quickly in the plasma region. The magnitude of E_{sol} fluctuations is quite small compared to the peak of the field. The field retains essentially the same shape as that in the uniform plasma reactor simulation at the beginning of this section; therefore, the stochastic heating power absorbed should also be about the same.

Particle energy time histories of Fig. 5.20 indicate that the plasma is approaching equilibrium. The electrons lost energy due to the decrease in their number and the energy given to the ions by the accelerating sheath. The average power lost to the walls was $\sim 6 \times 10^8$ erg/s while the stochastic heating reported in section 5.5.1 was $\sim 1.7 \times 10^6$ erg/s. Thus almost all of the power is being injected with the particles. Given the plasma parameters and field magnitude the collisional heating would have a maximum around 1.5×10^7 erg/s.

Obviously, much more energy is purposely being put into the particles than would be expected from the available heating processes. In actual reactors the ratio m_i/m_e is larger (36720 for Ar) leading to much smaller flux ($\sim .05$) and thus power ($\sim 2.5 \times 10^{-3}$) absorbed at the walls. In addition the ratio of surface area to volume is smaller resulting in a smaller ionization rate to maintain the same plasma density. u_{\perp} could also have been set smaller, and the injected particles would still have enough energy to get over the analytic sheath barrier. For this reason the power to the walls would be much less than present in this simulation, and physical heating mechanisms would be more than sufficient to balance the power absorbed at the walls. This simulation simply serves as an example of DADIPIC's ability to simulate all the relevant phenomena while allowing a quick relaxation to equilibrium with $m_i/m_e = 100$. Plus, the injected particles were intentionally given high energies to highlight some points about these types of simulations.

In Fig. 5.21 is have a comparison of V_s time histories from three different simulations. All three have similar plasma parameters, but the first two are 1-D with 14 cm lengths (100 cells) while the third is the 2-D simulation described above. The first has 50 particles per cell, the second has 250 particles per cell, and the 2-D run has 32 particles per cell. V_s collapses occasionally in the two 1-D simulations. The collapse of V_s occurs when the ion velocity falls below u_B . The drop below u_B is due to fluctuations in the overall po-

tential profile which cause fluctuations in the ion velocity. The potential fluctuates more in the 1-D simulations even though those simulations have more particles per cell because the global potential profile is determined by the difference between the total ion and electron numbers not the number of particles per cell. The number of particles per cell only affects the fluctuations from cell to cell which appears as noise superimposed over the general shape of the potential profile.

For these three simulations, the average difference between ion and electron numbers is 12, 120, and 680 respectively. To find the fluctuation in these numbers from time step to time step, consider the average number of particles for each species being absorbed at the walls each time step. For the three simulations these were 2.8, 14, and 64. Assuming a Gaussian distribution for the variation in these quantities (\pm the square root of the average), we find that the particle differences can vary by ± 3.3 , ± 7.5 , and ± 16 or fractional variations of $\pm .28$, $\pm .063$, and $\pm .023$. The large fractional change in net charge in the first simulation leads to significant changes in the potential profile which in turn causes the random drops in V_s . Thus for meaningful simulations we must not only consider the number of particles per cell but also the net difference between particle species.

The electron velocity distribution for the 2-D simulation of Fig. 5.22 along with the potential plot of Fig. 5.18 indicate some of the limitations of an analytic sheath boundary condition. The retarding potential is substantially larger than V_s . The cause is the assumption in the unresolved sheath boundary condition of a Maxwellian distribution while the actual electron distribution is substantially different than a Maxwellian. A more sophisticated model could find the flux to the wall versus V_s from the actual particle distribution. Assuming little change in the distribution from time step to time step, the distribution could be calculated only every few time steps (10 to 50). In this way the code would not be slowed from a velocity binning of the particles every time step.

5.6 ICP Reactor Simulation

Up to this point the DADIPIC method has been developed, implemented, and characterized as a technique for simulating the particles and fields in a low frequency, kinetic plasma. In this chapter it is shown that the method is ideally suited for the phenomena in ICP sources. Although these were the goals of the dissertation as stated in the introduction, this final section was included to provide a road map to a complete ICP simulation

methodology with DADIPIIC as the plasma/field solution algorithm.

5.6.1 Simulation Methodology

Many authors have developed models for ICPs over the years. The basic idea is to model the circuit driving the rf antenna and to couple a load representing the plasma to the circuit. The coupling and complex impedance of the load depend on the antenna and plasma geometries as well as the plasma properties. Most analytic models consider cylindrical ICPs driven by solenoidal or helical coils which allows the simplifying assumption of cylindrical coordinates with only radial spatial variation of quantities.

The first step in determining the plasma impedance is to determine the field variation in the plasma. In an early calculation Thomson[tho27] considered a uniform plasma with a real plasma conductivity. Later authors such as Eckhert[eck62] and Henriksen, et. al.[hen71] included finite collision frequency and assumed, nonuniform density profiles. As shown in the previous section, kinetic effects have been considered by several authors. A recent analytic model has included the collisionless heating in nonuniform ICPs with a planar coil; however, the results were obtained with an assumed, not self-consistent solution of the field profiles[vah94].

Once the field variation, driven current densities, and absorbed power are determined as functions of rf frequency, density, temperature, and collision frequency, the corresponding resistance and inductance of the plasma can be found. Denneman[den90], Godyak, et. al.[god94], and others have coupled the plasma impedance into circuit models for the whole ICP system by treating the plasma as a single turn secondary winding of a solenoidal transformer. This is a reasonable description for a collisional, cylindrical plasma with a small skin depth compared to its radius. The driven current exists in a thin annular region at the plasma surface (see Fig. 5.23). Given the models, experimentally measured currents and voltages in the driving circuit were used to find the plasma properties.

More complex geometries and self-consistent calculations of plasma parameters require the use of computer models. Codes, which solve for electromagnetic fields given the positions of conducting and dielectric structures and the antenna frequency, have been used to find the field profile by assuming the analytic form for the plasma conductivity[hop92], [hop93]. Codes are being developed to include the external circuit along with the actual reactor layout to determine power deposition[ste93]. Other codes model the plasma as a time

evolving fluid so the plasma density profile and temperature can be found self-consistently given the driving fields[dip94d]. All of the processes mentioned at the end of section 5.1 are included except stochastic heating. Another issue which must be dealt with in these codes is modeling the electrostatic sheaths[met86], [dip94a]. Discretization fine enough to resolve the sheath would be computationally prohibitive, and with quasi-neutral codes[dip94d] a true electrostatic field does not exist.

One could include the stochastic heating with a kinetic code such as DADIPIC. The electron-neutral collisions can be modeled by adding a PIC Monte-Carlo Collision (PIC-MCC) routine[bir91], [vah93] to the basic algorithm. Unfortunately, even the reduction in computational expense of DADIPIC over an explicit PIC code is insufficient for simulating these reactors to equilibrium. The ions are so slow that many hundreds of rf cycles may be required before equilibrium is reached. Since tens of time steps are required per rf cycle (irrespective of the plasma frequency), the cpu time for a particle simulation would be prohibitive.

Attempts have been made to include the stochastic heating in analytic fluid models by equating the analytic form for power deposition in a fluid, Eq. (5.14), to the power deposition due to stochastic heating[vah94], [lie94]. Solving this equation for the collision frequency results in a ν_{eff} to be used in the fluid model in place of the actual ν_{ne} . While this approach obtains the correct value for the real part of the plasma impedance, it does not account for the change in the imaginary part due to the collisionless effects. So the driving will still have an incorrect loading. In addition the appropriate ν_{eff} must be determined. A methodology is described below for using fluid and kinetic simulations in concert to overcome these problems and to model the ICP.

The methodology involves two codes. The first is a time-dependent simulation code, CI, which allows arbitrary configurations for conductors and dielectrics along with the option for a fluid or kinetic description of the different species in the plasma. Proper boundary conditions for fields and plasma as well as an external circuit connected to the driving antenna are required. The external circuit is connected to the impedance shown in Fig. 5.23 where Z_{icp} includes the plasma, the ICP reactor chamber, and the antenna. The power and circuit quantities are related through the equations

$$\mathcal{P}_{abs} = \frac{1}{2}|I|^2 R \quad (5.57)$$

$$V = I|Z| \quad (5.58)$$

where $R = \text{Re}\{Z\}$ and $L = \text{Im}\{Z\}$. Since the DARwin Direct Implicit field solution technique is still valid when particles are replaced by fluids, the DADIPIIC method could be used for the plasma and fields in such a code. The advantages of DADIPIIC fields are gained without the computational overhead of particles. Another option is to use a quasi-neutral code which adds complications in dealing with electrostatic sheaths.

CI is run in its fluid form to equilibrium. At this point the kinetic form is initialized with a frozen ion density background and electron particles with the correct profile and temperature. The electrons are reflected at the bounding walls, and only elastic collisions are included. In this way the power into the plasma due to collisional and stochastic heating can be measured as the change in kinetic energy of the electrons. The value of Z_{icp} can be found from a calculation which accounts for kinetic effects through the equations

$$R_{icp} = 2\mathcal{P}_{abs}/|I_{rf}|^2 \quad (5.59)$$

$$L_{icp} = \sqrt{|V_{rf}/I_{rf}|^2 - R_{icp}^2} \quad (5.60)$$

Now the second code, CII, which is a time-independent coupling code, is used. Time-harmonic dependences for currents and fields and a complex, collisional conductivity for the plasma are assumed. The plasma density and temperature again come from the fluid result of CI. The conductivity is taken to be

$$\sigma_{eff} = \frac{\kappa\omega_{pe}^2 \nu_{eff} - i\omega}{4\pi \nu_{eff}^2 + \omega^2} = \kappa\sigma(\nu_{eff}) \quad (5.61)$$

where $\sigma(\nu)$ was derived in section 5.2. With σ_{eff} two variables are available to change in order to match R_{icp} and L_{icp} with the fluid description. The terms ν_{eff} and κ are varied until the match is achieved. This tunes the complex impedance of the fluid plasma so it is equivalent to the impedance of the kinetic plasma. The spatial distribution of the fields and currents will be nearly the same. Certainly matching the complex impedance will be more correct than those methods which only match R_{icp} . The time-independent algorithm is used so that the κ and ν_{eff} parameter space can be quickly searched to find the optimum values. The search could be performed with a routine similar to the Monte-Carlo routine in appendix A used to find the root of the dispersion relation over the complex ω plane.

Now return to the fluid code. The values of κ and ν_{eff} are used in the fluid momentum and energy transport equations,

$$\dot{\mathbf{V}} + (\mathbf{V} \cdot \nabla)\mathbf{V} + \frac{q}{m} \left[\kappa\mathbf{E}_{sol} + \mathbf{E}_{irr} + \frac{\mathbf{V} \times \mathbf{B}}{c} \right] + \nabla p = -\nu_{eff}\mathbf{V} \quad (5.62)$$

and

$$\dot{T} + \nabla \cdot (\mathbf{VT}) - \frac{2}{3}T\nabla \cdot \mathbf{V} = \frac{2Q}{3n} \quad (5.63)$$

to get the proper effect on the fluid current and energy. Q is the heat generated due to collisions between unlike particles and contains the thermal conductivity and resistivity which depend on ν_{eff} . DiPeso, et. al[dip94d] gives a form for Q applicable for these types of simulations. κ changes the magnitude of the force on the fluid caused by the E-field without changing the field itself. Note that we need only change the value of ν_{eff} and add κ in the direction of the driven field; thus, the diffusion and E-field force will be unaffected in the other directions. The force from the B-field and electrostatic field are never affected. In 2-D the driven field is usually out of the simulation plane so ν_{eff} would not affect diffusion in the simulation.

We can again run the fluid code to equilibrium and repeat the whole process until the plasma characteristics show sufficiently small change. Initial estimates for κ and ν_{eff} can be found using results from the 1-D kinetic theory of section 5.2. Such a process would allow us to find general trends in ICP reactors and to investigate the effects of novel ideas without the need to build and experiment with many different reactors.

Another use of the kinetic portion of CI would be to determine the velocity distribution of the electrons in the reactor. Given the result from the fluid simulation or given density and temperature profiles from an experiment, the kinetic simulation could be initialized with immobile ions. In this case the electrons are allowed to be absorbed at the bounding walls. Ionizing and excitation collisions with the neutrals are included in the PIC-MCC package in addition to the elastic collisions. Since the ions are immobile, the simulation is run only long enough for the electrons to reach an equilibrium distribution. The resulting electron velocity distribution could then be used to help diagnose experimental results or calculate corrected collision rates for fluid simulations. As before an iteration between fluid and kinetic simulation would be necessary for the purely numerical investigations. For ion profiles obtained from experiment no further simulation is necessary.

5.6.2 Example of Methodology using Analytic Theory

In this section we will gauge the difference in the plasma impedance between a fluid and kinetic description for a uniform, cylindrical plasma. This will give us an idea of the magnitudes required for κ and ν_{eff} and the importance of collisionless heating. The

coupling analysis is similar to that found in Denneman[den90], Piejak, et. al.[pie92], and Lieberman[lie94]. For simplicity assume the plasma radius, r , is much greater than the skin depth so the 1-D Cartesian theory developed earlier can be used. A solenoidal coil of radius b with N turns is wrapped around the plasma.

The power into the fluid plasma is given by

$$\mathcal{P}_{abs} = S_x A. \quad (5.64)$$

A is the surface area $2\pi r l$, and S_x is given by Eq. (5.14). The current is

$$I_p = \int_0^l dz \int_0^\infty dx \frac{\omega_{pe}^2 E_o}{4\pi} \frac{\nu - i\omega}{\nu^2 + \omega^2} e^{-x/\delta} = \frac{\omega_{pe}^2 E_o l \delta}{4\pi} \frac{\nu - i\omega}{\nu^2 + \omega^2}. \quad (5.65)$$

Equating the power of Eq. (5.64) to that of Eq. (5.57), we find the plasma resistance

$$R_p = \frac{4\pi^2 \nu r}{\omega_{pe}^2 \delta l}. \quad (5.66)$$

Since an N turn solenoid has the B-field

$$B_z = \frac{4\pi N I}{c l}, \quad (5.67)$$

the inductance matrix components are[rei79]

$$\begin{aligned} L_{11} &= \frac{4\pi^2 b^2 N^2}{c l} \\ L_{12} = L_{21} &= \frac{4\pi^2 r^2 N}{c l} \\ L_{22} &= \frac{4\pi^2 r^2}{c l}. \end{aligned} \quad (5.68)$$

The voltages obey the equations

$$V_{rf} = i\omega L_{11} I_{rf} + i\omega L_{12} I_p \quad (5.69)$$

$$V_p = i\omega L_{21} I_{rf} + i\omega L_{22} I_p. \quad (5.70)$$

Since $V_p = -I_p R_p$, the above equations give $Z_{icp} = V_{rf}/I_{rf}$. The result is

$$R_{icp} = R_p N^2 \left[\frac{1}{1 + (c^2 l R_p / (4\pi^2 r^2 \omega))^2} \right] \quad (5.71)$$

and

$$L_{icp} = \frac{4\pi^2 r^2 N^2 \omega}{c^2 l} \left[\frac{b^2}{r^2} - \frac{1}{1 + (c^2 l R_p / (4\pi^2 r^2 \omega))^2} \right]. \quad (5.72)$$

Table 5.1: Impedance of the example ICP

	R_p	R_{icp}	L_{icp}	ν/ω	κ	ν_{eff}/ω	ν_{eff}^*/ω
ν only	6.47×10^{-13}	1.62×10^{-11}	1.402×10^{-10}	.2	—	—	—
κ, ν_{eff}	13.5×10^{-13}	3.37×10^{-11}	1.407×10^{-10}	—	1.06	.439	—
ν_{eff}	15.4×10^{-13}	3.85×10^{-11}	1.408×10^{-10}	—	—	—	.510

The power including stochastic heating, $S_x^{stoc} A$ is found from eq. (5.28). Integrating the current density Eq. (5.35), we find the corresponding current, I_{stoc} . In this case the plasma resistance is

$$R_p^{stoc} = \frac{2S_x^{stoc} A}{|I_{stoc}|^2}. \quad (5.73)$$

We can find κ and ν_{eff} from

$$S_x^{stoc} = \frac{(\omega_{pe}\kappa E_o)^2}{16\pi} \frac{\delta\nu_{eff}}{\nu_{eff}^2 + \omega^2} \quad (5.74)$$

and

$$|I_{stoc}|^2 = \frac{\omega_{pe}^4 \kappa^2 E_o^2}{16\pi^2} \frac{l^2 \delta^2}{\nu_{eff}^2 + \omega^2} \quad (5.75)$$

where δ is defined by Eq. (5.13). If we simply tried to match the S_x^{stoc} with a ν_{eff}^* , we would have used

$$S_x^{stoc} = \frac{(\omega_{pe} E_o)^2}{16\pi} \frac{\delta\nu_{eff}^*}{(\nu_{eff}^*)^2 + \omega^2}. \quad (5.76)$$

This leads to a different $|I_{stoc}|$ and thus a different R_p^{stoc} .

Consider the plasma of section 5.2 with $n_p = 2 \times 10^{11} \text{ cm}^{-3}$, $f = 10 \text{ MHz}$, $T_e = 3.75 \text{ eV}$, $\nu/\omega = .2$, $r = 30 \text{ cm}$, $l = 30 \text{ cm}$, $b = 31 \text{ cm}$, and $N = 5$. Table 5.1 shows the results for the circuit when only collisional heating is included, when fluid theory is set to match S_x^{stoc} and I_{stoc} , and when fluid theory is set to match only S_x^{stoc} .

As shown in the table, the inclusion of stochastic heating caused a factor of two change in R_{icp} . The use of κ and ν_{eff} made a slight refinement in Z_{icp} ($\sim 15\%$) versus the use of ν_{eff}^* alone. For this geometry R_p and the exact plasma current profile have little impact on L_{icp} . For cases where δ is significant compared to the reactor dimensions, the collisionless effects would impact L_{icp} as well as R_{icp} .

5.7 Summary

As we have seen collisionless heating plays an important role in the operation of ICP sources for plasma processing. Changes to the power absorbed by the plasma can affect the plasma density, uniformity, and sheath magnitude all of which are critical when processing material surfaces. The DADIPIC method has proven its ability to simulate the collisionless heating in such reactors because of its correct modeling of the kinetic effects and its freedom from plasma frequency time step constraints. With DADIPIC we can investigate the nonlinear B-field effects which can reduce the heating even for driving fields typically found in reactors. New combinations of effects can be found such as the surface wave heating of section 5.4. Here the 2-D configuration and B-field interact leading to more heating than would otherwise be expected.

Finally, it was shown that DADIPIC can serve as the core plasma/field algorithm which an ICP simulation code can be built around. PIC-MCC for collisions, an external circuit for the antenna, and a sheath model for the walls can all be added given DADIPIC's inherent flexibility and ability to handle bounded plasmas. The field algorithm could also be used with fluids for the plasma species if even faster run times were desired. The kinetic simulation of these ICP sources would not be possible without DADIPIC's combination of kinetic, low frequency, electrostatic, and magneto-inductive simulation.

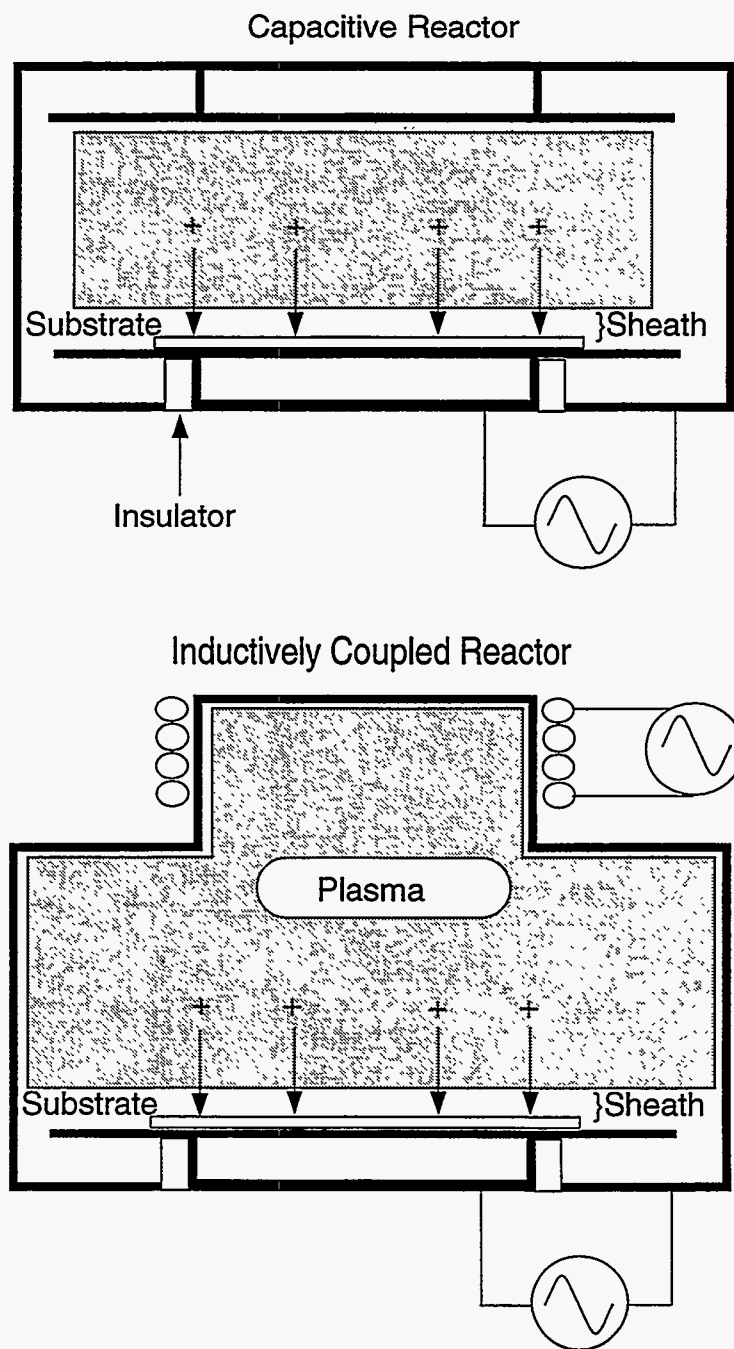


Figure 5.1: Idealized capacitively and inductively driven plasma reactors. The rf source drives electrostatic fields between the parallel plates of the capacitive reactor and inductive fields along the coiled antenna of the inductive reactor. The reactors are typically cylindrically symmetric.

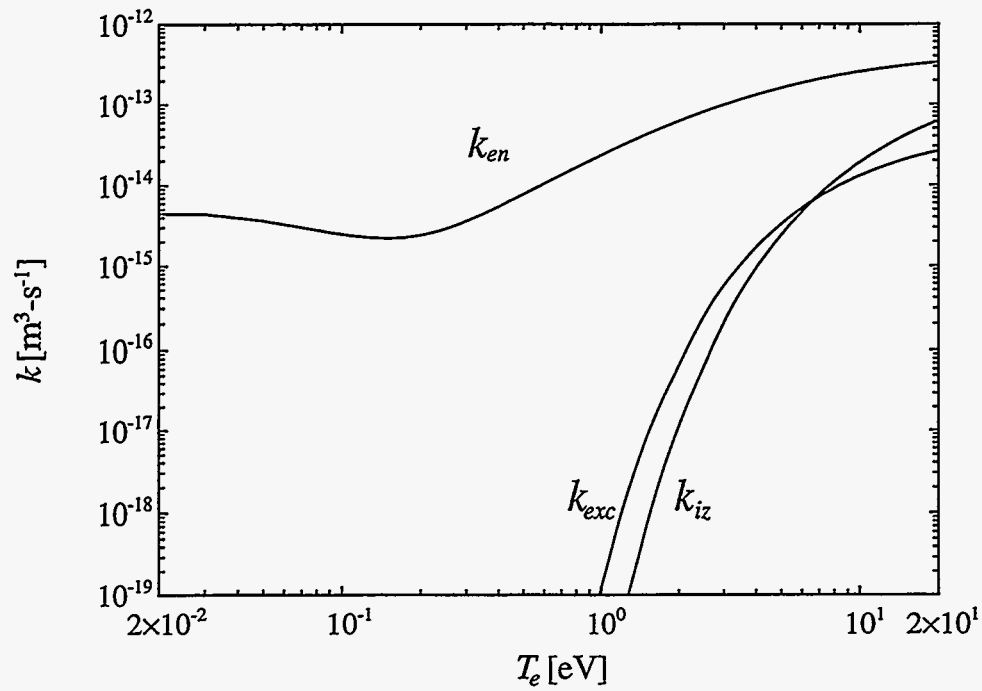


Figure 5.2: Ionization rate constants ($\# \text{ cm}^3/\text{s}$) in Ar versus electron temperature of a Maxwellian distribution from Vahedi[vah93].

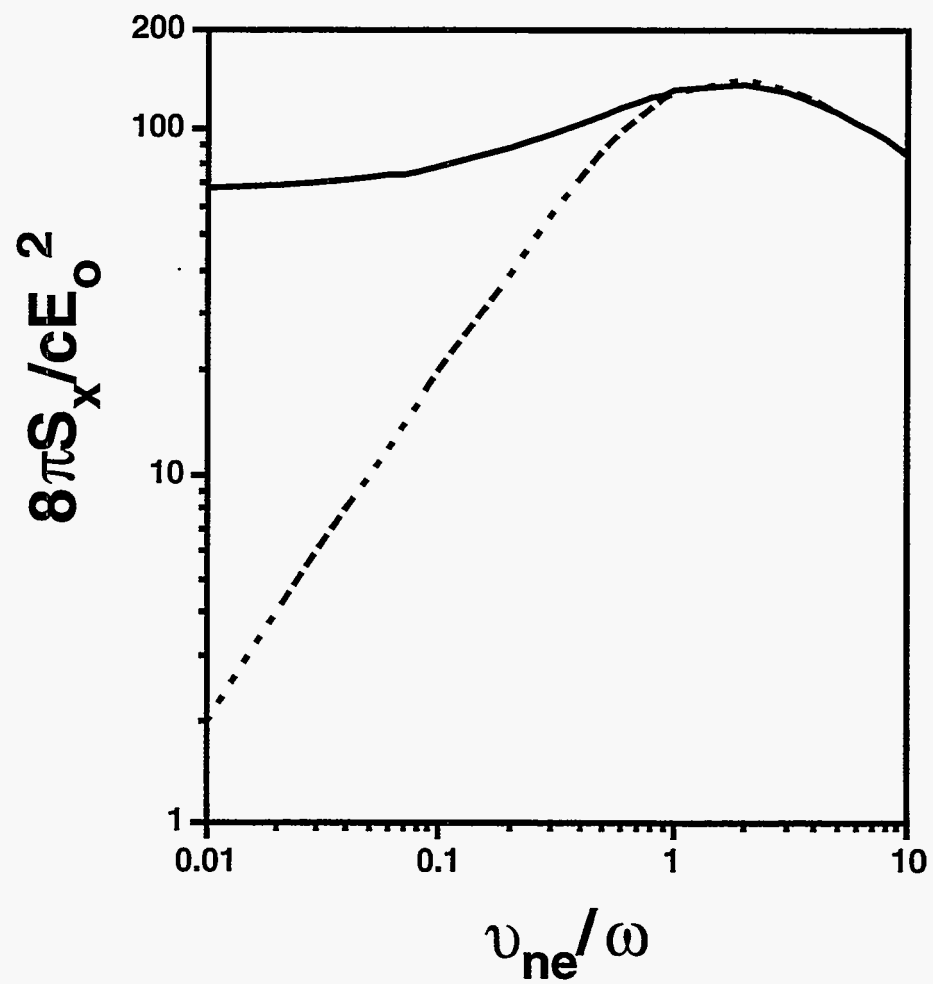


Figure 5.3: Comparison of the fluid and kinetic theories for the power deposition into a plasma versus ν/ω .

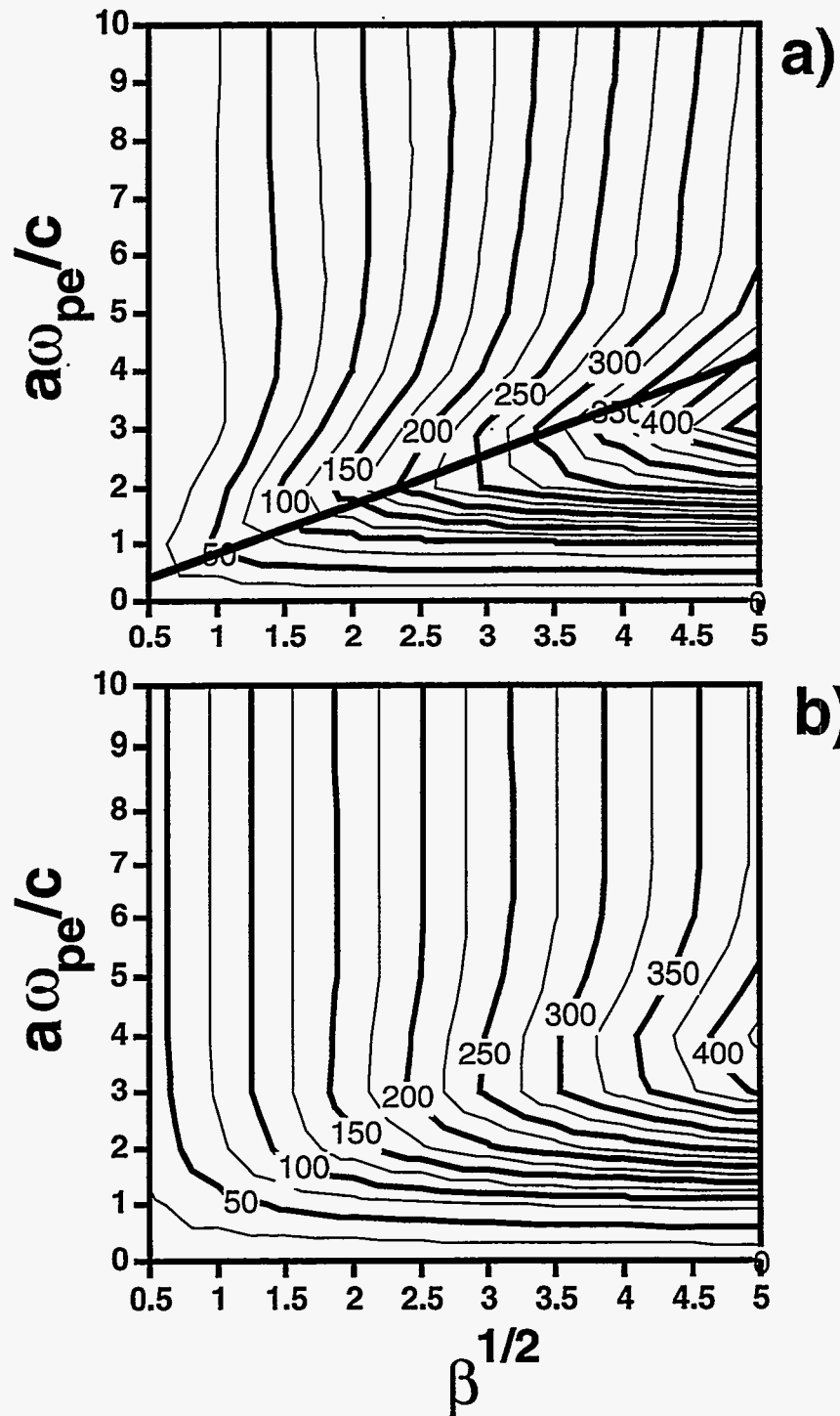


Figure 5.4: Contour plot of the power into a finite plasma slab versus the slab width, a , and the skin depth transit parameter, β : a) $\nu/\omega = 0$ and b) $\nu/\omega = 1$. The line across a) is for an electron with $\langle |v_x| \rangle = 2a\omega/\pi$.

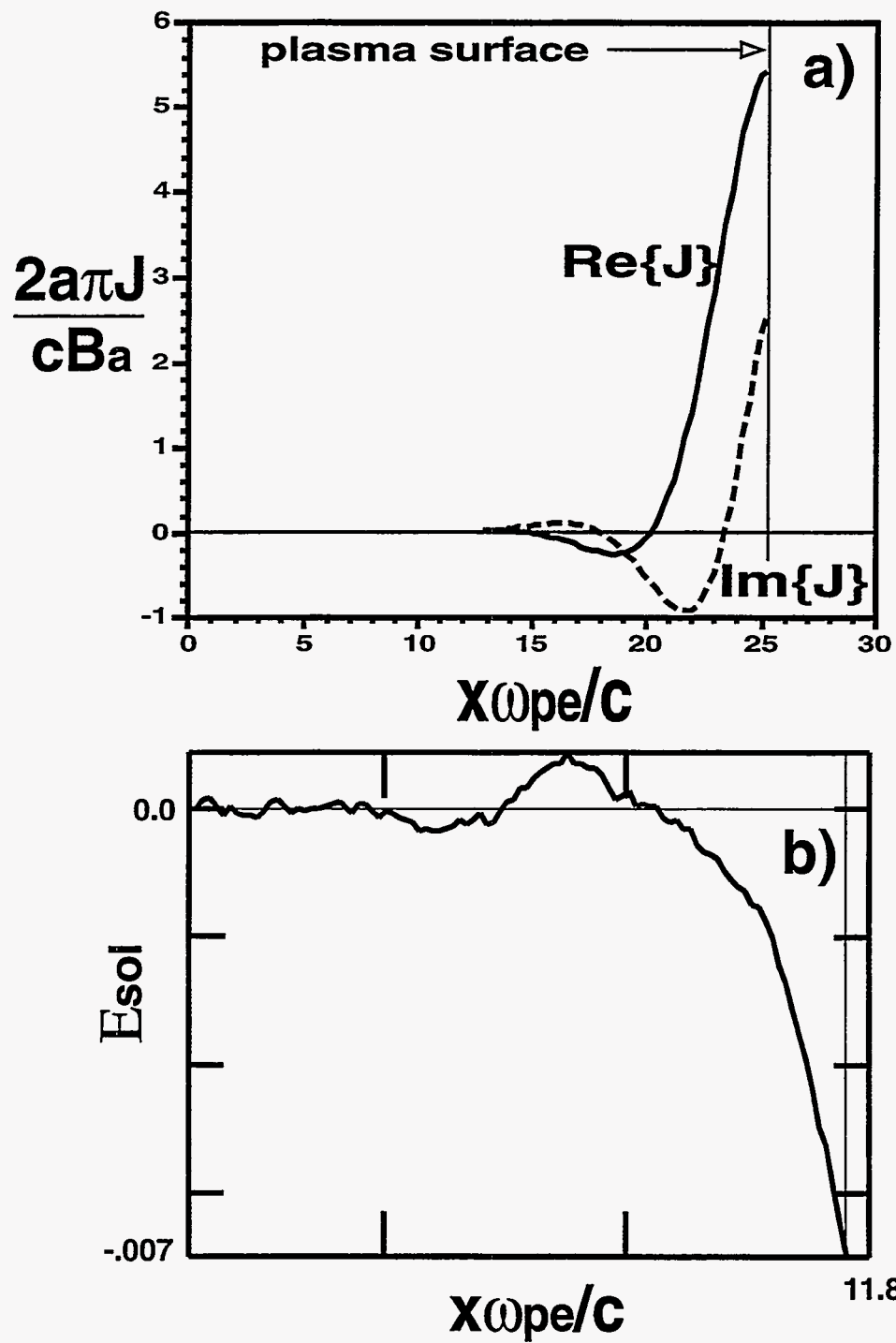


Figure 5.5: Current density versus position from theory and driven E-field versus position from DADIPIIC calculation for finite plasmas.

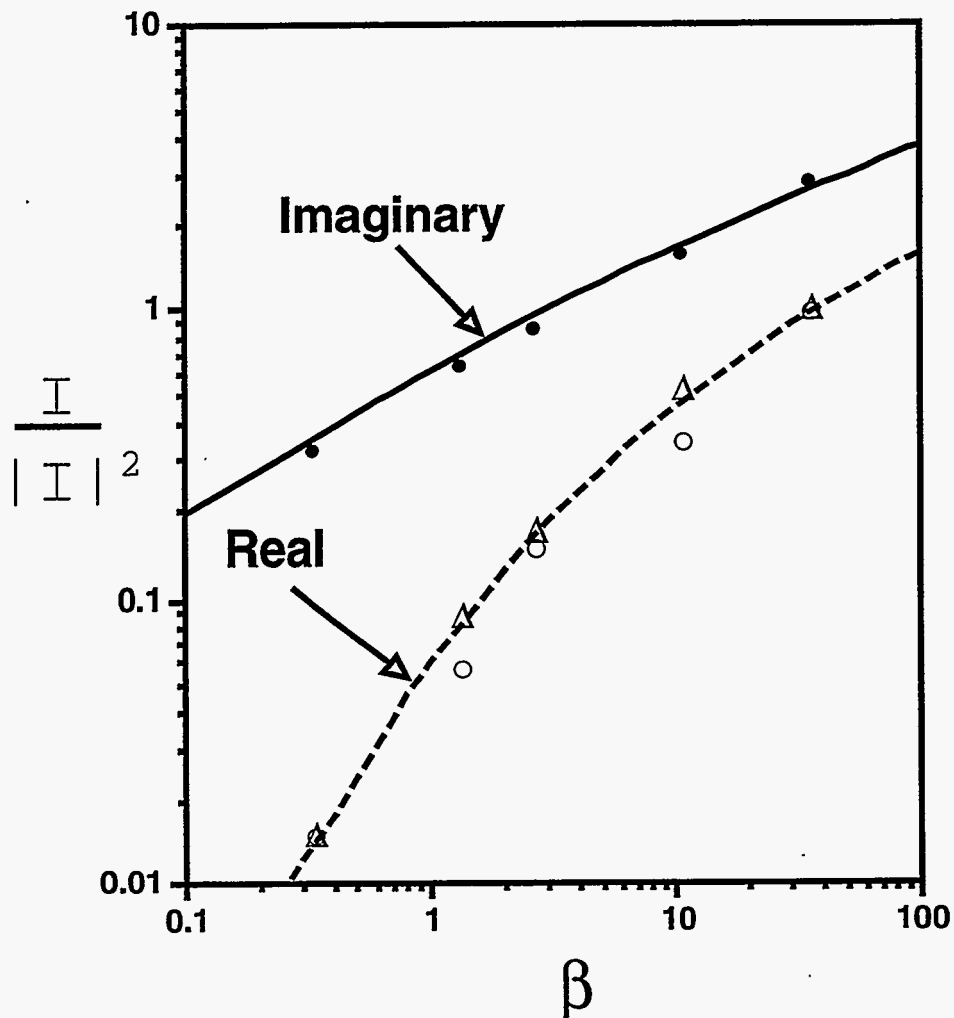
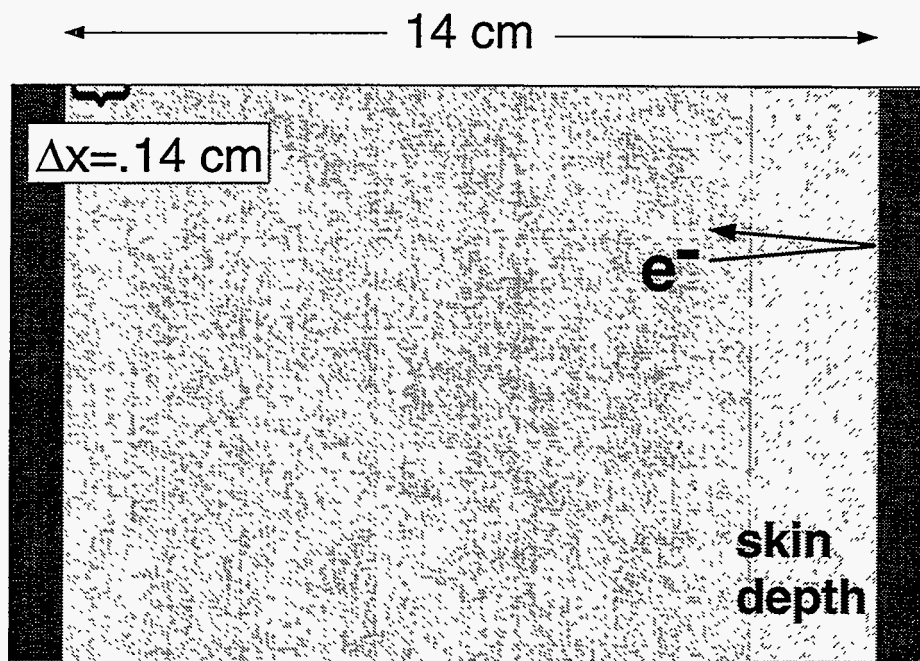


Figure 5.6: The real and imaginary parts of $I/|I|^2$. The dots and circles are from simulations with the B-field while the Δ s are for simulations where the B-field was turned off.



Conducting Wall:

$$E_{y,sol} = E_0 \cos(\omega t)$$

$$A_y = 0$$

$$\Phi = 0$$

$$E_{irr} = 0$$

Figure 5.7: Picture of the simulation region for the 1-D DADIPIC simulations of inductively couple plasma heating. E_y is specified on the conducting wall while conducting surface boundary conditions are used for all other field quantities. Electrons are specularly reflected off the walls.

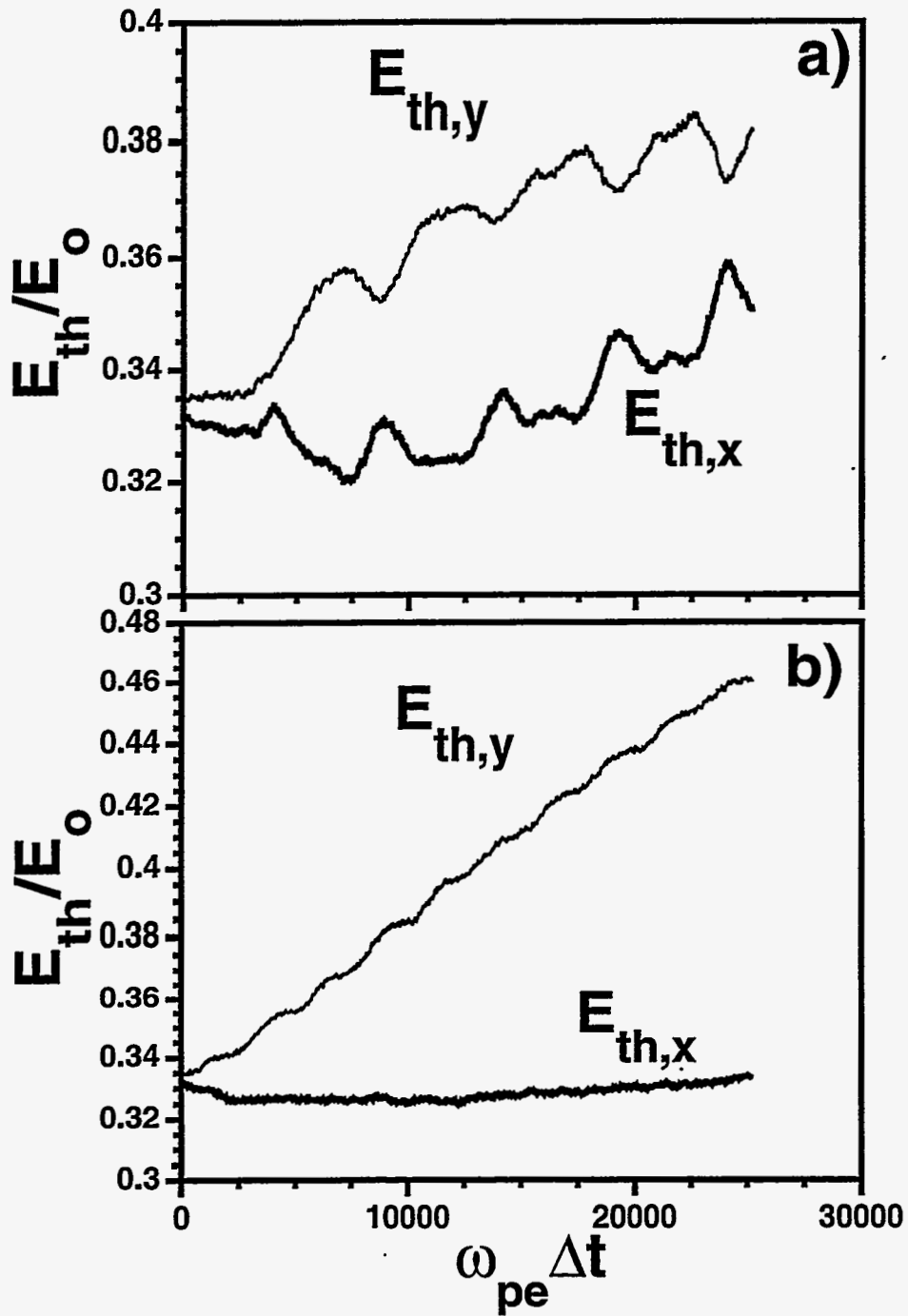


Figure 5.8: Change in the electron thermal energy in the x and y directions for 1-D simulations: a) B-field included in the simulation and b) B-field not included. Essentially no heating occurs in the direction normal to the driven field without the B-field.

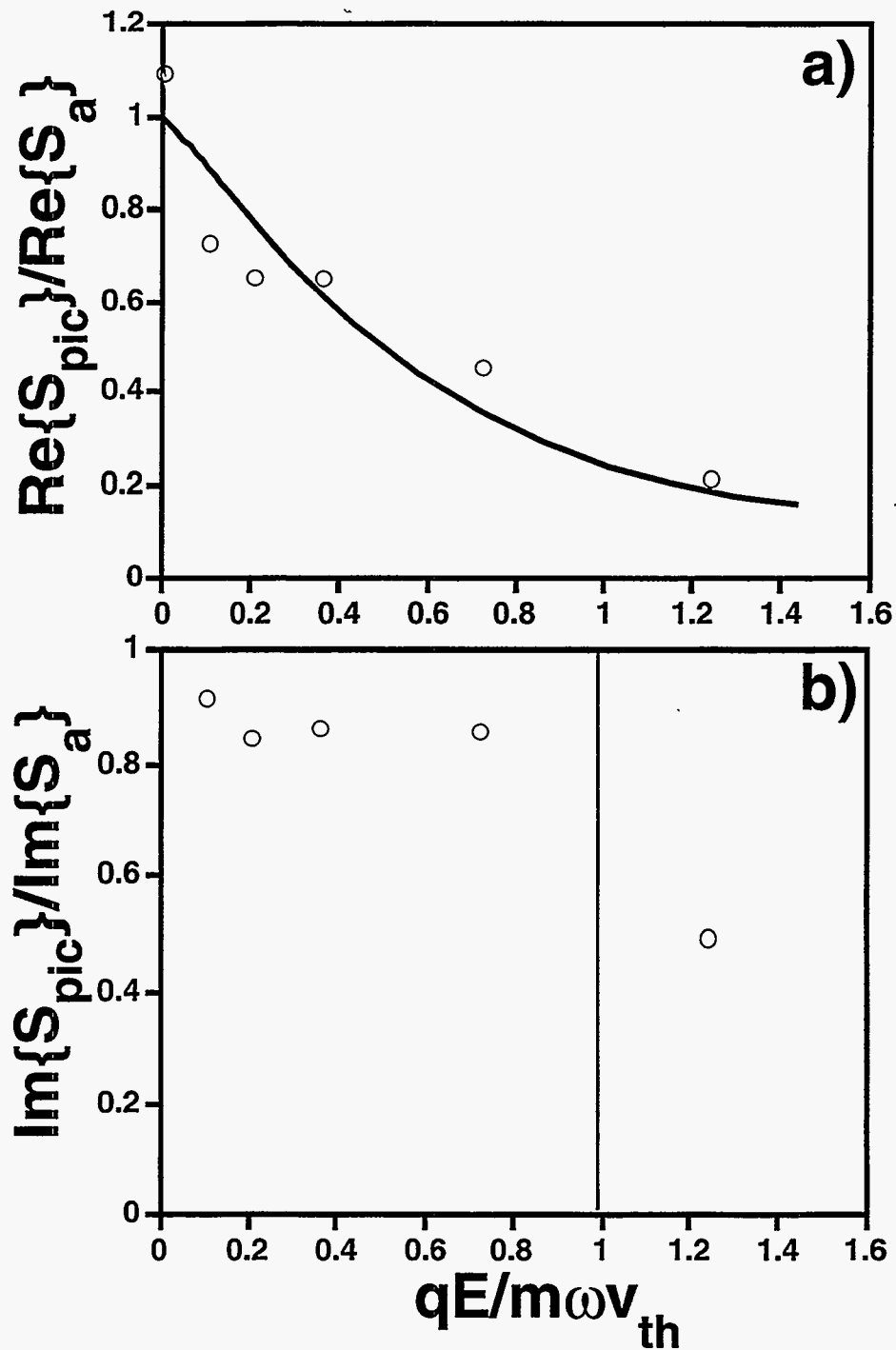
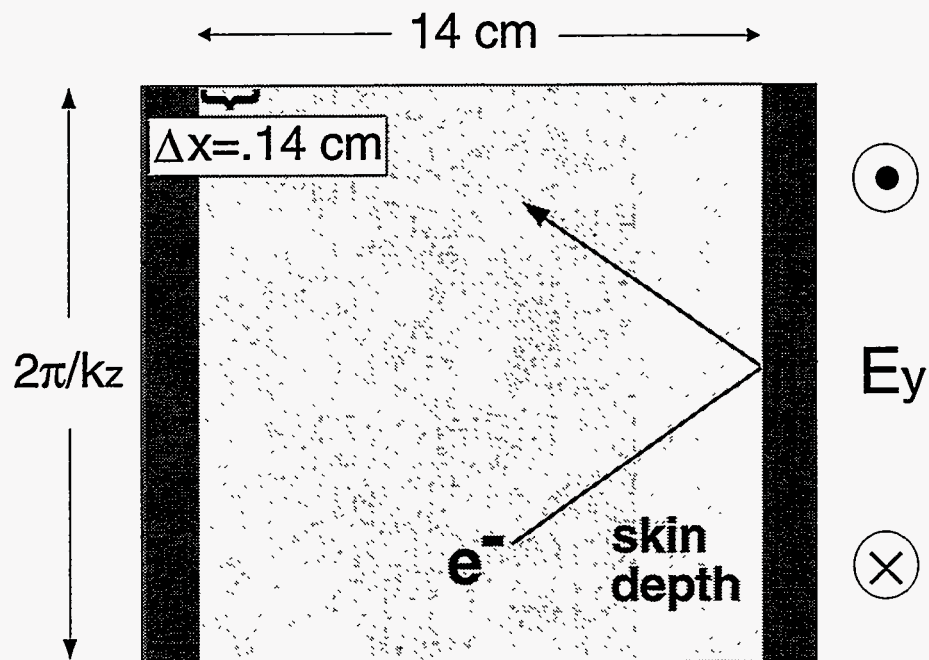


Figure 5.9: $I/|I|^2$ normalized to the vanishingly small driven field value versus v_{osc}/v_{th} : a) the real part and b) the imaginary part. The circles are simulation results. The line in a) is the reduction in electron flux to the wall due to the B-field. The line in b) is where $v_{osc}/c \sim |E_y|/|B_z|$.



Conducting Wall:

$$E_{y,\text{sol}} = E_0 \sin(kz) \cos(\omega t)$$

$$A_y = 0$$

$$\phi = 0$$

$$E_{\text{irr}} = 0$$

Figure 5.10: Picture of 2-D periodic simulations where the driven inductive E-field has a sinusoidal variation in z .

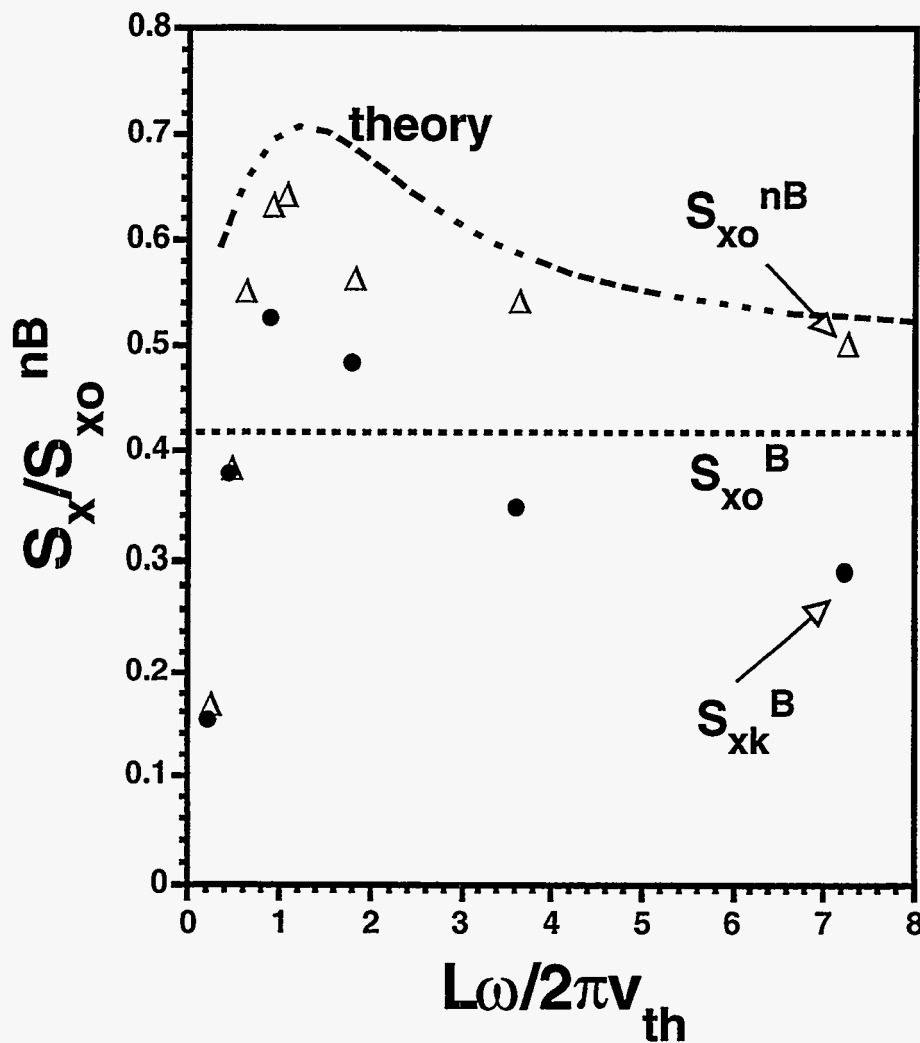


Figure 5.11: Results of the 2-D simulations with the spatial variation of the driving field parallel to the wall. The powers are normalized to the simulation with $k_z = 0$ and the B-field turned off. Simulations without the B-field are Δ s, simulations with the B-field are dots, and the simulation with the B-field and $k_z = 0$ is the horizontal line. Theory not including the B-field is the dashed line.

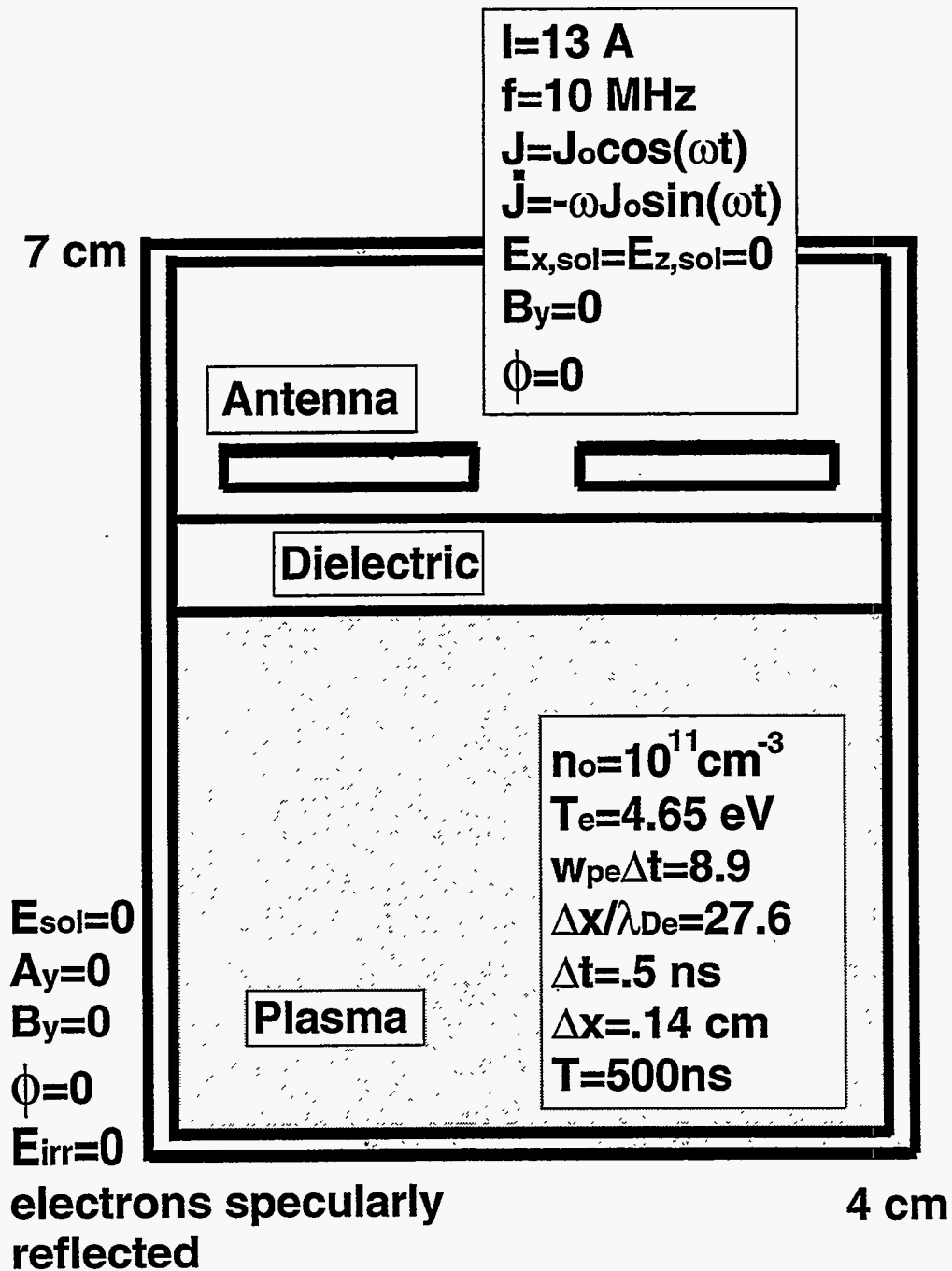


Figure 5.12: Picture of the 2-D inductively coupled reactor simulation.

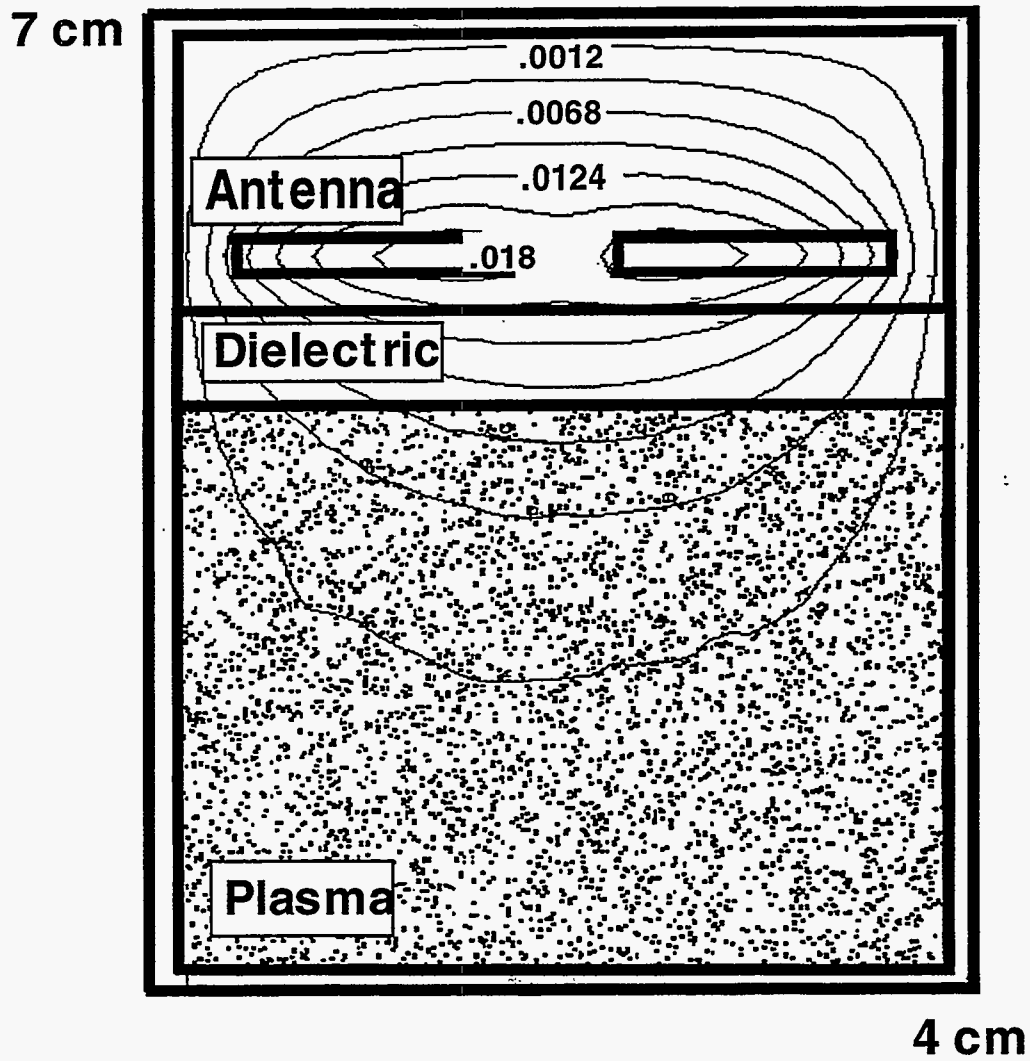


Figure 5.13: Contours of E_y at the peak of \dot{J}_y in the antenna in the 2-D ICP simulation with uniform plasma density.

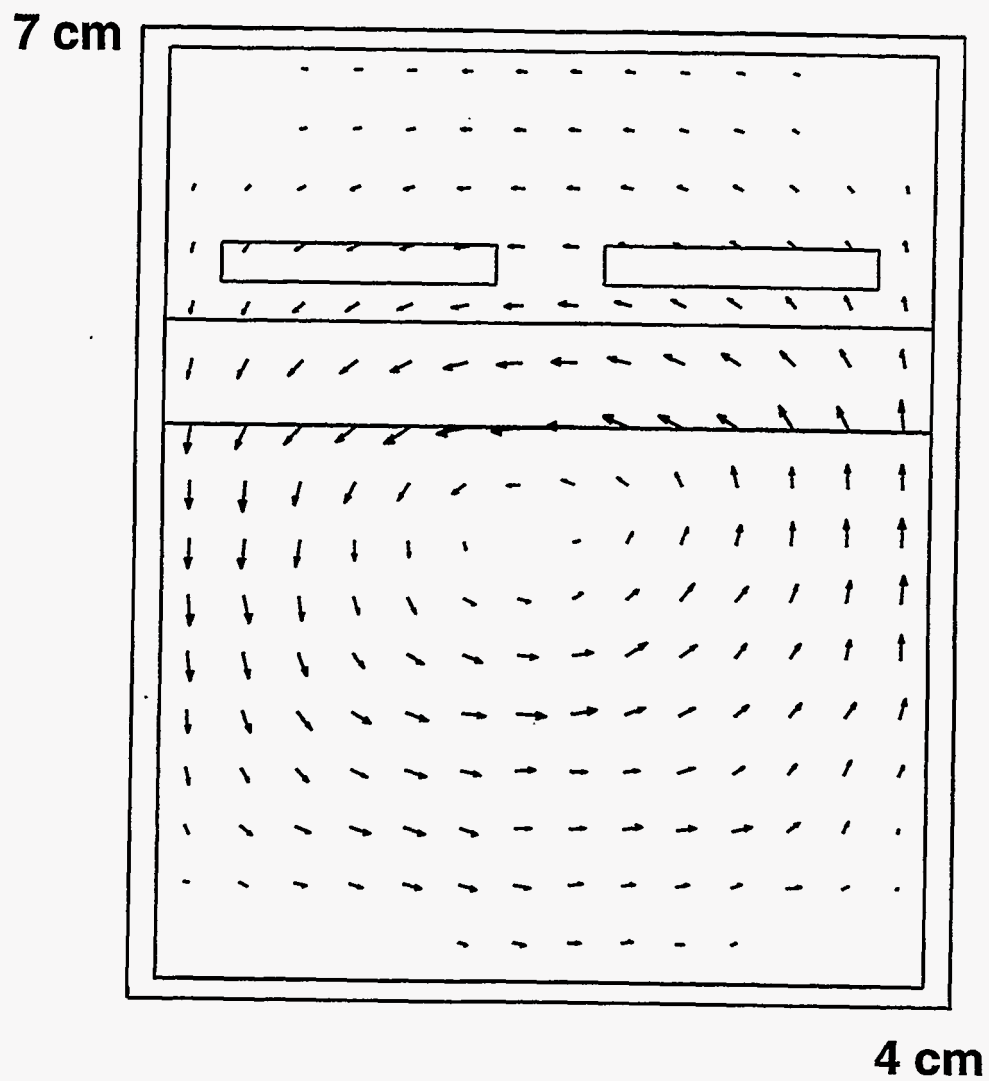


Figure 5.14: Vector plot of $B_{x,z}$ (largest vector = .177 gauss) at the peak of the driven E-field in the 2-D ICP simulation.

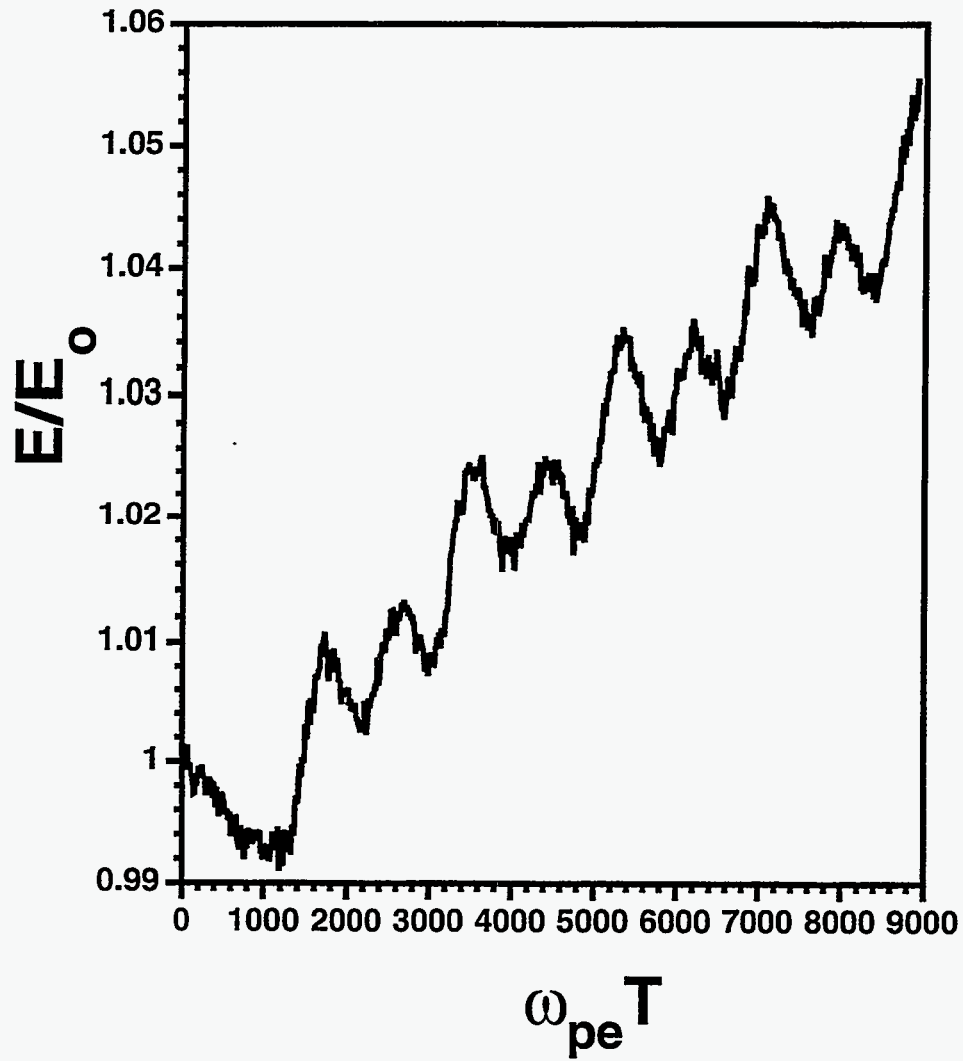


Figure 5.15: Change in particle total kinetic energy (normalized to the initial energy) for the 2-D ICP simulation with uniform plasma density.

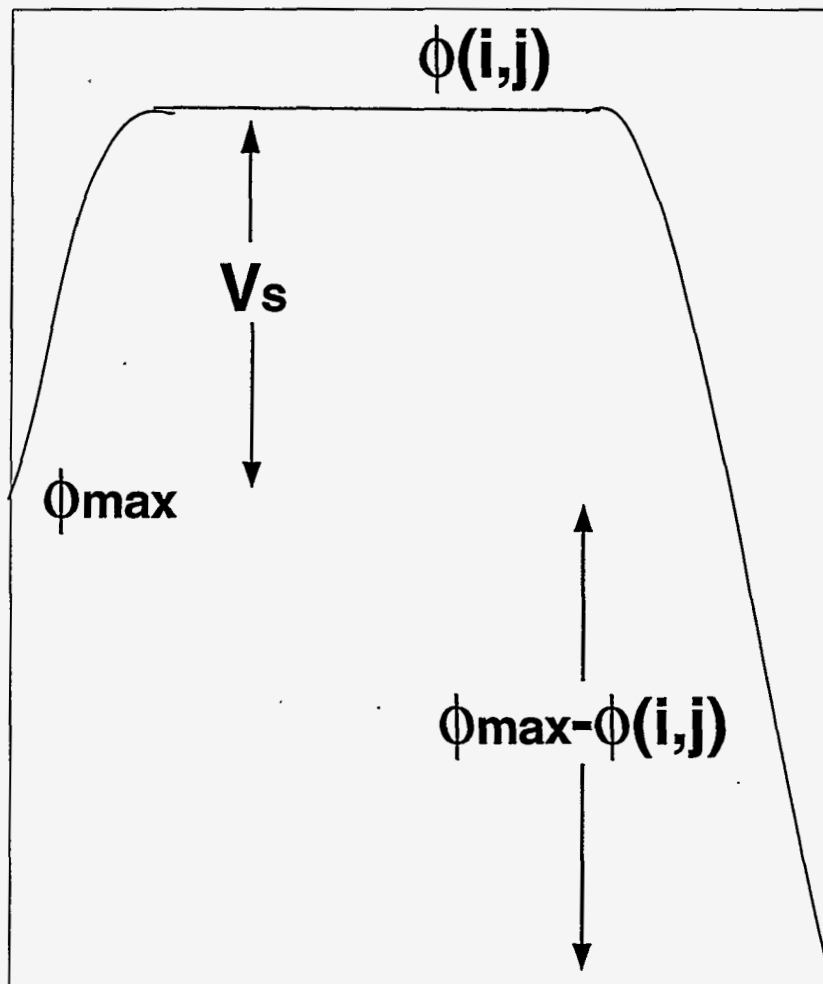


Figure 5.16: Assumed plasma potential profile for calculating the unresolved sheath potential, V_s . ϕ_{max} is the potential on the most positive conducting wall node.

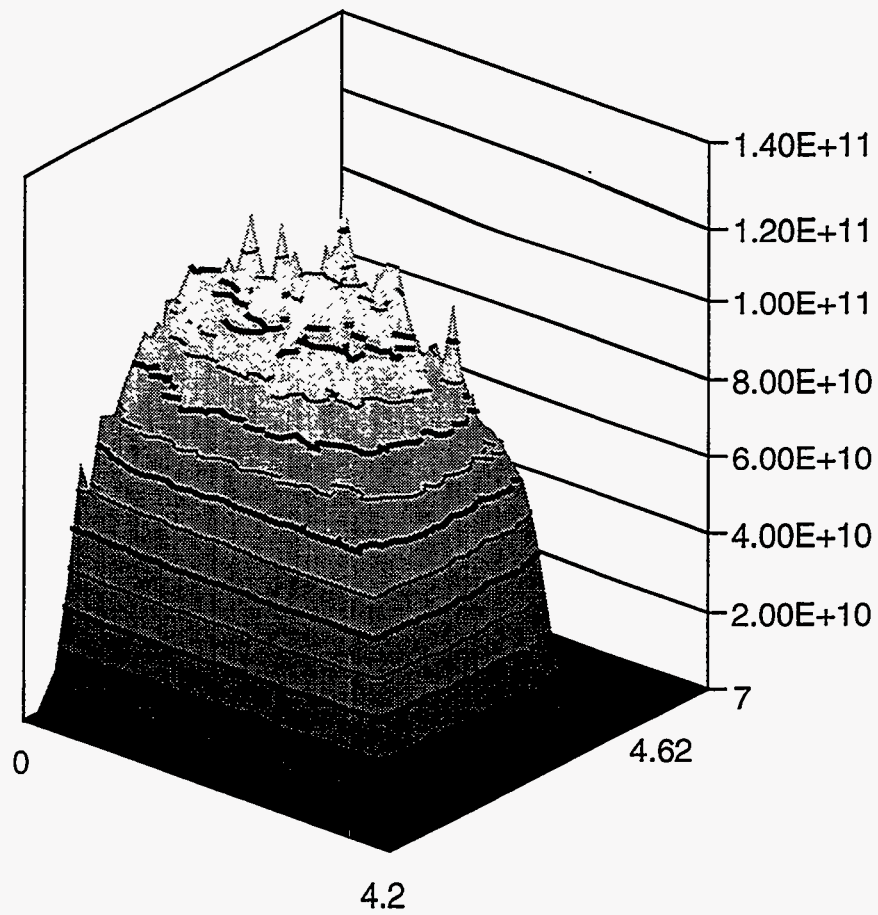


Figure 5.17: Density ($\#/cm^3$) profile at the end of the 2-D reactor simulations with the unresolved sheath boundary condition and electron/ion pair volume injection. The reactor dimensions are in cm.

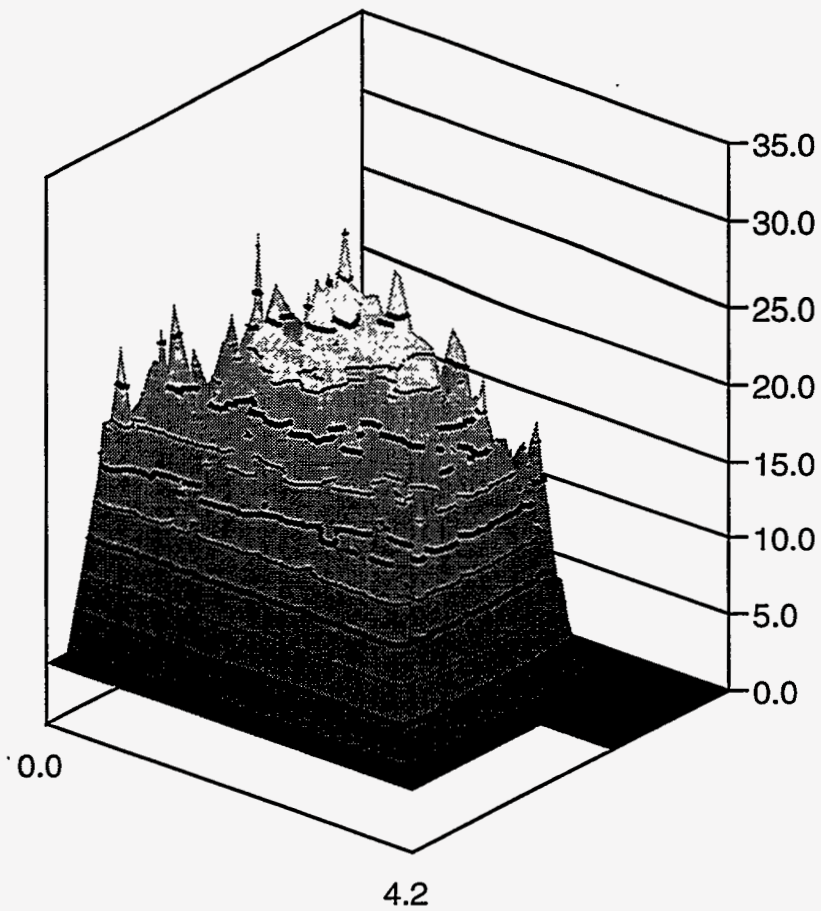


Figure 5.18: Potential (Volts) profile at the end of the 2-D reactor simulations with the unresolved sheath boundary condition and electron/ion pair volume injection. The reactor dimensions are in cm.

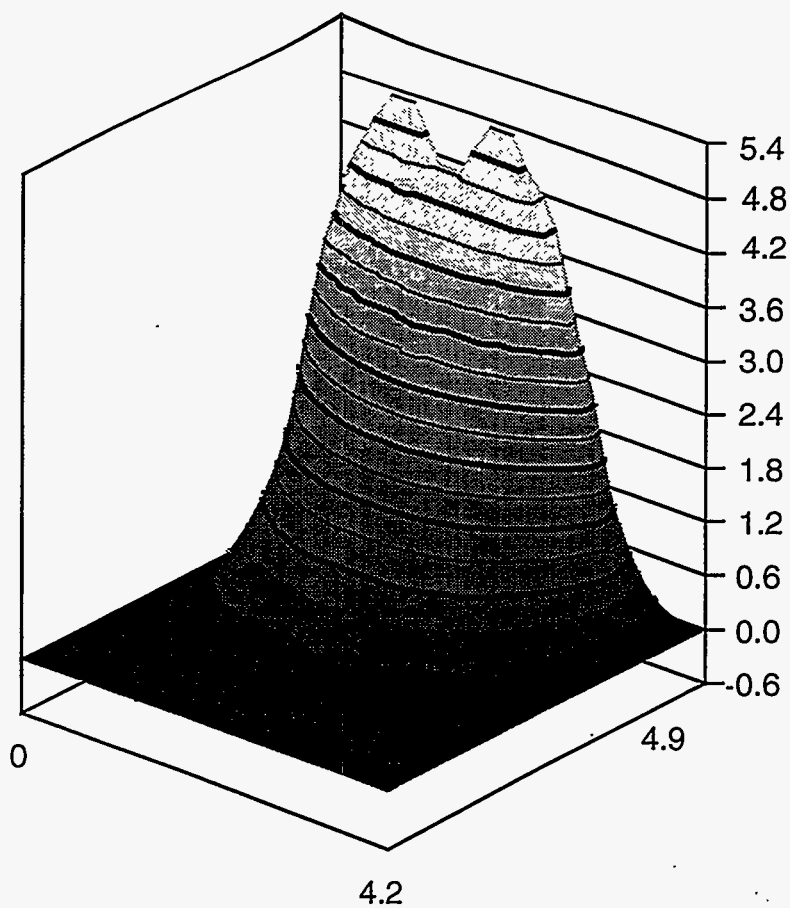


Figure 5.19: Driven E-field (V/cm) profile at the end of the 2-D reactor simulations with the unresolved sheath boundary condition and electron/ion pair volume injection. The reactor dimensions are in cm.

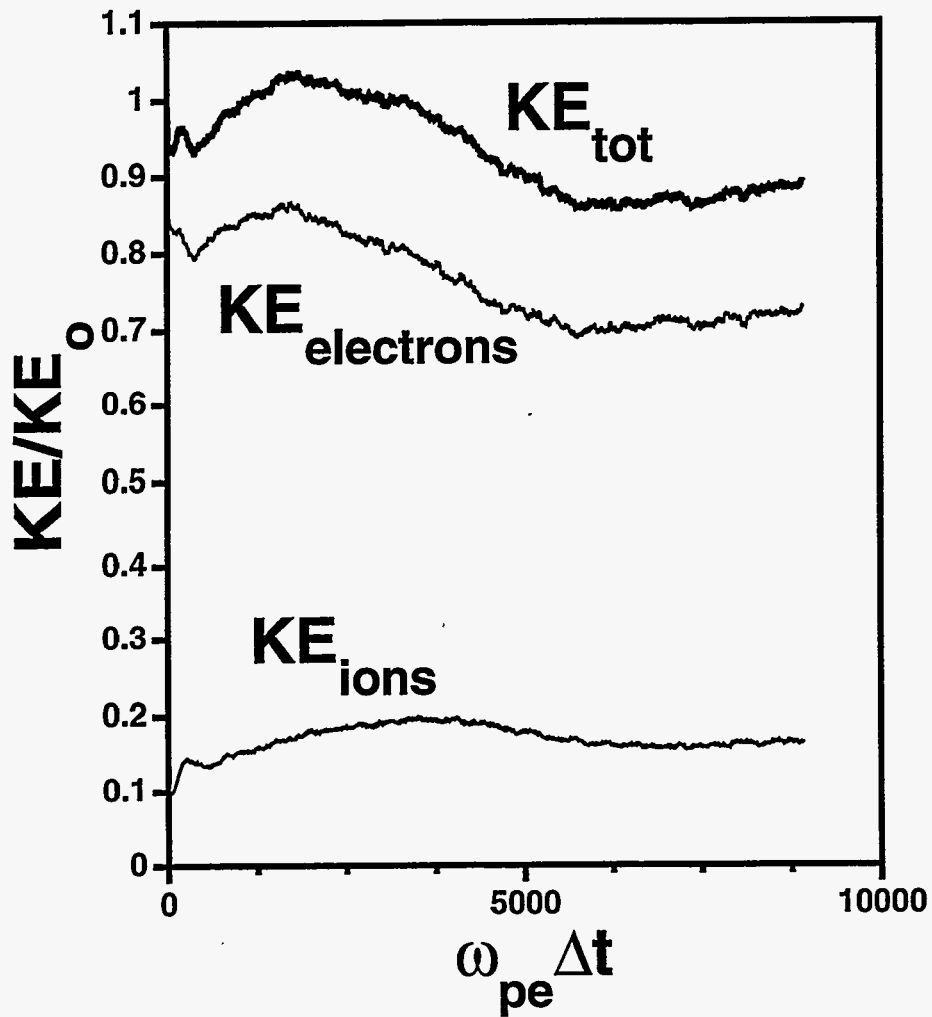


Figure 5.20: Time histories of the particle kinetic energies. The electrons lose energy as their particle number decreases and the electrostatic sheath builds. The ions gain energy falling through the sheath. At late time the energy levels off indicating the approach toward equilibrium.

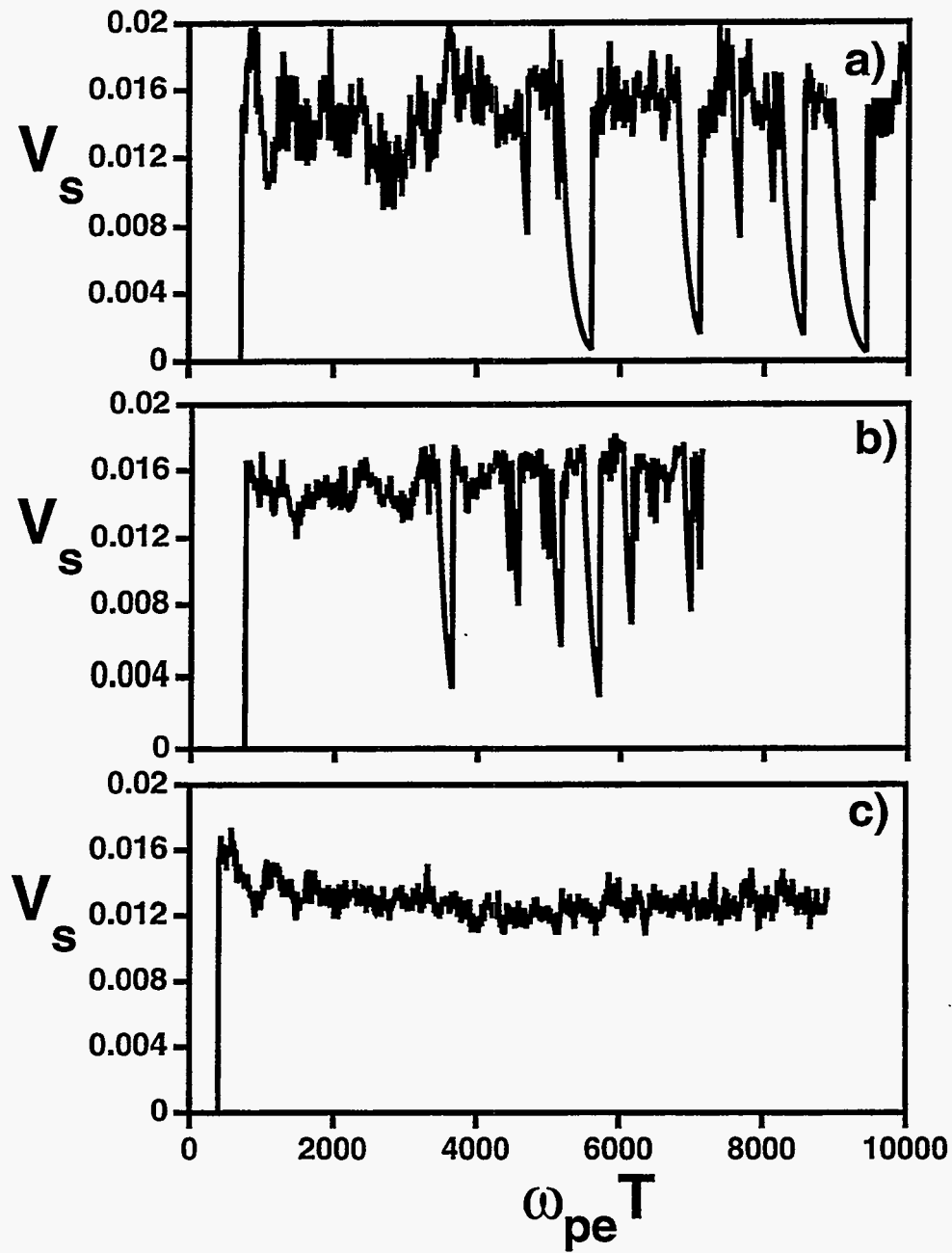


Figure 5.21: Comparison of the unresolved sheath voltage time histories for simulations with average differences between ion and electron particle numbers of: a) 12 particles, b) 120 particles, and c) 680 particles. The a) simulation has the most noisy V_s even though it was a 1-D simulation with the more particles per cell than the 2-D simulation of c).

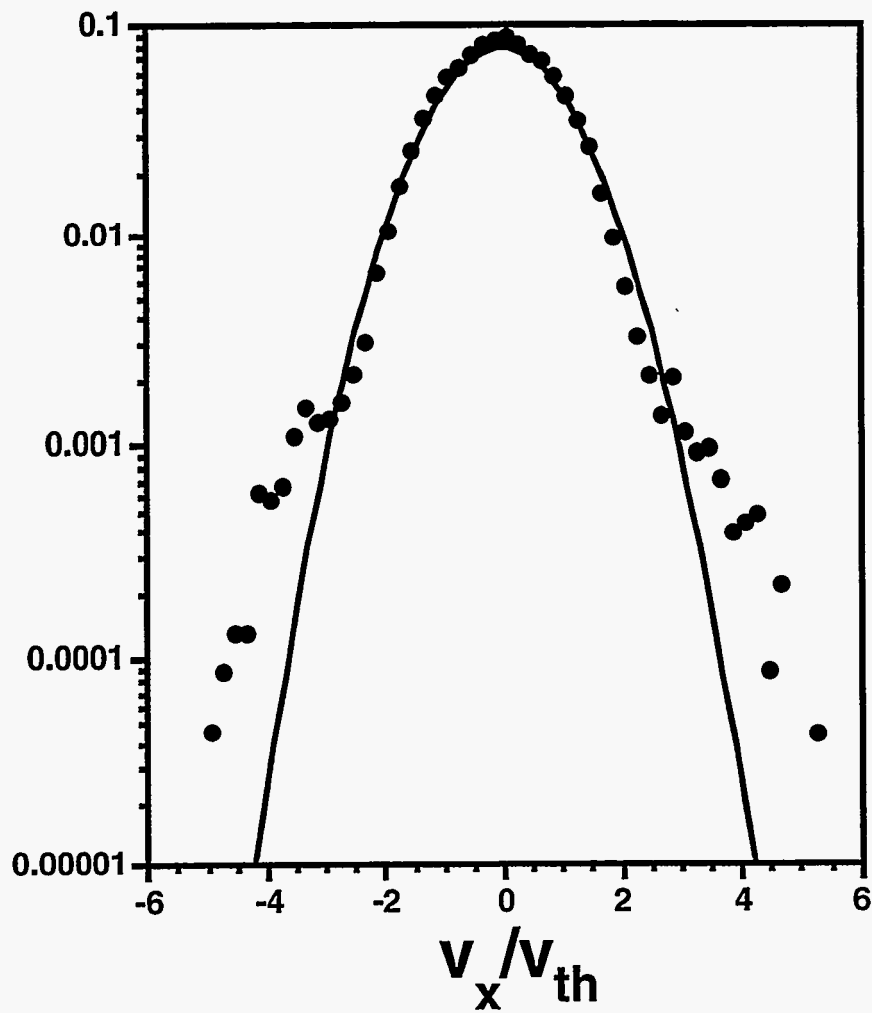


Figure 5.22: Electron velocity distribution (dots) of the 2-D unresolved sheath reactor simulation compared to a Maxwellian distribution (line) at the same temperature.

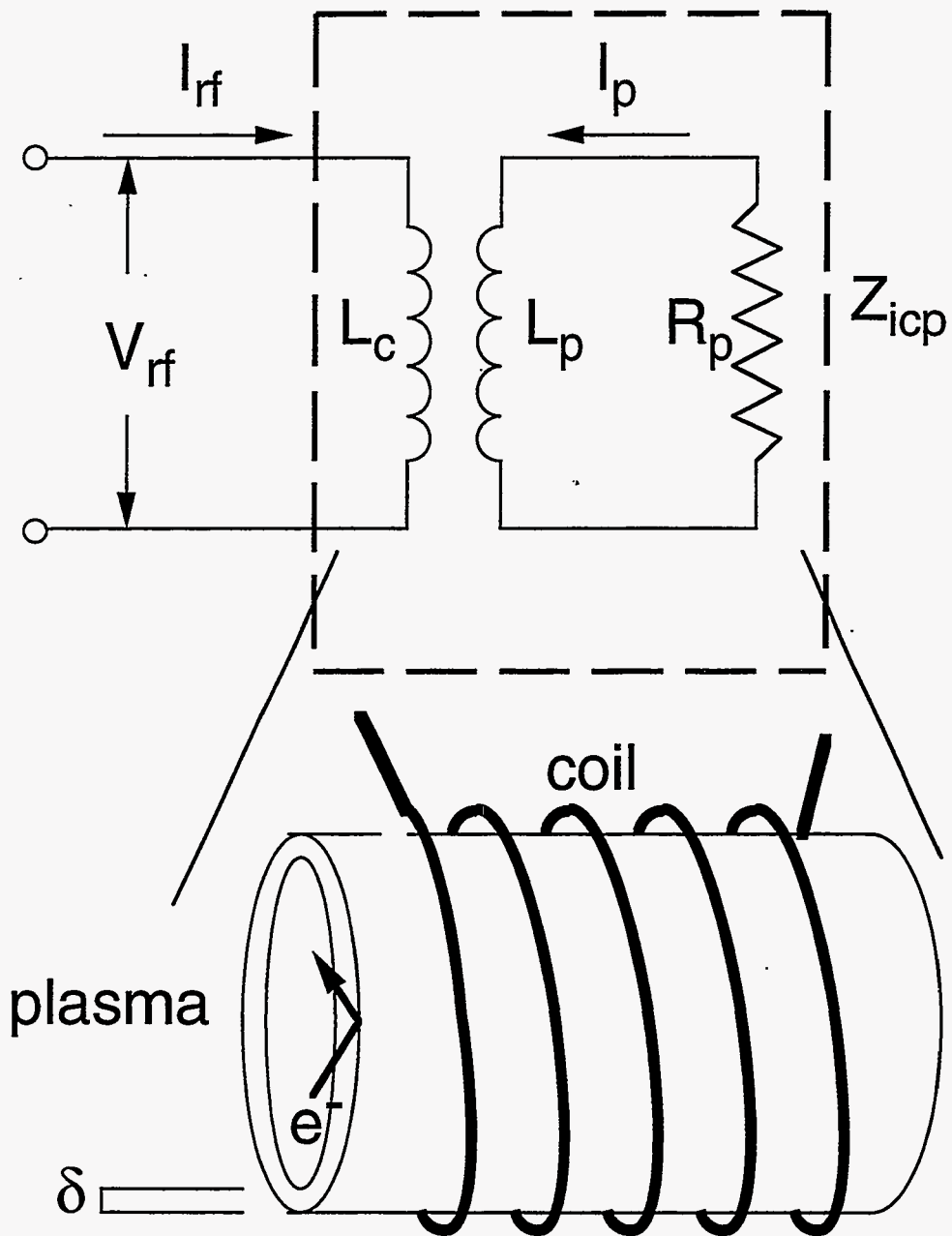


Figure 5.23: Picture of the idealized circuit to model a cylindrical ICP as the one turn secondary of a transformer.

Chapter 6

Conclusion

A new algorithm, DARwin Direct Implicit Particle-in-Cell (DADIPIC), has been investigated which shows great promise for simulating low frequency, electromagnetic plasma phenomena. This work has developed what will hopefully be only the initial incarnation of this method. The robustness of the method when applied to a wide range of phenomena, and the relative ease in handling boundary conditions argue for further investigation and implementation of the method.

The positive characteristics of the method arise out of the Darwin limit of Maxwell's equations with its set of elliptic equations for the fields. Given this limit the Courant condition for light propagation across the grid, $c\Delta t/\Delta x < 1$, is eliminated. Numerically solving these equations has been made much more efficient through the use of the Streamlined Darwin Field (SDF) equations. With these equations we can use Dynamic ADI to solve for the B-field, and Coupled Equation Dynamic ADI to solve for the solenoidal part of the E-field.

Though the Darwin method has been implemented numerically, it has never before been coupled with a particle implicit method for the electrostatic field. By using the Direct Implicit method for the electrostatic field, the constraint on resolving plasma oscillations, $\omega_{pe}\Delta t < 2$, is removed. In this way the Darwin limit can be used economically in dense plasmas while retaining the ability to simulate electron kinetic effects. In its present form the algorithm uses the bi-conjugate gradient method to solve the implicit electrostatic field equation.

A well defined numerical implementation of the method is of limited use without a measure of its performance. The discussions in Chapters 3 and 4 use linear theory and simulations to characterize the limits on spatial and temporal discretization for sta-

ble and accurate use of DADIPIC. The algorithm is shown to operate in agreement with linear theory. We found that the cyclotron frequency must be resolved, and the condition $3v_{th}\Delta t/\Delta x \sim 1$ must be met to minimize numerical heating or cooling. Relatively unrestrictive guidelines were developed that allow the large space and time scale capabilities of DADIPIC to be applied successfully even in circumstances highly stressful to the algorithm (ie. large density gradients, imposed magnetic fields, large electrostatic and electromagnetic fields).

The separation of the field solutions into several elliptic equations adds a certain flexibility to the DADIPIC method. The fields depend only upon the instantaneous values of the source terms which are calculated from plasma quantities. The fields are tied directly to the plasma and carry no memory of the previous fields from one time step to the next. The method, therefore, is not limited to any specific algorithm for the time advance of plasma quantities. The Moment Implicit method could be substituted for the Direct Implicit method as the way of implicitly advancing particles. On the other hand fluid quantities stored on the grid and obeying fluid transport equations could replace the particles altogether. It doesn't matter how the plasma advances from one time step to the next as long as the source terms are available for the fields at the next time step.

The use of elliptic equations also tends to decrease the noise in the fields caused by the finite number of simulation particles. This allows us to run more accurate calculations with the number of particles similar to an explicit code or to use fewer particles achieving similar accuracy in less cpu time. In addition with the separation of the field solutions, the different fields could be solved on different grids. As an example the characteristic scale length of importance for the electrostatic field may be significantly larger than for the magneto-inductive fields. In this case the electrostatic field could reside on a courser mesh reducing the cpu time required to solve for the electrostatic field.

Of course, the method still has its limits. The particle push and field solution still take significant amounts of cpu time. As a guide to future investigations of DADIPIC, the following avenues might lead to improvements of the present algorithm. The use of a δf method for the particles, or spatial filtering of smaller wavelengths may reduce the noise of fluctuations and enlarge the region of energy conservation. When kinetics are required, of course, particles are required. However, the combination of kinetic and fluid simulation recommended in Chapter 5 may be a way of integrating kinetic effects into a fluid simulation without requiring particles over the whole simulation.

By redefining the finite difference operator to be aligned with the local B-field it may be possible to diagonalize the implicit susceptibility and regain a five-point finite difference template. The relatively fast Dynamic ADI solution technique could then be applied to the implicit electrostatic field equation. For those phenomena where only the component of \mathbf{E}_{sol} out of the simulation plane is required, Ξ_y can be found with Dynamic ADI with no need for the slower CEDADI. DiPeso, et. al.[dip93] have shown a decrease in the computation time for CEDADI itself through the use of block tridiagonal methods. So the cpu time (3 s per time step on a Cray 2) for the test problem of Chapter 4 is not the minimum limit for DADIPIC.

In the near term DADIPIC will be used to simulate inductively coupled and other collisional bounded plasma sources. The results of Chapter 5 highlight the method's capability to model bounded plasmas. The agreement with 1-D kinetic theory gives us an idea of the resolution needed for 2-D simulations, and the 2-D simulations show DADIPIC's ability to model geometries similar to actual plasma processing reactors. The nonlinear geometric and B-field effects on collisionless heating emphasize the need for a low, frequency kinetic code since such results are not readily achieved with analytic theory or fluid simulation. It is this type of simulation which may lead to novel ideas for reactor configurations.

One final point must be emphasized. Although a large portion of this dissertation was devoted to the phenomena in ICP sources, this does not imply any limit on the applications of this method. With the algorithm adapted to a code which allows arbitrary 2-D structures, DADIPIC has the potential to simulate a wide range of bounded or unbounded low frequency, kinetic plasmas. The utility of the method lies in its inherent flexibility and unspecialized nature.

Appendix A

Calculation of Dispersion Relations and the Spectral Density

In this appendix the calculation of the dispersion relation, Eq. (3.24), and spectral density, Eq. (3.30), for the PIC plasma are discussed. The first step in this process is to find the ratio $[X/A]$. The deflection of a particle, $x_n^{(1)}$, from its zero-order orbit, $x^{(0)}$, at any time step n is given by the perturbing velocity, $v_{n-1/2}$, added over all previous time steps

$$x_n^{(1)} = \Delta t \sum_{q=1}^n v_{n-q+1/2}. \quad (\text{A.1})$$

In a similar manner the perturbing velocity depends on the perturbing acceleration which for this analysis is due only to the electrostatic field and has a harmonic variation. So $a_n^{(1)}(\mathbf{x}, t) = E_o \exp(i\mathbf{k} \cdot \mathbf{x}_0) z^n (\mathbf{k} \cdot \mathbf{v}_0 - \omega)$ where $z(u) = \exp[iu\Delta t]$. For an explicit scheme

$$v_{n+1/2} = \Delta t \sum_{q=1}^n a_{n-q}^{(1)}. \quad (\text{A.2})$$

Plugging Eq. (A.2) into Eq. (A.1), we find

$$\left[\frac{X}{A} \right]_{\omega - \mathbf{k} \cdot \mathbf{v}} = \frac{x_n^{(1)}}{a_n^{(1)}} = (\Delta t)^2 \sum_{q=1}^n q z^{-q}. \quad (\text{A.3})$$

For the D_1 implicit scheme the velocity depends on $\bar{a}_n = \frac{1}{2}(a_{n+1}^{(1)} + \bar{a}_{n-1})$ or

$$v_{n+1/2} = \Delta t \sum_{q=1}^n \bar{a}_{n-q+1}. \quad (\text{A.4})$$

For the D_1 case we find

$$\left[\frac{X}{A} \right]_{\omega - \mathbf{k} \cdot \mathbf{v}} = (\Delta t)^2 \left\{ \sum_{q=1}^n q z^{-q} + \frac{1}{2} \sum_{q=0}^n \frac{1}{(2z)^q} \right\}. \quad (\text{A.5})$$

These functions are averaged over a Maxwellian velocity distribution as in Eq. (3.23), and included in the dispersion relation Eq. (3.24). The result for the D_1 scheme, including spatial gridding effects, is

$$D_{D_1}(\mathbf{k}, \omega) = 1 + \frac{(\omega_{pe} \Delta t)^2}{K^2(k)} \sum_{\mathbf{p}} \mathbf{k}_{\mathbf{p}} \cdot \vec{\kappa}(\mathbf{k}) S^2(\mathbf{k}_{\mathbf{p}}) X(\mathbf{k}_{\mathbf{p}}, z(\omega)) \quad (\text{A.6})$$

where z is now only a function of ω . The function $X(\mathbf{k}_{\mathbf{p}}, z(\omega))$ is

$$X(\mathbf{k}_{\mathbf{p}}, z(\omega)) = \sum_{q=1}^n \left[q z^{-q} + \frac{1}{2(2z)^q} \right] \exp[-(k_p \lambda_{De} \omega_{pe} \Delta t)^2 q^2 / 2]. \quad (\text{A.7})$$

The notation for the sum in Eq. (A.6) is

$$\sum_{\mathbf{p}} = \sum_{p=-\infty}^{\infty} \sum_{s=-\infty}^{\infty}, \quad (\text{A.8})$$

and $\mathbf{k}_{\mathbf{p}}$ represents

$$\mathbf{k}_{\mathbf{p}} = \hat{x} \left(k_x - \frac{2\pi p}{\Delta x} \right) + \hat{z} \left(k_z - \frac{2\pi s}{\Delta z} \right). \quad (\text{A.9})$$

For the linear shape functions and second order finite difference operators used in this code, the form of the spatial functions in these equations is based around the function[bir85]

$$\text{dif}(\theta) = \sin(\theta)/\theta. \quad (\text{A.10})$$

The Fourier transforms of the various operators can then be written

$$S^2(\mathbf{k}_{\mathbf{p}}) = \text{dif}^4(k_{px} \Delta x / 2) \text{dif}^4(k_{sz} \Delta z / 2) \quad (\text{A.11})$$

$$\vec{\kappa}(\mathbf{k}) = \hat{x} k_x \text{dif}(k_x \Delta x) + \hat{z} k_z \text{dif}(k_z \Delta z) \quad (\text{A.12})$$

$$K^2(k) = k^2 \text{dif}^2(k \Delta x / 2). \quad (\text{A.13})$$

Now we must calculate the sums, S , with an estimate for the residual, $R_{\mathcal{P}}$. The convergence test is

$$\frac{\text{abs}(R_{\mathcal{P}})}{\text{abs}(S)} < \text{etest} \quad (\text{A.14})$$

where ϵ is set to 10^{-4} or less. The size of the remainder is estimated through the Cauchy integral test

$$\sum_{p=P+1}^{\infty} f_p < \int_{P+1}^{\infty} |f(x)| dx + f_{P+1} \quad (\text{A.15})$$

First consider the function

$$X(\mathbf{k}_p, z(\omega)) = \sum_{q=1}^{\infty} [q + 2^{-(q+1)}] u_q. \quad (\text{A.16})$$

Note for simplicity the approximation $q \rightarrow \infty$ has been made (an arbitrarily large number of simulation time steps). The following definitions are made:

$$a^2 = (k_p v_{th} \Delta t)^2 / 2, \quad (\text{A.17})$$

$$b = -\ln |z|, \quad (\text{A.18})$$

$$\alpha = a(Q + 1) - b/2a. \quad (\text{A.19})$$

If α is negative, and the approximation is used

$$\int_{\alpha}^{\infty} \exp[-u^2] du < \sqrt{\pi}, \quad (\text{A.20})$$

then the remainder for $q = Q$ is

$$R_Q < |u_{Q+1}| \left(Q + 1 + 2^{-(Q+2)} + \frac{1}{2a^2} \right) + \frac{(b + 1/2)\sqrt{\pi}}{2a^3} \exp[b^2/4a^2]. \quad (\text{A.21})$$

Notice, the remainder will not become small unless α is positive. For α positive we can make the estimate

$$\int_{\alpha}^{\infty} \exp[-u^2] du < \frac{1}{2\alpha} e^{-\alpha^2}. \quad (\text{A.22})$$

In this case the remainder is

$$R_Q < |u_{Q+1}| \left\{ Q + \frac{3}{2} + \frac{1}{2a^2} \left[1 + \frac{b + 1/2}{2a^2(Q + 1) - b} \right] \right\}. \quad (\text{A.23})$$

The sum, Eq. (A.16), is carried out until α is positive. After that the error test, Eq. (A.14), is applied each iteration to the remainder calculated by Eq. (A.23). Once the error test is met the iteration is stopped. A recursion relation suggested by Langdon[lan79a] decreases the numerical work required to evaluate this sum over exponentials.

After finding the $X(\mathbf{k}_p, z(\omega))$ terms for a particular \mathbf{k}_p the error in the sums over p must be estimated. The sum is calculated by adding the terms along the square

$-l \leq p \leq l, s = l$ or $-l$, and $-l \leq s \leq l, p = l$ or $-l$. After this the remainder is checked. Using the Cauchy integral test as before, we find for the case of $p + s > 0$

$$R_{\mathbf{P}} < |X(\mathbf{k}_r, z)| \iint | (k_p \sin(k_x \Delta) + k_s \sin(k_z \Delta)) S^2(k_p) | \left(\frac{\Delta}{2\pi} \right)^2 dk_p dk_s + |A_r| \quad (\text{A.24})$$

For this case let $\Delta = \Delta x = \Delta z$, $k_r = 2\pi l / \Delta$, and A_r represent the argument in the sum of Eq. (A.6). The double integral must exclude the region inside the square with sides of k_r or

$$\begin{aligned} \iint &= \int_{-\infty}^{-k_r} dk_p \int_{-k_r}^{k_r} dk_s + \int_{k_r}^{\infty} dk_p \int_{-k_r}^{k_r} dk_s \\ &+ \int_{-\infty}^{\infty} dk_p \int_{-\infty}^{-k_r} dk_s + \int_{-\infty}^{\infty} dk_p \int_{k_r}^{\infty} dk_s \end{aligned} \quad (\text{A.25})$$

The remainder is estimated as four times the second integral in Eq. (A.25).

$$\begin{aligned} R_{\mathbf{P}} &< |X(\mathbf{k}_r, z)| \int_{-\infty}^{\infty} dk_p \int_{k_r}^{\infty} dk_s \frac{(k_p + k_s) \sin^4(k_p \Delta / 2)}{(k_p \Delta / 2)^4 (k_s \Delta / 2)^4} \left(\frac{\Delta}{2\pi} \right)^2 + |A_r| \\ &< |X(\mathbf{k}_r, z)| \frac{32\pi}{3(k_r \Delta)^2 \Delta} + |A_r| \end{aligned} \quad (\text{A.26})$$

These error tests are, of course, conservative. Meeting them assures high accuracy in the calculation of the dispersion function, $D(k, \omega)$.

We can give the dispersion function a particular k and find the complex ω satisfying the root of the function. This determines the dispersion relation or normal modes for the numerical plasma. The roots are found using a simple, robust Monte-Carlo optimization algorithm. Given an initial square region in the complex ω plane, the algorithm picks a number of points, $j = 1, \dots, n$, randomly within the region. It calculates the value of $D(k, \omega_j)$ at each of the points. The maximum, err_{max} , and minimum, err_{min} , value of $D(k, \omega_j)$ is found for each set of points. An error limit is set as

$$err_{lim} = (err_{max} + err_{min}) / 2. \quad (\text{A.27})$$

The value of err_{lim} is used to narrow the bounds on the real, ω_r , and imaginary, ω_i , components of the frequency. The lower boundary on each component is set equal to the lowest value of the component where $D(k, \omega_j)$ is less than err_{lim} . The upper boundary on each component is set equal to the largest value of the component where $D(k, \omega_j)$ is less than err_{lim} . With the new bounds chosen the process is repeated until the separation between the bounds is less than a preset limit. As long as the root is within the initial

region, the method will find it without moving away from the root which could happen with a Newton's method. We also do not need to know or estimate the gradient of this complicated function.

The routine is initialized by finding the root for $k = 0$. $D(0, \omega)$ becomes for the rmD_1 scheme

$$((\omega_{pe}\Delta t)^2 + 2)z^3 - 5z^2 + 4z - 1 = 0. \quad (\text{A.28})$$

Initial bounds are chosen in the complex ω plane. As k is incremented, the bounds are centered around the root, $\omega_r + i\omega_i$, for the previous value of k with the assumption that a small change in k will only cause a small change in the root.

The dispersion function can also be used in Eq. (3.30) to find the spectral density. The sum in the spectral density equation is

$$\begin{aligned} S_{spden} = & \sum_{p=-\infty}^{\infty} \sum_{s=-\infty}^{\infty} \sum_{q=-\infty}^{\infty} \frac{S^2(\mathbf{k}_p)}{\sqrt{k_p^2 + k_s^2} \lambda_{De}} \\ & \exp\left[-\frac{1}{2}\left(\frac{\omega_q}{\omega_{pe}}\right)^2 \left(\frac{1}{(k_p^2 + k_s^2)\lambda_{De}^2}\right)\right] \end{aligned} \quad (\text{A.29})$$

Consider the sum over q first. Let

$$a = \frac{1}{2} \left(\frac{2\pi}{\omega_{pe}\Delta t \sqrt{k_p^2 + k_s^2} \lambda_{De}} \right)^2 \quad (\text{A.30})$$

and $b = \omega\Delta t/2\pi$. So we have

$$S_q = \sum_{q=-\infty}^{\infty} \exp[-a(b-q)^2] \quad (\text{A.31})$$

For those cases where $\sqrt{2a} > 2$, we shall assume convergence when q reaches $\pm(1 + 5/\sqrt{2a})$. Notice the exponential drops off very rapidly for larger q given the stipulation on the magnitude of a . When $\sqrt{2a} < 2$, we use Parseval's theorem to rewrite Eq. (A.31) obtaining another rapidly converging series. The theorem states

$$\sum_{q=-\infty}^{\infty} f(q) = \sum_{m=-\infty}^{\infty} F(2\pi m) \quad (\text{A.32})$$

where $F(k)$ is the Fourier transform of $f(x)$. Our sum becomes

$$\sum_{m=-\infty}^{\infty} \sqrt{\frac{\pi}{a}} e^{-i2\pi mb} e^{-(2\pi m)^2/4a} = \sqrt{\frac{\pi}{a}} \sum_{m=-\infty}^{\infty} \cos(2\pi mb) e^{-(2\pi m)^2/4a} \quad (\text{A.33})$$

For this case convergence is assumed after $m = \pm(1 + \sqrt{10a}/\pi)$. In either case we need to sum five or fewer terms.

To find the remainder for the whole sum, we first estimate the sum over q as

$$\begin{aligned} \sum_{q=-\infty}^{\infty} \exp[-a(b-q)^2] &< \int_{-\infty}^{\infty} \exp[-a(b-q)^2] dq + 1 \\ &< 1 + \sqrt{\frac{\pi}{a}} \end{aligned} \quad (\text{A.34})$$

The sum is again calculated by adding the terms along the square $-l \leq p \leq l, s = l$ or $-l$, and $-l \leq s \leq l, p = l$ or $-l$ before checking the remainder. The remainder is estimated with the sum

$$R_{\mathbf{P}} < \sum_{p=-\infty}^{\infty} \sum_{s=-\infty}^{\infty} \left\{ \frac{1}{\sqrt{(k_g p)^2 + (k_g s)^2} \lambda_{De}} + \frac{\omega_{pe} \Delta t}{\sqrt{2\pi}} \right\} \frac{\sin^4(k_g p) \sin^4(k_g s)}{k_g^8 p^4 s^4} \left(\frac{2}{\Delta} \right)^8 \quad (\text{A.35})$$

where only terms outside the square with sides of length l are included in the sum. As before $k \leq \pi/\Delta x$; therefore, we have neglected k in $k_{\mathbf{p}}$ allowing us to work only with $k_g p = 2\pi p/\Delta$. If we use the Cauchy integral test, we find, after simplifying the integrand and converting to polar coordinates,

$$\begin{aligned} R_{\mathbf{P}} &< \int_{k_r}^{\infty} \left\{ \frac{1}{k_r \lambda_{De}} + \frac{\omega_{pe} \Delta t}{\sqrt{2\pi}} \right\} \left(\frac{2}{k\Delta} \right)^4 2\pi k dk \left(\frac{\Delta}{2\pi} \right)^2 + |A_r| \\ &< \left\{ \frac{1}{k_r \lambda_{De}} + \frac{\omega_{pe} \Delta t}{2\sqrt{2\pi}} \right\} \frac{8}{\pi (k_r \Delta)^2} + |A_r| \end{aligned} \quad (\text{A.36})$$

The results from these sums are used to find the spectral densities shown in chapter 3.

Bibliography

- [all70] Allen, J.E. and J.G. Andrews, A Note on Ion Rarefaction Waves, *J. Plasma Phys.* 4, 187-194 (1970).
- [and88] Anderson, D.V., A.E. Koniges, and D.E. Shumaker, CPDES2: A Preconditioned Conjugate Gradient Solver for Linear Asymmetric Matrix Equations Arising from Coupled Partial Differential Equations in Two Dimensions, *Comput. Phys. Comm.* 51, 391-403 (1988).
- [bat93] Batchelor, D.B., L. A. Berry, E.F. Jaeger, K.C. Shaing, and J.C. Whitson, 2D Modeling of Power Deposition in Inductively Coupled Plasma Sources for Materials Processing, *Bull. Am. Phys. Soc.* 38, 2122 (1993).
- [bir85] Birdsall, C.K. and A.B. Langdon, "Plasma Physics via Computer Simulation," (McGraw Hill, New York, NY, 1985).
- [bir91] Birdsall, C.K., Particle-in-Cell Charged-Particle Simulations Plus Monte Carlo Collisions With Neutral Atoms, PIC-MCC, *IEEE Trans. Plas. Sci.*, 19, 65-85, (1991).
- [ble70] Blevin, H.A., J.A. Reynolds, and P.C. Thonemann, Penetration of an Electromagnetic Wave into a Hot Plasma Slab, *Phys. Fluids* 13, 1259-1264 (1970).
- [ble73] Blevin, H.A., J.M. Greene, D.L. Jolly, and R.G. Storer, The Anomalous Skin Effect in Cylindrical Plasmas, *J. Plasma Phys.* 10, 337-348 (1973).
- [bor70] Boris, J.P., Proc. Fourth Conf. Num. Sim. Plasmas, Naval Res. Lab., Wash., D.C., 3-67, 2-3 November 1970.
- [bra85] Brackbill, J.U. and D.W. Forslund, Simulation of Low-Frequency Electromagnetic Phenomena in Plasmas in "Multiple Time Scales," Computational Techniques Series, (Academic Press, New York, 1985).
- [bye78] Byers, J.A., B.J. Cohen, W.C. Condit and J.D. Hanson, *J. Comput. Phys.* 27, 363 (1978).
- [che74] Chen, F.F., "Introduction to Plasma Physics," (Plenum Press, New York, NY, 1974).

- [coh84] Cohen, B.I., A.B. Langdon, and A. Friedman, Smoothing and Spatial Grid Effects in Implicit Particle Simulation, *J. Comp. Phys.* **56**, 51-64 (1984).
- [coh89] Cohen, B.I., A.B. Langdon, D.W. Hewett, and R.J. Procassini, Performance and Optimization of Direct Implicit Particle Simulation, *J. Comput. Phys.* **81**, 151-168 (1989).
- [coh94] Cohen, R.H., Stochastic Heating and Turning of electrons in Low-frequency Inductive Discharges, Lawrence Livermore Nat. Lab. memo July 15, 1994.
- [dar20] Darwin, C.G., *Phil. Mag.*, **39**, 537 (1920).
- [den79] Denavit, J., Collisionless Plasma Expansion into a Vacuum, *Phys. Fluids* **22**, 1384-1392 (1979).
- [den81] Denavit J., Time-Filtering Particle Simulations with $\omega_{pe}\Delta t \gg 1$, *J. Comput. Phys.* **42**, 337-366 (1981).
- [den90] Denneman, J.W., Determination of Electromagnetic Properties of Low-Pressure Electrodeless Inductive Discharges, *J. Phys. D: Appl. Phys.* **23**, 293-298 (1990).
- [dip91] DiPeso, G., E.C. Morse, and R.W. Ziolkowski, δf and Particle Simulations of Parametric Instabilities, *J. Comput. Phys.* **96** 325-338 (1991).
- [dip93] DiPeso, G., D.W. Hewett, and D.J. Larson, The Use of Block Tridiagonal Methods to Improve Convergence of DADI Solutions to Coupled Elliptic Partial Differential Equations, *Comp. Phys. Comm.* **77**, 33-45 (1993).
- [dip94a] DiPeso, G. and V. Vahedi, Analytic Sheath Resolution in High Density Plasma Source Simulations, 15th Int. Conf. on the Numerical Simulation of Plasmas, King of Prussia, PA, Sept. 7-9 (1994).
- [dip94b] DiPeso, G., D.W. Hewett, and G.F. Simonson, Extension of the Darwin Model to Quasineutral Plasmas, *J. Comput. Phys.* **111**, 237-247 (1994).
- [dip94c] DiPeso, G., Analytic Sheath Resolution in Inductively Coupled Plasma Simulations, 15th Inter. Conf. Num. Sim. Plasmas, King of Prussia, PA, 3B20, 7-9 September 1994.
- [dip94d] DiPeso, G., V. Vahedi, D.W. Hewett, and T.D. Rognlien, Two-Dimensional Self-consistent Fluid Simulation of Radio Frequency Inductive Sources, *J. Vac. Sci. Technol. A* **12**, 1387-1396 (1994).
- [dos79] Doss, S. and K. Miller, Dynamic ADI Methods for Elliptic Equations, *SIAM J. Numer. Anal.* **16**, 837 (1979).
- [eck62] Eckert, H.U., Diffusion Theory of the Electrodeless Ring Discharge, *J. Appl. Phys.* **33**, 2780-2788 (1962).

- [eck74] Eckert, H.U., The Induction Arc: A State-of-the-Art Review, *High Temp. Sci.* **6**, 99-134 (1974).
- [fle75] Fletcher, R., Conjugate Gradient Methods for Indefinite Systems in "Numerical Analysis," Lecture Notes in Mathematics Series, A. Dold and B. Eckmann, eds., (Springer-Verlag, New York, 1975).
- [fri90] Friedman, A., A Second-Order Implicit Particle Mover with Adjustable Damping, *J. Comput. Phys.* **90**, 292-312 (1990).
- [for88] Forrester, A.T., "Large Ion Beams: Fundamentals of Generation and Propagation," (John Wiley & Sons, New York, NY, 1988).
- [god86] Godyak, V.A., "Soviet Radio Frequency Discharge Research," Delphic Associates, Falls Church, VA (1986).
- [god90] Godyak, V.A., Dynamic Model of the Electrode Sheaths in Symmetrically Driven RF Discharges, *Phys. Rev. A*, **42**, 2299-2312 (1990).
- [god94] Godyak, V.A., R.B. Piejak, and B.M. Alexandrovich, Electrical Characteristics and Electron Heating Mechanism of an Inductively Coupled Argon Discharge, *Plasma Sources Sci. Tech.* **3**, 169-176 (1994).
- [gol89] Golub, G.H. and C.G. Van Loan, "Matrix Computations," (The Johns Hopkins University Press, Maryland, 1989).
- [hen71] Henriksen, B.B., D.R. Keefer, and M.H. Clarkson, Electromagnetic Field in Electrodeless Discharge, *J. Appl. Phys.* **42**, 5460-5464 (1971).
- [hew78] Hewett, D.W. and C.W. Nielson, A Multidimensional Quasineutral Plasma Simulation Model, *J. Comput. Phys.* **29**, 219-236 (1978).
- [hew80] Hewett, D.W., A Global Method of Solving the Electron-Field Equations in a Zero-Inertia-Electron-Hybrid Plasma Simulation Code, *J. Comput. Phys.* **38**, 378-395 (1980).
- [hew87a] Hewett, D.W. and J. K. Boyd, Streamlined Darwin Simulation of Nonneutral Plasmas, *J. Comput. Phys.* **70**, 166-181 (1987).
- [hew87b] Hewett, D.W. and A.B. Langdon, Electromagnetic Direct Implicit Plasma Simulation, *J. Comput. Phys.* **72**, 121-155 (1987).
- [hew88] Hewett, D.W., G.E. Frances, and C.E. Max, *Phys. Rev. Lett.*, **61**, 893 (1988).
- [hew92a] Hewett, D.W., D. J. Larson, and S. Doss, Solution of Simultaneous Partial Differential Equations Using Dynamic ADI: Solution of the Streamlined Darwin Field Equations, *J. Comput. Phys.* **101**, 11-24 (1992).
- [hew92b] Hewett, D.W. and D.J. Larson, "The Best of Gymnos: A User's Guide," LLNL Internal Report, UCRL-UR-110499, 1992.

- [hew94] Hewett, D.W., Low-Frequency Electromagnetic (Darwin) Applications in Plasma Simulation, *Comp. Phys. Comm.* **84**, 243-277 (1994).
- [hoc65] Hockney, R.W., A Fast Direct Solution of Poisson's Equation Using Fourier Analysis, *J. Assoc. Comput. Mach.* **12**, 95-113 (1965).
- [hoc66] Hockney, R.W., Computer Simulation of Anomalous Plasma Diffusion and Numerical Solution of Poisson's Equation, *Phys. Fluids* **9**, 1826-1835 (1966).
- [hoc71] Hockney, R.W., Measurements of Collision and Heating Times in a Two-Dimensional Thermal Computer Plasma, *J. Comput. Phys.* **8**, 19-44 (1971).
- [hop92] Hopwood, J., Review of Inductively Coupled Plasmas for Plasma Processing, *Plasma Sources Sci. Tech.* **1**, 109-116 (1992).
- [hop93] Hopwood, J., C.R. Guarnieri, S.J. Whitehair, and J.J. Cuomo, Electromagnetic Fields in a Radio-Frequency Induction Plasma, *J. Vac. Sci. Technol. A* **11** 147-151 (1993).
- [ich73] Ichimaru, S., "Basic Principles of Plasma Physics: A Statistical Approach", *Frontiers in Physics* vol. 41 (W.A. Benjamin, Inc., Reading, MA, 1973).
- [jol76] Jolly, D.L., The Anomalous Skin Effect in a Cylindrical Mercury Arc Plasma, *Plas. Phys.* **18**, 337-340 (1976).
- [kau71] Kaufman, A.N. and P.S. Rostler, The Darwin Model as a Tool for Electromagnetic Plasma Simulation, *Phys. Fluids* **14**, 446-448 (1971).
- [kra86] Krall, N.A. and A.W. Trivelpiece, "Principles of Plasma Physics," (San Francisco Press, Inc., San Francisco, CA, 1986).
- [lan70] Langdon, A.B., Effects of the Spatial Grid in Simulation Plasmas, *J. Comput. Phys.* **6**, 247-267 (1970).
- [lan79a] Langdon, A.B., Analysis of the Time Integration in Plasma Simulation, *J. Comput. Phys.* **30**, 202-221 (1979).
- [lan79b] Langdon, A.B., Kinetic Theory for Fluctuations and Noise in Computer Simulation of Plasma, *Phys. Fluids* **22** (1), 163-171 (1979).
- [lan83] Langdon, A.B., B.I. Cohen, and A. Friedman, Direct Implicit Large Time-Step Particle Simulation of Plasmas, *J. Comput. Phys.* **51**, 107-138 (1983).
- [lan85] Langdon, A.B. and D.C. Barnes, Direct Implicit Plasma Simulation in "Multiple Time Scales," *Computational Techniques Series*, (Academic Press, New York, 1985).
- [lar92] Larson, D.J., "Plasma Simulation using the Streamlined Darwin Field Model with Applications to the Generation of Large Transient Potentials within Anisotropic Plasmas," PhD thesis, U. C. Davis, 1992.

- [lib90] Liboff, R.L., "Kinetic Theory: Classical, Quantum, and Relativistic Descriptions," (Prentice-Hall, Inc., Englewood Cliffs, NJ, 1990).
- [lie88] Lieberman, M.A., Analytic Solution for Capacitive RF Sheath, *IEEE Trans. on Plas. Sci.*, **16**, 638-644 (1988).
- [lie94] Lieberman, M.A. and A.J. Lichtenberg, "Principles of Plasma Discharges and Materials Processing," (John Wiley & Sons, Inc., New York, NY, 1994).
- [mas81] Mason, R.J., Implicit Moment Particle Simulation of Plasmas, *J. Comput. Phys.* **41**, 233-244 (1981).
- [mas85] Mason, R.J., Hybrid and Collisional Implicit Plasma Simulation Models in "Multiple Time Scales," Computational Techniques Series, (Academic Press, New York, 1985).
- [met86] Metze, A., D.W. Ernie, and H.J. Oskam, Application of the Physics of Plasma Sheaths to the Modeling of RF Plasma Reactors, *J. Appl. Phys.* **60**, 3081-3087 (1986).
- [mom66] Momota, H., Stability of a Uniform Plasma Composed of Streams in the Absence of an External Field, *Prog. Theor. Phys.* **35**, 380-390 (1966).
- [nie76] Nielson, C.W. and H.R. Lewis, "Particle-Code Methods in the Nonradiative Limit," Methods in Comp. Phys., vol. 16, (Academic Press, New York, 1976).
- [nob77] Noble, B. and J.W. Daniel, "Applied Linear Algebra," (Prentice Hall, Inc. 1977).
- [oku72] Okuda, H., Verification of Theory for Plasma of Finite-Size Particles, *Phys. Fluids* **15**, 1268-1274 (1972).
- [pie92] Piejak, R.B., V.A. Godyak, and B.M. Alexandrovich, A Simple Analysis of an Inductive RF Discharge, *Plas. Sources Sci. Technol.*, **1**, 179-186 (1992).
- [pip49] Pippard, A.B., The High Frequency Skin Resistance of Metals at Low Temperatures, *Physica* **15**, 45-54 (1947).
- [pre89] Press, Flannery, Teukolsky, and Vetterling, "Numerical Recipes," (Cambridge University Press, Cambridge, 1989).
- [rei79] Reitz, J.R., F.J. Milford, and R.W. Christy, "Foundations of Electromagnetic Theory," (Addison-Wesley, Reading, MA, 1979).
- [reu49] Reuter, G.E.H. and E. H. Sondheimer, The Theory of the Anomalous Skin Effect in Metals, *Proc. Roy. Soc. A* **195**, 336-364 (1949).
- [rey69] Reynolds, J.A., H.A. Blevin, and P.C. Thonemann, Anomalous Skin Effect in Bounded Plasmas, *Phys. Rev. Lett.* **22**, 762-764 (1969).
- [roa76] Roache, P.J., "Computational Fluid Dynamics," p42. (Hermosa Publishers, Albuquerque, NM, 1976).

- [sch79] Schmidt, G., "Physics of High Temperature Plasmas," (Academic Press, NY, 1979).
- [sel63] Self, S.A., Exact Solution of the Collisionless Plasma-Sheath Equation, *Phys. Fluids* **6**, 1762-1768 (1963).
- [sgr76] Sgro, A.G. and C.W. Nielson, *Phys. Fluids* **19**, 126 (1976).
- [ste93] Stewart, R.A., P. Vitello, D.B. Graves, E.F. Jaeger, and L.A. Berry, Plasma Uniformity in High Density Inductively Coupled Plasma Tools, *40th Nat. Symp. of the Amer. Vac. Soc.*, Orlando, FL, November 15-19, 1993.
- [tan93] Tanaka, M., A Simulation of Low-Frequency Electromagnetic Phenomena in Kinetic Plasmas of Three Dimensions, *J. Comput. Phys.* **107**, 124-145 (1993).
- [tho27] Thomson, J.J., The Electrodeless Discharge through Gases, *Phil. Mag.* **4**, 1128-1140 (1927).
- [ton29] Tonks, L. and I. Langmuir, A General Theory of the Plasma of an Arc, *Phys. Rev.* **34**, 876-922 (1929).
- [tur93] Turner, M.M., Collisionless Electron Heating in an Inductively Coupled Discharge, *Phys. Rev. Lett.* **71**, 1844-1847 (1993).
- [vah93] Vahedi, V., "Modeling and Simulation of RF Discharges Used for Plasma Processing," Ph.D. thesis, U.C. Berkeley, 1993.
- [vah94] V. Vahedi, M.A. Lieberman, G. DiPeso, T.D. Rognlien, and D. Hewett, Analytic Model of Power Deposition in Inductively Coupled Plasma Sources, *submitted to J. Appl. Phys.* (1994).
- [wei59] Weibel, E.S., Spontaneously Growing Transverse Waves in a Plasma due to an Anisotropic Velocity Distribution, *Phys. Rev. Lett.* **2**, 83-84 (1959).
- [wei67] Weibel, E.S., Anomalous Skin Effect in a Plasma, *Phys. Fluids* **10**, 741-748 (1967).
- [wen93] Wendt, A.E., L.J. Mahoney, C.J. Richards, and J.L. Shohet, Electron Density and Energy Distributions in a Planar Inductively Coupled Plasma, presented at the *AVS 2nd Workshop on High Density Plasmas*, San Francisco, CA, August 1993.
- [yu65] Yu, S.P., G.P. Kooyers, and O. Buneman, A Time Dependent Computer Analysis of Electron-Wave Interaction in Crossed-Fields, *J. Appl. Phys.* **36**, 2550-2559 (1965).